Rangin, C., Silver, E., von Breymann, M. T., et al., 1990
Proceedings of the Ocean Drilling Program, Initial Reports, Vol. 124

11. SITE 768[1]

Shipboard Scientific Party[2]

HOLE 768A

Date occupied: 27 November 1988

Date departed: 27 November 1988

Time on hole: 18 hr, 30 min

Position: 8°00.05′N, 121°13.16′E

Bottom felt (rig floor; m, drill-pipe measurement): 4395.5

Distance between rig floor and sea level (m): 11.10

Water depth (drill-pipe measurement from sea level, m): 4384.4

Total depth (rig floor; m): 4405.00

Penetration (m): 9.50

Number of cores (including cores with no recovery): 1

Total length of cored section (m): 9.50

Total core recovered (m): 8.80

Core recovery (%): 92

Oldest sediment cored:
Depth (mbsf): 8.80
Nature: nannofossil marl with foraminifers
Age: Pleistocene
Measured velocity (km/s): data not available (see text)

HOLE 768B

Date occupied: 28 November 1988

Date departed: 30 November 1988

Time on hole: 2 days, 10 hr, 45 min

Position: 8°00.05′N, 121°13.19′E

Bottom felt (rig floor; m, drill-pipe measurement): 4395.5

Distance between rig floor and sea level (m): 11.10

Water depth (drill-pipe measurement from sea level, m): 4384.4

Total depth (rig floor; m): 4759.60

Penetration (m): 364.10

Number of cores (including cores with no recovery): 40

Total length of cored section (m): 364.10

Total core recovered (m): 293.79

Core recovery (%): 81

Oldest sediment cored:
Depth (mbsf): 354.4
Nature: clay
Age: late Miocene
Measured velocity (km/s): 1.57

HOLE 768C

Date occupied: 1 December 1988

Date departed: 13 December 1988

Time on hole: 11 days, 16 hr, 45 min

Position: 8°00.04′N, 121°13.18′E

Bottom felt (rig floor; m, drill-pipe measurement): 4395.5

Distance between rig floor and sea level (m): 11.10

Water depth (drill-pipe measurement from sea level, m): 4384.4

Total depth (rig floor; m): 5666.5

Penetration (m): 1271.0

Number of cores (including cores with no recovery): 100

Total length of cored section (m): 915.00

Total core recovered (m): 525.69

Core recovery (%): 57

Oldest sediment cored:
Depth (mbsf): 1046.60
Nature: claystone interbedded with fine tuff
Age: early Miocene
Measured velocity (km/s): 2.63

Basement:
Depth (mbsf): 1046.60
Nature: pillow basalts and dolerite sills
Measured velocity (km/s): 3.41

Principal results: Three holes were drilled at Site 768 (8°00.0′N, 121° 13.2′E, water depth 4384.4 mbsl) in the Sulu Sea (Table 1). The Sulu Sea originated as a back-arc basin in the late(?) early Miocene, although its exact timing must await basement dating because of uncertainties in the age of the basal sediments. At Site 768, initial radiolarian-bearing red clay was deposited on basement, followed by 250 m of pyroclastic flows. The depositional depth of the tuffs is not known for certain, but the presence of radiolarian red clay just above and below the tuffs could indicate abyssal depths below the carbonate compensation depth (CCD).

The source of the pyroclastic rocks is not known for certain. The sedimentary section increases in thickness toward the west, and the lower units show bottom lap-out to the east on the seismic records, tentatively implying a Cagayan source. Red-clay deposition continued above the tuffs, for about 30 m, after which the dominant lithology was greenish claystone. Sands and silts are abundant in the claystone, indicating much turbidity current deposition. Quartz is abundant in lithologic Units II and III, and metamorphic grains are present, indicating a continental source.

The clay mineralogy shows high illite and low smectite in these units, reversing in Unit I, again representing a dominant continental source in Units II and III. Increasing turbidites and the stratigraphic hiatus in Unit III could record the collision of the Cagayan Ridge with the north Palawan Ridge. Renewal of volcanism began during NN11 at 255 mbsf, but major volcanism was noticed in the Pleistocene, associated with higher oceanic productivity. The onset of volcanism and the decrease in terrigenous turbidites may coincide with the development of the Sulu Trench. High terrigenous influx from middle Miocene through the Pliocene may coincide with the collision of Dangerous Grounds with the Cagayan Ridge and the more recent collision of the Philippine Mobile Belt with the Cagayan, Palawan, and Sulu ridges.

[1] Rangin, C., Silver, E., von Breymann, M. T., et al., 1990. *Proc. ODP, Init. Repts.*, 124: College Station, TX (Ocean Drilling Program).
[2] Shipboard Scientific Party is as given in the list of participants preceding the contents.

Table 1. Coring summary, Site 768.

Core no.	Date (Nov. 1988)	Time (UTC)	Depth (mbsf)	Cored (m)	Recovered (m)	Recovery (%)
124-768A-						
1H	27	2120	0-9.5	9.5	8.80	92.6
Coring totals				9.5	8.80	92.6
124-768B-						
1H	28	0400	0-4.0	4.0	3.89	97.2
2H	28	0530	4-13.5	9.5	9.98	105.0
3H	28	0630	13.5-23.0	9.5	9.98	105.0
4H	28	0730	23.0-32.5	9.5	10.15	106.8
5H	28	0845	32.5-42.0	9.5	9.70	102.0
6H	28	0945	42.0-51.5	9.5	10.00	105.2
7H	28	1045	51.5-61.0	9.5	9.91	104.0
8H	28	1145	61.0-70.5	9.5	9.95	105.0
9H	28	1235	70.5-80.0	9.5	10.04	105.7
10H	28	1330	80.0-89.5	9.5	10.08	106.1
11H	28	1423	89.5-99.0	9.5	10.04	105.7
12H	28	1530	99.0-108.5	9.5	10.08	106.1
13H	28	1615	108.5-118.0	9.5	10.05	105.8
14H	28	1720	118.0-127.5	9.5	10.08	106.1
15H	28	1825	127.5-137.0	9.5	9.91	104.0
16H	28	1920	137.0-146.5	9.5	9.74	102.0
17H	28	2015	146.5-156.0	9.5	10.13	106.6
18H	28	2110	156.0-165.5	9.5	10.05	105.8
19H	28	2155	165.5-173.8	8.3	8.34	100.0
20H	28	2310	173.8-183.3	9.5	10.07	106.0
21H	29	0015	183.3-192.8	9.5	9.62	101.0
22H	29	0140	192.8-201.0	8.2	8.21	100.0
23H	29	0245	201.0-209.2	8.2	8.21	100.0
24H	29	0335	209.2-209.6	0.4	0.38	95.0
25X	29	0500	209.6-219.3	9.7	0.60	6.2
26X	29	0550	219.3-228.9	9.6	4.24	44.1
27X	29	0640	228.9-238.6	9.7	4.65	47.9
28X	29	0740	238.6-248.2	9.6	8.42	87.7
29X	29	0835	248.2-257.8	9.6	6.00	62.5
30X	29	0930	257.8-267.5	9.7	3.76	38.7
31X	29	1035	267.5-277.2	9.7	9.77	101.0
32X	29	1130	277.2-286.8	9.6	3.66	38.1
33X	29	1230	286.8-296.4	9.6	5.43	56.5
34X	29	1330	296.4-306.1	9.7	3.88	40.0
35X	29	1530	306.1-315.8	9.7	3.79	39.1
36X	29	1730	315.8-325.5	9.7	5.08	52.4
37X	29	1940	325.5-335.1	9.6	4.56	47.5
38X	29	2155	335.1-344.8	9.7	6.18	63.7
39X	29	2355	344.8-354.4	9.6	5.18	53.9
40X	30	0150	354.4-364.1	9.7	0	0
Coring totals				364.1	293.79	80.7
124-768C-						
1R	2	0425	353.2-362.9	9.7	6.68	68.8
2R	2	0525	362.9-372.4	9.5	6.49	68.3
3R	2	0630	372.4-382.1	9.7	1.00	10.3
4R	2	0725	382.1-391.8	9.7	1.76	18.1
5R	2	0815	391.8-401.4	9.6	4.78	49.8
6R	2	0930	401.4-411.1	9.7	4.13	42.6
7R	2	1040	411.1-420.7	9.6	8.11	84.5
8R	2	1140	420.7-430.2	9.5	4.65	48.9
9R	2	1245	430.2-439.9	9.7	3.59	37.0
10R	2	1345	439.9-449.6	9.7	4.84	49.9
11R	2	1445	449.6-459.2	9.6	7.32	76.2
12R	2	1545	459.2-468.9	9.7	1.98	20.4
13R	2	1715	468.9-478.5	9.6	5.38	56.0
14R	2	1815	478.5-488.2	9.7	5.87	60.5
15R	2	1920	488.2-497.9	9.7	5.39	55.5
16R	2	2030	497.9-507.5	9.6	1.67	17.4
17R	2	2140	507.5-517.2	9.7	5.97	61.5
18R	2	2300	517.2-526.9	9.7	5.73	59.1
19R	3	0005	526.9-536.6	9.7	2.97	30.6
20R	3	0100	536.6-546.3	9.7	5.18	53.4
21R	3	0210	546.3-555.8	9.5	1.86	19.6
22R	3	0320	555.8-565.5	9.7	3.52	36.3
23R	3	0440	565.5-575.2	9.7	7.11	73.3
24R	3	0545	575.2-584.9	9.7	7.05	72.7
25R	3	0715	584.9-594.6	9.7	0.07	0.7
26R	3	0900	594.6-604.3	9.7	8.97	92.5
27R	3	1045	604.3-613.9	9.6	8.73	90.9
28R	3	1210	613.9-623.5	9.6	9.29	96.8

Table 1 (continued).

Core no.	Date (Nov. 1988)	Time (UTC)	Depth (mbsf)	Cored (m)	Recovered (m)	Recovery (%)
124-768C- (Cont.)						
29R	3	1430	623.5-633.1	9.6	9.28	96.6
30R	3	1615	633.1-642.8	9.7	9.19	94.7
31R	3	1745	642.8-652.4	9.6	6.40	66.6
32R	3	1925	652.4-662.1	9.7	8.60	88.6
33R	3	2115	662.1-671.8	9.7	8.24	84.9
34R	3	2340	671.8-681.4	9.6	9.29	96.8
35R	4	0130	681.4-691.1	9.7	7.91	81.5
36R	4	0300	691.1-700.8	9.7	9.21	94.9
37R	4	0455	700.8-710.5	9.7	8.37	86.3
38R	4	0630	710.5-720.2	9.7	5.16	53.2
39R	4	0800	720.2-729.9	9.7	6.36	65.5
40R	4	0920	729.9-739.6	9.7	6.08	62.7
41R	4	1030	739.6-749.3	9.7	9.17	94.5
42R	4	1135	749.3-758.5	9.2	4.96	53.9
43R	4	1245	758.5-768.1	9.6	3.84	40.0
44R	4	1430	768.1-777.7	9.6	4.72	49.1
45R	4	1610	777.7-787.4	9.7	4.16	42.9
46R	4	1730	787.4-796.9	9.5	2.25	23.7
47R	4	1900	796.9-806.6	9.7	1.83	18.8
48R	4	2045	806.6-815.5	8.9	7.73	86.8
49R	4	2250	815.5-825.2	9.7	9.93	102.0
50R	5	0030	825.2-834.9	9.7	4.68	48.2
51R	5	0215	834.9-844.6	9.7	6.87	70.8
52R	5	0340	844.6-854.3	9.7	8.08	83.3
53R	5	0510	854.3-864.0	9.7	8.81	90.8
54R	5	0635	864.0-873.7	9.7	7.02	72.4
55R	5	0825	873.7-883.4	9.7	4.81	49.6
56R	5	0950	883.4-893.1	9.7	8.82	90.9
57R	5	1130	893.1-902.4	9.3	0.92	9.9
58R	5	1250	902.4-912.0	9.6	8.00	83.3
59R	5	1415	912.0-921.7	9.7	9.33	96.2
60R	5	1630	921.7-931.4	9.7	9.63	99.3
61R	5	1845	931.4-941.0	9.6	6.45	67.2
62R	5	2030	941.0-950.3	9.3	5.40	58.0
63R	5	2230	950.3-960.0	9.7	9.84	101.0
64R	6	0020	960.0-969.7	9.7	3.29	33.9
65R	6	0225	969.7-979.4	9.7	7.44	76.7
66R	6	0455	979.4-989.0	9.6	6.18	64.4
67R	6	0655	989.0-998.7	9.7	9.90	102.0
68R	6	0835	998.7-1008.3	9.6	8.83	92.0
69R	6	1015	1008.3-1017.6	9.3	6.93	74.5
70R	6	1205	1017.6-1027.2	9.6	6.18	64.4
71R	6	1345	1027.2-1036.9	9.7	6.08	62.7
72R	6	1530	1036.9-1046.6	9.7	2.18	22.5
73R	6	1800	1046.6-1056.3	9.7	0.98	10.1
74R	6	2045	1056.3-1065.9	9.6	1.73	18.0
75R	6	2300	1065.9-1075.6	9.7	2.18	22.5
76R	7	0050	1075.6-1080.6	5.0	2.93	58.6
77R	7	0240	1080.6-1085.6	5.0	2.33	46.6
78R	7	0450	1085.6-1090.6	5.0	2.21	44.2
79R	7	0640	1090.6-1095.6	5.0	2.78	55.6
80R	7	0800	1095.6-1100.6	5.0	3.10	62.0
81R	7	0940	1100.6-1105.6	5.0	2.48	49.6
82R	7	1115	1105.6-1110.6	5.0	1.93	38.6
83R	7	1245	1110.6-1115.6	5.0	3.20	64.0
84R	7	1430	1115.6-1120.6	5.0	3.23	64.6
85R	7	1630	1120.6-1126.6	6.0	1.77	29.5
86R	7	1900	1126.6-1136.3	9.7	3.23	33.3
87R	7	2145	1136.3-1146.0	9.7	2.45	25.2
88R	8	0045	1146.0-1155.7	9.7	2.84	29.3
89R	8	0300	1155.7-1165.3	9.6	6.03	62.8
90R	8	0520	1165.3-1174.9	9.6	8.34	86.9
91R	8	0740	1174.9-1184.5	9.6	2.15	22.4
92R	8	1050	1184.5-1191.5	7.0	4.38	62.6
93R	8	1415	1191.5-1200.7	9.2	4.95	53.8
94R	8	1735	1200.7-1210.4	9.7	1.34	13.8
95R	8	1945	1210.4-1220.0	9.6	2.02	21.0
96R	8	2145	1220.0-1229.7	9.7	3.63	37.4
97R	8	2350	1229.7-1239.4	9.7	3.82	39.4
98R	9	0150	1239.4-1249.1	9.7	4.63	47.7
99R	9	0345	1249.1-1258.5	9.4	4.24	45.1
100R	9	0610	1258.8-1268.5	9.7	2.35	24.2
Coring totals				915.0	525.69	57.5

Note: Depths are drill-pipe measurements corrected to sea level.

Paleomagnetic results recorded an excellent reversal stratigraphy through the Gilbert (5 Ma), and possibly Reversals 5D and 5E in the tuffs of Unit IV. We recorded the Cobb Mountain Event at 1.1 Ma. Logging was successful, including the seismic stratigraphy and lithodensity logs, plus a very good borehole televiewer (BHTV) log in the basement and the tuffs. The logs matched the results from physical properties measurements well, including a major velocity increase between the pillow basalts and upper sill, which we recognized as acoustic basement on the seismic line. Borehole breakouts were prominent in the basement, both in the sill, the pillows, and in the upper 60 m of the tuffs. Basement breakouts trended approximately 300°, indicating a maximum horizontal stress direction of 30°.

A good correspondence between the maturity of the organic material and the generation of thermogenic hydrocarbons was observed. The organic-lean pyroclastic sequence shows high gas concentrations, indicating migration of light hydrocarbons.

The drilling results at Site 768 demonstrate a back-arc spreading origin for the Sulu Sea in early Neogene time; an origin by trapping in the Paleogene can be ruled out. The complex depositional history of the continent-derived turbidites and brown clays, as well as the stratigraphic hiatus recorded in the sequence, provide a complete record of the Neogene subduction and collisions surrounding the Sulu Sea.

BACKGROUND AND OBJECTIVES

The Sulu Sea is rimmed by structurally complex continental platforms and volcanic ridges (Figs. 1–3). The Palawan and Sulu ridges trend northeastward and connect to the south with northern Borneo. These two ridges are separated by the Sulu Sea and collide to the northeast with the Philippine Mobile Belt (Luzon-Visayas-Mindanao). These twin-pronged collisions have left the Sulu Sea with a shallow sill depth of 200 m and have provided potential sediment sources to the basin from all sides. Because of its position interior to these platforms and ridges, the Sulu Sea is expected to record the complex history of collision, subduction, and rifting that appears to have characterized the Philippine region during the Neogene. Drilling Site 768 was designed to determine that history.

Two deep basins are present between these ridges and are divided by the Cagayan Ridge, a prominent east-northeast-trending underwater relief, considered to be volcanic in origin. The Northwest Sulu Basin is a thick pile of folded sediments topped disconformably by undeformed clastics dated middle Miocene at their base. The Southeast Sulu Basin is characterized by a fairly flat acoustic basement blanketed by no more than 1 km of horizontally layered sediment. This basin is presently subducting southward below the Sulu Archipelago (Fig. 2).

Several different hypotheses have been put forth for the origin of the Southeast Sulu Basin. One is back-arc spreading behind the Sulu or Cagayan ridges (Holloway, 1981; Mitchell et al., 1986; Rangin, 1989). A second is a trapped marginal basin from a once much-larger ocean basin (Lee and McCabe, 1986). A third could be initial rifting of the China mainland, associated with the development of the South China Sea.

Determining the age of the Sulu Sea can provide constraints on these alternative origins. Back-arc rifting behind Cagayan Ridge is not expected to be younger than the age of collision with Dangerous Grounds, thought to be about 15 Ma. A younger age would imply rifting behind the Sulu Ridge. An age of early Miocene would be consistent with back-arc rifting behind either the Sulu or Cagayan ridges. A mid-Oligocene age is consistent with back-arc rifting behind either ridge, or rifting associated with the opening of the South China Sea. An age of middle Eocene would support the Lee and McCabe (1986) hypothesis of a trapped marginal basin related to a larger ocean basin, whereas any other age would negate their magnetic anomaly interpretation (Fig. 3).

The stratigraphy will help sort out some of these alternatives as well. A trapped ocean basin of any age should show sediments of the open ocean grading upward to those of an enclosed basin. A rifted back-arc basin should show evidence of growth through time: initial volcaniclastic sedimentation, followed by finer turbidites with sequences that represent the history of the basin. An origin related to rifting of the China margin should show evidence of early continental provenance, becoming rapidly more isolated from that source. The latter provenance will have to be discriminated from that of the basement of the Philippines, which should be present in any case. Finally, basement geochemistry will be used to discriminate arc signature from mid-ocean ridge basalts (MORB).

The deep crust of the Sulu Sea is rather thin (5.8 km), on the basis of refraction data (Murauchi et al., 1973; Fig. 4). Seismic reflection data (Mascle and Biscarrat, 1978) reveal that the acoustic basement is locally marked by southeast-facing tilted blocks. Heat flow values (Sclater et al., 1976) are high (80–180 mW/m^2), implying that the crust is young, probably mid-Tertiary in age. Rocks dredged along a submarine ridge northwest of Site 768 have an arc-tholeiite or MORB-type geochemical signature (Kudrass et al., this volume). A petrologic objective at Site 768 was to determine if the basin represents structurally thinned arc crust or true back-arc spreading.

The undisturbed sedimentary section we drilled at Site 768 was expected to record successive collision processes along the margins of this small basin during Neogene time. In addition to the middle Miocene collision of the Cagayan Ridge with the North Palawan-Reed Bank microcontinent, sedimentation into the Sulu Sea would have recorded the active late Neogene collision of the Philippine Mobile Belt with the rifted South China Sea continental margin.

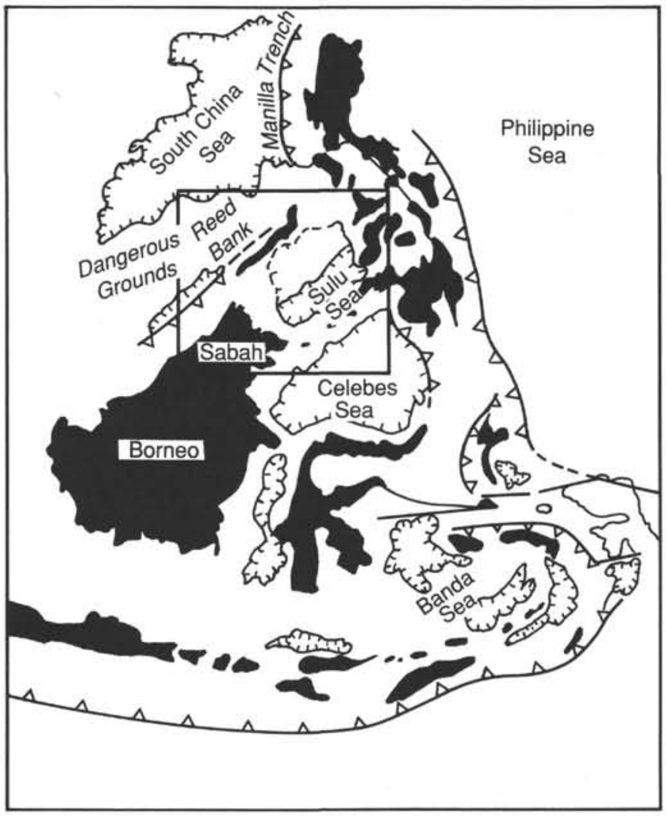

Figure 1. Simplified map of the Sulu Sea. An expanded map of the outlined section is shown in Figure 2.

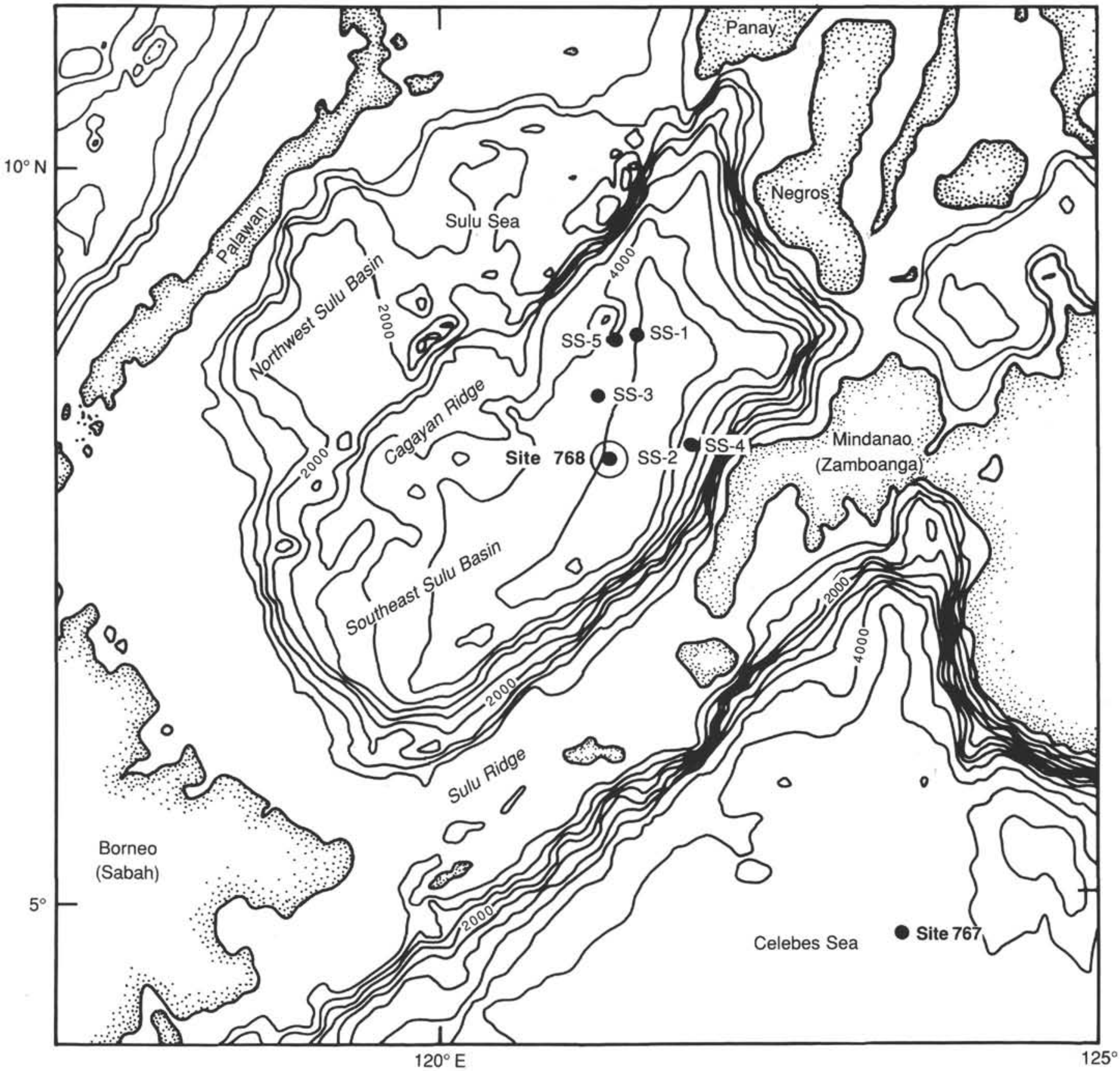

Figure 2. Bathymetric map of the Sulu Sea with proposed Sites SS-1 to SS-5 and location of Site 768.

The Philippine Mobile Belt, elongated north-south from Luzon in the north to Mindanao in the south, is one of the best examples of amalgamation of exotic terranes along a continental margin. The exotic origin of this belt relative to the China mainland or to the rifted fragments of this margin (North Palawan-Reed Bank-Dangerous Grounds) has been documented by stratigraphic and tectonic studies (Karig, 1983; Mitchell et al., 1986, Stephan et al., 1986), and paleomagnetic studies (McCabe and Cole, 1988). The exotic belt extends far to the south in Halmahera (Hall, 1988; Hall et al., 1988). Most of the exotic terranes were probably amalgamated before the late Oligocene far from their present position (Jolivet et al., 1989) and then drifted en masse before collision with the Eurasian Plate. Drilling at Site 768 would allow dating the age of clastic deposition in the basin derived from this collision.

Paleoceanographic Objectives

A major objective was to establish the stratigraphic history of the basin, particularly to determine if its paleoenvironment reflects a basin with an open, closed, or restricted circulation. Are these expected changes caused by collision processes or by independent paleoceanographic events? Another important aspect was to recognize in this deep-seated basin the sedimentary gaps observed in the biostratigraphic record along the margins of the basin, particularly in the central Philippines (Müller and Daniel, 1981).

Determination of Regional Stress

The Sulu Sea is being subducted beneath the Sulu Ridge along the Sulu Trench on its southeast side. It is also subducting

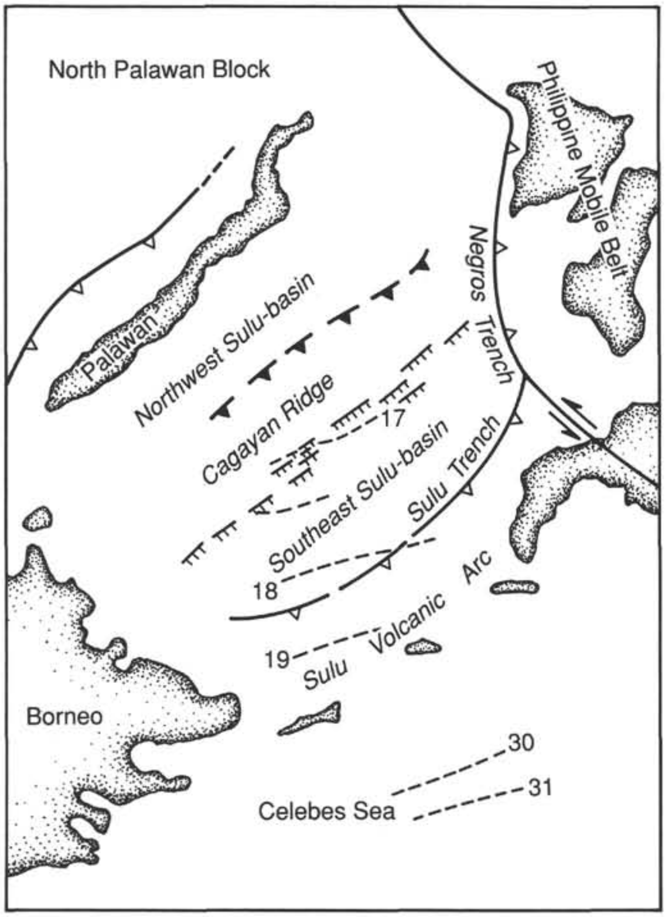

Figure 3. Structural sketch map of the Sulu Sea. Magnetic anomalies identified by Lee and McCabe (1986) are reported.

beneath Negros and Panay islands on its northeast side. At present, it is integrally part of the Cagayan Ridge, northwest Sulu Basin, and the Palawan, which are all colliding with the Philippine Mobile Belt between Panay and Mindoro. The degree of coupling between the Sulu Basin and the adjacent subduction zones is not known. Stress orientation measurements in the Sulu Sea are designed to determine whether southeast- or northeast-directed convergence most impacts the Sulu Basin, or the degree to which the two effects add vectorially. Does the collisional effect overwhelm other stresses? Is stress concentrated at the indentors, leaving the Sulu Basin in a state of reduced stress? Stress magnitude, measured by hydrofracture, will tell us the degree to which the rocks undergo tectonic stress in excess of lithostatic.

The Sulu Sea has been subjected to a complex stress system associated with convergent motion between the Eurasian and Australian plates during the Cenozoic, and more recently convergence between Eurasia and the Philippine Sea Plate. Stress measurement only tells us about instantaneous stresses, but an understanding of the stress field in the modern kinematic setting can be useful for inferring a stress history based largely on kinematics.

Site Selection

The site is located in the western part of the Sulu Sea, where the sedimentary section laps onto a tilted basement block. Site 768 was preferred because basement is less deep, and the arc affinity of rocks dredged just to its southeast makes the other site considered less desirable for obtaining oceanic crust (see "Seismic Stratigraphy" section, this chapter, and Hinz and Block, this volume). Site 768 is located on MCS Line SO49-05, at shotpoint 1723 in a water depth of 4384 mbsl. Acoustic basement is smooth, dipping slightly to the northwest. The overlying sedimentary section appears complete and is approximately 1000 m thick. The lower part of the sedimentary section thickens toward bounding faults, which indicates that sedimentation took place during faulting. Overlying sediments truncate the tilted lower section. These observations indicate that the site selected was appropriate for an investigation of the pre-rift, syn-rift, and post-rift stages that correspond to the opening history of this basin.

OPERATIONS

Site 768 (proposed Site SS-2) is located in the southeastern Sulu Sea, about 55 nmi west-northwest of Dulunguin Point on the Zamboanga Peninsula (Island of Mindanao). Most of the transit to the new site was made while surveying at reduced speed to adjust the arrival schedule to the global positioning system (GPS) operating window. The records obtained during the survey are presented in the "Undersea Geophysics" chapter (this volume) and discussed in the "Seismic Stratigraphy" section (this chapter).

The site location was critical, and three beacons and over 8 hr were required before a satisfactory launch was made. The first beacon signal failed shortly after launch, and the second beacon was dropped out of position. Official site arrival was at 0815 hr (UTC), 27 November 1988.

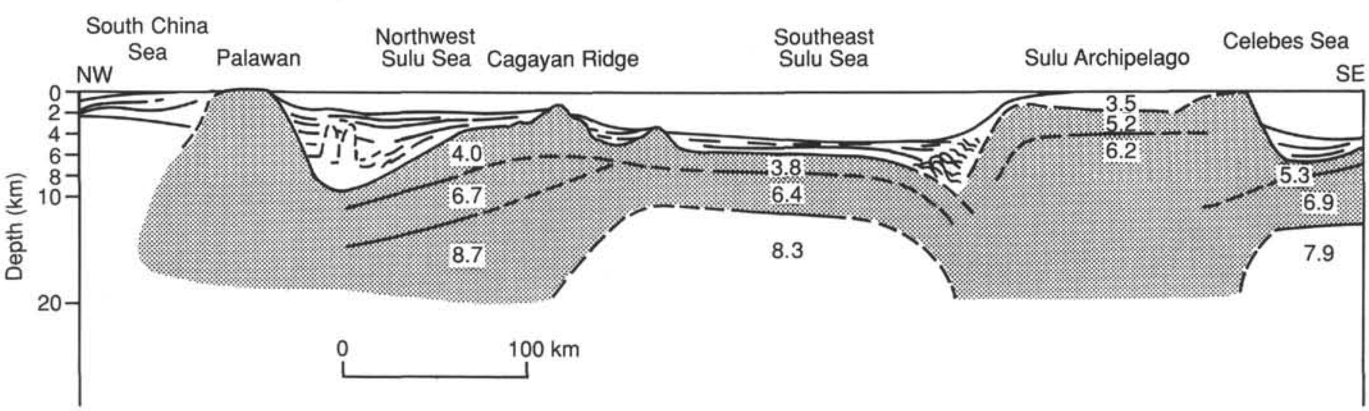

Figure 4. Seismic refraction section of the Sulu Sea (from Murauchi et al., 1973 and Mascle and Biscarrat, 1978).

Hole 768A

Hole 768A was spudded with a seafloor advanced hydraulic piston corer (APC) at 2045 hr (UTC), 27 November 1988. The depth established by the "mud-line" core was 4384.4 mbsl, which compares with a precision depth recorder (PDR) depth of 4406 mbsl. The initial core was followed by a jetting test to determine the conductor casing point for the planned reentry installation. The bit was jetted to 99 mbsf before it was stopped in stiff sediments. We then drilled an additional 2 m for a temperature probe run. The temperature measurement, as at Site 767, again failed to provide usable data (see "Operations" section, "Site 767" chapter, this volume).

The core bit was then pulled above the seafloor in preparation for the APC/extended core barrel (XCB) hole that would also serve as the exploratory penetration for the eventual reentry hole.

Hole 768B

Continuous APC cores were taken to 210 mbsf, where refusal was reached when the corer failed to penetrate a hard-sand layer. Core quality and recovery were excellent. Recovery, aided by some core swelling, averaged 104% for the interval.

We continued XCB coring in clay, with reduced recovery because of the interbeds of silt, hard chalk, sand, and ash. Hole conditions remained good, with the sediment becoming firmer with depth. Core 124-768B-40X was retrieved from a total depth of 364 mbsf with a failed cutter shoe. The lower (cutting structure) part of the shoe had broken off completely, allowing the core catchers, spacers, and core to fall out of the inner barrel assembly.

At about the time the XCB coring ceased, a medical emergency arose; the ship's Third Officer apparently contracted acute appendicitis. Attempts by the ship's Manila agent to arrange an on-site helicopter for evacuation were unsuccessful, and it was necessary for the vessel to get underway and proceed to a roadstead off Zamboanga. The patient was evacuated by a Philippine Air Force helicopter at 2300 hr (UTC), 30 November 1988, and was flown to Manila, where he underwent surgery later in the day. The total delay for the medical evacuation was 17 hr.

Hole 768C

The vessel navigated back to Site 768 and detected the positioning beacon signal without difficulty. Hole 768C was spudded at 1800 hr (UTC), 1 December 1988, and was drilled to 353 mbsf with no coring. Continuous RCB coring then began and proceeded with generally good recovery through clay interbedded with silty and sandy strata. The sediments increased in induration and volcanogenic components below 600 mbsf.

Hole conditions remained excellent. At about 900 mbsf, the sediments gave way to about 200 m of massive volcanic tuffs that cored easily and produced excellent core recovery. Basaltic basement was encountered at about 1046 mbsf, but the rate of penetration remained high in the highly altered pillow basalt flows. At 1271 mbsf, we met our scientific drilling objectives, and coring ceased.

In preparation for logging, the hole was conditioned by a wiper trip. The bit was released, and the hole was filled with KCl-inhibited bentonite mud. With the pipe set in the upper tuffs at 809.5 mbsf, the BHTV-temperature tools were run downhole to a firm bridge at 870.5 mbsf. Upcoming logs were obtained for 870.5–809.5 mbsf.

The pipe was pulled up to about 100 mbsf, and the sidewall entry sub and seismic stratigraphic tool string were rigged up. At this site the seismic stratigraphic combination consisted of Schlumberger long-spaced sonic, phasor resistivity, and natural gamma-ray tools plus the L-DGO temperature tool.

Downgoing logs were obtained through pipe from the seafloor to 181.5 mbsf and open-hole from 181.5 mbsf to a firm bridge at 231.5 mbsf. The pipe was then run downhole to 1060.4 mbsf, and downgoing logs were obtained from 1083.6 to 1260.5 mbsf. Open-hole upcoming logs were obtained from 1260.5 to 689.5 mbsf while pulling pipe. At 689.5 mbsf the tool string stuck, and it was necessary to lower pipe around the tool while it circulated to free it. With the tool in pipe, pipe was raised to 604.5 mbsf. We then lowered the tool into the open hole and resumed logging while pulling pipe. Open-hole logs were obtained for the interval from 634.5 to 124.8 mbsf, and through-pipe logs were obtained for the interval from 124.8 to 0.0 mbsf.

With pipe set at 1088.5 mbsf, the borehole televiewer was lowered to 1249.9 mbsf for a second run. Upcoming logs were obtained from 1249.9 to 949.1 mbsf, partially while pulling pipe.

The Schlumberger geochemical combination was rigged up, but this run was aborted while still in pipe at 954 mbsf because of failure of the gamma-ray spectroscopy tool. Troubleshooting undertaken during a minicone drop was unsuccessful, so the geochemical combination was rigged down and the Schlumberger lithoporosity combination was rigged up instead. At this site the lithoporosity combination consisted of general-purpose inclinometer, lithodensity, neutron porosity, and natural gamma-ray tools. Downgoing logs were obtained through pipe from 0 to 1088.5 mbsf and in the open hole from 1088.5 to 1235.5 mbsf. Upcoming logs were obtained in the open hole from 1257.5 to 764.5 mbsf. We experienced strong drags during the final 50 m of this interval, and the tool stuck at 764.5 mbsf. Pipe was lowered to free the tool, the tool was raised into pipe, and pipe was raised to 604.5 mbsf. After lowering the tool into the open hole and as far down as the first bridge, open-hole logs were obtained from 645.8 to 124.8 mbsf while pulling pipe. Through-pipe logs were obtained from 124.5 to 0 mbsf.

Rig down from logging was completed at 1220 hr (UTC) on 12 December 1988, 3.2 days after the start of hole conditioning. A free-fall funnel (FFF) was deployed in anticipation of the hydrofracture experiment, another BHTV was run, and geochemistry logged. The underwater TV camera was run down the drill string to observe the retraction from the hole. The funnel and its floating reflectors were clearly visible.

The drill string was recovered, but the planned trip and reentry for the hydrofracture experiment had to be deferred, since a second medical emergency had developed. The ship's doctor had become ill with an acute abdominal condition and required evacuation to a hospital. No long-range helicopters were available, so the vessel headed toward Zamboanga, where the doctor was taken ashore in the ship's inflatable Zodiac boat. The vessel was underway from Zamboanga at 0800 hr (UTC), 13 December 1988. Because of scientific priorities, the ship proceeded to prospectus Site SS-5 (later renamed Site 769) instead of returning for the hydrofracture and additional logging at Hole 768C.

LITHOSTRATIGRAPHY

Sedimentary Units

The sedimentary section overlying the basaltic basement at Site 768 is 1046.6 m thick. The section can be divided into five lithologic units (Table 2 and Fig. 5) on the basis of visual descriptions and smear slide analyses of the recovered core. Figure 6 shows variations in relative abundance vs. depth for several key sediment components that are indicators of varying provenance within the sequence.

Unit I

Depth: 0–122.5 mbsf
Interval: Core 124-768B-1H through Section 124-768B-14H-3

Table 2. Lithologic units, Site 768.

Unit	Depth (mbsf)	Thickness (m)	Age
I	0–123.0	122.5	late Pliocene to Holocene
II	122.5–652.4	529.9	middle Miocene to late Pliocene
III	652.4–806.6	154.2	early to middle Miocene
IV	806.6–1003.6	197.0	early Miocene
V	1003.6–1046.6	43.0	early Miocene

Thickness: 122.5 m
Age: late Pliocene to Holocene

Unit I consists of thin- to thick-bedded marl with varying proportions of nannofossils and foraminifers, and sparse thin beds of volcanic ash. The marl beds are greenish gray to gray and are mostly massive and bioturbated (Fig. 7). Some thin to medium beds display normally graded bedding, planar lamination, and rare convolute and cross lamination (Fig. 8). Planktonic foraminifers and fewer benthic foraminifers as well as nannofossils, and clay are the principal components of the marl. The minor components are siliceous biogenic material (spicules, diatoms, radiolarians, and silicoflagellates), bioclasts, and volcanic detritus (glass, rock fragments, feldspar, and hornblende). The carbonate ($CaCO_3$) content of the sediment averages 40% (see "Inorganic Geochemistry" section, this chapter).

Most of the marl is interpreted as pelagic sediment because it is predominantly massive and bioturbated. Deposition must have taken place above the CCD, which currently is deeper than the water depth (4384.4 mbsl) at Site 768. However, some beds show features that indicate deposition by turbidity currents. These beds have sharp bases with concentrations of coarser foraminifers and bioclasts near the base, are normally graded, and show planar and convolute lamination. Bioturbation is only present in the upper portion of these beds. The proportion of recognized turbidite beds is 7% of the thickness of Unit I, but this is a minimum estimate because the structures that display possible deposition by density currents may have been destroyed by bioturbation or drilling disturbance.

The ash layers in Unit I are thin to very thin, normally graded beds of sand- to silt-size material that lack internal lamination, except for rare beds with planar lamination. The beds have sharp bases, and the tops are gradational as a result of bioturbation (Fig. 9). Volcanic ash also appears in irregular patches within the marl because of bed disturbance by bioturbation.

The ash beds consist of variable proportions of volcanic glass, lithic fragments, and crystals (plagioclase, hornblende, pyroxene, opaque minerals, and biotite). In the upper part of Unit I (0–45 mbsf), dark gray to black crystal-vitric ash predominates; lithic fragments are absent or are very minor (Fig. 10). Between 45 and 85 mbsf, the ashes are more glass rich and contain fewer crystals and more common lithic fragments. These black to light gray layers are classified as vitric ash with minor crystals and lithic fragments. In the lower part of Unit I, below 85 mbsf, the ash composition is more varied, and there are lithic-vitric, vitric-crystal, crystal-vitric, and vitric ashes. Within this lower interval, there is a clear trend toward increasing crystal content and decreasing glass and lithic content within the ash, a trend that continues downward into the upper part of Unit II.

The ash layers are thought to have been deposited primarily as ash falls because nonvolcanic material is usually absent from the layers. A few ash layers contain significant amounts of nannofossils and/or foraminifers, which indicate that they have been remobilized from shallower water and deposited by turbidity currents.

The lower limit of this unit is defined where clay and silty clay become the dominant rock types in the sequence.

Unit II

Depth: 122.5–652.4 mbsf
Interval: Section 124-768B-14H-3 through Core 124-768C-31R
Thickness: 529.9 m
Age: middle Miocene to late Pliocene

Unit II is composed mainly of alternating clay, silty clay, clayey silt, silt, and some sand. (The more clay-rich rock types become increasingly consolidated downward through the unit, and in the section below 350 mbsf they are referred to as claystone, silty claystone, and clayey siltstone.) The upper 77 m of the unit is primarily clay interpreted as hemipelagic in origin, whereas the remainder is interpreted as fine-grained turbidites interbedded with hemipelagic clay. The minor lithotypes are marlstone and very thin to thin ash beds, the latter occurring only in the upper part of the unit (down to Section 124-768B-29X-4; 255 mbsf). The sequence is dark gray to dark greenish gray and olive green in color.

The turbidites are primarily thin to medium bedded, with some thick beds. In the middle and upper part of Unit II, there is a general upward trend toward thinner and less frequent turbidite beds and thicker hemipelagic clay beds, indicating a decrease in the input of turbidites through time. From the base of the unit to 480 mbsf (middle Miocene), the turbidite beds make up 75% or more of the thickness of the section. From 480 to 200 mbsf (middle to late Miocene), there is a steady decrease in the proportion of turbidite beds, and above 200 mbsf turbidite beds are very rare, so that dark greenish gray bioturbated clay makes up most of the interval. The thickest turbidite deposits occur in Cores 124-768C-8R and -17R: they are over 2.5 m thick and grade from medium sand to silty claystone. The sand-grade material is less cohesive than the finer deposits, and it is possible that some thick sandstone beds may have been washed out during drilling.

The turbidite beds display normal grading, most commonly with basal clayey silt or silty clay grading up to clay (Fig. 11). Some thick beds have silt or, rarely, sand at the base. The beds have sharp bases, and the basal sand, silt, and clayey silt commonly have planar lamination. Convolute and cross laminations also occur in some beds. The upper clay portions of the graded beds are typically thicker than laminated basal intervals, and are massive and gray, with a transition to greenish gray, bioturbated hemipelagic clay toward the top. Trace fossils recognized in the bioturbated claystone include *Planolites, Zoophycos* (Fig. 12), and *Chondrites*. Hemipelagic clay is distinguished from turbidite clay in most instances on the basis of its greenish gray color and greater degree of bioturbation, but in some beds the distinction is not clear. The carbonate content of the hemipelagic clay is very low (typically $<1\%$), indicating that deposition occurred below the CCD.

The main components of the silt- and sand-size sediments are detrital quartz, feldspar, rock fragments, and plant debris. Some laminae contain concentrations of plant debris as high as 20%, with fragments up to 5 mm across in Cores 124-768C-1R and -3R. Minor but significant components are tourmaline, zircon, and epidote. This association of grain species indicates a continental origin for these turbidites.

Calcareous beds occur commonly at the top of Unit II (Fig. 12) and sporadically through the remainder of the sequence, becoming less frequent toward the bottom. In Cores 124-768C-14H and -15H, medium to thin nannofossil marl occurs interbedded with claystone in a transitional sequence below the boundary with Unit I. Below this transition, thin to very thin marlstone beds occur interbedded with claystone. These beds commonly

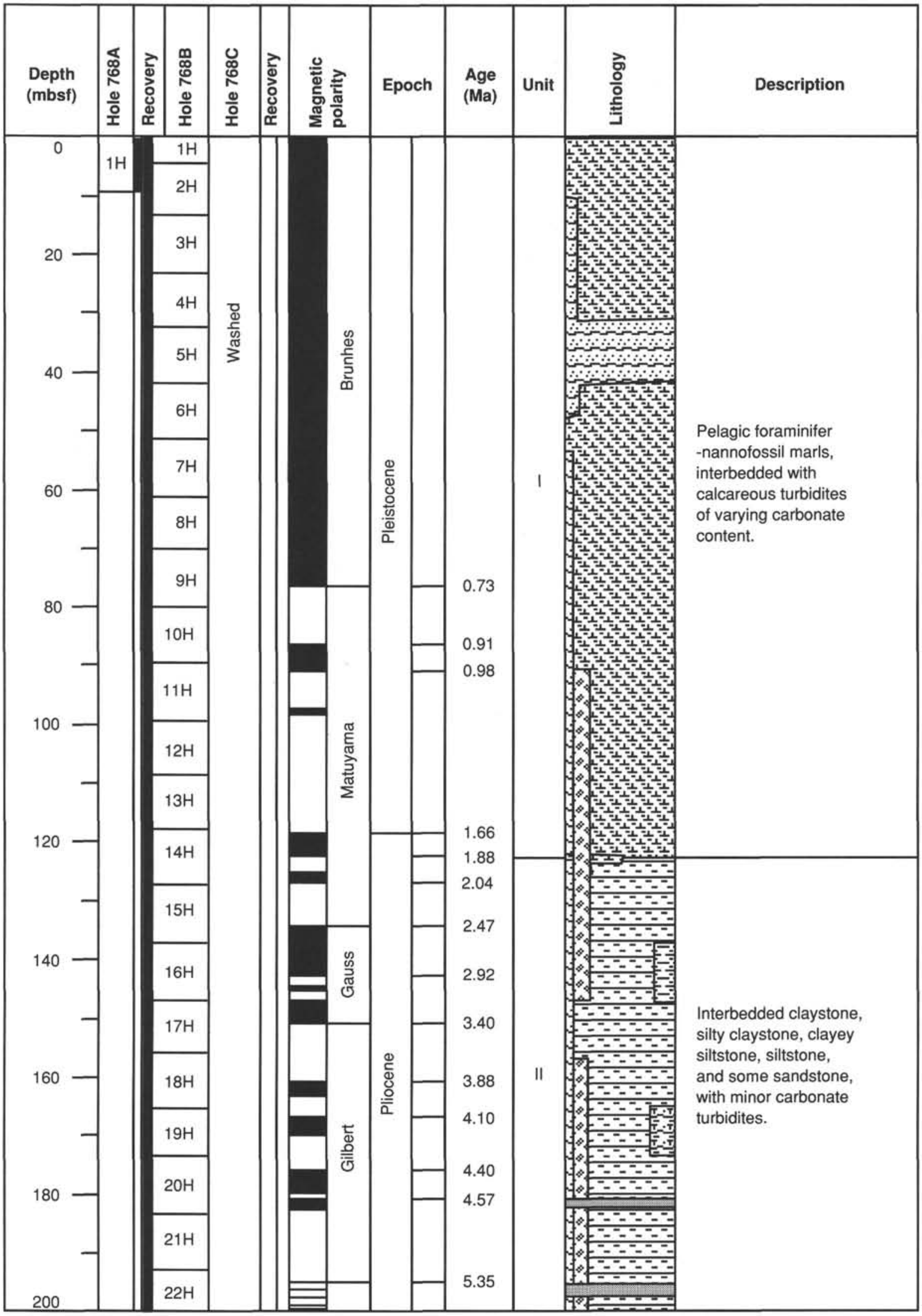

Figure 5. Graphic log of lithologic variations and units at Site 768.

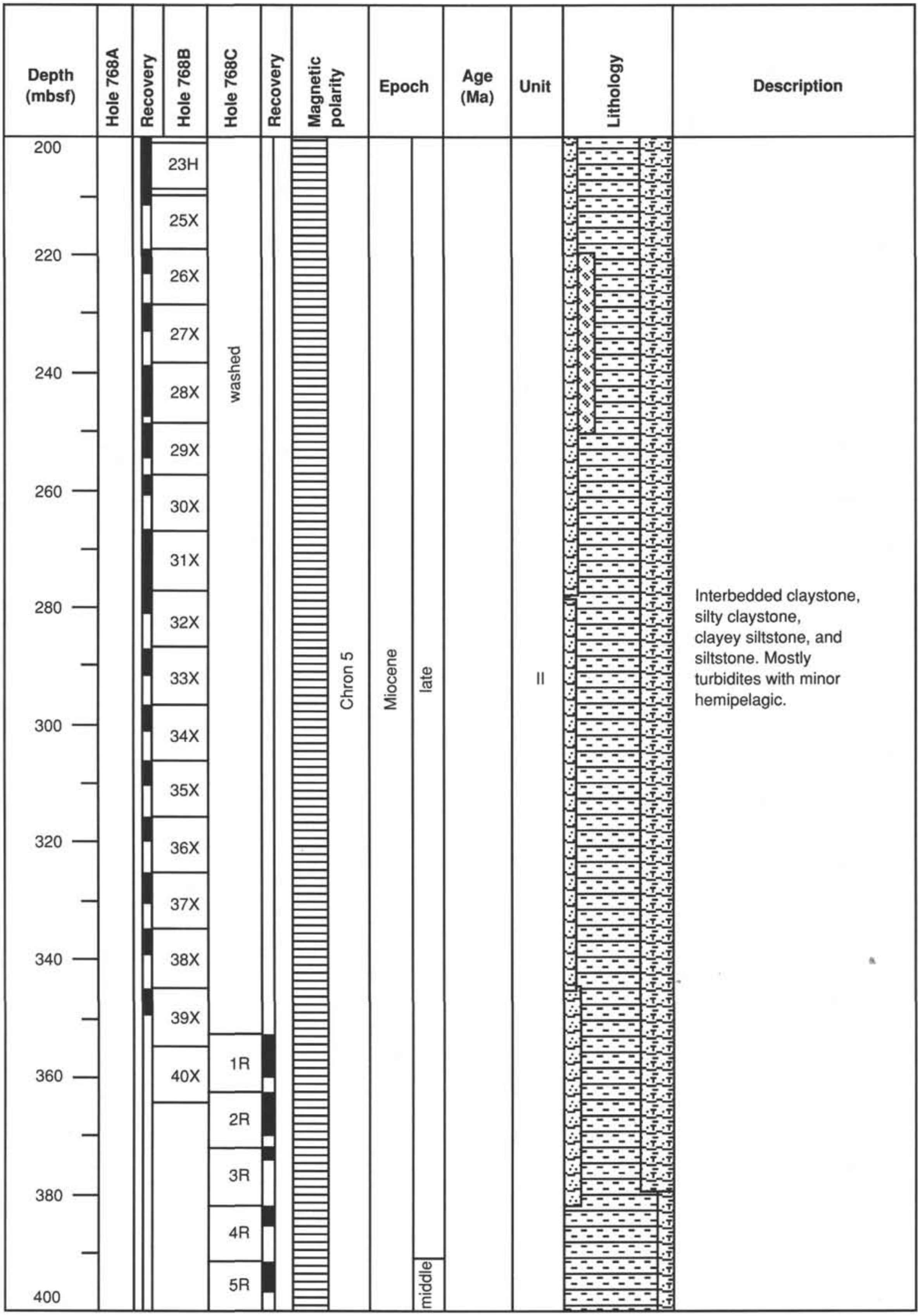

Figure 5 (continued).

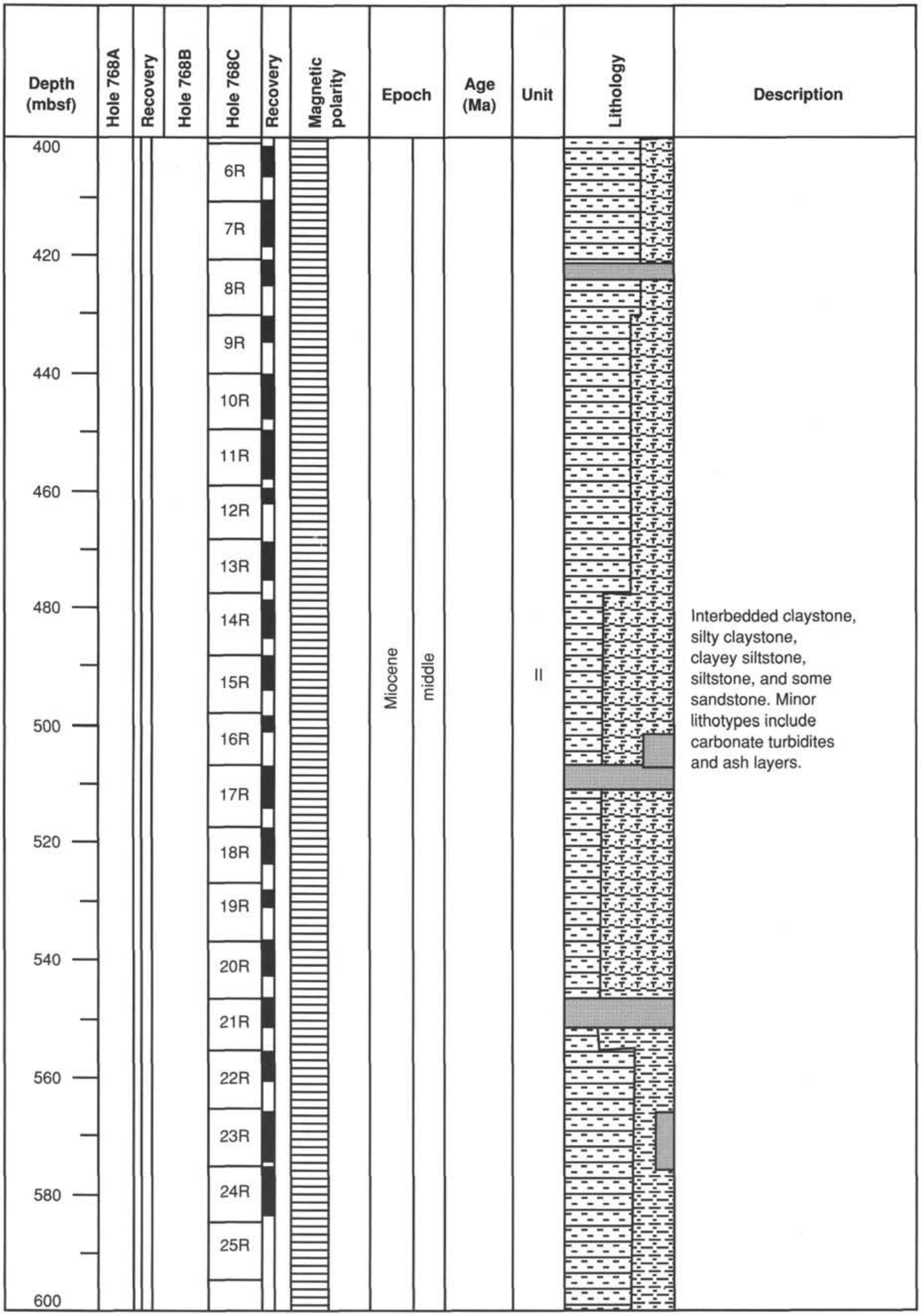

Figure 5 (continued).

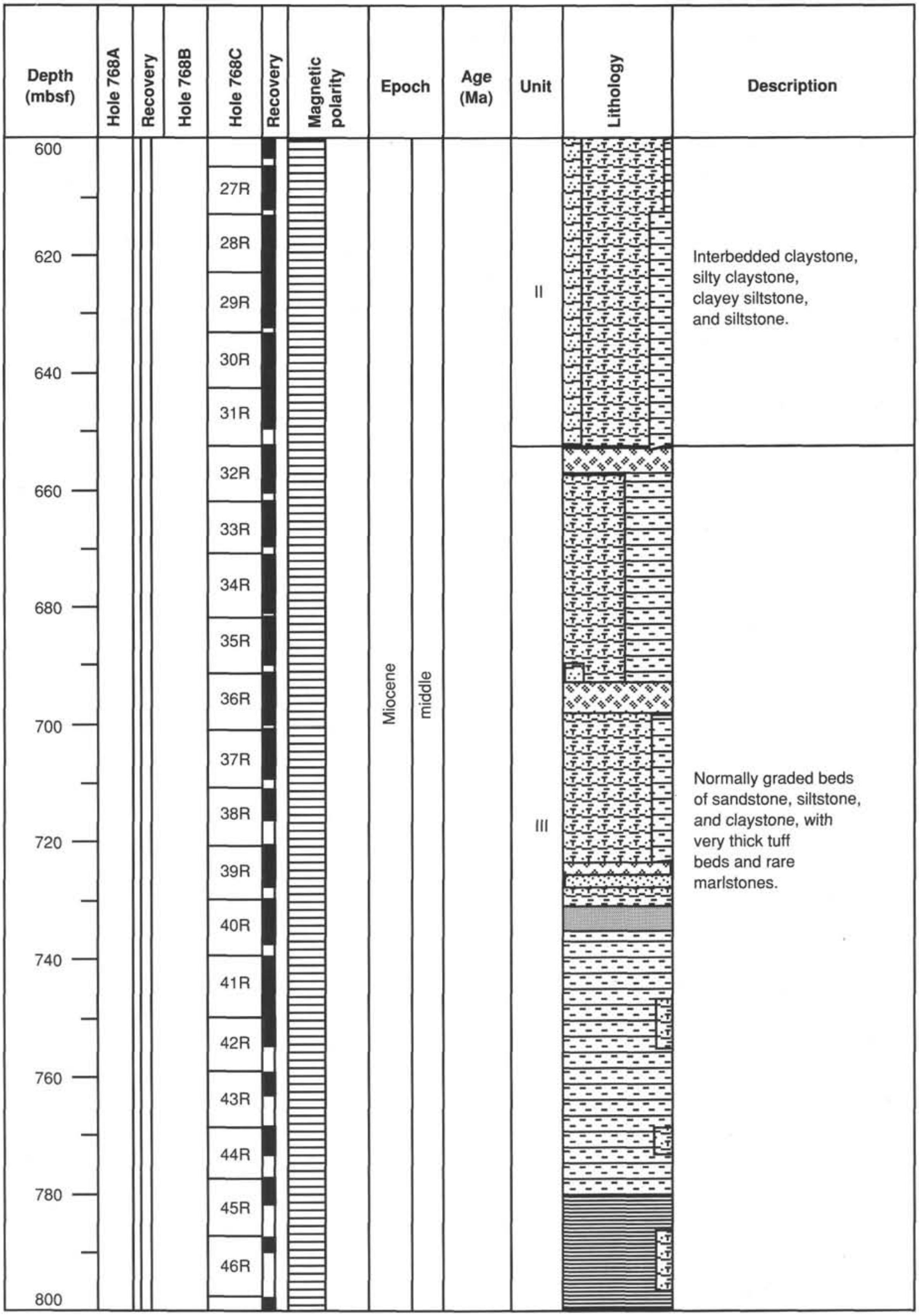

Figure 5 (continued).

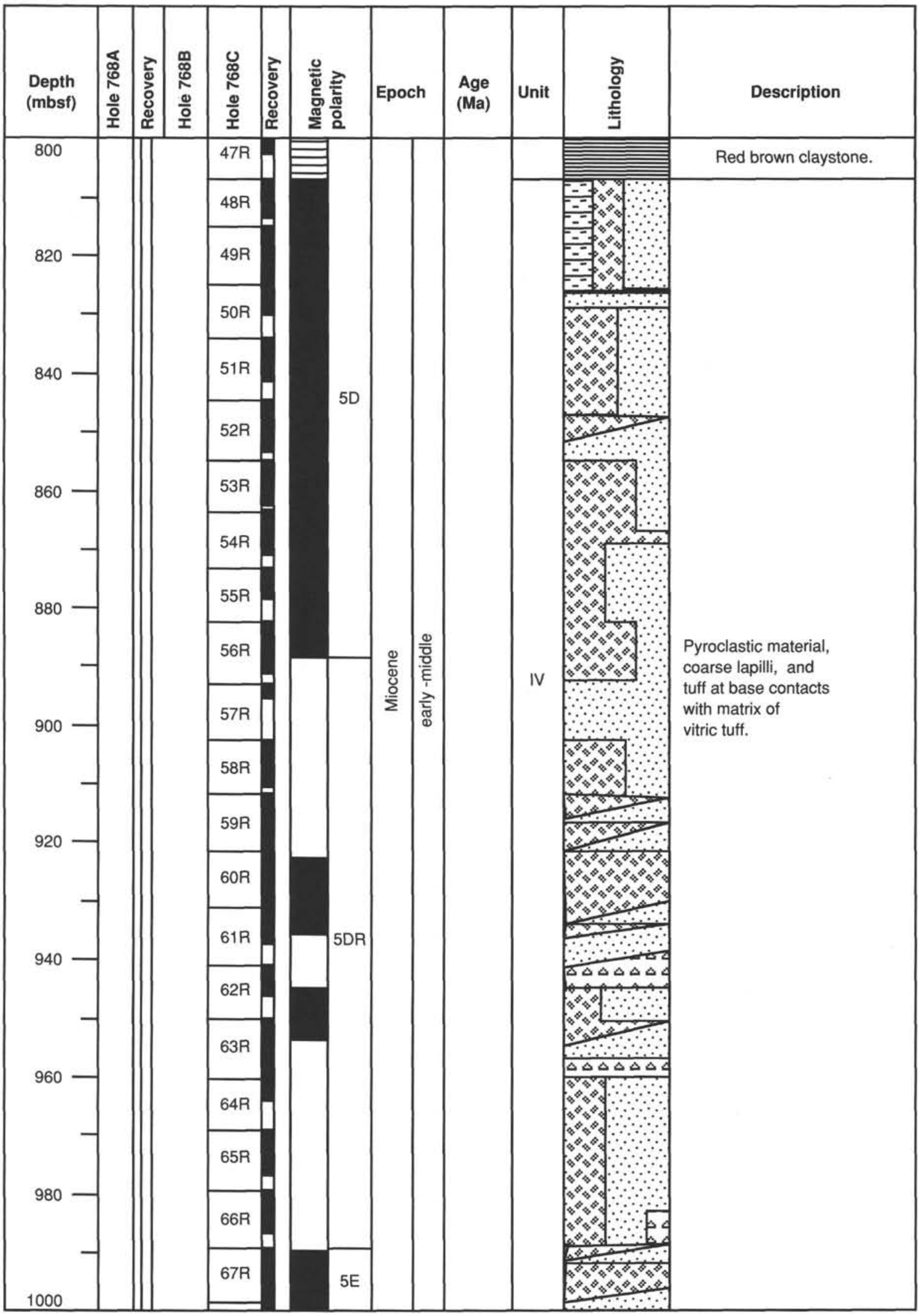

Figure 5 (continued).

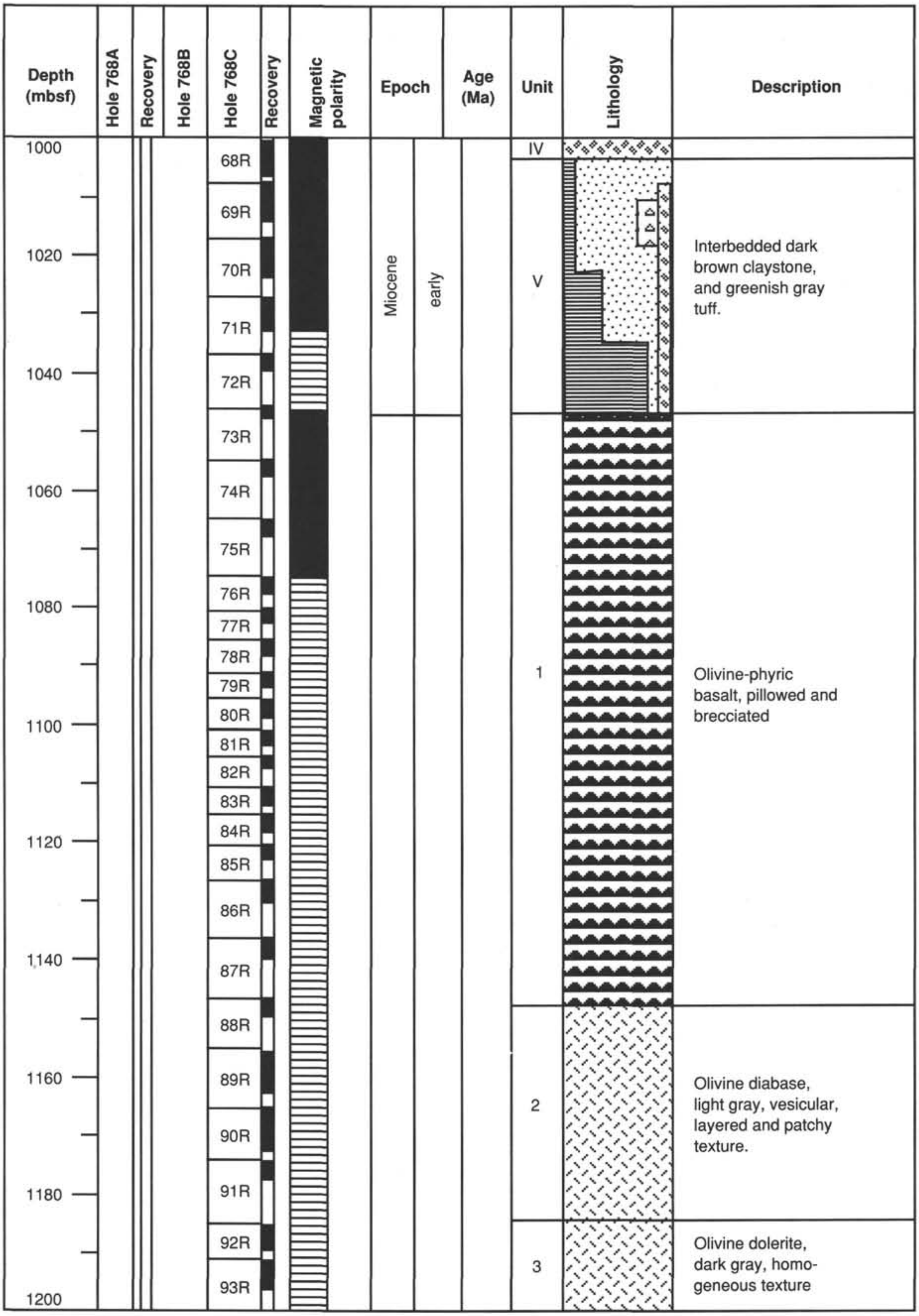

Figure 5 (continued).

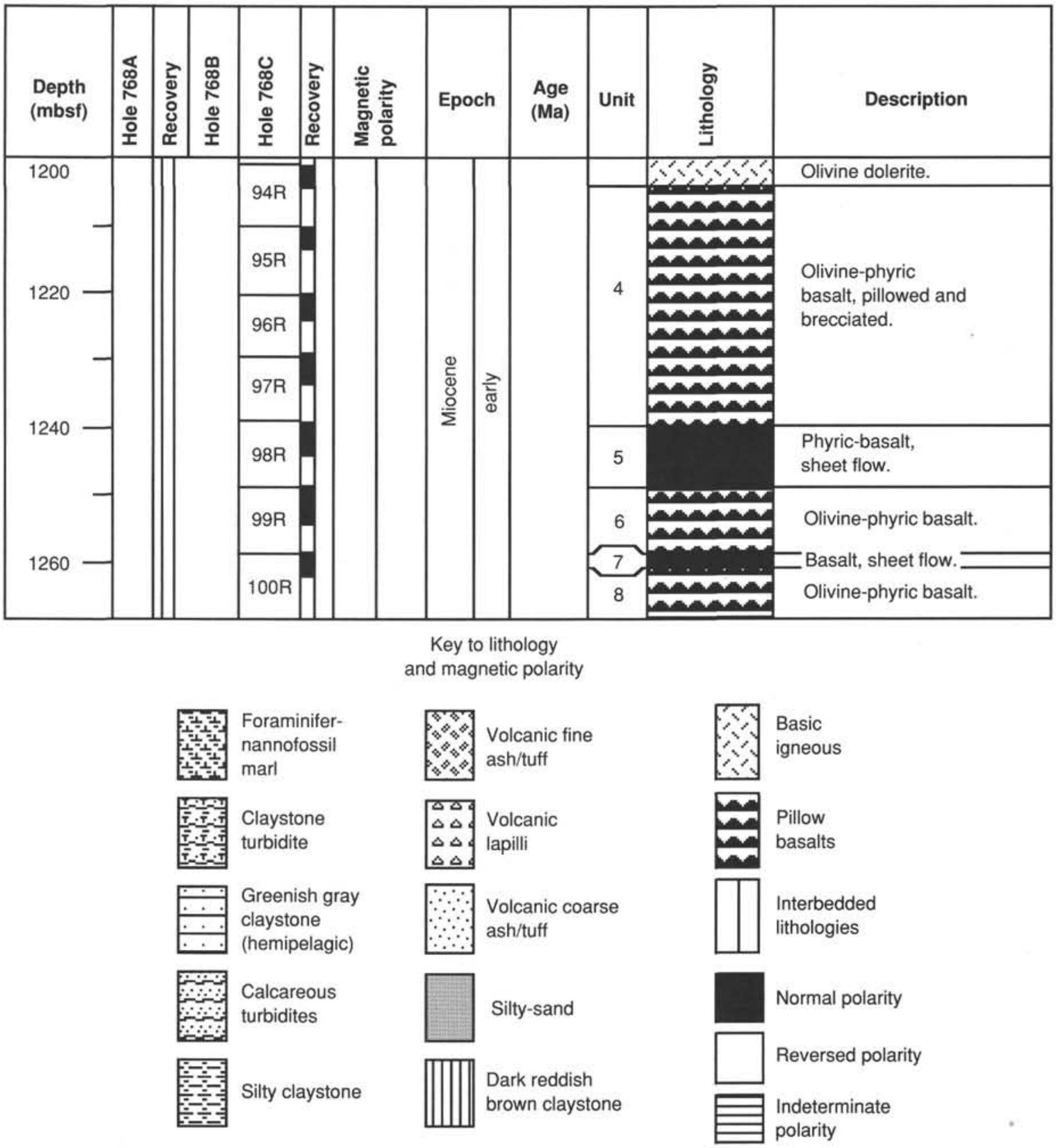

Figure 5 (continued).

have sharp basal contacts and diffuse, bioturbated tops, and in some cases show normal grading and fine planar lamination. They are interpreted as turbidite deposits that resulted from the redeposition of a mixture of biogenic ooze and clay originally accumulated above the CCD.

The volcanic ashes in the upper part of Unit II are present as very thin to thin beds or as irregular patches caused by bioturbation of the layers. The ash beds have sharp bases, normal grading, and gradational, bioturbated tops. A few have scoured bases and parallel lamination. They range from fine silt to fine sand in size and are dark green to gray. The principal components are rock fragments, glass, plagioclase, and hornblende, with minor biotite, pyroxene, and opaques. A significant change in ash composition occurs at a depth of 180 mbsf (Fig. 10). Above this level, crystal and vitric-crystal ashes dominate, whereas crystal-lithic to lithic ashes are most abundant below this depth. Some of the deeper ashes are altered and have large amounts of clay and zeolite minerals.

Most of the ash layers are interpreted to be air-fall deposits because of their sharp bases, normal grading, and lack of contamination of nonvolcanic materials. However, there are a few beds that have scoured bases and parallel lamination, indicating redeposition by turbidity currents.

The different rock types of Unit II exhibit varied effects of diagenesis. As noted above, the clay-rich sediments of Unit II become increasingly consolidated downward through the section, but the sand and silt layers are largely unlithified throughout. Authigenic pyrite occurs commonly as micronodules or as disseminated crystals within claystone below 200 mbsf. The redeposited marl beds also become increasingly indurated with depth. The shallow marl beds show variable recrystallization of nannofossils to granular micrite, and form well-indurated marl-

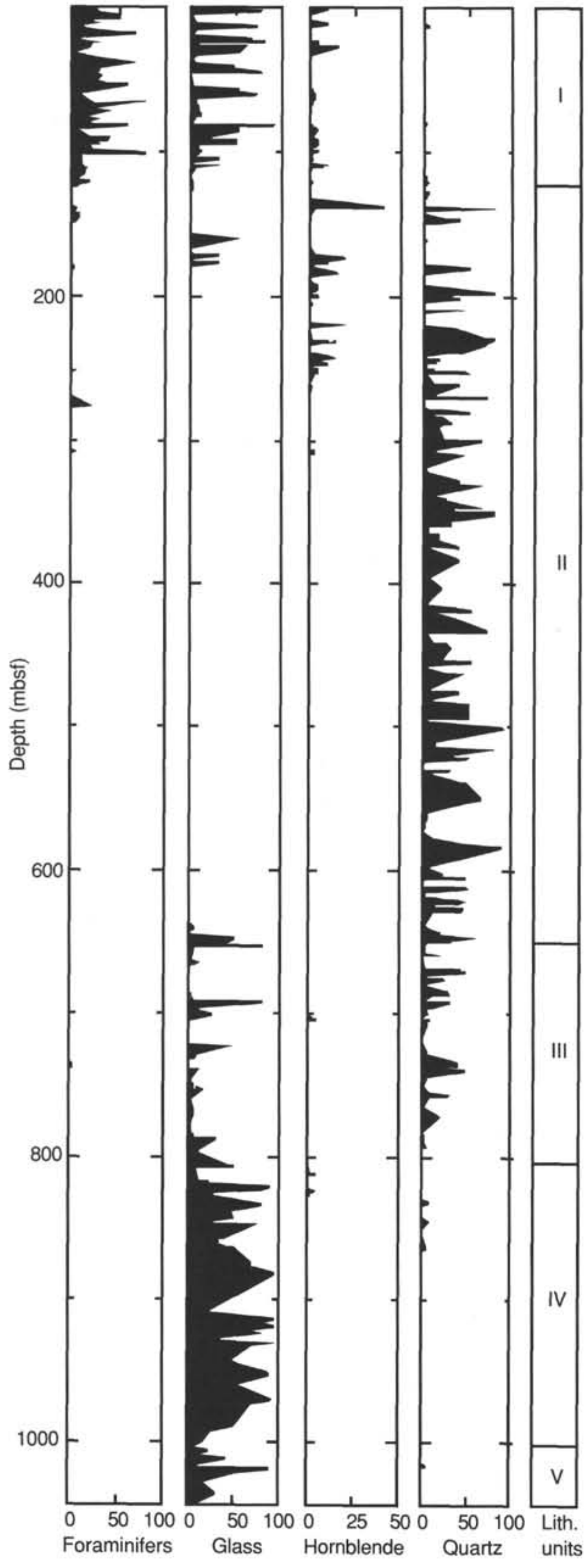

Figure 6. Abundance plot of variation with depth for several sediment components that are important indicators of provenance at Site 768. Foraminifers are a major component in the pelagic marl of Unit I, but they are almost completely absent in the underlying units. Glass and hornblende are found in discrete ash layers in Units I, II, and III and in the voluminous pyroclastic strata of Unit IV. Quartz is found primarily in beds interpreted as terrigenous turbidites in Units II and III.

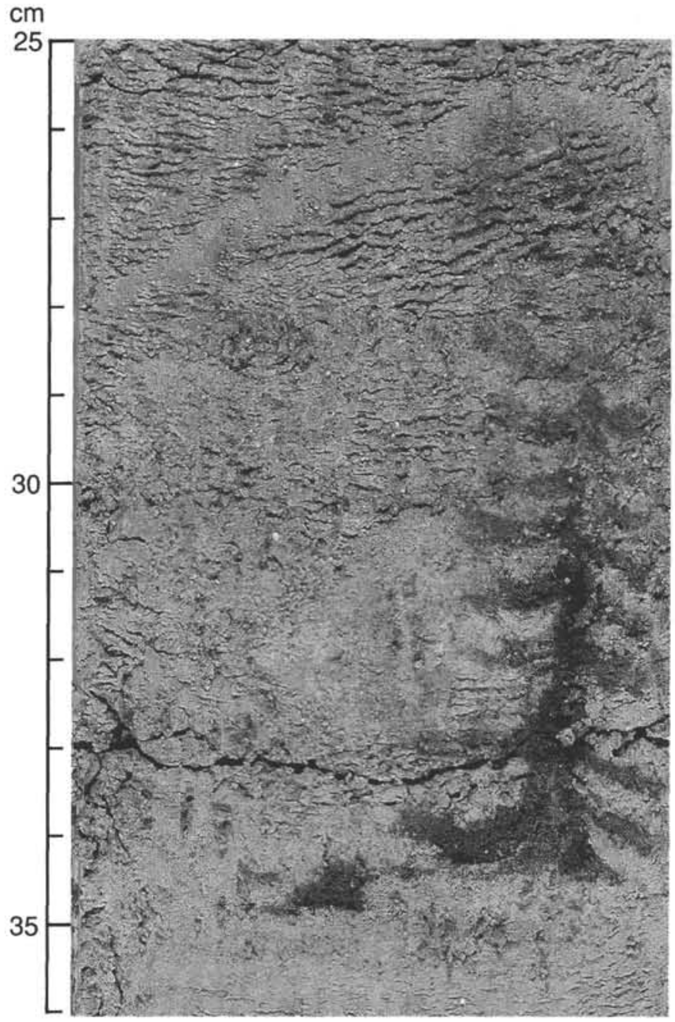

Figure 7. The trace fossil *Zoophycos* in marl of Unit I (Section 124-768B-5H-1, 25–36 cm).

stone beds below 350 mbsf. One thin dolomitized marlstone bed occurs above this level in the core catcher of Core 124-768C-25X (Fig. 13). Alteration of ashes increases dramatically at a depth of about 150 mbsf, as indicated by the increased abundance of clay and zeolites within these beds (Fig. 10, category "Others").

Unit III

Depth: 652.4–806.65 mbsf
Interval: Core 124-768C-32R to Section 124-768C-48R-1 at 5 cm
Thickness: 154.25 m
Age: early to middle Miocene

The upper part of Unit III is composed of hemipelagic claystone with interbedded turbidites of sandstone, siltstone, and claystone; a few very thick tuff beds; and rare marlstone. The lower part, below 733 mbsf, consists mostly of hemipelagic claystone. The top of the unit is placed at the top of the highest very thick tuff bed.

Within the upper part of Unit III, turbidites make up over 50% of the thickness of the section. The typical turbidites consist of siltstone, clayey siltstone, silty claystone, and claystone, which are present in medium to thin, normally graded beds with sharp bases. The lower part of the typical graded bed is clayey siltstone or very thin siltstone with faint planar lamination, which grades up into silty claystone and claystone. Sandstone is present in very thick or thick beds in Cores 124-768C-40R and -41R.

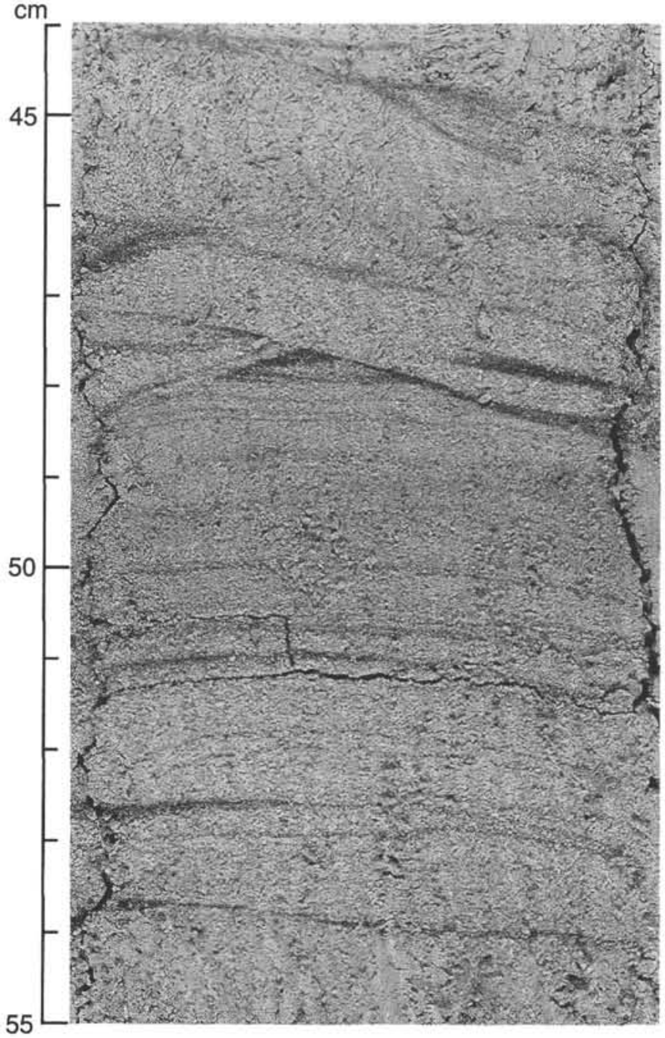

Figure 8. Planar and cross lamination in foraminifer marl turbidite of Unit I (Section 124-768B-10H-2, 44–55 cm).

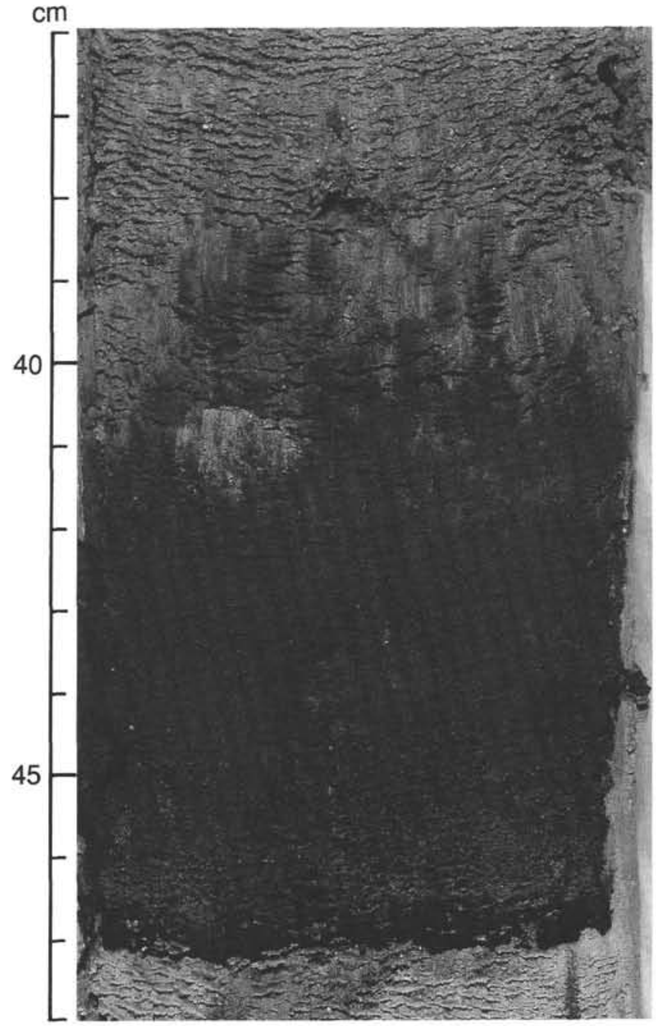

Figure 9. Thin, sharp-based dark ash bed with bioturbated top in Unit I (Section 124-768B-4H-7, 36–48 cm).

The sandstone beds are dark greenish gray and fine upward from a sharp base. They show planar lamination, with concentrations of plant material along some laminae, and may include pebble-size claystone clasts in the lower portion. The tops of these beds are disturbed by drilling, but they appear to fine up into claystone. The structures and sequences in these graded beds in the upper part of Unit III indicate that they were deposited by turbidity currents (fine beds) and related mass flow processes (thick sand beds).

The silt and sand compositions in the graded beds demonstrate a continental provenance. The principal components of the sandstones are rounded quartz, rock fragments, and feldspar, with minor glass and amphibole. The silt is composed of rock fragments, quartz, feldspar, and glass.

Gray homogeneous claystone in the upper parts of the graded beds is overlain by bioturbated, dark greenish gray claystone, which is interpreted as hemipelagic in origin. The low carbonate content of the claystone (typically $<1\%$) indicates that deposition occurred below the CCD. Pyrite and carbonate (dolomite?) nodules occur in the bioturbated claystone.

Tuff occurs in three very thick upward fining sequences between 2.5 and 4.7 m thick in the upper part of Unit III (Cores 124-768C-32R, -36R, and -39R). These sequences have sharp bases and show parallel layering in the lower part, grading up into thickly and thinly laminated coarse or fine tuff. In the upper parts of the sequences, the laminations are convolute or wavy, and dish-and-pillar structures provide evidence of water escape during deposition. In Core 124-768C-32R, granule- to pebble-size claystone clasts occur 1.2–1.8 m from the base of the bed. Fine plant debris is concentrated along laminae in Cores 124-768C-32R and -36R.

These tuff beds are gray to dark greenish gray. The principal components are volcanic glass, rock fragments, feldspar, up to 20% quartz, plant debris, and minor amounts of hornblende, pyroxene, and opaques. We interpret these beds as reworked pyroclastic material mixed with small amounts of terrigenous clastic sediment that was deposited in the basin by sediment gravity flows. The abundance of angular glass shards indicates that the volcanic material was produced by coeval volcanic activity, rather than by being eroded from older volcanic rocks.

Very thin- to thin-bedded marlstone occurs rarely in the upper part of Unit III (Cores 124-768C-33R and -35R). It is olive to olive gray and is well indurated. We interpret these beds as turbidites similar to the marl layers found in Unit II.

Claystone is the principal lithology in the lower part of Unit III (below 733 mbsf). Although sedimentary structures are obscured by severe drilling-induced fracturing in much of this interval, the claystone appears to be massive, with common mot-

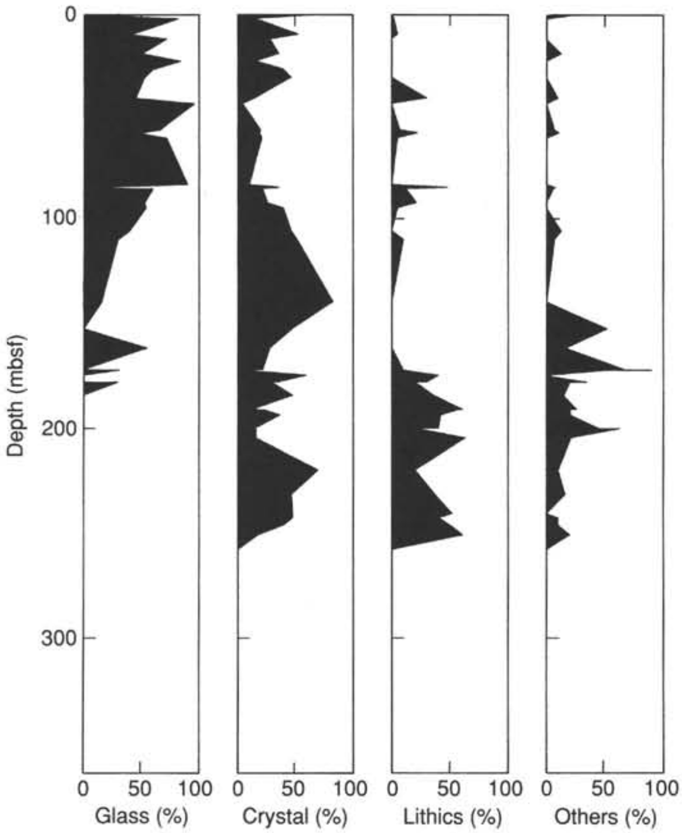

Figure 10. Abundance plot vs. depth for ash layer components in Units I and II, Hole 768B. The plot for "Others" includes clay above 150 mbsf, and clay plus diagenetic zeolites below 150 mbsf.

tling caused by bioturbation. The claystone is dark greenish gray, which becomes very dark grayish brown below 780 mbsf (Cores 124-768C-45R to -47R). It consists of clay minerals with very minor feldspar, quartz, rock fragments, and opaque minerals; it has a very low carbonate content (<1%). This interval represents dominantly hemipelagic deposition below the CCD.

The greenish gray claystone in the upper part of this interval includes rare graded clayey siltstone to claystone beds and rare graded sandstone. These beds contain quartz, feldspar, and lithic fragments, and are interpreted as terrigenous turbidites similar to those in the upper part of Unit III. The brown claystone at the base of Unit III includes a few graded silty claystone beds, in which the silt component is mostly feldspar, rock fragments, and glass; these are likely to be reworked tuff deposits.

Unit III is transitional between Units II and IV in terms of composition and provenance. The basal claystone includes volcanogenic turbidites related in composition to the pyroclastic rocks that make up the underlying Unit IV, and sporadic thick redeposited tuff beds are present up to the top of the unit. Terrigenous turbidites rarely appear in the lower part of the unit, but they do dominate the upper part of the section and are identical to the turbidites that constitute much of Unit II. Unit III, therefore, represents an interval of waning volcanic influence on sedimentation but an increasing influx of turbidites with continental provenance.

Unit IV

Depth: 806.6–1003.6 mbsf
Interval: Section 124-768C-48R-1 at 5 cm to Section 124-768C-68R at 44 cm
Thickness: 197.0 m
Age: early Miocene

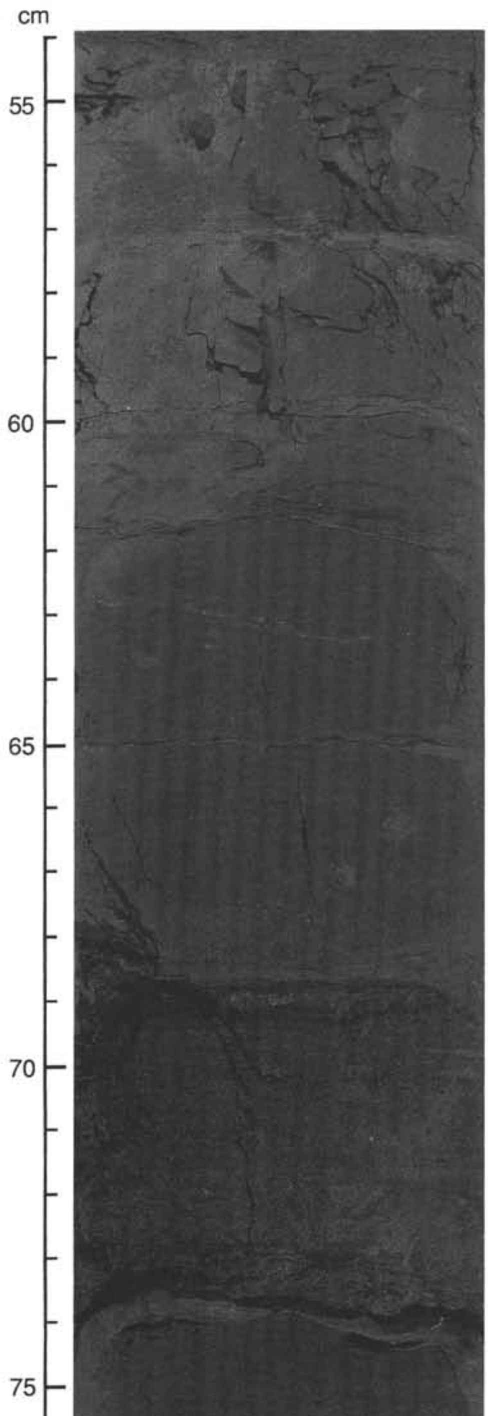

Figure 11. Silty turbidite bed in Unit II (Section 124-768C-18R-4, 54–77 cm). The lower interval of the turbidite bed is formed by sharp-based, planar-laminated silt grading into faintly laminated to massive clay in the upper part. The hemipelagic background sedimentation is represented by mottled bioturbated clay (57–61.5 cm). The base of another, very thin turbidite bed occurs at 57 cm.

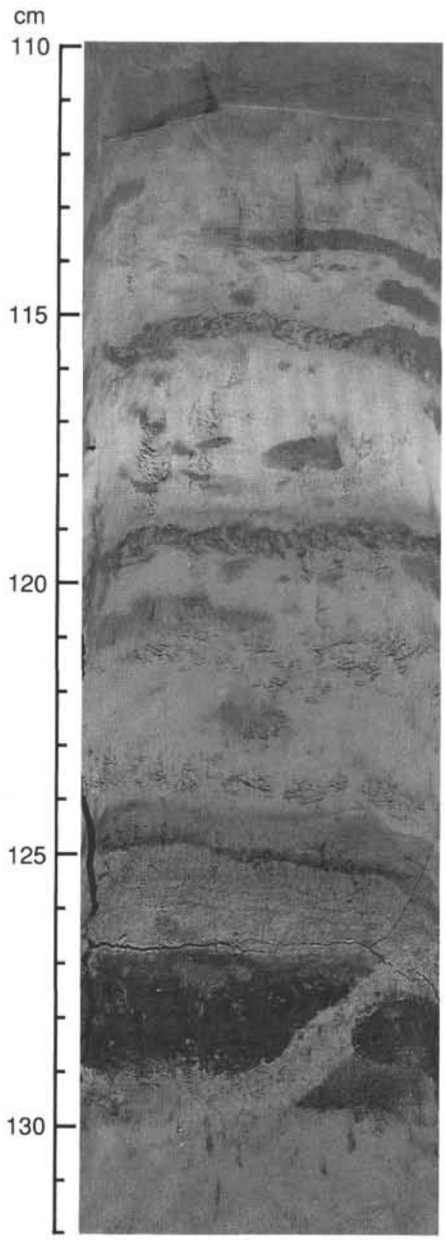

Figure 12. Marl (112–124 cm) and ash (127–129 cm) layers in Unit II (Section 124-768B-17H-6, 110–132 cm). The marl layer shows a slight fining-upward trend of the grain size, which indicates that it is a turbidite. It grades upward into clays that represent hemipelagic background sedimentation. Note the large *Zoophycos* burrow within the upper part of the marl bed, and a large oblique burrow that cuts the dark ash layer.

Unit IV is composed almost exclusively of coarse and fine vitric tuff and lapillistone in very thick graded units interpreted as submarine pyroclastic flow deposits, which are interspersed with zones of alternating thin- to medium-bedded coarse and fine tuff. Thin to medium beds of claystone are interbedded with tuff at the top and near the base of the unit. The major portion of the pyroclastic material throughout the unit is partially devitrified glass shards and pumice, with some rock fragments, minor plagioclase, and very minor pyroxene and opaque minerals. Small amounts of hornblende and biotite are present near the top of Unit IV, but they are absent through the remainder of the unit.

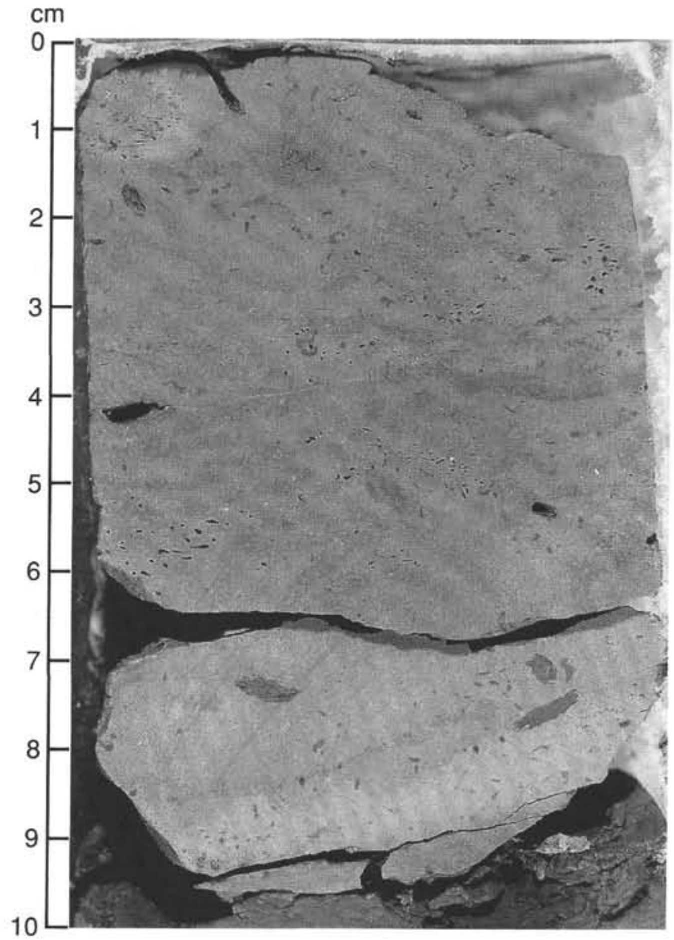

Figure 13. Dolomitized marl bed in Unit II (Section 124-768B-25X-CC, 0–10 cm) with helminthoid burrows (vugs, partially infilled with clay) and *Zoophycos*.

The thick-graded pyroclastic units show a regular sequence of depositional features. Figure 14 presents an idealized sequence: many of the sequences in this unit are incomplete and show only some of these structures. The bases of the thickest sequences are marked by a sharp planar or scoured contact overlain by a thin (2–10 cm), reverse-graded coarse tuff (Fig. 15) or lapillistone. Massive coarse vitric tuff or lapillistone overlies this basal zone and consists of pumice and lesser dense volcanic fragments in a matrix of vitric tuff (Fig. 16), in some cases with rip-up clasts of pebble to cobble size (Fig. 17).

This massive tuff grades up into layered coarse tuff composed of alternating layers of lighter vitric tuff and darker lithic-vitric tuff (Fig. 18). In many beds the layered coarse tuffs are the lowest parts of the sequence. As the material fines up from coarse to fine tuff, the layers become thinner, and the fine tuffs in the upper parts of the sequences have thick to thin planar laminae (Fig. 19). In the highest parts of the sequences, thin graded beds of fine tuff with planar to wavy, convolute, and cross lamination (Fig. 20) grade up into very fine tuff that is massive and commonly bioturbated.

There is a general trend from more lithic and crystal-rich vitric tuff in the lower parts of the thick tuff sequences to purer vitric tuff at the top. The layering in the coarse tuffs is defined by color variations between light and dark grayish green (Fig. 18) that reflect smaller-scale rhythmic variations in grain size and composition. The darker layers are finer and contain higher

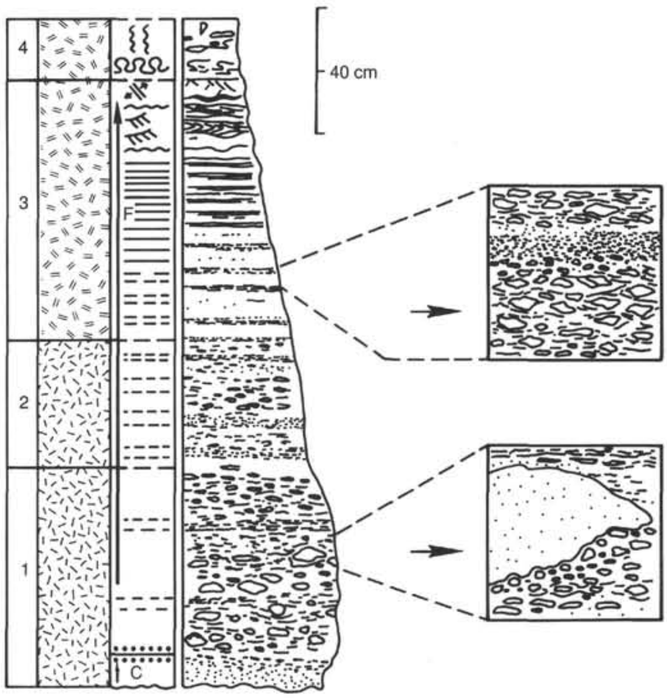

Figure 14. Generalized sequence of lithologies and structures in thick pyroclastic depositional units in Unit IV. 1 = Massive to crudely stratified coarse tuff or lapillistone with reverse grading at base (cf. Fig. 15). 2 = Layered coarse tuff (cf. Fig. 18). 3 = Planar-laminated fine tuff (cf. Fig. 19) grading up into thin-graded beds of fine tuff with wavy lamination and cross-lamination (turbidites; cf. Fig. 20). 4 = Bioturbated fine tuff. C = coarsening upward and F = fining upward.

concentrations of volcanic lithic fragments, pyroxene, and opaques; the lighter layers are coarser and richer in pumice clasts, which are commonly flattened parallel to bedding (Fig. 21). The coarser and finer layers grade into each other. The layers are up to 5 cm thick in the lower part of each sequence, decreasing to thick and thin laminations toward the top.

In the lapillistone and coarser tuff, altered glass shards and pumice are flattened around coarser lithic fragments. The rip-up clasts near the bases of the sequences have irregular margins, with coarse grains of ash penetrating the fine ash of the clasts. This implies that the clasts were firm but not fully indurated when they were reworked. Some large clasts of very fine tuff have a darker outer rind that indicates some alteration during deposition.

These very thick, upward-fining sequences of tuff are interpreted as the deposits of mass flows of pyroclastic material. The reverse grading at the base and the persistent planar layering and lamination through most of the sequences indicate deposition by dense laminar flows. The upper parts of the sequences show repeated, normally graded bedding and cross-lamination that indicate deposition of fine ash by turbidite flow. These may be caused by the reworking of the upper part of the major pyroclastic flows or the result of a succession of thin turbidites following such an event.

Separating some of the major pyroclastic flow units are thinner intervals of thin- to medium-bedded, graded vitric tuff. The graded beds have sharp bases and may have either coarse or fine tuff at the base. At the top and bottom of Unit IV, these beds grade up into thin intervals of claystone; but throughout the bulk of the unit, no nonvolcanic sediment separates the graded tuffs. These beds are interpreted as turbidites that resulted from the redeposition of ash from a shallower source.

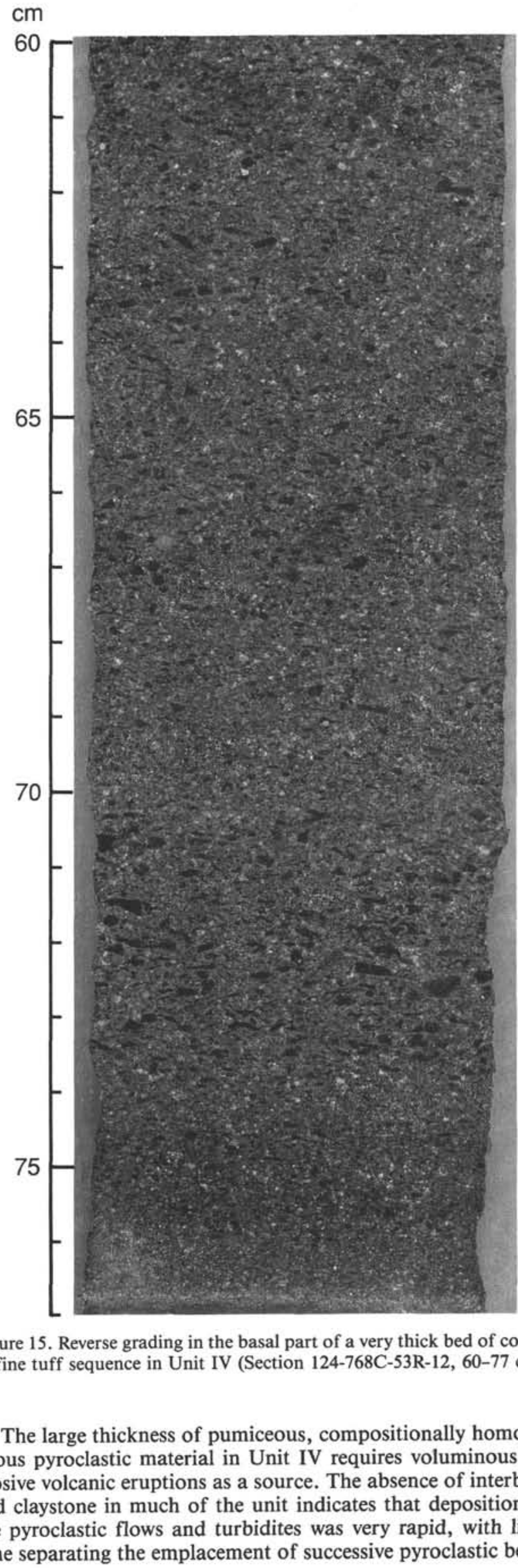

Figure 15. Reverse grading in the basal part of a very thick bed of coarse to fine tuff sequence in Unit IV (Section 124-768C-53R-12, 60–77 cm).

The large thickness of pumiceous, compositionally homogeneous pyroclastic material in Unit IV requires voluminous explosive volcanic eruptions as a source. The absence of interbedded claystone in much of the unit indicates that deposition of the pyroclastic flows and turbidites was very rapid, with little time separating the emplacement of successive pyroclastic beds.

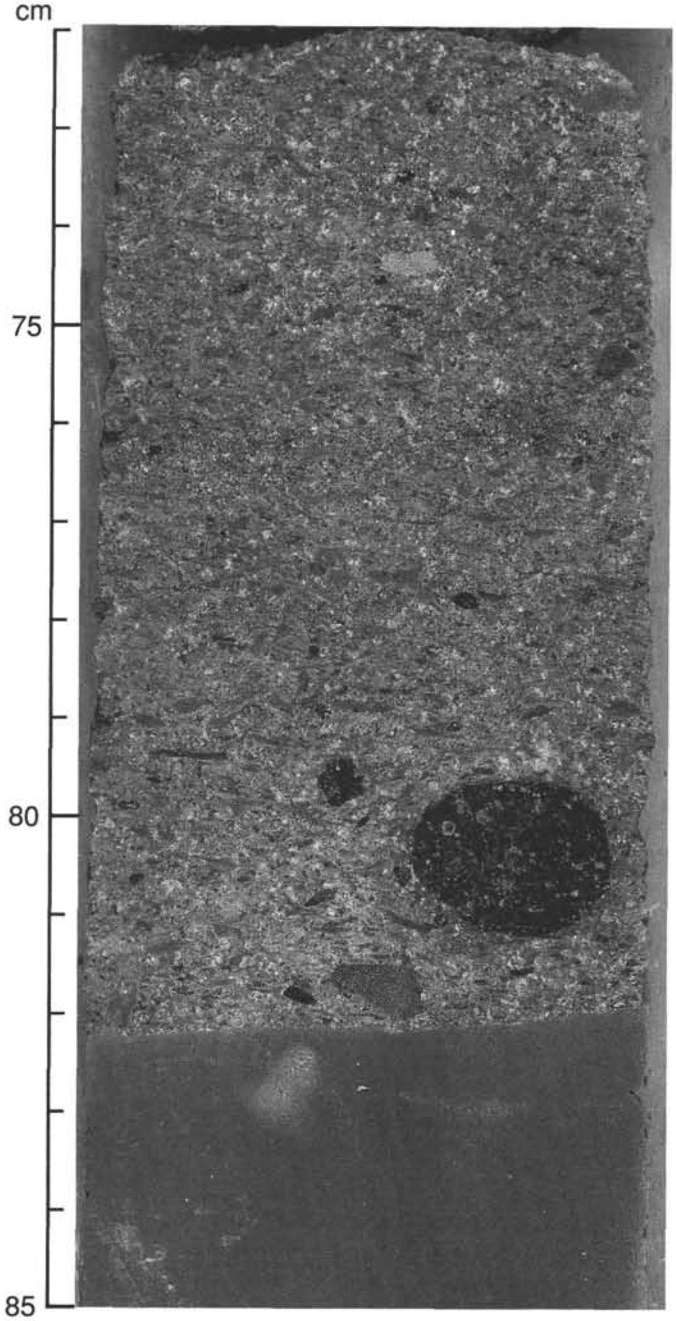

Figure 16. Rounded, dense volcanic pebbles and smaller elongated pumice lapilli above sharp basal contact of thick-graded coarse tuff bed in Unit IV (Section 124-768C-58R-1, 72–85 cm).

The tuff and lapillistone in Unit IV are somewhat friable in the upper part, but they are well lithified in the lower part. Much of the pumiceous glass has devitrified to brown to green clay and celadonite(?), quartz, and zeolites. Murky aggregates of clay minerals also surround the pumice clasts and crystals, and probably represent a clay cement precipitated in the intergranular pore space during diagenesis.

Unit V

Depth: 1003.6–1046.6 mbsf
Interval: Section 124-768C-68R-4 at 44 cm through Core 124-768C-72R

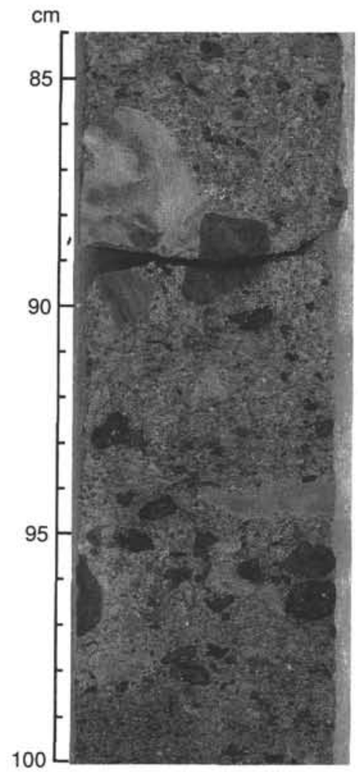

Figure 17. Large rip-up clasts of fine tuff (light gray) and rounded dense volcanic pebbles within medium bed of coarse tuff in Unit IV (Section 124-768C-62R-3, 84–100 cm).

Thickness: 43.0 m
Age: early Miocene

Unit V consists of an alternation of dark brown hemipelagic claystone and greenish gray tuff. The hemipelagic claystone occurs in massive, medium to thick beds that are bioturbated in places. It consists of clay minerals with a minor silt-size component of glass, feldspar, and rock fragments. The absence of biogenic carbonate indicates deposition below the CCD. The contacts between claystone beds and underlying fine tuff are gradational.

The tuff occurs in normally graded beds up to 3.6 m thick. The thick beds may show reverse grading from coarse tuff to lapillistone near the base, which then grade from planar-laminated coarse tuff to fine tuff that has thick to thin planar lamination throughout. The fine tuff beds show convolute lamination, and in Section 124-768C-69R-3, water escape structures occur. Thin beds of fine tuff have sharp bases, normal grading, and show planar and ripple lamination. The tuff is dominantly vitric, with higher concentrations of lithic fragments, feldspar, and pyroxene in the darker laminae. The thicker tuff beds may be the product of either pyroclastic flows or turbidites, whereas the thin beds are interpreted as distal turbidites of reworked pyroclastic material.

Unit V overlies basaltic basement, although the contact is not preserved in the cores.

Distribution of Graded Beds

A variety of graded beds of differing lithology and structure are characteristic of the sedimentary sequence at Site 768, especially Units II through V. Figure 22 plots the frequency per core of all types of graded beds through the sequence, as well as the percent thickness per core for carbonate, terrigenous, and vol-

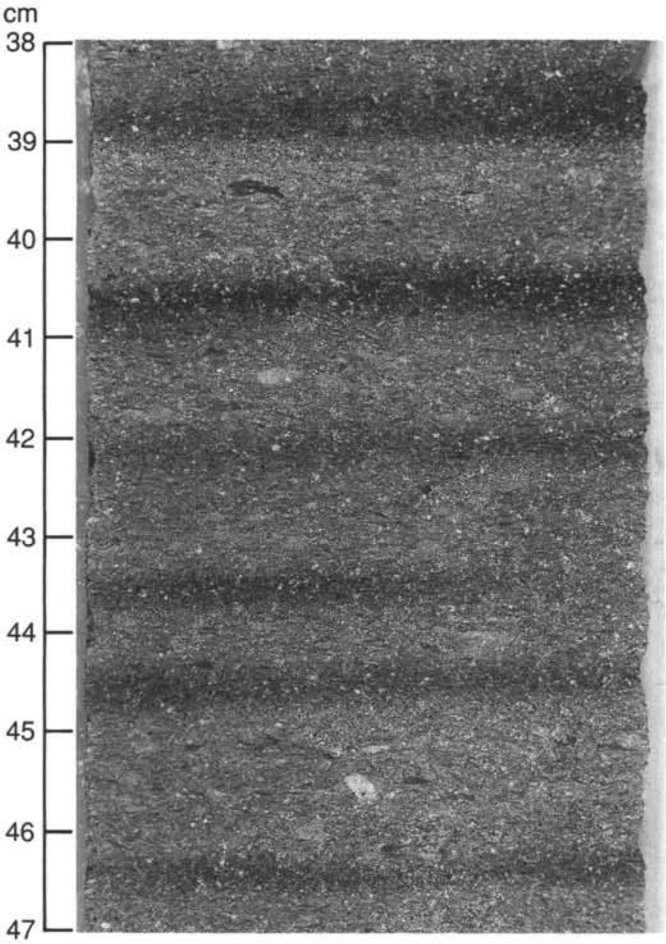

Figure 18. Crudely stratified coarse tuff in lower part of very thick coarse to fine tuff sequence (Section 124-768C-60R-6, 38–47 cm). The darker layers are finer and contain higher concentrations of lithic fragments, pyroxene, and opaques, whereas the lighter layers are coarser and richer in pumice lapilli.

canic-graded beds. These data have been compiled from the visual core descriptions for Holes 768A, 768B, and 768C.

In most instances, the graded beds have been interpreted as turbidites, except in Unit IV, in which the thick pyroclastic units are the products of high-density, laminar sediment gravity flows. The thickness of the turbidite deposits has been measured from the sharp base up to the transition to hemipelagic clay. The transition from the clay at the top of the turbidite to hemipelagic clay is marked by a color change that commonly coincides with a change from massive to bioturbated clay. In the pyroclastic deposits there is typically no hemipelagic component to the sequence. Graded ash beds interpreted as air-fall deposits in Units I and II have not been included in the dataset.

Figure 22 illustrates several significant features of the sedimentary sequence at Site 768. Pyroclastic mass-flow deposits dominated the lowest part of the section, up to 800 mbsf, which corresponds to Units IV and V. An interval of about 40 m above this level contains very few graded beds and corresponds to the period of slow pelagic sedimentation at the bottom of Unit III. Turbidites of terrigenous clastic composition increase in number and percentage of core thickness above 750 mbsf, reaching a maximum between 600 and 400 mbsf; this interval corresponds to the upper part of Unit III and the lower part of Unit II.

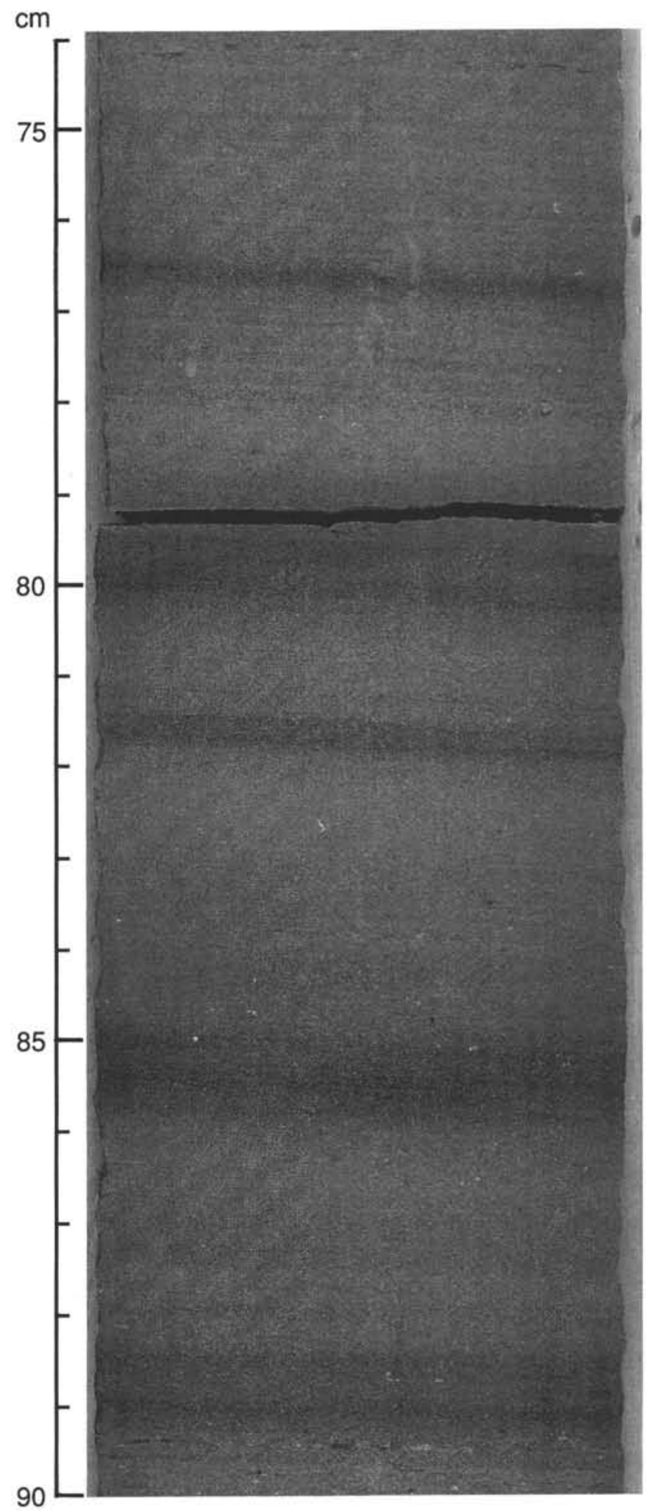

Figure 19. Fine tuff with planar lamination in the upper part of a very thick graded tuff sequence (Section 124-768C-60R-1, 74–91 cm).

Above 400 mbsf, terrigenous turbidites decrease in abundance, and carbonate turbidites form a minor but significant component of the sequence, which corresponds to the upper part of Unit II. Above 120 mbsf (Unit I), only carbonate turbidites are present.

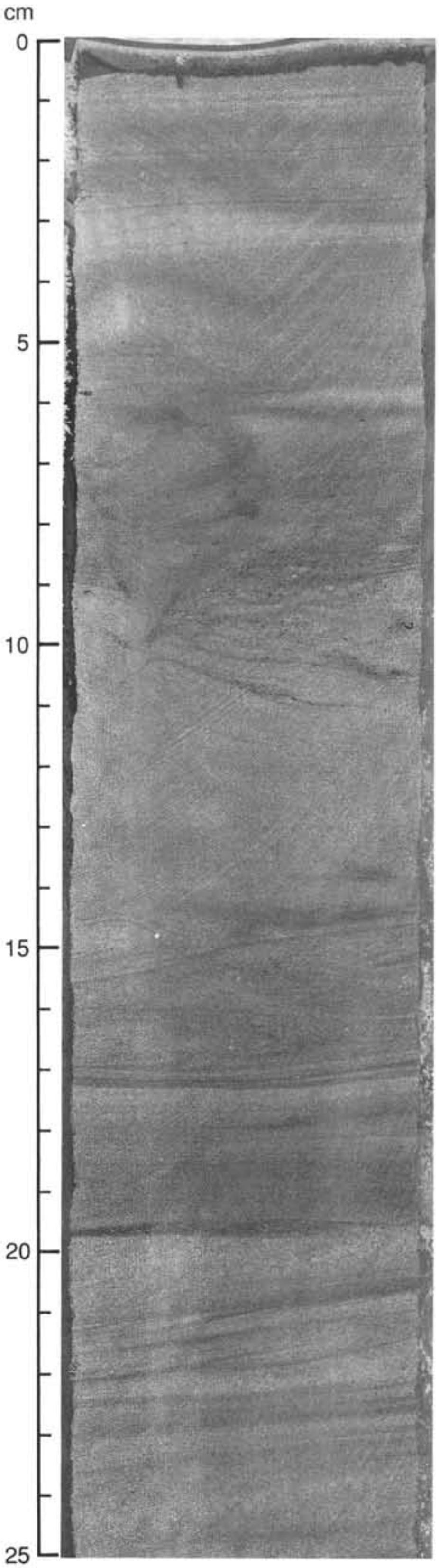

Figure 20. Fine tuff near the top of a very thick-graded tuff sequence (Section 124-768C-68R-6, 0–25 cm), showing planar lamination (top and bottom), low-angle cross-lamination (20–23 cm), and convolute lamination (9–17 cm).

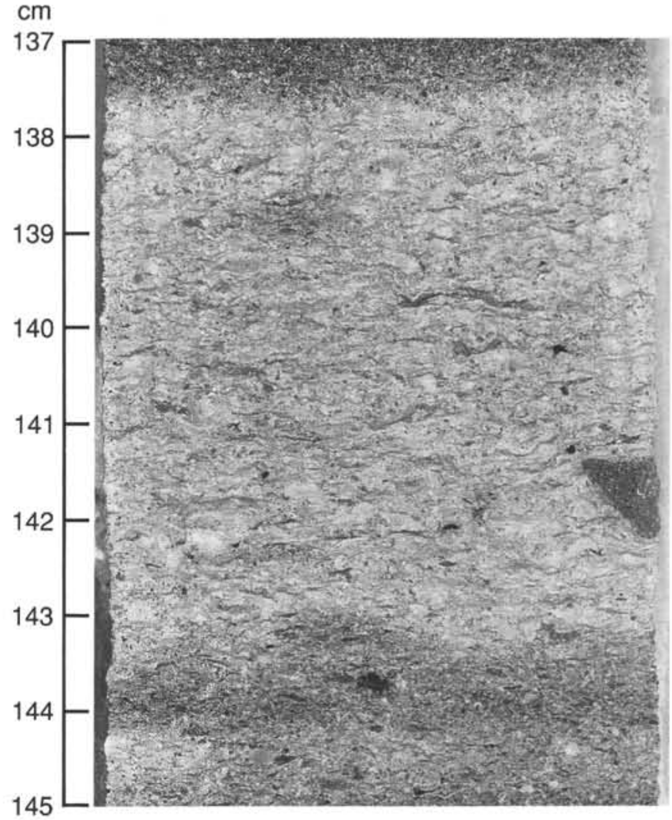

Figure 21. Flattened pumice fragments in coarse tuff bed in Unit IV (Section 124-768C-62R-1, 137–145 cm).

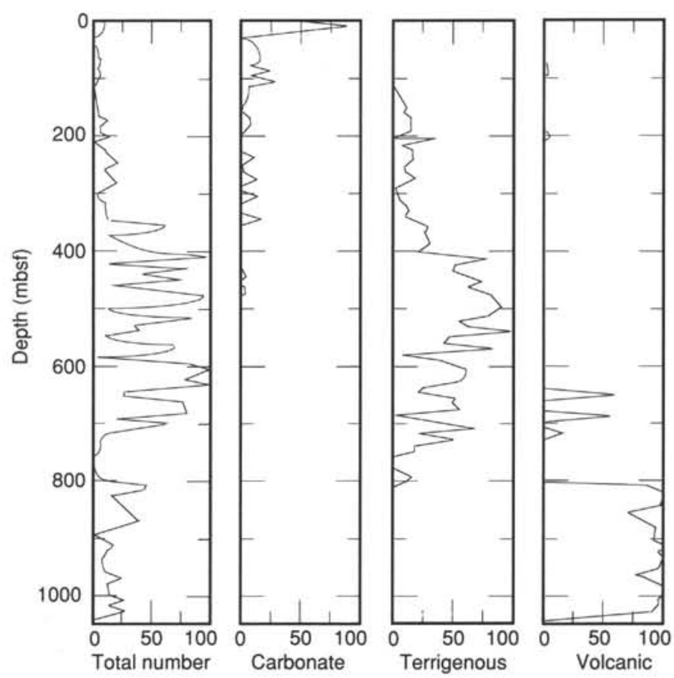

Figure 22. Plot of frequency and thickness data vs. depth for graded beds at Site 768. The first column plots the total number of graded beds per core vs. depth. The other columns plot the aggregate thickness per core of graded beds of different compositions: carbonate, terrigenous (quartz + clay), and volcanic (excluding airfall ash beds in Units I and II).

Clay Mineralogy

The mineralogy of the <2-μm-size fraction of 88 samples from Site 768 was investigated by X-ray diffraction (XRD) with the methods described in the "Explanatory Notes" chapter (this volume). The data are shown in Table 3 and Figure 23.

Smectite

Smectite is abundant in Unit I, averaging almost 60%. It decreases progressively with depth in Unit II, reaching levels below 10% at the base of the unit. Low values continue in the upper half of Unit III and rise rapidly to over 70% at the base. Analyses are sparse in Unit IV as these hard tuffs are very difficult to disaggregate. Smectite peaks in diffractograms from Unit IV are noticeably narrow and sharp, indicating better crystallinity and/or decreased mixed layering than in any other sample analyzed on Leg 124. The analyzed samples in Unit IV are dominated either by smectite or by a 10Å phase, blue-green in bulk, which is probably celadonite, a ferroan form of illite. One sample from Unit V contained only smectite.

Illite

Illite averages about 20% in Unit I. In Unit II a progressive increase in illite abundance from around 20% in the uppermost part to over 50% in the lower part mimics in reverse the progressive decrease in smectite and appears to represent a fairly continuous change from a volcanic source for the upper part of Unit II to a continental source region in the lower part of the unit. Illite is abundant but somewhat variable in Unit III. In Unit IV some analyses show an abundant 10Å phase, probably celadonite as discussed above. Illite is absent in Unit V.

Kaolinite

Kaolinite is present in Units I, II, and III at levels around 10%–15%. In Unit IV the 7Å phase is $<10\%$ of the diffracting clays and, although assignments are made in Table 3, the abundances of both kaolinite and chlorite in Unit IV are near detection limits and of dubious value. Kaolinite is absent in the sample from Unit V.

Chlorite

Chlorite is present in Unit I at levels around 10%–15%. In Unit II chlorite averages around 15% and varies from 0% to 26%. Chlorite abundances listed for Unit IV are near detection limits and are unreliable, as noted in the preceding discussion of kaolinite.

Continentality Index

To illustrate the variations in the importance of continental sources, we have calculated a "continentality index," which is the log of the ratio of the sum of the abundances of smectite plus illite plus chlorite divided by the abundance of smectite (see the discussion in the "Lithostratigraphy" section, "Site 767" chapter, this volume). The variation of the "continentality index" with depth at Site 768 is shown in Figure 24.

Continentality in Unit I is around 0.2, a value interpreted to indicate low continental influence during this interval of pelagic deposition. In Unit II the continentality increases with increasing depth to a value well above 1.0, implying a strong continental influence on the lower parts of this unit. This increase coincides with the increasing proportion of turbidite clay relative to hemipelagic clay downward through Unit II. Continentality falls rapidly with depth in Unit III to levels below 0.2, coincident with the decrease in abundance of terrigenous turbidites, indicating a rapid change in source region during the deposition of this unit. Continentality is variable in Unit IV and zero in Unit V.

Table 3. Clay mineralogy data, Site 768.

Core, section, interval (cm)	Depth (mbsf)	Smectite (wt%)	Illite (wt%)	Kaolinite (wt%)	Chlorite (wt%)
124-768B-					
1H-2, 65–71	2.15	56.42	21.17	11.21	11.20
2H-1, 13–19	4.13	51.13	22.00	12.94	13.93
3H-1, 127–133	14.77	52.29	26.29	9.11	12.31
4H-1, 60–66	23.60	52.21	21.37	12.19	14.23
5H-2, 70–76	34.70	42.76	32.68	0	24.67
6H-1, 120–126	43.20	54.93	30.41	14.66	0
7H-1, 59–65	52.09	83.00	6.75	4.86	5.39
8H-1, 59–65	61.59	53.49	22.33	9.67	14.51
9H-1, 49–55	70.99	53.78	23.74	5.83	16.65
10H-1, 50–56	80.50	65.44	18.70	9.15	6.71
11H-1, 12–18	89.62	61.32	19.17	19.51	0
12H-5, 48–54	105.48	56.67	23.00	7.74	12.59
13H-1, 50–56	109.00	63.77	20.29	15.94	0
14H-2, 57–63	120.07	52.01	25.49	12.00	10.50
15H-1, 60–66	128.30	70.95	15.98	13.09	0
16H-1, 27–33	137.27	48.93	29.32	12.79	8.96
17H-1, 50–56	147.00	54.37	21.21	12.93	11.49
18H-1, 50–56	156.50	58.86	21.97	11.98	7.19
19H-1, 47–53	165.97	34.41	28.32	21.89	15.38
20H-1, 45–51	174.25	41.20	26.74	16.95	15.11
21H-1, 50–56	183.80	33.37	39.76	15.45	12.03
25X-CC, 17–23	209.77	30.92	41.96	13.41	13.71
26X-1, 59–65	219.89	34.99	38.68	13.77	12.53
27X-1, 105–111	229.95	21.54	50.14	14.16	14.16
28X-1, 52–58	239.12	39.70	40.26	10.02	10.02
29X-1, 52–58	248.72	52.06	27.94	10.00	10.00
30X-1, 110–116	258.90	30.52	42.61	13.44	13.43
31X-1, 110–116	268.60	25.20	47.48	13.66	13.66
32X-1, 82–88	278.02	26.84	46.84	26.32	26.32
33X-2, 7–13	288.37	12.35	59.83	11.63	16.19
34X-1, 48–54	296.88	16.92	54.67	14.57	13.84
35X-1, 71–77	306.81	36.89	37.71	12.70	12.70
37X-1, 58–64	326.08	28.51	43.14	17.39	10.96
38X-1, 34–40	335.44	37.11	37.42	13.26	12.21
39X-1, 60–66	345.40	13.41	50.49	16.50	19.60
124-768C-					
1R-3, 80–86	337.00	35.83	40.53	10.22	13.42
2R-1, 49–55	363.39	34.91	40.36	12.37	12.36
3R-1, 31–37	372.71	15.54	52.46	11.89	20.11
4R-1, 82–88	382.92	21.37	51.82	13.23	13.22
5R-1, 44–50	392.24	10.35	52.38	12.71	24.56
6R-2, 88–94	403.78	39.58	42.90	9.08	8.44
7R-1, 103–109	412.13	20.20	50.35	12.98	16.57
8R-1, 60–66	421.30	30.22	47.89	9.63	12.26
9R-1, 46–52	430.66	12.58	55.63	14.13	17.66
10R-1, 45–51	440.35	14.83	53.28	16.58	15.04
11R-5, 47–53	456.07	26.40	47.87	8.38	17.35
12R-1, 134–140	460.54	23.55	48.75	10.65	17.05
13R-2, 69–75	471.09	14.96	51.80	15.01	18.23
14R-1, 79–85	479.29	13.82	53.73	13.10	19.35
15R-1, 66–72	488.86	15.83	55.34	10.16	18.65
16R-1, 44–50	498.34	25.81	52.01	8.87	13.31
17R-2, 71–77	509.71	43.66	42.02	0	14.32
18R-3, 138–144	521.58	14.53	59.67	8.16	17.64
19R-1, 37–43	527.27	15.94	53.22	16.31	14.53
20R-1, 122–128	537.82	12.33	51.72	16.06	19.87
21R-1, 58–64	546.88	63.33	24.57	0	12.10
22R-1, 44–50	556.24	12.78	53.64	16.42	17.16
23R-2, 73–79	567.73	21.34	44.52	16.37	17.77
24R-2, 30–36	577.00	10.59	56.05	15.70	17.66
26R-1, 110–116	595.70	10.47	52.20	14.32	23.01
27R-1, 45–51	604.75	8.04	52.47	18.30	21.19
28R-1, 50–56	614.40	6.33	52.39	18.61	22.67
29R-1, 100–106	624.50	9.87	54.68	16.60	18.84
30R-1, 60–66	633.70	5.51	56.33	16.61	21.35
31R-1, 44–50	643.24	11.48	60.41	8.92	19.19
32R-5, 94–100	659.34	8.00	62.40	9.55	20.05
33R-2, 22–28	663.82	3.98	60.31	14.38	21.33
34R-1, 52–58	672.32	5.95	60.94	12.42	20.69
35R-2, 50–56	683.40	5.68	69.98	9.11	25.23
36R-2, 132–138	693.92	45.34	44.25	0	10.41
37R-2, 22–28	702.52	6.64	58.27	12.81	22.28
37R-2, 131–137	703.61	0	0	100.00	0
38R-3, 22–28	713.72	0	54.79	19.07	26.14
39R-3, 50–56	723.70	81.27	14.54	4.19	0
40R-3, 10–16	733.00	45.79	38.63	0	15.58
41R-1, 34–40	739.94	29.62	51.26	19.12	0
42R-1, 45–51	749.75	35.40	44.72	0	19.88
43R-1, 93–99	759.40	29.44	46.02	24.54	0
44R-1, 93–99	769.03	29.08	53.14	0	17.78
45R-1, 59–65	778.29	57.79	31.88	0	10.33
46R-1, 76–82	788.16	75.53	19.15	0	5.32
47R-1, 50–56	797.40	77.50	17.91	4.59	0
48R-3, 76–82	810.36	71.43	18.93	0	9.64
50R-1, 40–46	828.60	24.73	65.59	9.68	0
51R-1, 76–82	838.66	76.33	23.67	0	0
52R-1, 90–96	845.50	8.66	85.40	0	5.94
59R-6, 19–23	919.69	100.00	0	0	0
72R-1, 82–88	1037.72	100.00	0	0	0

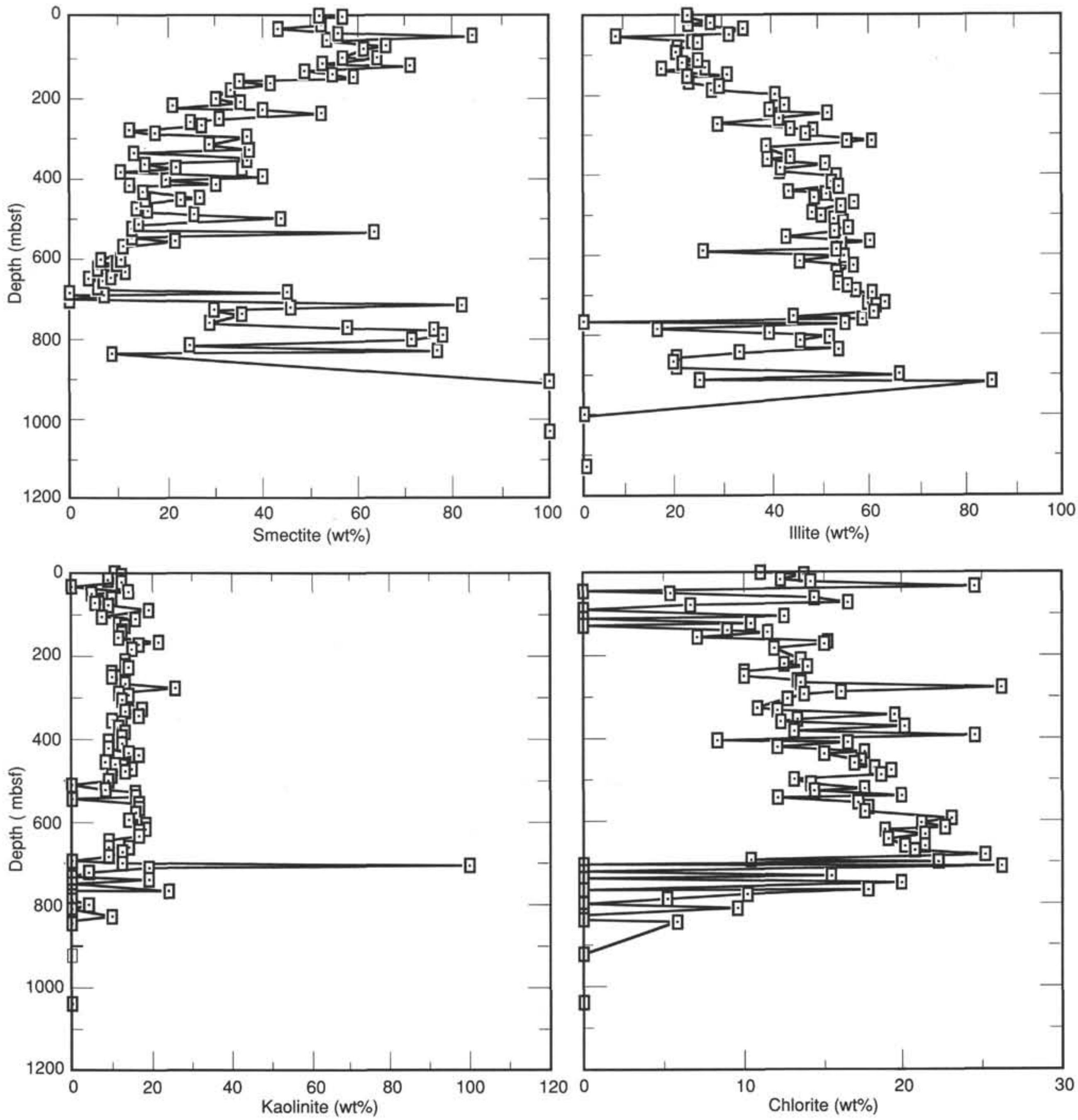

Figure 23. Abundance of smectite, illite, kaolinite, and chlorite in the <2-μm size fraction, Site 768.

Summary

The variation in clay mineralogy at Site 768 indicates a sequence of source changes during the history of deposition. After the initial deposition of a highly smectitic sediment, perhaps derived from local weathering of the basement, the tuffs of Unit IV were deposited with little externally derived clay. Most of the clay minerals in Unit IV are probably the result of diagenetic alteration of the tuffs. In Unit III, an initially smectitic, presumably volcanic source gave way rapidly to a highly continental, illite-rich source. Following the deposition of Unit III, Unit II reflects a long progressive change back to smectite-rich, noncontinental sediments that continue in Unit I in association with abundant calcium carbonate.

Chemistry of Volcaniclastic Deposits

Volcaniclastic sediments constitute an important component of the sedimentary sequence of Site 768. They occur either as thin laminae to thin beds of air-fall ashes, as thick upward-fining flows of primary or reworked pyroclastic materials, or as dispersed components within some of the rock types. The air-fall ashes, occurring above 255 mbsf, include vitric to lithic types with varying amounts of crystals (Fig. 10). The volcaniclastic flow units, which occur between 652.4 to 1036.9 mbsf, are mostly vitric, subordinately lithic, and have a low crystal content. Details on the distribution, composition, and sedimentological features of the volcaniclastic deposits are described in the previous sections.

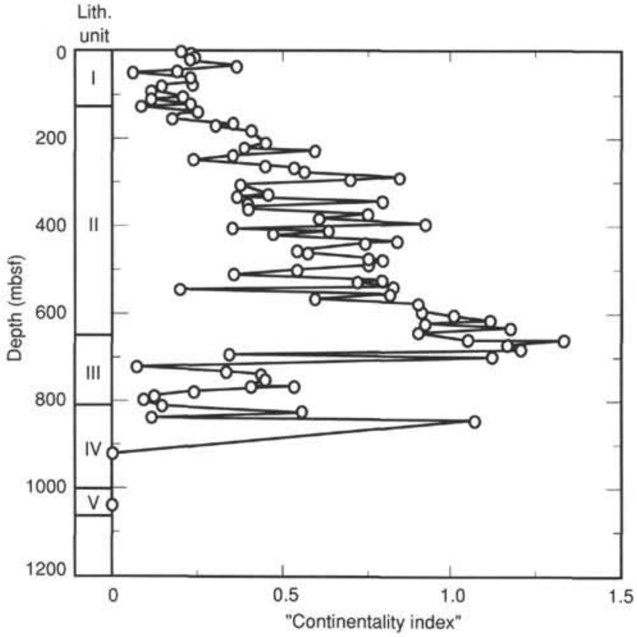

Figure 24. "Continentality" index vs. depth at Site 768. See text for discussion (in "Clay Mineralogy" subsection, "Lithostratigraphy" section, this chapter).

Ten representative samples of the volcaniclastic deposits have been analyzed by X-ray fluorescence (XRF). These include two samples of the vitric and lithic ashes, and eight samples of the fine and coarse tuffs from the volcaniclastic flow units. Major and some trace elements (Nb, Zr, Y, Sr, Rb, Zn, Cu, Ni, Cr, V, Ce, and Ba) have been determined for all tuff samples. However, only major elements were analyzed on two of the ash samples (124-768B-6H-1, 23 cm, and 124-768B-8H-1, 33 cm) because of the insufficient amount of sample for trace element analysis. The details of the analytical technique are described in the "Explanatory Notes" section (this volume).

The chemical data on the analyzed samples are reported in Table 4.

Air-fall Ashes between 0 and 255 mbsf

The lithic ash in Sample 124-768B-6H-1, 23 cm, is andesitic in chemical composition. Loss on ignition (LOI) is low for a rock containing volcanic glass (about 15%), and the well-preserved magmatic mineralogy implies that the original chemical composition is largely preserved and that the alkalis underwent minor postmagmatic changes. The K_2O content, assumed to be close to the primary value, relates this rock to the K-rich calc-alkaline series. This reference is in agreement with the petrographic data, particularly with the occurrence of biotite among the crystals.

The vitric ash (Sample 124-768C-8H-1, 33 cm) is fairly fresh, as confirmed by the low LOI, and could represent the bulk com-

Table 4. XRF chemical analyses of representative ash and tuff samples, Site 768.

Core, section, interval (cm)	Major elements											
	SiO_2	TiO_2	Al_2O_3	Fe_2O_3	MnO	MgO	CaO	Na_2O	K_2O	P_2O_5	Total[a]	LOI
124-768B-6H-1, 23	55.62	0.85	18.13	7.92	0.17	2.58	6.19	3.40	3.64	0.51	99.02	2.88
124-768B-8H-1, 33	69.12	0.23	15.18	2.58	0.07	1.42	3.07	3.47	2.90	0.18	98.22	3.48
124-768C-32R-1, 19	76.96	0.20	12.32	1.52	0.03	0.94	1.56	4.00	1.38	0.04	98.96	3.66
124-768C-32R-3, 106	67.46	0.36	15.48	6.36	0.04	3.30	2.33	2.95	0.78	0.08	99.14	7.32
124-768C-49R-2, 12	55.19	0.92	17.25	11.27	0.37	3.82	6.81	3.39	0.81	0.19	99.98	7.55
124-768C-49R-3, 22	65.71	0.44	16.15	4.49	0.25	1.78	4.56	4.13	0.65	0.12	98.28	13.03
124-768C-56R-1, 99	73.08	0.48	13.72	2.66	0.05	1.86	3.49	3.55	0.47	0.07	99.40	12.13
124-768C-61R-1, 135	75.45	0.53	12.23	3.47	0.10	2.72	2.62	2.14	1.28	0.13	100.66	10.82
124-768C-62R-4, 74	49.26	1.12	17.64	9.36	0.18	10.48	7.49	3.01	0.82	0.17	99.53	6.97
124-768C-70R-3, 58	62.50	0.81	15.27	7.33	0.41	3.23	4.57	3.16	0.66	0.20	98.13	4.40

	Trace elements											
	Nb	Zr	Y	Sr	Rb	Zn	Cu	Ni	Cr	V	Ce	Ba
124-768C-32R-1, 19	6	149	20	92	85	47	21	8	6	30	39	496
124-768C-32R-3, 106	5	186	16	218	26	41	36	18	20	73	45	955
124-768C-49R-2, 12	2	63	28	421	12	110	175	19	11	346	22	333
124-768C-49R-3, 22	2	110	29	602	7	47	40	5	0	75	28	704
124-768C-56R-1, 99	3	161	39	149	7	40	24	2	0	77	28	336
124-768C-61R-1, 135	3	126	47	175	18	36	18	5	0	29	17	219
124-768C-62R-4, 74	3	65	21	132	9	80	101	188	456	305	0	24
124-768C-70R-3, 58	2	73	33	680	6	97	40	9	12	135	24	523

Sample compositions:

124-768B-6H-1, 23 (42.23 mbsf) = Lithic ash. C: gl, rf, pl, opx, cpx, mt, bio.
124-768B-8H-1, 33 (61.33 mbsf) = Vitric ash. C: gl, rf, pl, hbl, cpx, bio, mt.
124-768C-32R-1, 19 (652.59 mbsf) = Vitric tuff. C: gl, pl.
124-768C-32R-3, 106 (656.43 mbsf) = Crystal vitric tuff. C: rf, gl, pl, hbl.
124-768C-49R-2, 12 (817.12 mbsf) = Crystal vitric tuff. C: rf, gl, pl, hbl.
124-768C-49R-3, 22 (818.72 mbsf) = Vitric tuff. C: gl, pl, hbl.
124-768C-56R-1, 99 (884.39 mbsf) = Vitric tuff. C: gl, pl, cpx.
124-768C-61R-1, 135 (932.75 mbsf) = Vitric tuff. C: gl, pl.
124-768C-62R-4, 74 (946.24 mbsf) = Crystal vitric tuff. C: gl, pl, cpx, hbl.
124-768C-70R-3, 58 (1021.18 mbsf) = Vitric tuff. C: gl, pl.

Note: Major element values given in wt% oxide, and trace element values in ppm. Abbreviations: rf = rock fragments, gl = glass, opx = orthopyroxene, cpx = clinopyroxene, hbl = hornblende, pl = plagioclase, bio = biotite, and mt = magnetite. LOI = loss on ignition.

[a] Totals systematically below 100% were obtained from on-board analyses and are interpreted as resulting from hydration of the sample between ignition and weighing.

position of the magma, since the crystal content is low and consists of early crystallized phases. The composition of this ash is rhyolitic, with a high-K serial character.

Volcaniclastic Flows between 652.4 and 1036.9 mbsf

The analyzed samples from the volcaniclastic flow units include five vitric and two crystal-vitric tuffs that represent the dominant lithology in these deposits. One crystal-vitric tuff (Sample 124-768C-62R-4, 74 cm) containing a significant lithic component constitutes a minor lithology. The vitric tuffs, though not strictly identifiable with the erupted magma, can be considered broadly representative of magmatic compositions, given the low crystal content. Their composition, however, could have been changed during diagenetic alteration. Diagenesis varies considerably with depth, but it generally increases with depth.

In most samples, the high water contents indicated by the high LOI values (carbonates are missing in the analyzed samples) imply that a significant mobilization of elements possibly occurred during diagenesis. The interpretation of the chemical data, therefore, must be restricted to generic references to magmatic types. Better information can be obtained from the chemistry of the less-altered samples (particularly Samples 124-768C-32R-1, 19 cm, and 124-768C-70R-3, 58 cm, which show the low values of LOI). The abundance of major and trace elements that are immobile or less mobile during alteration, such as Ti, Zr, Y, Nb, and Ce, can provide further information for magmatic affinities.

The major element chemistry of the vitric tuffs shows large compositional variations. Contents of SiO_2 indicate that these rocks can be referred to intermediate to persilicic magmas of dacitic to rhyolitic composition. In the K_2O vs. SiO_2 diagram (Fig. 25), the freshest vitric tuffs are found in the rhyolite (Sample 124-768C-32R-1, 19 cm) and dacite (Sample 124-768C-70R-3, 58 cm) fields of calc-alkaline rock series near the boundary with the low-K calc-alkaline series. For the more altered samples, this diagram is less significant because of possible important variations of the K_2O content during diagenetic transformation.

The crystal-vitric tuffs are less rich in SiO_2 than the vitric tuffs, as a consequence of the higher concentration of crystals (mainly plagioclase and hornblende), and possibly because of the different composition of the glass component. Their chemistry, though not representative of the source magma, can provide some indication of the composition of less fractionated magmas, which were probably dacite and andesite with calc-alkaline affinity. Sample 124-768C-62R-4, 74 cm, has a basaltic composition, implying that less fractionated magmas could have contributed to the volcaniclastic units.

Values of more incompatible, stable trace elements and of Ti show significant variations relative to Zr and could support comagmatic relationships of these rocks. Covariations of Ti and Zr are shown in Figure 25.

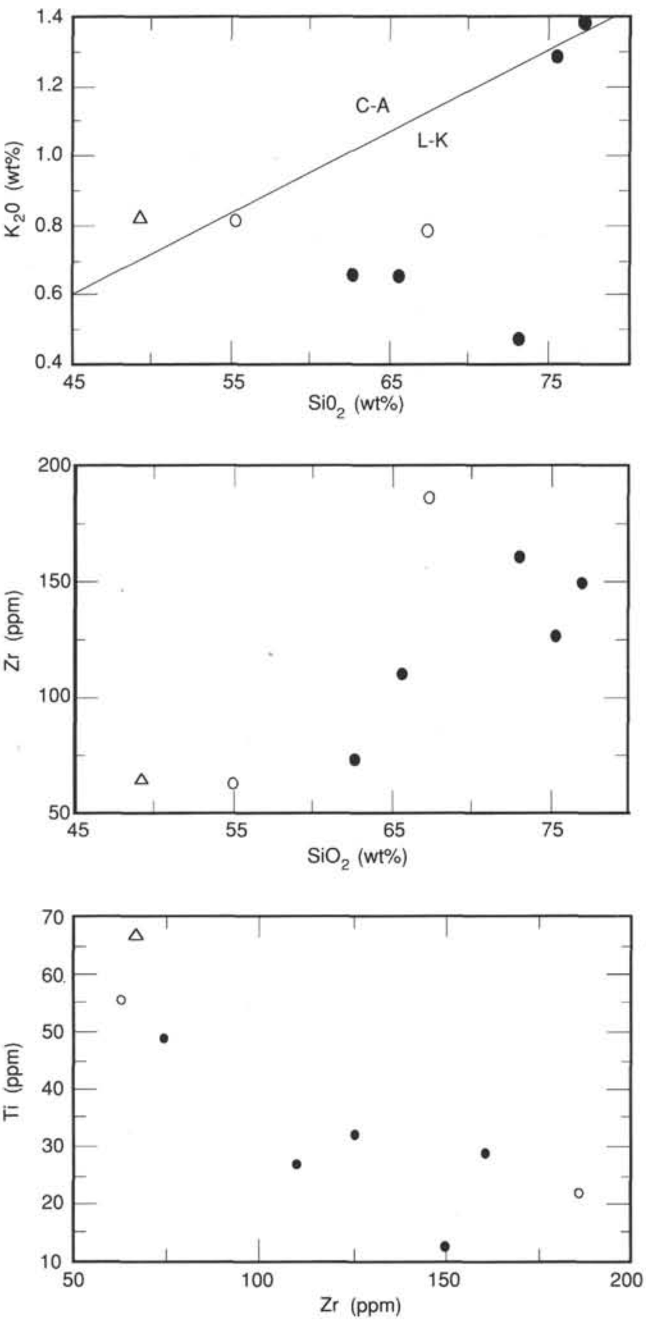

Figure 25. Variation diagrams of selected major and trace elements tuff samples from volcaniclastic flows, Site 768. In the K_2O-SiO_2 diagrams, the boundaries of calc-alkaline (C-A) and low-K calc-alkaline (L-K) series are after Ewart (1979). Closed circle = vitric tuff, open circle = crystal-vitric tuff, and triangle = crystal-vitric tuff with lithic clasts.

Depositional Environment and Processes

The sedimentary sequence at Site 768 records three major phases of deposition in the Sulu Sea. During early Miocene time, pyroclastic deposits dominated the sedimentary record, preceded and followed by pelagic brown clay. A long period of deposition of hemipelagic clay with interbedded turbidites of continental origin followed, extending from the middle Miocene to the end of the Pliocene. Pleistocene sedimentation took place above the CCD and is dominated by pelagic marl.

The initial deposit overlying the basaltic basement is dark grayish brown hemipelagic claystone with interbedded turbidites of pyroclastic material (Unit V). The claystone contains a sparse fauna of fish teeth and poorly preserved radiolarians and was deposited slowly within a pelagic environment below the CCD. The turbidites are the precursors of a thick interval of vitric tuff and lapillistone (Unit IV) that dominates the lower Miocene sedimentary sequence in the basin.

The pyroclastic sediments occur in very thick upward-fining units that were deposited by a combination of sediment gravity flow processes: the coarser pyroclastic material was deposited by laminar mass flow events, and the finer tuffs at the tops have the characteristics of redeposition by turbidity currents. These deposits are the products of subaerial or shallow submarine explosive volcanism generating sediment gravity flows that carried the material to the site of deposition in deep water. The absence of any terrigenous or pelagic material in Unit IV indicates that these pyroclastic rocks were deposited over a short period of time.

A return to calmer pelagic sedimentation in the late early Miocene (NN5?) is marked by the reappearance of brown claystone with very fine-grained volcaniclastic turbidites at the base of Unit III, grading upward into greenish gray hemipelagic claystone that makes up much of the lower part of the unit. Sparse biostratigraphic data for this interval (see "Biostratigraphy" section, this chapter) indicates either a period of slow sedimentation spanning late early through much of middle Miocene time (NN4 or NN5 through NN8), or a possible hiatus in middle Miocene time, or both, although core recovery is poor for this interval.

Sporadic deposition of reworked ash resumed in the late middle Miocene (NN9), present as thick mass flow units mixed with variable amounts of terrigenous clastic material (detrital quartz and plant debris) in the upper part of Unit III. The volcanic components of these beds include fresh volcanic glass, indicating that explosive volcanism continued in late middle Miocene time, albeit on a much reduced scale compared to the early Miocene.

The first influence of a continental source on sedimentation at Site 768 took place in late early Miocene or early middle Miocene time, represented by very rare, fine-grained turbidite deposits with silt-size quartz in the lower part of Unit III. The proportion of terrigenous turbidites (with quartz, feldspar, rock fragments, and plant debris) increases rapidly in the middle of Unit III, becoming the dominant lithology in the upper half of Unit III and the lower half of Unit II (715–410 mbsf). The redeposited sediment is generally fine, consisting of turbidites of silt and clay, with rare sandstone turbidite beds. These strata represent the distal deposits of a turbidite depositional system that had its source area in a continental landmass bordering the basin.

The peak of turbidite deposition occurred within Zone NN9 (late middle Miocene) and is contemporaneous with a major sea-level lowstand in Zones NN8 and NN9 (Haq et al., 1987a, 1987b, 1988), the lowest sea level recorded during Miocene time, and also to a peak in tectonic activity in the Mindoro-Panay area prior to Zone NN11 (Müller and Daniel, 1981; Rangin et al., 1985) associated with a widespread gap from Zones NN6 to NN10. One or both of these events resulted in the rapid delivery of terrigenous sediment into the deep basin. An upward decrease in the proportion of silt in the terrigenous turbidites occurs through the upper half of Unit II, accompanied by a decrease in turbidite bed thickness and an increase in the proportion of hemipelagic clay. These trends reflect a waning turbidite influx through late Miocene and Pliocene time.

Renewed volcanic activity in the area is indicated by the presence of thin air-fall ash beds and minor redeposited ash in the sequence above Core 124-768C-29X (255 mbsf). The record of young ashes at Site 768 shows that volcanism began in the late Miocene (Zone NN11) and continued into the Pleistocene. There is a change from crystal and lithic ashes in the early stages to vitric ashes in the more recent deposits.

Prior to Pleistocene time, deposition at Site 768 occurred entirely below the CCD. Carbonate sedimentation below Unit I is confined to thin redeposited nannofossil marl layers that occur sporadically through Units III and II. In the latest Pliocene, there was a major change from deposition of hemipelagic clay to a more carbonate-rich sequence of biogenic marl (mixed sediments of clay and pelagic carbonate), presumably in response to a deepening of the CCD in the basin. In the Sulu Sea the CCD currently lies at 4800 m (Linsley et al., 1985), about 200 m deeper than that calculated by Berger et al. (1976) for the western Pacific. This level is also substantially deeper than the CCD of the South China Sea, which presently lies at approximately 4000 m (Rottman, 1979). The present water depth at Site 768 is 4384.4 mbsl, well above the present CCD. The high carbonate content of surface sediments in Holes 768A and 768B support this interpretation.

Figure 26 plots percent carbonate vs. depth for pelagic sediments (excluding turbidites) in Cores 124-768B-1H to -18H (0–160 mbsf) (for data, see "Inorganic Geochemistry" section, this chapter). The transition from Pliocene hemipelagic sediments devoid of carbonate to the carbonate-rich latest Pliocene to Pleistocene sediments occurs over a zone 14.15 m thick (133.15–119.0 mbsf), extending from Sections 124-768B-15H-4, 115 cm, to 124-768B-14H-1, 50 cm. The base of this transition occurs at ~2.47 Ma at the Gauss/Matuyama boundary. Given a sedimentation rate for this interval of 19 m/m.y. calculated from paleomagnetic stratigraphy (see "Sediment Accumulation Rates" section, this chapter), this transition took place over roughly 750 k.y.

A trend of gradually increasing carbonate content (maximum 60%) is seen in the lower part of Unit I, from 123 to 100 mbsf, followed by a sharp drop to about 25% carbonate just above 100 mbsf, within the later part of the Matuyama paleomagnetic epoch. Following a modest increase in carbonate content between 95 and 70 mbsf, there is another sharp drop to low values (<20%) around 60 mbsf (early Brunhes paleomagnetic epoch). Above 50 mbsf carbonate values fluctuate about an average of 40%. The two zones of low carbonate values within the marl of Unit I may reflect times of temporary shallowing of the CCD within the basin, resulting in the increased dissolution and decreased sedimentation rate of biogenic carbonate sediment. Alternatively, these zones could represent times of increased terrigenous clay input, causing dilution of the biogenic carbonate sediment.

Structures

Most of the sediments and sedimentary rocks recovered at Site 768 are too poorly indurated and too incompetent to show clear fracturing. Microfaults with slickensides observed in the

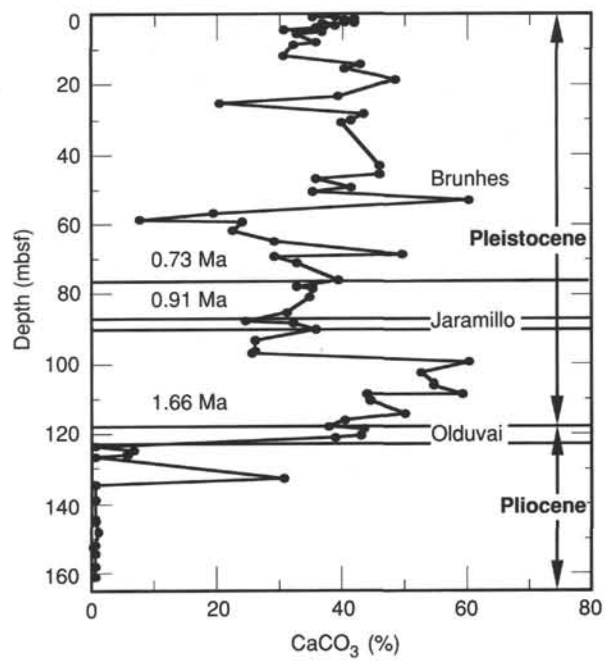

Figure 26. Plot of carbonate vs. depth for pelagic sediments (excluding turbidite beds) in Unit I and uppermost Unit II, Site 768 (Cores 124-768B-1H to -18H). Paleomagnetic datum levels and the position of the Pliocene/Pleistocene boundary are also shown. Note the rapid increase in carbonate content across the Pliocene/Pleistocene boundary.

poorly indurated upper part of the column occur in conjugate sets and indicate a vertical maximum compression direction parallel to the axis of the core. These faults may be caused by drilling disturbance. However, in the more indurated lower part of the column, especially in Unit IV and in the basement, three types of natural fractures were distinguished (Fig. 27).

Compaction or Shrinkage Cracks and Microfaults

These structures occur throughout Unit IV. A good example occurs in Section 124-768C-51R-3, 61–67 cm (Fig. 28). It shows a set of parallel microfaults (0.5-cm spacing, averaging 3 cm long) with apparent dips of about 45° in the plane of the split-core surface and associated conjugate fractures. The dip-separation is always normal and does not exceed 2 mm. Most of the faults terminate downward in silica-filled tear fractures that dip in the opposite direction to the microfaults and make a 50° clockwise angle with the projected fault trace. The displacement along the microfaults has been accommodated by dilation of the tear fractures, which narrow downward and end within 1–1.5 cm of the intersection. These fractures occur in the top part of a fine-grained vitric tuff, the top of which was cracked under the load of the overlying sediments.

Normal Faults

Normal faults mainly occur in tuff between Cores 124-768C-49R and -59R, and most have high apparent dip angles (mean 80°, range between 40° and 90°). Offset laminae, rare slickensides, and related silica-filled gash fractures attest to a normal apparent motion along the faults. Most of the fault traces are linear, but some are curved. The curved portions are marked either by pressure-solution zones, which are the same greenish gray color as the surrounding matrix, or by gash fractures filled with white silica, depending on the orientation of the curve relative to the direction of the shear (Fig. 29). The dip separation varies widely, from 1 to 30 cm. Some faults widen toward the top and are then filled by a wedge of tectonic microbreccia.

Considering the high mean dip of the normal faults and the paucity of fractures above Core 124- 768C-49R and below Core 124-768C-59R, it is reasonable to consider that Hole 768C cross-cut a normal fault zone almost 20 m wide between approximately 800 and 900 mbsf. If so, this could indicate that extension of the Sulu Sea Basin continued after deposition of the tuff sequence (Unit IV). Fractures are absent in the section above Unit IV, but this could be a result of the incompetence of the overlying section, so a minimum age for the extensional faulting cannot be established from the core data. Although compaction cannot be excluded for the genesis of these faults, their localization within a narrow zone indicates that they are tectonic in origin.

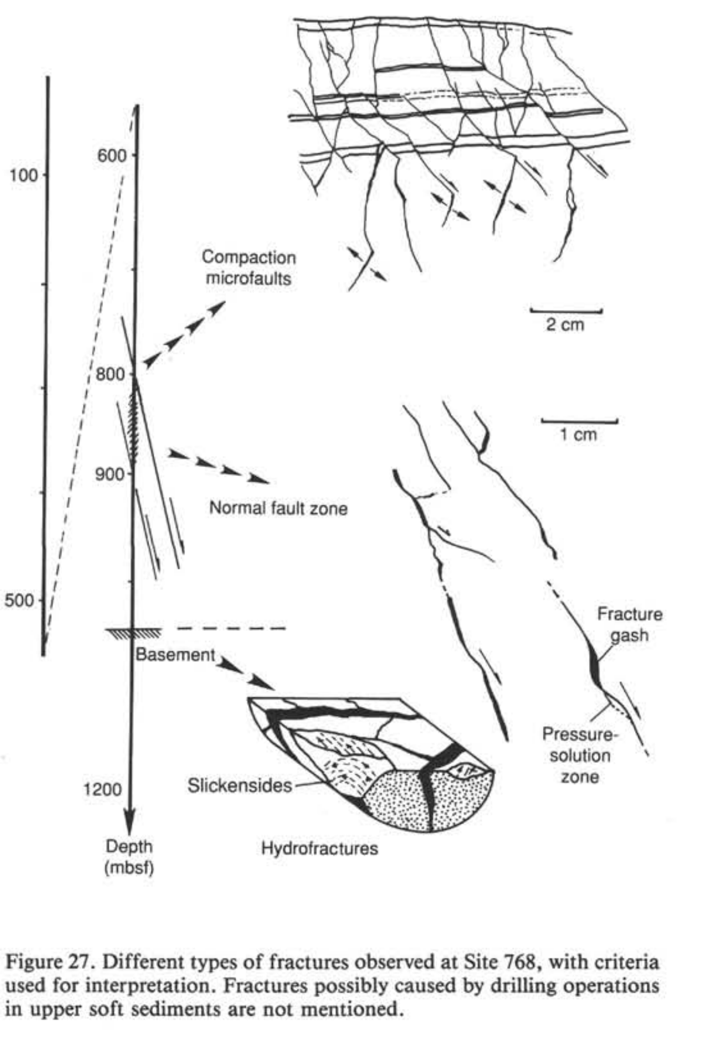

Figure 27. Different types of fractures observed at Site 768, with criteria used for interpretation. Fractures possibly caused by drilling operations in upper soft sediments are not mentioned.

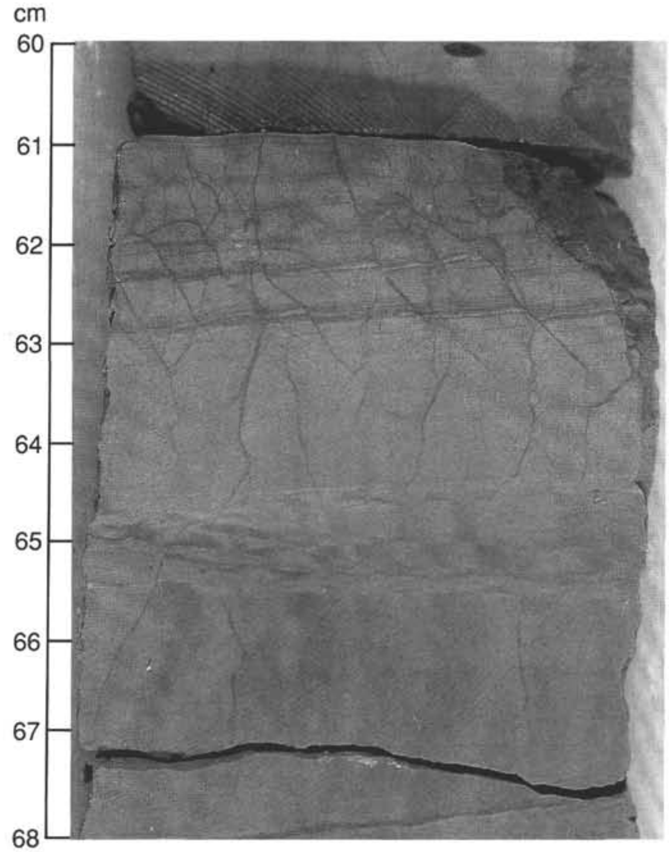

Figure 28. Microfaults in fine tuff, Unit IV (Section 124-768C-51R-3, 60–68 cm).

Hydrofractures

These occur in the basalt and diabase of the basement. Numerous V-shaped tear-fractures and microfaults affect both pillows and intrusive rocks. They are usually filled with calcite in the upper part of the basement and with gypsum and reddish hematite(?) in the lower part. Hematite(?) occupies the outer edges of wide cracks with complex fills and also appears alone

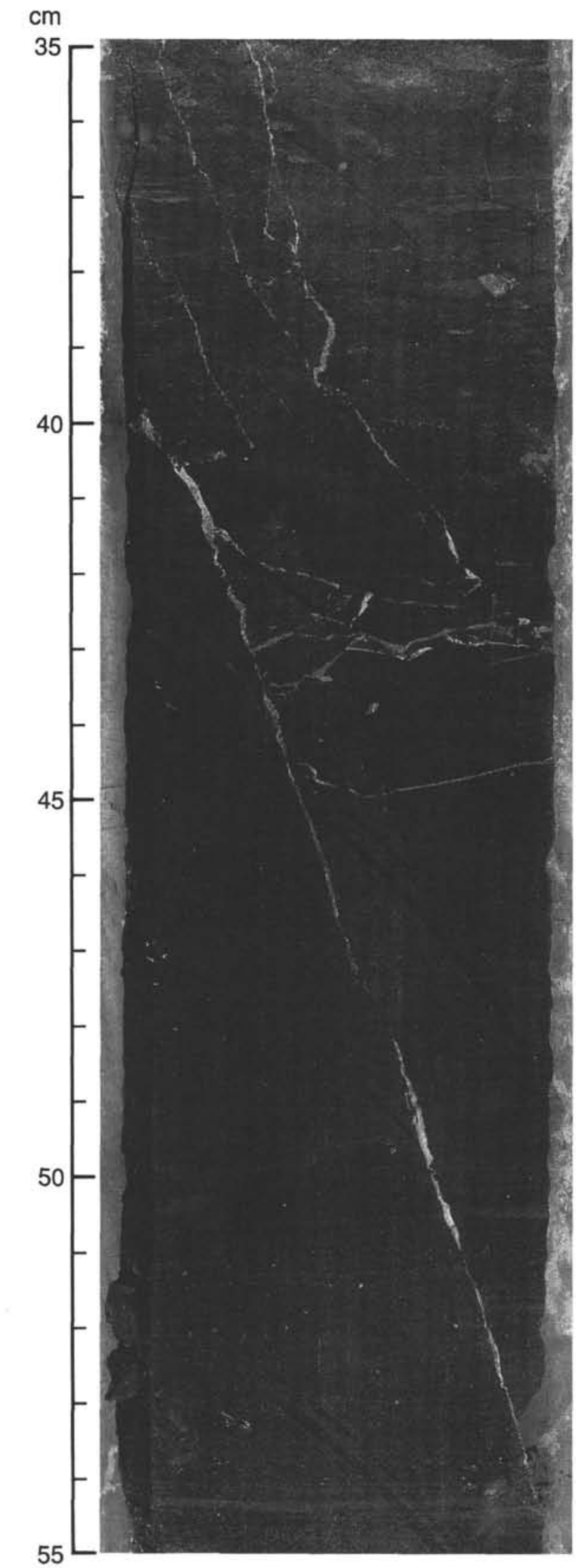

Figure 29. Normal microfaults (with gashes and pressure-solution zones) in Unit IV (Section 124-768C-49R-4, 35–55 cm).

in the thinnest joints, indicating that it formed during the first of several episodes of fluid crystallization.

Many of the microfault surfaces exhibit well-preserved slickensides that are commonly curved, with small radii of curvature, indicating rotation of individual small blocks about axes that were not parallel to the fault surface. The slickensides indicate normal, reverse, strike-slip (right lateral in Section 124-768C-96R-2, 100 cm), or a combination of vertical and strike-slip motions. In addition, neither the azimuth (relative to the core split), dip, nor pitch of the faults seem to have any consistency.

Many fractures filled with calcite or gypsum are even horizontal, perpendicular to the lithostatic pressure. This can be interpreted as the result of contraction caused by cooling or a result of fluid injection in cooling joints, or both. The variability in orientation of the fractures and faults in the basalt and diabase implies that they are not related to regional deformation of the basement.

BIOSTRATIGRAPHY

Summary

Three holes were drilled at Site 768 in the Sulu Sea. One core was obtained from Hole 768A of Pleistocene age. Hole 768B was cored to a depth of 364.1 mbsf; Hole 768C was washed down to a depth of 352.2 mbsf, then cored to a depth of 1271.0 mbsf. Basement was reached at a depth of 1046.6 mbsf in Core 124-768C-73R. The sediments range in age from Pleistocene to early Miocene.

The upper 125 mbsf of the sedimentary section, in Hole 768A and Cores 124-768B-1H through -14H, consist of marls that contain rich nannofossil and foraminifer associations (see "Lithostratigraphy" section, this chapter). These fossils give a Pleistocene to upper Pliocene age for these sediments. Abundant radiolarians and diatoms were found in the upper 60 cm in Holes 768A and 768B. Their preservation and frequencies rapidly deteriorate with depth. Core 124-768B-7H is the deepest core containing remains of diatoms. In Cores 124-768B-13H through -15H, the calcareous microfossils show increasing signs of dissolution with depth. The underlying sediments in Hole 768B, as well as in Hole 768C, are interpreted as deposited below the CCD.

In Cores 124-768B-16H to -40R, and in Cores 124-768C-1R to -42R, calcareous microfossils were mainly found in turbidites. They are abundant in the thin, carbonate-rich turbidites in Cores 124-768B-16H through -21H. The low numbers of benthic foraminifers, and the absence of the remains of shelf-dwelling organisms, indicate that the turbidites were derived from a deep source. The carbonates in the deeper cores are recrystallized and barren of fossils. Calcareous fossils are rare in the siliciclastic turbidites that are found in Cores 124-768B-16H through -39X and in Cores 124-768C-1R through -42R. The foraminifer faunas in the carbonate turbidites consist mostly of small, size-sorted specimens. The faunas in the siliciclastic turbidites were interpreted as derived from shallow water and generally contain long-ranging species only. Therefore, age determinations were mainly derived from nannofossils.

In Cores 124-768B-16H through -39X and in Cores 124-768C-1R through -40R, a continuous upper Pliocene to middle Miocene record was found. The Pliocene/Miocene boundary was recognized in Core 124-768B-23H (203 mbsf); the boundary between the upper and middle Miocene is at the top of Core 124-768C-5R (392 mbsf). A 4–5-Ma difference in age between Cores 124-768C-40R (upper middle Miocene Zone NN8) and 124-768C-42R (lower middle Miocene Zone NN5) could indicate the presence of a hiatus. However, the sediments in these cores show no visual sign of a discontinuity, and it is not certain if the nannofossils of Zone NN5 are reworked or just displaced, as within the other turbidites.

From Core 124-768C-33R downward, the number and frequency of the siliciclastic turbidites decreased. The clays in between contain rare ichthyoliths and arenaceous foraminifers. Core 124-768C-42R, at a depth of 758 mbsf, is the deepest core in which calcareous microfossils are found. However, they might be reworked. Arenaceous foraminifers and ichthyoliths are common in the coarse fraction of Cores 124-768C-40R through -47R, indicating low rates of sediment accumulation in those cores. Frequencies of these fossils remain on the same order of magnitude across a change in color from mainly grayish to dominantly reddish brown clays, which occurs in Core 124-768C-45R (see "Lithostratigraphy" section, this chapter).

Reddish brown clays were present in Cores 124-768C-45R through -47R and in Cores 124-768C-69R through -72R. The volcanic ashes in between (Cores 124-768C-48R through -68R; 806.6 mbsf to 1008 mbsf) are mostly barren. The ichthyolith faunas in the red clays do not contain age-diagnostic types. Rich and moderately well-preserved radiolarians are present in Core 124-768C-47R and in the top of the volcanic ashes (Core 124-768C-48R). They give a late early Miocene age. Radiolarians in the reddish clays in Cores 124-768C-69R through -72R are very poorly preserved and could not be assigned to a specific zone. However, they also indicate a late early Miocene age for the sediments overlying basement, which was encountered in Core 124-768C-73R at a depth of 1046.6 mbsf.

Nannofossils

Only one core was recovered from Hole 768A (0–9.5 mbsf); it yielded a rich and well-preserved Pleistocene nannofossil assemblage. The presence of *Emiliania huxleyi* throughout the core assigns this interval to upper Pleistocene Zone NN21. The nannofossil zonation scheme used for this site is the one proposed by Martini (1971).

Hole 768B was drilled down to 364.1 mbsf. The top 118 mbsf of Pleistocene sediments mainly consist of light greenish gray nannofossil and foraminifer marls or oozes that contain well-preserved, common to abundant Pleistocene nannofossils with few reworked Pliocene species. *Emiliania huxleyi* is present from the top of Section 124-768B-1H-1 to Sample 124-768B-4H-5, 23–24 cm (29.35 mbsf). This interval belongs to Zone NN21 and should not be older than 0.275 m.y.

Samples 124-768B-4H-6, 23–24 cm, to 124-768B-7H-1, 25–26 cm (27.7–51.7 mbsf), contain a Pleistocene assemblage, without *E. huxleyi* or *Pseudoemiliania lacunosa,* and therefore belong to Zone NN20. The last occurrence (LO) of *P. lacunosa* was detected in Sample 124-768B-7H-2, 28–29 cm (53.28 mbsf). This globally synchronous event in tropical and subtropical waters has an age of 0.47 m.y.

The sediments between Samples 124-768B-10H-5, 97–98 cm (86.9 mbsf), and 124-768B-10H-CC are characterized by the dominance of a small *Gephyrocapsa* sp. and the scarcity of *Gephyrocapsa oceanica.* This interval is assigned to the small *Gephyrocapsa* acme zone that corresponds to the Jaramillo paleomagnetic event (see "Paleomagnetics" section, this chapter) and is very close to 0.93 m.y. (Gartner, 1988).

The Pliocene/Pleistocene boundary is determined by the LO of *Discoaster brouweri.* However, they are extremely rare within the uppermost Pliocene. Very rare specimens of *D. brouweri* and *Discoaster pentaradiatus* were observed together with more common *Cyclococcolithus macintyrei* in Sample 124-768B-14H-1, 70–71 cm (118.70 mbsf), at the top of the Olduvai paleomagnetic event, which corresponds well with the results obtained from other areas (Müller, 1985). The precise determination of this boundary at Site 768 is difficult because of reworking.

On the same level, strong dissolution can be observed. A very distinct lithologic change occurs just below the Pliocene/Pleistocene boundary. The Pleistocene nannofossil and foraminifer marl and ooze are replaced by dark gray to greenish gray clays with some interbedded calcareous turbidites in the Pliocene. Nannofossils are very rare in the clay, but they generally are common in the calcareous turbidites.

The sediments between Samples 124-768B-14H-5, 40–41 cm, and 124-768B-14H-CC contain *D. brouweri,* but no *Discoaster pentaradiatus,* indicating Zone NN18. The LO of *D. pentaradiatus* in Sample 124-768B-15H-1, 66–67 cm (128.1 mbsf), marks the top of Zone NN17. The age of this datum is approximately 2.2 m.y. The next useful datum is the LO of *Discoaster surculus,* found in Sample 124-768B-15H-4, 102–103 cm (133.0 mbsf). This datum defines the top of Zone NN16 and has an age of about 2.4 m.y. The base of Zone NN16 was recognized by the LO of *Reticulofenestra pseudoumbilica* in Sample 124-768B-17H-6, 116–117 cm (155.1 mbsf). The boundary between Zones NN16 and NN15 corresponds to the upper/lower Pliocene boundary, which has an estimated age of 3.4 m.y. The boundary between Zones NN15 and NN14 is determined in Sample 124-768B-19H-3, 128–129 cm (169.7 mbsf).

The subdivision of the lower Pliocene is very diffficult because the index fossils are very rare. Therefore, Zones NN12–NN14 are grouped together. The *D. quinqueramus* Zone NN11 of the upper Miocene was encountered from Samples 124-768B-23H-2, 85–86 cm (203.4 mbsf), to the bottom of the hole.

Nannofossils are only present in the upper part of the sedimentary sequence recovered from Hole 768C. They are usually rare and poorly preserved. Few middle to late Miocene marker species were found. *Discoaster quinqueramus,* diagnostic for Zone NN11, is present in Sample 124-768C-1R-4, 42–43 cm (358.1 mbsf). Its first occurrence (FO) is used to define the bottom of NN11 and has been dated at 8.2 m.y. The sediments of Cores 124-768C-3R and -4R are barren of nannofossils.

The next datum was found in Sample 124-768C-5R-1, 33–34 cm (392.1 mbsf), with the LO of *Discoaster hamatus.* The LO of *D. hamatus* defines the top of Zone NN9 and the boundary between the upper and middle Miocene. The interval between 358.1 and 392.1 mbsf probably belongs to Zone NN10, which was determined in Sample 124-768C-2R-3, 50–51 cm. Zone NN8 was encountered from Samples 124-768C-38R-3, 150–151 cm, to 124-768C-40R-4, 132–133 cm (735.1 mbsf).

Two distinct laminated turbidites occur within Sections 124-768C-42R-1 and 124-768C-42R-3. Both contain *Sphenolithus heteromorphus* and other species typical for nannoplankton Zone NN5, such as *Cyclicargolithus floridanus, Cyclicargolithus abisectus,* and rare *Discoaster deflandrei.* However, it is possible that they are reworked, because few specimens of *Sphenolithus heteromorphus* and *Cyclicargolithus abisectus* were also found in Sample 124-768C-40R-4, 132–133 cm, together with *Catinaster coalitus* of Zone NN8. Two alternate interpretations are possible: either it exists as a hiatus between Zones NN8 and NN5, considering the assemblages as autochthonous or displaced, or there is only a significant decrease in sedimentation rate if they are reworkings.

Nannofossils are absent from Core 124-768C-43R to the basement.

Foraminifers

The samples from Core 124-768A-1H and from Cores 124-768B-1H to -14H contain rich and diverse planktonic foraminifer faunas that are generally well preserved. Some samples show signs of size sorting: Sample 124-768B-2H-5, 59–62 cm, contains small-sized specimens only, whereas large-sized specimens were found in Sample 124-768B-10H-CC. This indicates that at least part of the foraminifer faunas are displaced. The low numbers of benthic foraminifers (<1%) in these samples imply a deep source for the displaced material.

The LO of the pink variety of *Globigerinoides ruber* is found in Sample 124-768B-2H-CC; this datum occurred 120 Ka ago (Thompson et al., 1979). The change in coiling direction of *Globorotalia menardii* occurs between Samples 124-768B-14H-CC (left-coiling *G. menardii*) and 124-768B-15-2, 58–61 cm (right-coiling *G. menardii*). This change is considered here to mark the lower boundary of Zone NN22.

Samples from Cores 124-768C-13H to -15H show increasing signs of dissolution with depth. The sediments from most of Core 124-768B-15H, as well as from all deeper cores, were deposited below the CCD. Foraminifers are confined to carbonate-rich turbidites (Cores 124-768B-16H to -21H) and siliciclastic turbidites (Cores 124-768B-16H to -39X and Cores 124-768C-1R to -39R). The faunas in the carbonate-rich turbidites are size sorted, consisting mainly of small-sized, moderately well to well preserved specimens. Benthic foraminifers are rare; the faunas consist mainly of planktonic foraminifers, implying that the carbonate-rich turbidites were derived from a deep-water source.

Within the siliciclastic turbidites, rare foraminifers are found that are mostly moderately to poorly preserved. The faunas consist mainly of species with globular chambers (*Globigerinoides* spp. and *Globigerina* spp.), whereas benthic foraminifers are common to abundant in many samples. Probably, these faunas represent populations from shelf areas, where planktonic foraminifers with a deep habitat would have been scarce. Age-diagnostic planktonic forms are rare in both the calcareous and the siliclastic turbidites. Only a few samples could be dated.

The presence of *Sphaeroidinella dehiscens* in Sample 124-768B-17H-4, 54–57 cm, gives a late Pliocene age (Zones N19/N20 or N21). Sample 124-768B-19H-2, 90–92 cm, and 124-768B-19H-5, 49–51 cm, are considered to belong to Zone N18, given the presence of *Globorotalia margaritae* and absence of *S. dehiscens*. The presence of *Globorotalia plesiotumida* in Samples 124-768B-22H-3, 69–72 cm, and 124-768B-36X-1, 128–130 cm, indicates late Miocene (Zone N17) as the oldest age.

In Hole 768C, the number and thickness of the siliciclastic turbidites decreases from Core 124-768C-33R downward. In the clays between the turbidites, agglutinated foraminifers were found. Sample 124-768C-39R-CC is the deepest sample containing calcareous foraminifers. Below that, only agglutinated foraminifers were found in Cores 124-768C-40R to -47R and in Cores 124-768C-69R to -72R (the volcanic ashes in Cores 124-768C-48R to -68R are barren). They are accompanied by ichthyoliths and indicate deposition below the CCD, with low rates of sediment accumulation.

Diatoms

As with Site 767 in the Celebes Sea, Site 768 in the Sulu Sea contains a well-preserved diatom flora only within the upper part of Cores 124-768A-1H and 124-768B-1H. Below the light brown soupy unit of approximately the upper 60 cm, preservation of diatoms rapidly degrades, and concentration of siliceous fossils becomes low. In fact, the profile of biogenic silica degradation appears almost identical to that seen in the Celebes Sea. The carbonate-free fraction of these sediments appears very similar to non-acid-treated sediments of the deeper water Site 767. Fragments of diatoms were noted down to Core 124-768B-7H. Most of these fragments showed signs of strong dissolution. No diatom fragments were found below Core 124-768B-7H. As with the Celebes Basin, primary siliceous productivity in the Sulu Basin appears to have been too low to develop a significant contribution of diatom frustules to the sediments. The diatom assemblage represented in the uppermost sediments of Site 768 is the same as that found at Site 767, representing the *Pseudoeunotia doliolus* Zone of the late Quaternary, with a shelf-derived component, as indicated by the presence of benthic diatoms, which are less abundant at Site 768 in the Sulu Sea.

Radiolarians

Upper Neogene sediments from Site 768 contain abundant radiolarians in the uppermost sediments, but the fossils rapidly degrade with depth, paralleling the dissolution pattern noted in the diatoms. With the exception of very rare fragments within turbidites, radiolarians are absent throughout the remainder of sedimentary Unit I, all of Unit II, and most of Unit III (see "Lithostratigraphy" section, this chapter). The interval barren of siliceous microfossils spans Hole 768B from Core 124-768B-8H (70.5 mbsf) to the base of this hole at 364.1 mbsf (Core 124-768B-40X) and Hole 768C from the top (362.9 mbsf) to Core 124-768C-46R-CC (796.9 mbsf).

An abundant and moderately well-preserved radiolarian assemblage was recovered from reddish-brown pelagic claystone recovered in Core 124-768C-47R near the base of sedimentary Unit III. This assemblage contains abundant *Stichocorys wolffii, Stichocorys delmontensis,* common *Calocycletta costata,* and *Calocycletta virginis.* Also present are *Didymocyrtis tuberia, D. violina, D. mammifera, Cyrtocapsella cornuta, Cyrtocapsella tetrapera,* and rare *Dorcadospyris forcipata* and *D. dentata*(?). These species define the *Calocycletta costata* Zone of an upper lower Miocene succession.

A sample from Core 124-768C-48R-3, 104–106 cm, contains a radiolarian assemblage that includes abundant *S. wolffii* and common *C. virginis,* along with *Didymocyrtis prismatica, D. tuberia, C. cornuta,* and rare *S. delmontensis* and *Dorcadospyris forcipata. Calocycletta costata* is present, but in contrast with assemblages within overlying samples, this taxon is rare at this level, indicating that this sample lies near the base of the *C. costata* Zone.

The core catcher of Core 124-768C-48R contains a radiolarian assemblage that is highly diluted by volcanogenic debris. The assemblage includes *S. wolffii, C. virginis, D. prismatica, D. tuberia, D. violina, D. forcipata, C. tetrapera,* and *C. cornuta.* We did not see *C. costata* (were unable to find it?). One broken (thus unconfirmed) specimen of *Lychnocanoma elongata* was found. Given the apparent lack of *C. costata,* this assemblage appears to fall within the upper part of the *Stichocorys wolffii* Zone, still in the upper part of the lower Miocene. *Stichocorys wolffii* is present in great abundance in Cores 124-768C-47R and -48R, reaching more than 50% of the radiolarian fauna. This phenomenon is typical of Pacific sediments during this time interval (Romine and Lombari, 1985).

Absolute and relative dating of these biostratigraphic zones are difficult, because of the considerable variation in published chronostratigraphic correlations for the early Miocene. For example, Berggren et al. (1985a, 1985b) correlated the *C. costata* Zone entirely within nannofossil Zone NN4, whereas Haq et al. (1987a, 1987b, 1988) and others correlate this zone with the middle part of Zone NN4 to the lower part of Zone NN5. Most chronostratigraphic correlations place the base of the *C. costata* Zone at about 17.3 Ma.

Radiolarians were not found in the thick pyroclastic successions underlying Core 124-768C-49R. Some dark reddish and greenish pelagic sediments were recovered overlying pillow basalts in the interval of 1003.6 mbsf (124-768C-69R) to basement at 1046.6 mbsf (124-768C-72R). Radiolarians are present in certain levels of this sequence, but abundance is very low in all samples, and preservation is generally very poor. Most samples from this interval contain radiolarians that are preserved as casts, largely or wholly replaced by celadonite (glauconite). Processing the sediment with oxidation techniques that use hydrogen peroxide and Calgon degrades or destroys these fossil remains, but the fossils are retained when the sediment is processed with the kerosene method. With most specimens, positive identification is impossible but the distinctive outline of certain forms makes tentative identification possible.

Radiolarians identified from sediments of Sections 124-768C-69R-CC through 124-768C-72R-CC include *C. virginis, D. forcipata*(?), *C. tetrapera, C. cornuta, D. prismatica,* and a few forms that appear transitional between *D. prismatica* and *D. tuberia. Theocorys spongoconum*(?), a heavily silicified, solution-resistant species, is common in these samples, although it is rare in the well-preserved assemblage above the volcanic rocks. Thus far, only a single specimen of *S. wolffii* has been found below the pyroclastic rocks, in Sample 124-768C-70R-CC. Single-specimen data must be judged with caution, especially given poor preservation, but if this occurrence is verified by further observations, then these sediments are still within the *S. wolffii* Zone. Considering the great abundance of *S. wolffii* in sediments overlying the pyroclastic rocks, it seems surprising that this taxon is so rare in sediments below, although Moore (1969) considers this species to be solution susceptible. Discounting this specimen, the sediment may range from the *S. wolffii* Zone down to the *C. tetrapera* Zone.

Paleomagnetic evidence indicates that the pyroclastic sediments began within Chron 5E, at about 18.4 Ma, and ended in Chron 5C, at about 17.4 Ma. Given these datums, the radiolarian fauna recovered from Cores 124-768C-69R through -72R are most likely still within the *S. wolffii* Zone (see "Paleomagnetics" section, this chapter). Cessation of basalt emplacement was, therefore, during or prior to this time. No biosiliceous fossils are present in sediments intercalated between basalt pillows.

Ichthyoliths

In Hole 768C, ichthyoliths are present in the pelagic clays in most of the sequence. However, in Cores 124-768C-1R to -39R they are very rare; only sporadic specimens were found. They are more common in samples from Cores 124-768C-40R to -47R and Cores 124-768C-69R to -72R. Still, none of the samples contain more than 50 unbroken specimens. "Triangle with triangular projection," with a Cenozoic range, was found in nearly all samples.

The presence of "small triangle many striations together" with "flexed triangle shallow inbase ≥ 120" in Sample 124-768C-40R-CC indicates an early or middle Miocene age. In the cores below that, the ichthyoliths give less good age constraints. "Flexed triangle 102–112," which ranges from the upper Oligocene to Holocene, was found in Samples 124-768C-45R-CC and 124-768C-46R-1, 101–104 cm. "Rounded apex triangle" (middle Eocene to Holocene) was found in Sample 124-768C-69R-2, 117–120 cm. The volcanic ashes in Cores 124-768C-48R to -68R are barren.

PALEOMAGNETICS

Introduction

To establish the magnetostratigraphy and to observe the paleolatitude change of Site 768, remanent magnetization was measured throughout the cores. Measurements were carried out with the 2G-Enterprise pass-through rock magnetometer for archive halves and discrete samples. All the archive halves and samples measured were demagnetized with the three-axial coil system attached to the magnetometer, which is capable of generating a 20-mT alternating field (AF).

We also measured volume magnetic susceptibility for all cores at 10-cm intervals to assess the relative amount of magnetic minerals within the sediments.

Magnetostratigraphy

Hole 768B

The natural remanent magnetization of all the archive halves of cores from Hole 768B were measured at 10-cm intervals. Measurements were carried out at natural remanent magnetization (NRM) and at least one step of AF demagnetization at 10 or 15 mT. One section of each core was demagnetized progressively at 5, 10, 15, and 20 mT to determine an appropriate demagnetization level. Magnetic directions and intensities after demagnetization are shown in Figure 30. The declination values are corrected with core orientation data obtained with the multishot core orientation tool. Because the orientation data was not available for Cores 124-768B-1H and -16H, declinations were corrected to match those of the cores that followed.

The paleomagnetic records of the APC cores were generally excellent. We could easily identify all widely accepted reversals younger than the top of the Sidufjall Subchron, except for the lower part of the two Réunion Subchrons, which were supposed to be situated between Cores 124-768B-14H and -15H. In addition to these reversals, we found two short normal intervals within the reversed Matuyama Chron below and above the Jaramillo Subchrons. The characteristics and ages of these subchrons will be discussed later.

Most of the reversals are so well defined that their depths can be assigned within the error of the measurement interval of 10 cm. The magnetic intensity, however, dropped about 3 orders of magnitude from 10 to 0.01 mA/m at a depth near 188 mbsf, which corresponds approximately with the bottom of the Sidufjall Subchron. Below this depth, it became difficult to identify the reversal boundaries. Thereafter, we determined the reversal depths by means of the two following sample characteristics, with insufficient cleaning of recent secondary magnetization: (1) directions stay normal in normal polarity but tend to scatter in reversed polarity; and (2) intensity tends to be weaker in reversed polarity than in normal polarity.

Shore-based measurements with more sensitive magnetometers and more intensive demagnetization may be able to clarify the reversal depths. The depths and ages of identified reversals are shown in Table 5. The ages of the reversals are from Berggren et al. (1985a, 1985b). The ages of the Réunion Subchrons are taken from Harland et al. (1982).

Depth and age relations are illustrated in Figure 31. Data points below the bottom of the Sidufjall Subchron were not independently determined, but were determined to obtain a linear age-depth relation. However, we were able to find some indications of reversal near the expected depths. Points in Figure 31 are represented by three line segments: (1) from the seafloor to the Brunhes/Matuyama boundary, (2) from the Brunhes/Matuyama boundary to the bottom of the Jaramillo Subchron, and (3) below the Olduvai Subchron. Each segment yields a sedimentation rate of 105, 45, and 21 m/m.y., respectively. Although we have no confirmed control point between the bottom of the Jaramillo and the Olduvai subchrons, both the second and third segments are extended until they cross each other, because (1) we have evidence, which will be discussed below, that a constant sedimentation rate continues to the depth of the short normal subchron below the Jaramillo Subchron, and (2) a lithologic change is observed near the point where the lines cross.

The short normal subchron below the Jaramillo Subchron found at Celebes Sea Site 767 was again observed at this site. A comparison of reversal depth between these two sites (Fig. 32) gives an excellent linear relation (correlation coefficient = 0.9994) from the Brunhes/Matuyama boundary to the bottom of the short subchron. This fact strongly suggests that the sedi-

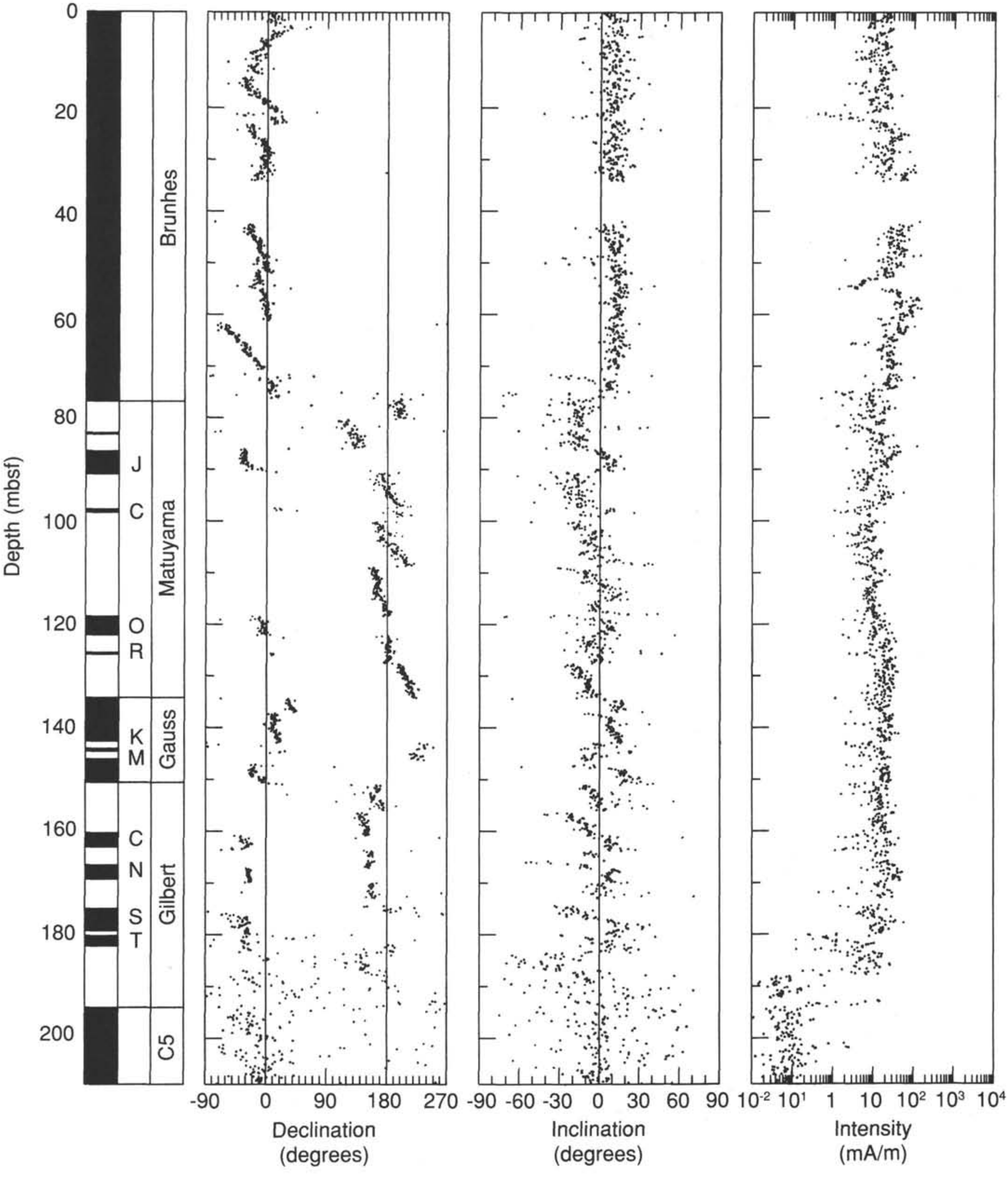

Figure 30. Magnetostratigraphic plot of declination, inclination, and intensity for Cores 124-768B-1H to -23H. The declinations are corrected by orientation data.

Table 5. Reversal ages and depths for Holes 768B and 767B.

Chron	Subchron	Age (Ma)	768B (mbsf)	767B (mbsf)
Brunhes				
		0.73	76.3	48.8
Matuyama	(???)		82.5	
			82.8	
	Jaramillo	0.91	86.1	60.2
		0.98	90.6	66.5
	Cobb Mt.	(1.11)	97.5	74.1
		(1.12)	98.1	74.9
	Olduvai	1.66	118.5	
		1.88	122.2	
	Réunion 2	[a]2.01	125.6	
		[a]2.04	126.0	
	Réunion 1	[a]2.12		
		[a]2.14		
		2.47	134.4	
Gauss	Kaena	2.92	142.9	
		2.99	144.4	
	Mammoth	3.08	144.9	
		3.18	146.4	
		3.40	151.0	
Gilbert	Cochiti	3.88	160.9	
		3.97	163.7	
	Nunivak	4.10	167.2	
		4.24	170.0	
	Sidufjall	4.40	175.7	
		4.47	[a]180	
	Thvera	4.57	[a]181	
		4.77	[a]183	
		5.35	[a]195	
Chron 5				
R-Subchron		5.68	[a]200	
		5.89	[a]203	

Note: The ages of Réunion Subchrons were taken from Harland et al. (1982). The ages of Cobb Mountain Subchron are calculated assuming a constant sedimentation rate in Hole 767B. Others are from Berggren et al. (1985a, 1985b).

[a] These ages and depths indicate a lower reliability of reversal identification.

mentation rates of both basins remained unchanged throughout the duration, because it seems unlikely that two different basins have changed sedimentation rates in the same fashion.

If we assume a constant sedimentation rate at Site 767 from the seafloor to the bottom of the Jaramillo Subchron, which gives a correlation coefficient of 0.9997, the age of the top of the subchron and its duration are calculated to be 1.11 Ma and 12,000 yr, respectively. Because linear relations between Sites 767 and 768 are excellent, calculations with the data from Site 768 yield very similar estimations (1.11 Ma and 11,000 yr, respectively). In the Site 767 report, we indicated that this subchron would be correlated to the Cobb Mountain Subchron, which has an age of 1.12 ± 0.02 Ma when calculated by means of K-Ar dating (Mankinen et al., 1978). The confirmation of the constant sedimentation rate assures the assignment.

Another short magnetic reversal observed in Site 768 is situated above the Jaramillo Subchron at 82.6 mbsf. It is so short that we could observe it only in three 10-cm intervals (Fig. 33), so that the overall length is about 30 cm. Two of the measurements, however, have completely normal directions. Although there remains the possibility of a Brunhes secondary overprint, the age and duration of the subchron is calculated to be 0.85 Ma and 5,000 yr, respectively. Shore-based intensive demagnetization experiments will clarify if the subchron is real or not.

Additional measurements and sampling were carried out at most well-defined reversal boundaries to study the precise structure of magnetic reversals. The measurement of archive halves was made every 5 mm, and discrete samples were taken at 5-cm

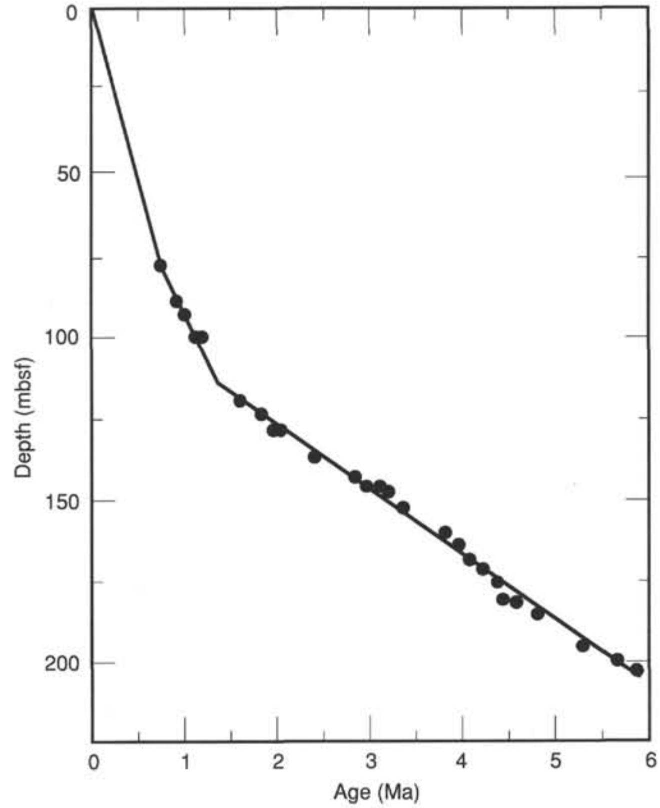

Figure 31. Plot of reversal depth vs. age for Cores 124-768B-1H to -23H.

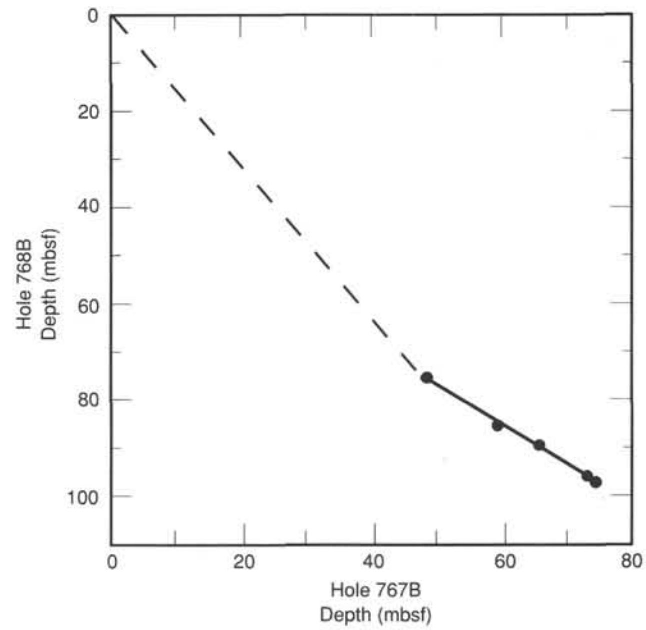

Figure 32. Correlation of reversal depths between Holes 767B and 768B.

intervals across each reversal boundary. Because of the long sensor region of the cryogenic magnetometer, the data requires deconvolution and will be processed in shore-based studies.

In XCB cores, pass-though measurements gave scattered directions, because the sensor region of the magnetometer was longer than individual "biscuit structures." This resulted in a

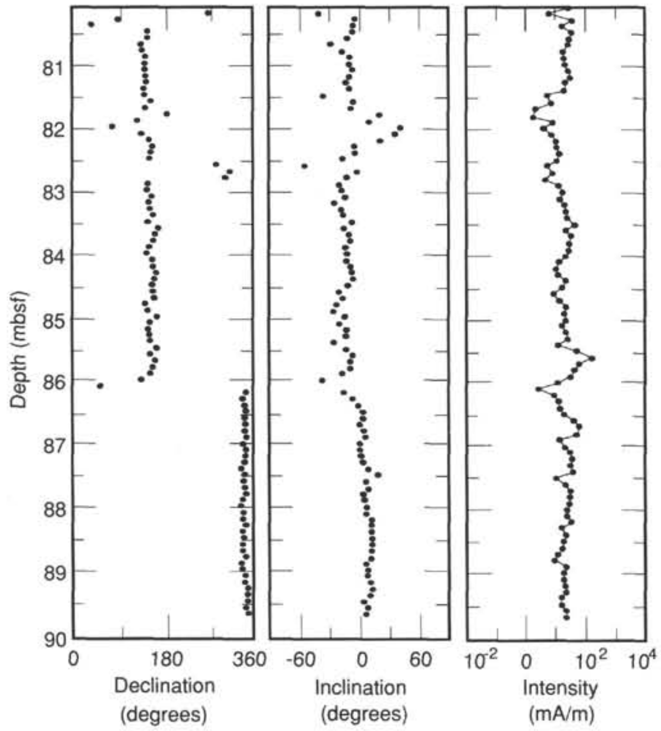

Figure 33. Magnetostratigraphic plot of declination, inclination, and intensity for Core 124-768B-10H.

summing up of the magnetizations of several biscuits that had different orientations. Meanwhile, the measurement of discrete samples also met with difficulty, it being generally too weak even for the cryogenic magnetometer. Magnetic directions and intensities of selected stronger samples are shown in Figure 34. Shore-based measurements with more sensitive magnetometers are required to establish the magnetostratigraphy of these cores.

Hole 768C

The lithology of Hole 768C is divided into several units: clayey Cores 124-768C-1R to -47R, volcaniclastic Cores 124-768C-48R to -72R, and basement (see "Lithostratigraphy" section, this chapter).

Cores 124-768C-1R to -47R (Lithologic Units II and III)

Although magnetic intensity increased slightly from that at the bottom of Hole 768B, some samples were still too weak for the shipboard magnetometers. We selected more strongly magnetized samples and measured them with progressive demagnetization at 2, 5, 10, 15, and 20 mT. Cores 124-768C-41R to -47R were too fractured for us to take meaningful samples. Magnetic directions and intensities after demagnetization at 20 mT are shown in Figure 35.

Calcareous nannofossil studies assign the age as Chron 5C for most of this section. The abundance of positive inclination measurements seems to support this result, although the number of measurements is insufficient in the middle and lower parts of this section. Shore-based measurement with more sensitive magnetometers and stronger demagnetization levels will be helpful to fill the gaps.

Cores 124-768C-48R to -72R (Lithologic Units IV and V)

Within the pyroclastic sediment, the length of each biscuit within individual cores became longer, and we again started measuring the archive halves. The intensity of these samples varied from 0.1 to 400 mA/m, staying within the range of measuring capability of the cryogenic magnetometer. Figure 36 shows the magnetic direction and intensity of the archive halves measured after demagnetization at 20 mT. The polarities are obvious in the upper and lower third of this section. For the middle third, it is difficult to determine polarities.

Progressive demagnetization experiments in Sample 124-768C-60R, 2.0–5.0 cm (Fig. 37), seem to indicate that the demagnetization was insufficient and that the direction is situated between the primary and secondary magnetizations. Because magnetic directions tend to scatter in reversed polarity intervals in cases of insufficient removal of secondary magnetization, we decided that the scattered portion is reversed in polarity.

The assignment of each polarity zone to the time scale was tied to a radiolarian datum boundary between the *Calocycletta costata* and *Stichocorys wolffii* zones found in Core 124-768C-48R. The left column in Figure 36 shows our chron assignments. This assignment gives a fairly constant sedimentation rate throughout these cores and a basement age of 18.8 Ma (Fig. 38). The age of the reversal boundaries and the radiolarian zone boundary are taken from Berggren (1985a, 1985b). Because ambiguity remains in the polarity data in the middle part of the sequence, the assignment of chron numbers also contains uncertainty. However, the age of the basement cannot be much older than the age of the radiolarian zone boundary, because the number of reversals observed below the horizon does not appear to be large.

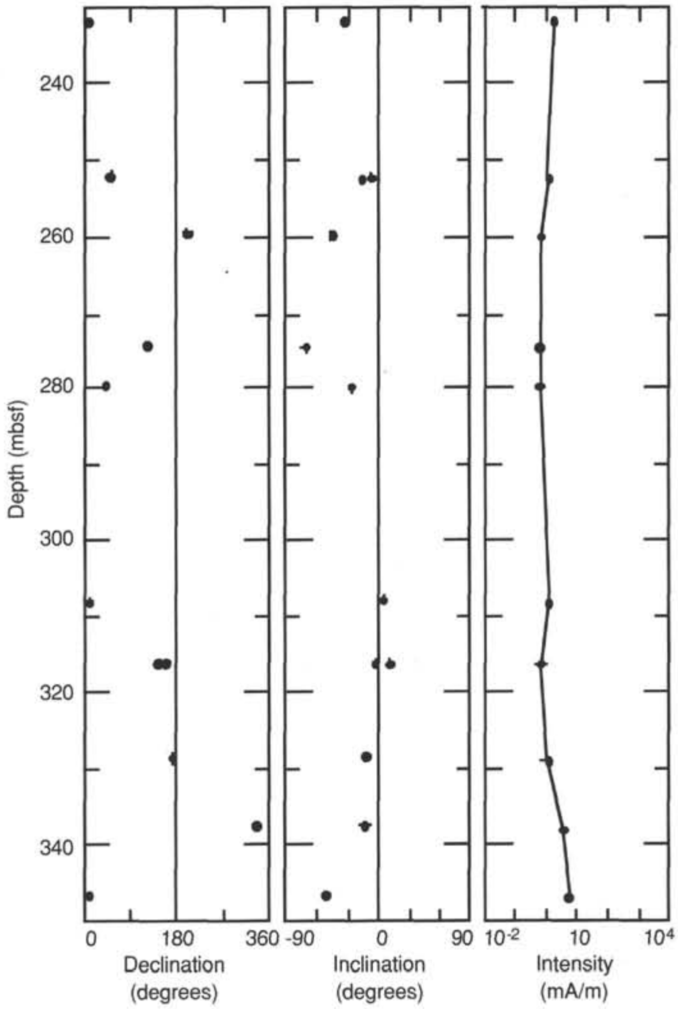

Figure 34. Magnetostratigraphic plot of declination, inclination, and intensity for Cores 124-768B-27X to -39X.

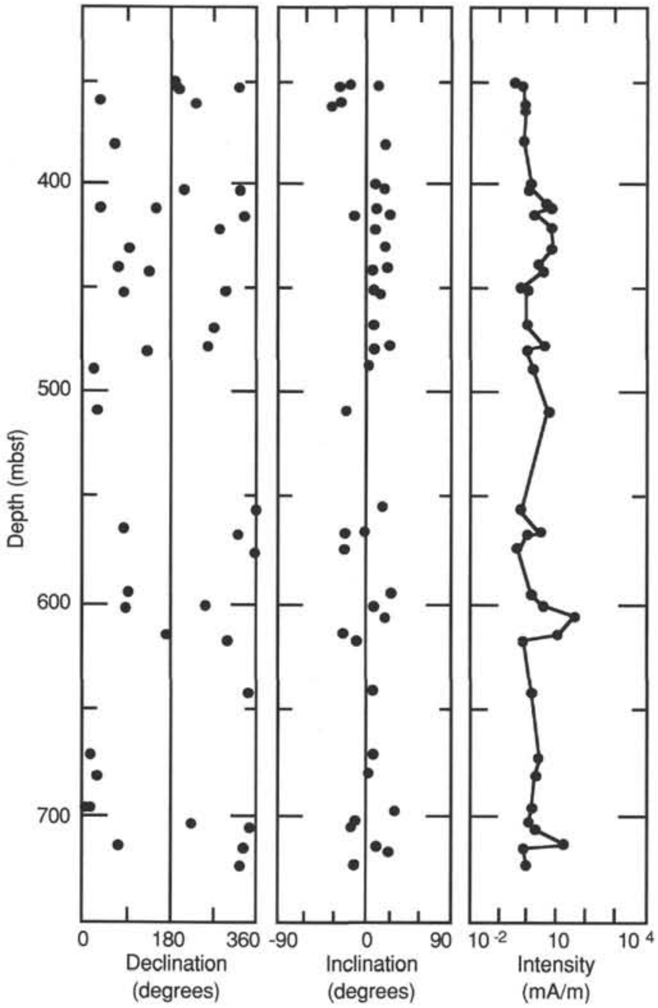

Figure 35. Magnetostratigraphic plot of declination, inclination, and intensity for Cores 124-768C-1R to -39R.

The polarity zone assignment is highly dependent on the numerical age assignment of the radiolarian zone boundary. Although all the time tables cited (Barron et al., 1985; Berggren et al., 1985a, 1985b; Haq et al., 1987a, 1987b, 1988) give fairly consistent ages for this zone boundary, its reliability was not confirmed by the literature on board. The age of the basement, therefore, may contain a large degree of ambiguity, if the numerical age of the zone boundary is uncertain.

Paleolatitude

It is clear that the inclination, hence the magnetic latitude, has remained unchanged throughout the sediment column, as shown by the inclination in the stable portions of Figures 30, 34, and 36. Actually, the mean inclination calculated from the upper part of these figures yields very similar values (10°, 9°, and 10°, respectively). We conclude that the Sulu Sea has not undergone significant north-south movement since its formation.

Basement

In the basement, we measured the archive halves of pieces of basalt and dolerite longer than the sensor region of the cryogenic magnetometer. A minicore sample was taken from each core. Figure 39 shows the magnetic directions and intensities of archive half measurement after 20-mT AF demagnetization.

The origin of two inclination sign changes at about 1160 mbsf is not clear. Because the pieces are part of a dolerite sill that extends from Cores 124-768C-88R to -94R, there should not be an actual magnetic polarity change. We consider that this polarity change may be attributed to insufficient removal of secondary magnetization for two reasons: (1) the NRM direction of measured pieces around 1160 mbsf is positive (30° to 60°); and (2) preliminary demagnetization experiments of discrete samples with the Molspin spinner magnetometer indicates that 20-mT AF demagnetization is too marginal to reveal primary directions (Fig. 40). If secondary magnetization of the pieces is a little more stable than in the other part, the dolerite can easily have a positive inclination.

It is interesting to observe that the magnetic inclination, which has low values near the top of the unit that are consistent with the overlying sediments, becomes rather high at 1070 mbsf. This may indicate that the basement suffered a tilting before the end of its formation. Although the true amount of tilting cannot be determined solely with our data, the apparent tilting to the north is about 20°, assuming reversed polarities. If normal polarity is assumed, tilting of the basement would be about 40° to the south, which seems to be unrealistic.

Magnetic Susceptibility

The magnetic susceptibility distribution for Site 768 is shown in Figure 41. Four major susceptibility units were identified at Site 768 within the sediment column cored.

From 0 to 180 mbsf, two large pulses of magnetic susceptibility were observed, with average values varying from 40 to 140 $\times$ 10^{-6} cgs. Superimposed on these two main pulses are large excursions in susceptibility, with values exceeding 700 $\times$ 10^{-6} cgs. The uppermost pulse extends from 0 to 120 mbsf and is much more variable than the lower pulse. Large, sharp increases in susceptibility were observed throughout this unit. A major low in magnetic susceptibility occurs from 30 to 40 mbsf, corresponding to a large layer of silty calcareous sand. The lower pulse has fewer large excursions superimposed on it and ends abruptly at approximately 180 mbsf. Larger volumes of highly susceptible minerals, assumed to accompany the pyroclastic rocks and ashes observed throughout the interval, are the major cause of the high susceptibility values throughout this unit.

The second major susceptibility unit extends from 180 to 735 mbsf and is characterized by low susceptibility values that average 30 $\times$ 10^{-6} cgs at the top of the unit, increase to 40 $\times$ 10^{-6} cgs at approximately 400 mbsf, and remain around 40 $\times$ 10^{-6} cgs throughout the remainder of the unit. Several large spikes of 150–500 $\times$ 10^{-6} cgs occur sporadically throughout this susceptibility unit and correlate with major graded beds contained within the lithology.

From 735 to 805 mbsf, values within Susceptibility Unit 3 increase from an average of 40 to 200 $\times$ 10^{-6} cgs. Poor core recovery throughout this interval obstructs the details of this unit, but it is clear that this Susceptibility Unit 3 is a transition from the low susceptibility values above and the very high values of Susceptibility Unit 4 below.

Susceptibility Unit 4 extends from 805 mbsf to the basement. The unit is characterized by highly variable swings in susceptibility from lows of 20 $\times$ 10^{-6} to highs of as much as 2300 $\times$ 10^{-6} cgs. This unit correlates well with the pyroclastic and brown clay lithologic units found above the basement in Hole 768C. The pyroclastic rocks are graded in fining-upward sequences, and high susceptibility values are associated with the lower parts of the graded sequence, with susceptibility values decreasing toward the top of the graded beds.

Magnetic susceptibility values were measured in the basement basalts with the pass-through loop. Values in solid sections of the core averaged from 3000 to 4000 $\times$ 10^{-6} cgs. Be-

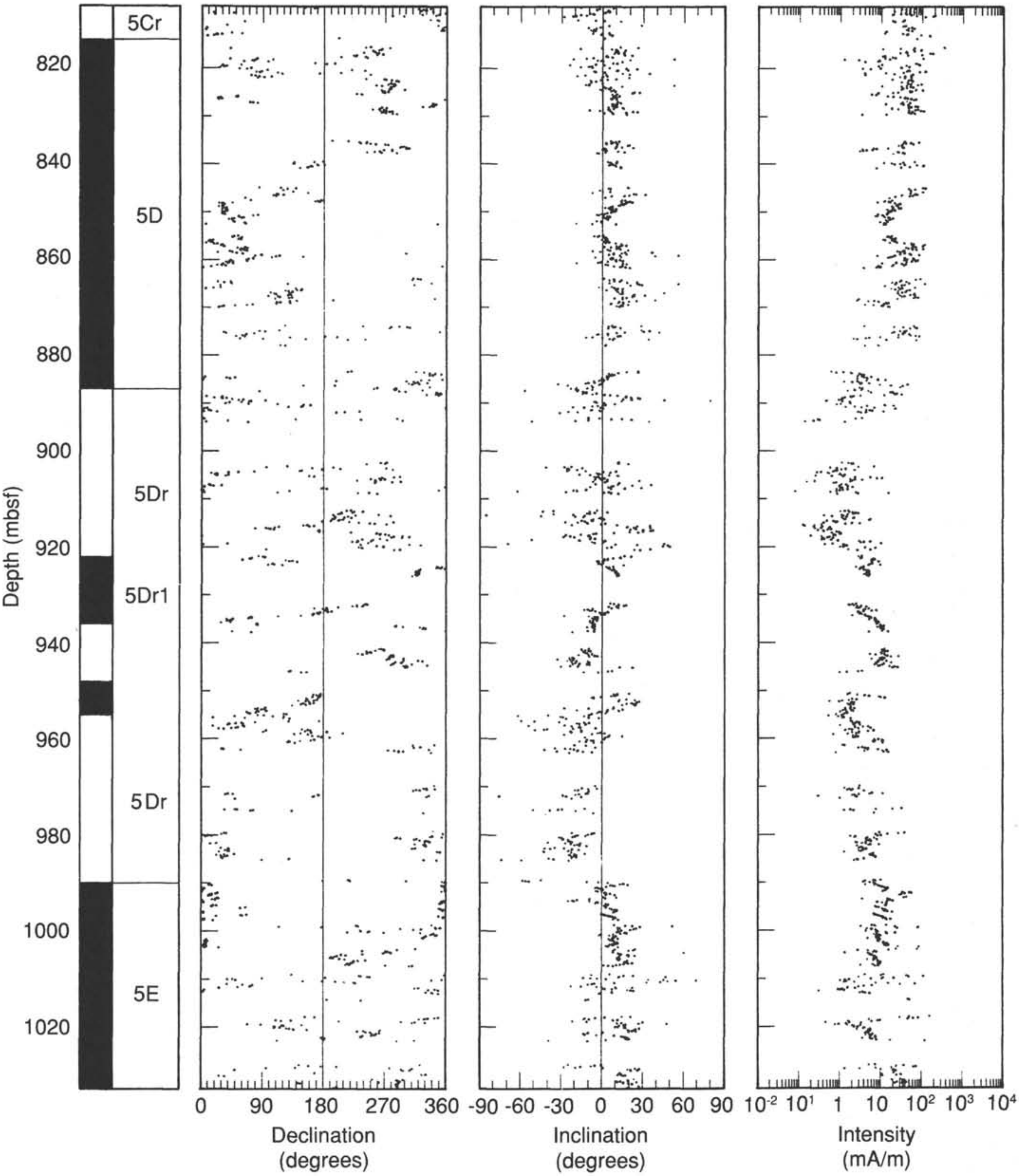

Figure 36. Magnetostratigraphic plot of declination, inclination, and intensity for Cores 124-768C-48R to -71R and assignment of chrons.

cause of the fact that the basalt core did not fill the liner as much as the sediment above basement, the values obtained within the basement cannot be compared with those obtained from the sediment above basement. Discrete susceptibility was not done on individual samples.

The correlation between Holes 768B and 768C is shown in Figure 42. This correlation was made by matching peak spacings between the two holes rather than on the basis of peak height. The correlation is tentative at best, given the short amount of overlap between the two holes.

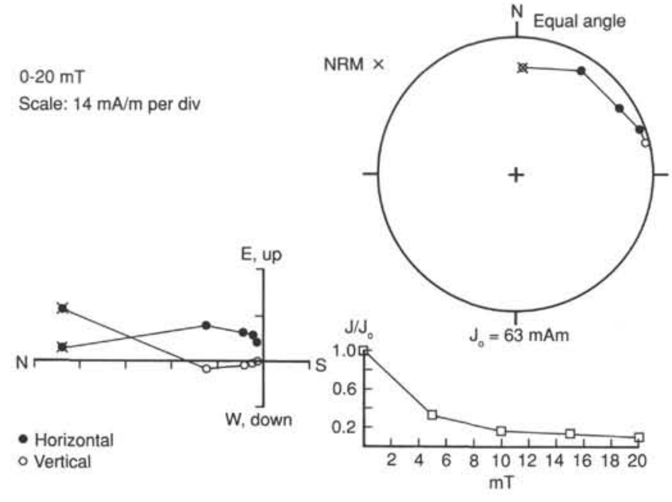

Figure 37. Zijderveld vector diagram for the 5-cm position of the archive half of Sample 124-768C-60R, 2–5 cm.

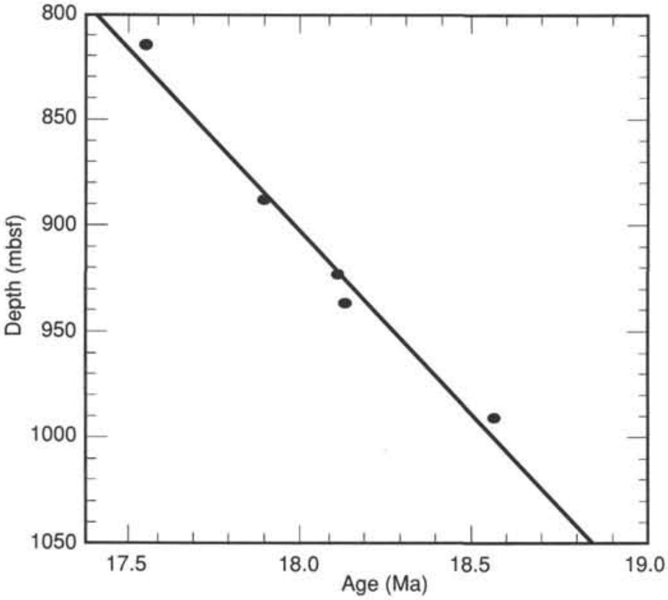

Figure 38. Plot of reversal depths vs. age for Cores 124-768C-48R to -71R.

SEDIMENT ACCUMULATION RATES

Sediment accumulation rates were determined at Site 768 by means of magnetostratigraphy and biostratigraphy. The time scale of Berggren et al. (1985a, 1985b) was used for correlation of the magnetostratigraphic and biostratigraphic zones. Calcareous nannoplankton zones are described in Martini (1971), and radiolarian zones are defined by Riedel and Sanfilippo (1978).

The magnetostratigraphic record in Hole 768B was determined from oriented APC cores and extends from the top of the Hole 768B to Core 124-768B-23H (209.2 mbsf). The magnetostratigraphic data is excellent throughout this interval, extending back into Chron 5 with virtually no gaps in the record except the second reversal of the Réunion Subchron, which apparently occurs between Cores 124-768B-14H and -15H. The sedimentation rate record determined from the magnetostratigraphic history is shown in Figure 43.

Two major portions of the curve are identified with approximately linear trends, with one transitional segment between them.

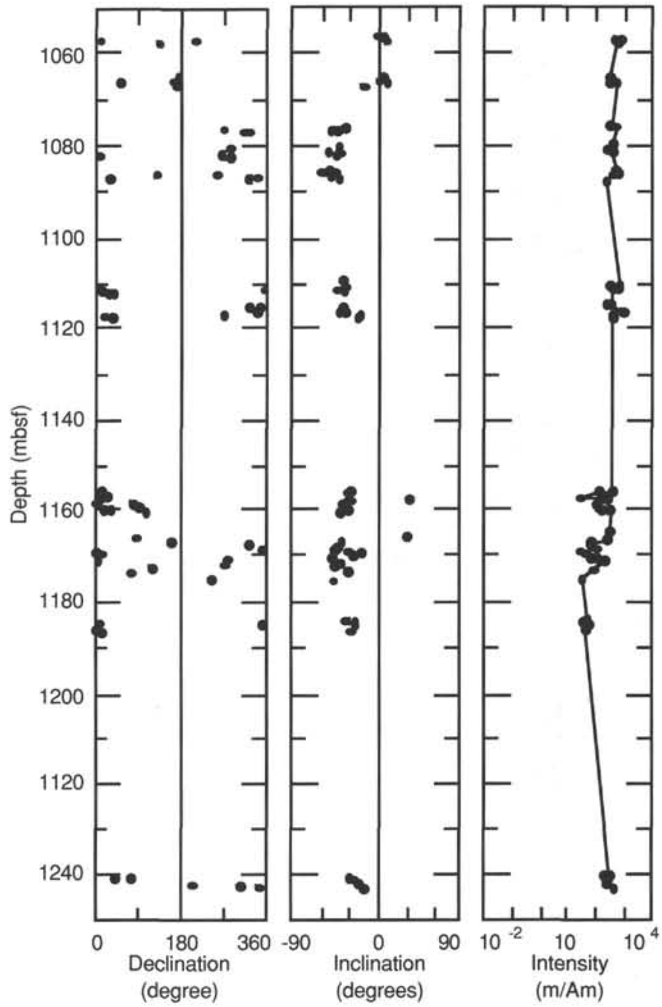

Figure 39. Magnetostratigraphic plot of declination, inclination, and intensity for Cores 124-768C-72R to -99R.

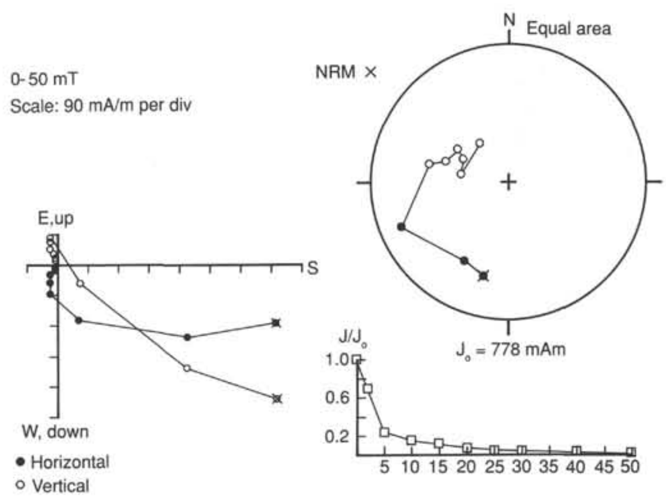

Figure 40. Zijderveld vector diagram for Sample 124-768-90R-3, 15–17 cm.

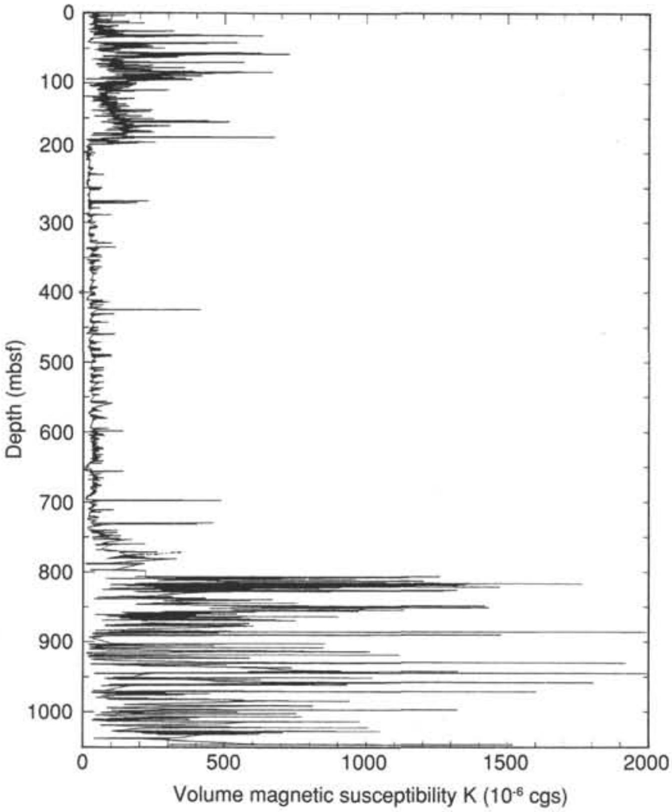

Figure 41. Magnetic susceptibility data, Site 768. This is a compilation of data from Holes 768B (0–350 mbsf) and 768C (353 mbsf to basement).

From the top of Hole 768B to the Brunhes/Matuyama boundary (76.3 mbsf), the sedimentation rate is approximately 105 m/m.y. A transition in sedimentation rates occurs from the Brunhes/Matuyama boundary to the top of the Olduvai Subchron (118.5 mbsf). Sedimentation rates average 45 m/m.y. throughout this interval, with higher rates (56 m/m.y.) in the upper portion of the interval and lower rates (23 m/m.y.) toward the bottom of the interval. From the top of the Olduvai Subchron to the Gilbert/Chron 5 boundary (195.0 mbsf), the curve remains fairly linear with an average sedimentation rate of 22 m/m.y. for the entire interval.

Several small variations are present within the interval from the top of the Olduvai to the Gilbert/Chron 5 boundary (Fig. 43). From the base of the Olduvai Subchron (122.2 mbsf) to the top of the Mammoth Subchron (144.9 mbsf), the sedimentation rate averages 19 m/m.y. From the base of the Mammoth Subchron (146.4 mbsf) to the top of the normal Nunivak Subchron (167.2 mbsf), sedimentation rates average 23 m/m.y. Identification of the normal Sidufjall and Thvera subchrons, between 175 and 182 mbsf, are not certain, and the sedimentation rates throughout this interval may not be accurate (Fig. 43). A comparison of sedimentation rates calculated from the magnetostratigraphy with rates calculated from the biostratigraphy do not give consistent rates of sedimentation for this interval.

The Gilbert/Chron 5 boundary was tentatively identified and is supported by biostratigraphic data. The average sedimentation rate from the top of the Nunivak Subchron (167.2 mbsf) to the Gilbert/Chron 5 boundary (195.0 mbsf) is 22 m/m.y. No magnetostratigraphic boundaries were identified below the Gilbert/Chron 5 boundary in Hole 768B. Below this point all sedimentation rates were determined from the biostratigraphy.

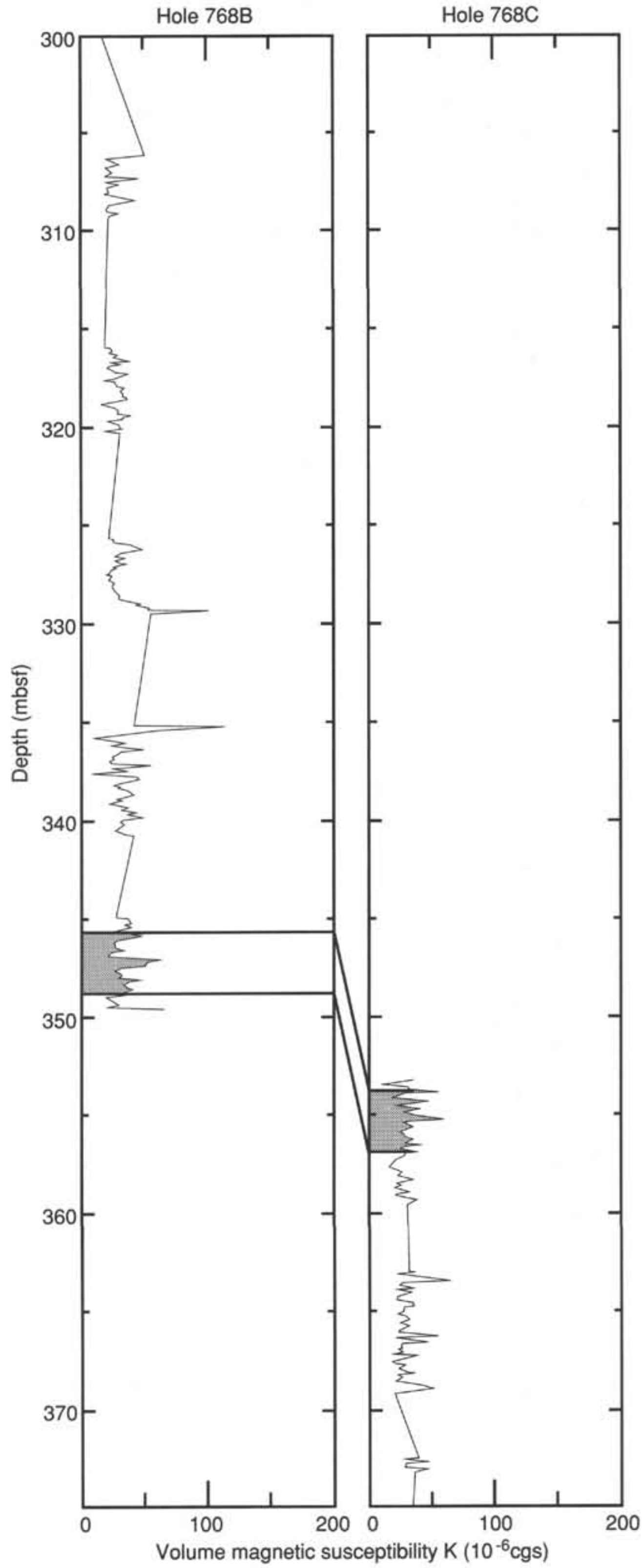

Figure 42. Magnetic susceptibility correlation of Holes 768B and 768C.

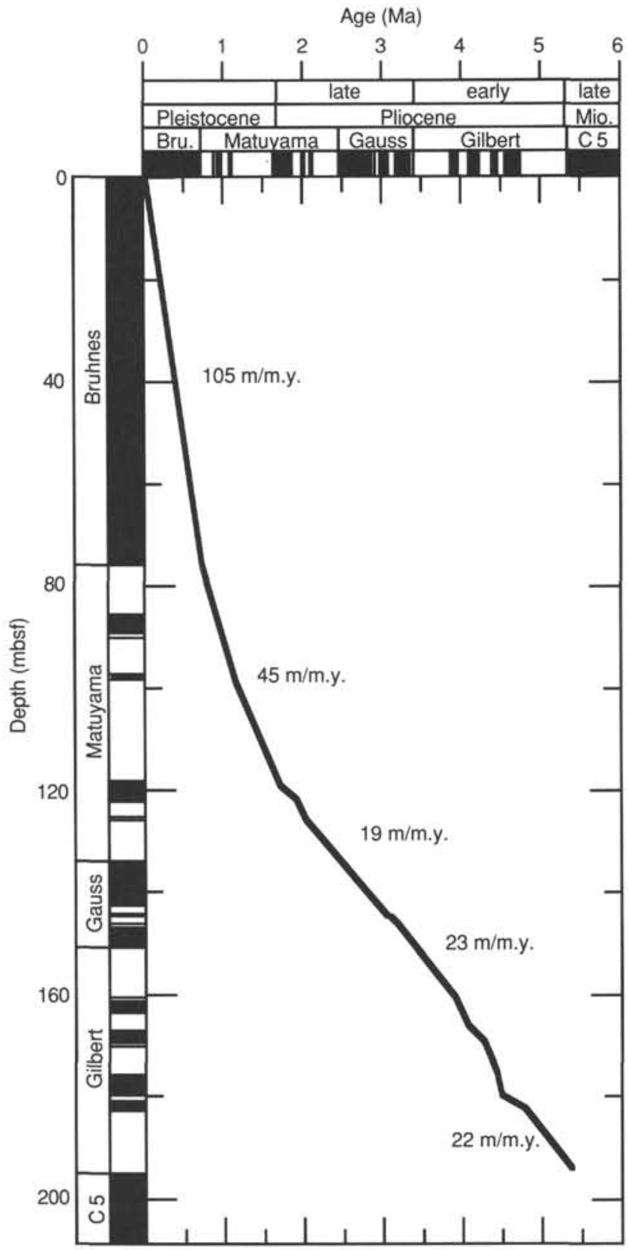

Figure 43. Sedimentation rates determined from magnetostratigraphic data from Cores 124-768B-1H to -23H.

Hole 768C was rotary cored from 352.2 to 1268.5 mbsf. Sedimentation rate calculations depend solely on biostratigraphy in this hole down to Core 124-768C-48R (815.5 mbsf). Below this depth no identifiable biozone boundaries and few taxa are identifiable. From Core 124-768C-48R to Core -71R, core recovery was excellent with well-lithified pyroclastic sediment occurring in long (up to 1 m) biscuits. The archive halves of these cores were measured with the cryogenic magnetometer and interpreted as seen in Figure 36, with the top of the interval occurring in Chron 5CR and the base in Chron 5E.

The top of the interval is tied to the age scale, with the identification of the *C. costata/S. wolffii* boundary in Section 124-768C-48R-3. In Core 124-768C-69R several poorly preserved lower Miocene radiolarian species were identified, constraining the interpretation of the paleomagnetic data. Sedimentation rates calculated from this magnetostratigraphic interpretation are shown in Figure 44, with an average calculated sedimentation rate of 161 m/m.y.

Brown clays are present from 1003 mbsf to the basement at 1046.6 mbsf. No confident magnetostratigraphy was determined in the brown clays. Magnetic studies on the upper cores in the basement show it to be normally magnetized. If we assume that the brown clays were deposited at a slower rate than the overlying pyroclastic rocks, they may all be of normal polarity, in which case they all belong to Chron 5E, have a maximum age at the basement of 19.1 Ma, and have minimum sedimentation rates of 101 m/m.y. On the other hand, the brown clays may contain a polarity reversal within the interval, in which case the base would most probably belong to Chron 6, have an age range of 19.35–20.45 Ma at the basement, and have minimum sedimentation rates of 24 m/m.y.

Sedimentation rates determined from the biostratigraphic zones are shown in Figure 45; the biozone boundaries and sedi-

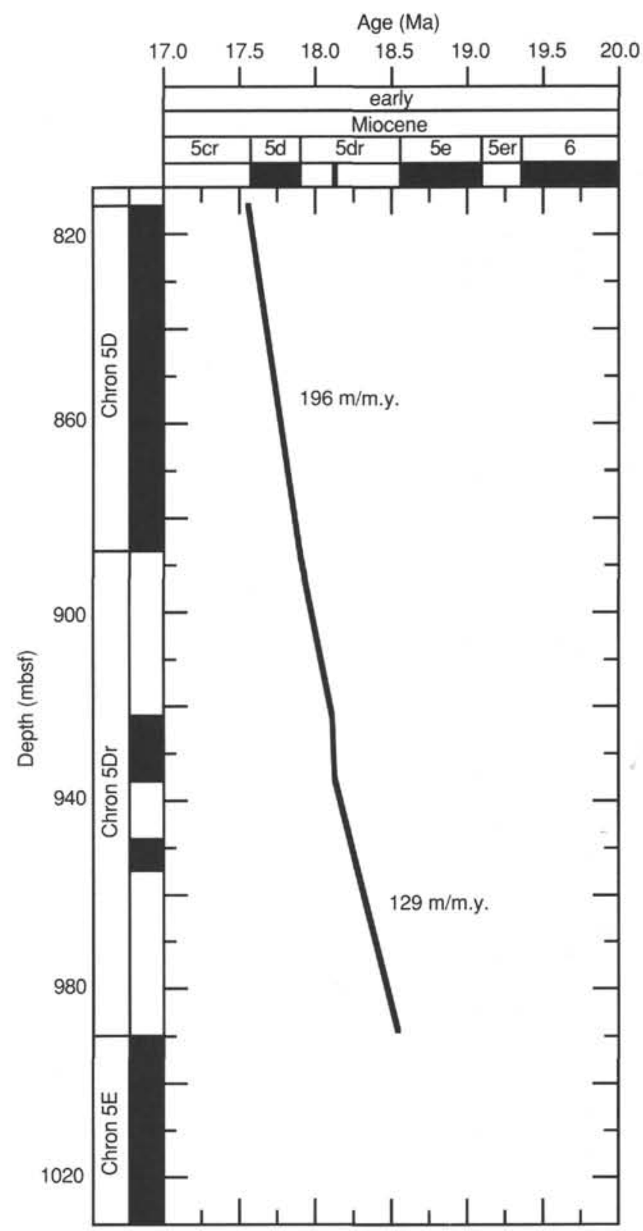

Figure 44. Sedimentation rates determined from magnetostratigraphic data from Cores 124-768C-48R to -71R.

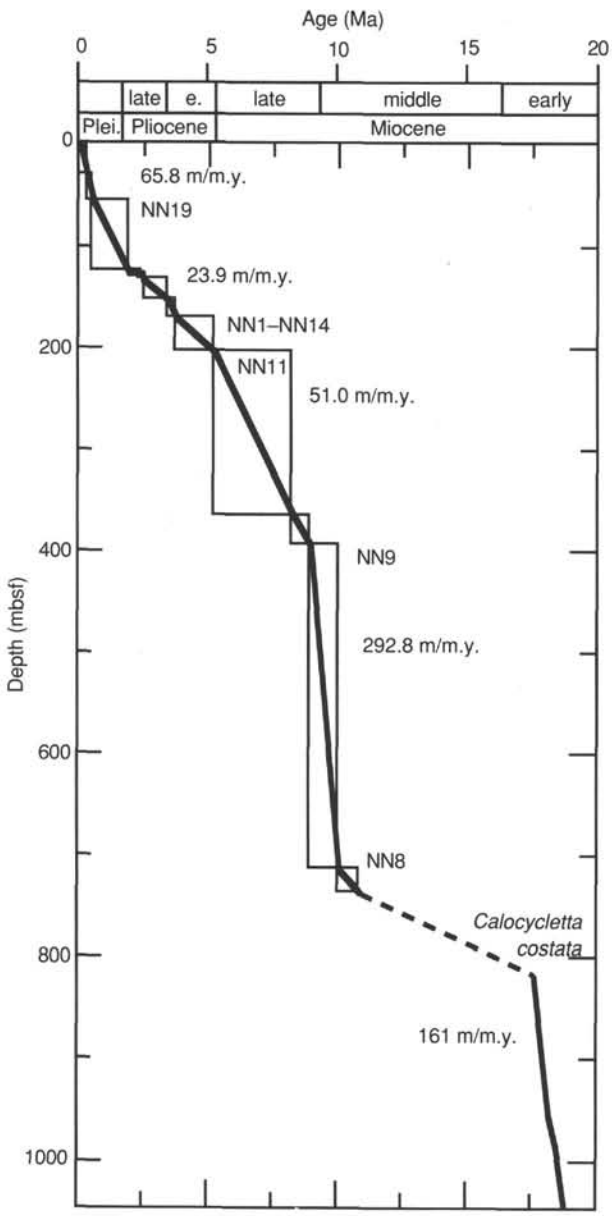

Figure 45. Sedimentation rates, Site 768. Rates calculated from biostratigraphic data for the upper 750 m are determined by nannofossil Zones NN21 through NN8. The base of the radiolarian *Calocycletta costata* Zone ties the sedimentation rate calculations made below with the magnetostratigraphic data.

mentation rates for individual biozones are presented in Table 6. The sedimentation rate, determined from the magnetostratigraphy of Cores 124-768C-48R through -71R, is included with this graph to summarize the sedimentation rates of Site 768. The sedimentation rates determined in the top 200 m of Hole 768B are very similar to those determined by means of magnetostratigraphy.

The determination of sedimentation rates from biostratigraphic zonations depended almost solely on nannofossil zonations. Foraminifers, radiolarians, and diatoms were absent or poorly preserved and were not useful in determining biozones for sedimentation rate calculations except in Core 124-768C-48R. The preservation of calcareous nannofossils varied throughout

Table 6. Ages, depths, and sedimentation rates for individual biozones identified at Site 768.

Biozone	Age (Ma)	Depth (mbsf)	Sed. rate (m/m.y.)
NN21	0–0.275	0–29.3	106.4
NN20	0.275–0.474	29.3–53.2	120.4
NN19	0.474–1.89	53.2–124.4	50.3
NN18	1.89–2.35	124.4–127.5	6.7
NN17	2.35–2.45	127.5–133.0	55.0
NN16	2.45–3.40	133.0–151.5	19.5
NN15	3.40–3.70	151.5–169.8	61.0
NN12–NN14	3.70–5.20	169.8–203.4	22.4
NN11	5.20–8.20	203.4–362.9	53.2
NN10	8.20–8.90	362.9–392.1	41.8
NN9	8.90–10.0	392.1–714.2	292.8
NN8	10.0–10.8	714.2–735.7	26.9
C. costata/S. wolffii	17.3	811.9	

the holes drilled at Site 768, with several zones left undifferentiated because of this problem. Radiolarians were poorly preserved but recognizable in Cores 124-768C-48R and -69R.

Five major intervals are recognized with essentially linear trends. From the top of NN21 to the base of NN19, an average sedimentation rate of 65.8 m/m.y. was calculated. An average rate of 23.9 m/m.y. was calculated from the top of NN18 to the base of NN12. The interval from the base of NN12 to the base of NN10 was calculated to have a sedimentation rate of 51.0 m/m.y. A sedimentation rate of 292.8 m/m.y. was calculated for nannofossil Zone NN9. Sedimentation rates decreased beginning in NN8 with a sedimentation rate for that zone of 26.9 m/m.y.

Radiolarians were identified in Core 124-768C-48R with the boundary between the *C. costata/S. wolffii* zones located in Section 124-768C-48R-3. Sedimentation rates between the base of NN8 and this radiolarian marker cannot be accurately established because of confusion in the nannofossil record caused by the mixing of assemblages from Zones NN8 and NN5.

Nannofossil Zones NN7 and NN6 were not observed, which presented the probability of a hiatus during this interval.

SEDIMENT INORGANIC GEOCHEMISTRY

This section summarizes the results of shipboard analyses of calcium carbonate and dissolved constituents in the interstitial water of the cores drilled at Site 768. Dissolved sulfate and ammonium distributions up to 200 mbsf are characteristic of organic decomposition during bacterial sulfate reduction. The dissolved Ca, Mg, and Si profiles as well as the pH profile indicate the alteration of volcanic material, the formation of smectite, and the dolomitization of biogenic carbonates.

Calcium Carbonate

We analyzed a total of 411 sediment samples for their inorganic carbon content at Site 768, with the ODP shipboard standard method (see "Explanatory Notes" chapter, this volume). The results are given in Table 7, and the depth distribution is shown in Figure 46. With the exception of a few samples, sediments in the uppermost 120 m are characterized by a high carbonate content, consistent with the observed calcareous oozes of Unit I, and are indicative of their deposition above the CCD (see "Lithostratigraphy" section, this chapter). Below 120 mbsf, most of the carbonate values are <2%. The sporadic high carbonate values in Unit II reflect the alternation of low-carbonate terrigenous sequences with graded carbonate turbidites. The pyroclastic deposits recovered below 650 mbsf are very low in carbonate components, as evidenced by the low $CaCO_3$ concentrations in these samples.

Table 7. Results of calcium carbonate analysis, Site 768.

Core, section interval (cm)	Depth (mbsf)	$CaCO_3$ (%)
124-768B-1H-1, 37–40	0.37	36.2
124-768A-1H-1, 66–68	0.66	40.0
124-768B-1H-1, 145–146	1.45	42.7
124-768B-1H-2, 22–23	1.72	41.4
124-768B-1H-2, 75–78	2.25	43.0
124-768A-1H-2, 75–77	2.25	37.7
124-768B-1H-3, 0–3	3.00	38.0
124-768B-1H-3, 23–26	3.23	40.0
124-768A-1H-3, 72–74	3.72	36.7
124-768A-1H-4, 0–3	4.50	31.5
124-768B-2H-1, 68–71	4.68	37.6
124-768A-1H-4, 95–97	5.45	33.3
124-768A-1H-5, 40–42	6.40	41.0
124-768B-2H-2, 111–114	6.61	40.9
124-768A-1H-6, 55–57	8.05	36.4
124-768B-2H-4, 28–31	8.78	32.7
124-768B-2H-6, 0–3	11.50	31.2
124-768B-3H-1, 65–68	14.15	44.1
124-768B-3H-2, 57–58	15.57	41.4
124-768B-3H-4, 69–72	18.69	49.7
124-768B-3H-6, 0–3	21.00	11.1
124-768B-3H-6, 51–54	21.51	64.9
124-768B-4H-1, 40–43	23.40	40.1
124-768B-4H-2, 82–84	25.32	20.8
124-768B-4H-4, 66–69	28.16	44.2
124-768B-4H-6, 0–3	30.50	42.6
124-768B-4H-6, 39–42	30.89	40.6
124-768B-5H-2, 98–100	34.98	61.3
124-768B-5H-4, 61–63	37.61	73.1
124-768B-5H-5, 0–3	38.50	76.7
124-768B-5H-5, 75–77	39.25	74.5
124-768B-6H-1, 103–105	43.03	46.8
124-768B-6H-3, 69–71	45.69	47.1
124-768B-6H-4, 37–39	46.87	36.8
124-768B-6H-6, 0–3	49.50	42.3
124-768B-6H-6, 105–107	50.55	36.1
124-768B-7H-2, 45–47	53.45	61.5
124-768B-7H-4, 63–65	56.63	19.7
124-768B-7H-6, 0–3	59.00	7.9
124-768B-7H-6, 60–62	59.60	24.8
124-768B-8H-1, 82–84	61.82	23.1
124-768B-8H-3, 99–101	64.99	29.9
124-768B-8H-4, 25–27	65.75	37.0
124-768B-8H-6, 0–3	68.50	50.7
124-768B-8H-6, 66–68	69.16	30.0
124-768B-9H-1, 63–65	71.13	33.5
124-768B-9H-4, 75–77	75.75	40.3
124-768B-9H-6, 0–3	78.00	33.6
124-768B-9H-6, 67–69	78.67	36.0
124-768B-10H-1, 80–82	80.80	35.3
124-768B-10H-4, 75–77	85.25	31.7
124-768B-10H-6, 0–3	87.50	25.1
124-768B-10H-6, 84–86	88.34	32.7
124-768B-11H-1, 77–79	90.27	36.4
124-768B-11H-3, 83–85	93.33	26.7
124-768B-11H-5, 73–75	96.23	26.8
124-768B-11H-6, 0–3	97.00	26.0
124-768B-12H-1, 71–73	99.71	61.6
124-768B-12H-3, 50–51	102.50	54.1
124-768B-12H-5, 60–62	105.60	56.1
124-768B-12H-6, 0–3	106.50	56.0
124-768B-12H-7, 52–54	108.52	44.7
124-768B-12H-7, 71–73	108.71	60.5
124-768B-13H-1, 47–49	108.97	44.8
124-768B-13H-2, 30–31	110.30	21.2
124-768B-13H-2, 55–56	110.55	45.6
124-768B-13H-4, 103–106	114.03	51.4
124-768B-13H-6, 0–3	116.00	7.2
124-768B-13H-6, 42–44	116.42	41.2
124-768B-13H-7, 48–51	117.98	38.7
124-768B-14H-1, 82–84	118.82	44.4
124-768B-14H-2, 82–83	120.32	44.1
124-768B-14H-3, 9–11	121.09	39.9
124-768B-14H-4, 79–80	123.29	0.4
124-768B-14H-5, 74–77	124.74	6.8
124-768B-14H-6, 0–3	125.50	51.6
124-768B-14H-6, 29–31	125.79	5.9

Table 7 (continued).

Core, section interval (cm)	Depth (mbsf)	$CaCO_3$ (%)
124-768B-14H-6, 129–130	126.79	0.7
124-768B-15H-4, 95–96	132.95	31.2
124-768B-15H-6, 0–3	135.00	0.4
124-768B-16H-2, 66–69	139.16	0.7
124-768B-16H-5, 55–58	143.55	38.4
124-768B-16H-6, 0–3	144.50	0.3
124-768B-16H-6, 71–74	145.21	0.6
124-768B-17H-2, 59–61	148.59	1.2
124-768B-17H-4, 97–100	151.97	0.7
124-768B-17H-5, 0–3	152.50	0.2
124-768B-17H-6, 71–74	154.71	0.4
124-768B-18H-2, 85–87	158.35	0.4
124-768B-18H-4, 82–84	161.32	0.4
124-768B-18H-6, 0–3	163.50	39.9
124-768B-18H-6, 75–77	164.25	0.7
124-768B-19H-2, 60–62	167.60	0.4
124-768B-19H-5, 78–80	172.28	0.7
124-768B-19H-6, 0–3	173.00	0.2
124-768B-20H-1, 68–70	174.48	0.5
124-768B-20H-4, 76–78	179.06	0.9
124-768B-20H-6, 0–3	181.30	0.2
124-768B-20H-6, 89–91	182.19	0.7
124-768B-21H-1, 95–97	184.25	0.6
124-768B-21H-3, 64–66	186.94	0.6
124-768B-21H-5, 0–3	189.30	0.2
124-768B-21H-6, 85–87	191.65	0.5
124-768B-22H-1, 87–89	193.67	0.7
124-768B-22H-3, 91–93	196.71	0.5
124-768B-22H-5, 0–3	198.80	0.1
124-768B-22H-5, 84–86	199.64	0.6
124-768B-23H-1, 66–68	201.66	0.2
124-768B-23H-3, 70–72	204.70	0.2
124-768B-23H-5, 0–3	207.00	0.1
124-768B-23H-5, 82–84	207.82	0.2
124-768B-26X-1, 68–70	219.98	0.7
124-768B-26X-3, 0–3	222.30	20.1
124-768B-26X-3, 44–46	222.74	0.8
124-768B-27X-1, 95–97	229.85	0.2
124-768B-27X-2, 137–139	231.77	56.9
124-768B-27X-3, 0–3	231.90	0.1
124-768B-27X-3, 80–82	232.70	0.3
124-768B-28X-1, 60–62	239.20	2.7
124-768B-28X-3, 69–70	242.29	0.2
124-768B-28X-5, 0–3	244.60	0.2
124-768B-28X-5, 43–45	245.03	0.2
124-768B-29X-1, 85–87	249.05	0.2
124-768B-29X-3, 0–3	251.20	0.9
124-768B-29X-3, 77–79	251.97	0.7
124-768B-29X-4, 67–69	253.37	0.5
124-768B-30X-1, 104–106	258.84	0.3
124-768B-30X-2, 0–3	259.30	4.7
124-768B-30X-2, 65–67	259.95	1.3
124-768B-30X-3, 29–31	261.09	1.6
124-768B-31X-1, 33–35	267.83	1.5
124-768B-31X-2, 43–46	269.43	2.2
124-768B-31X-3, 33–35	270.83	2.0
124-768B-31X-6, 0–3	275.00	0.3
124-768B-32X-1, 126–129	278.46	2.6
124-768B-32X-2, 0–3	278.70	1.1
124-768B-32X-2, 10–12	278.80	5.6
124-768B-32X-3, 10–12	280.30	18.0
124-768B-33X-1, 62–64	287.42	0.8
124-768B-33X-2, 69–72	288.99	1.2
124-768B-33X-3, 0–3	289.80	1.0
124-768B-33X-3, 60–62	290.40	0.7
124-768B-34X-1, 57–60	296.97	2.9
124-768B-34X-2, 59–61	298.49	4.4
124-768B-34X-3, 0–3	299.40	0.9
124-768B-34X-3, 16–18	299.56	4.3
124-768B-35X-1, 97–100	307.07	0.9
124-768B-35X-2, 0–3	307.60	44.6
124-768B-35X-2, 5–6	307.65	44.6
124-768B-35X-2, 74–76	308.34	0.7
124-768B-35X-3, 27–29	309.37	0.5
124-768B-36X-1, 33–36	316.13	14.6
124-768B-36X-2, 95–97	318.25	0.7
124-768B-36X-3, 0–3	318.80	0.2
124-768B-36X-3, 28–31	319.08	0.2

Table 7 (continued).

Core, section interval (cm)	Depth (mbsf)	$CaCO_3$ (%)
124-768B-37X-1, 42–45	325.92	0.5
124-768B-37X-2, 77–79	327.77	0.7
124-768B-37X-3, 0–3	328.50	0.3
124-768B-37X-CC, 42–44	329.98	0.6
124-768B-38X-1, 41–44	335.51	0.4
124-768B-38X-2, 88–90	337.48	0.2
124-768B-38X-3, 0–3	338.10	0.1
124-768B-38X-3, 67–69	338.77	0.4
124-768B-38X-4, 84–86	340.44	0.4
124-768B-39X-1, 53–55	345.33	0.4
124-768B-39X-2, 15–17	346.45	55.6
124-768B-39X-2, 84–86	347.14	0.6
124-768B-39X-3, 95–97	348.75	0.4
124-768B-39X-4, 15–17	349.45	0.2
124-768C-1R-1, 13–15	353.33	0.4
124-768C-1R-3, 108–110	357.28	1.4
124-768C-1R-4, 0–3	357.70	0.2
124-768C-1R-4, 91–93	358.61	0.2
124-768C-2R-1, 30–32	363.20	55.5
124-768C-2R-3, 80–82	366.70	0.4
124-768C-2R-4, 0–3	367.40	2.1
124-768C-3R-1, 0–3	372.40	1.2
124-768C-3R-1, 67–70	373.07	0.5
124-768C-3R CC, 13–16	373.35	48.6
124-768C-4R-1, 119–121	383.29	0.3
124-768C-4R-2, 0–3	383.60	0.5
124-768C-5R-1, 113–116	392.93	0.7
124-768C-5R-2, 107–109	394.37	0.7
124-768C-5R-3, 0–3	394.80	0.3
124-768C-5R-3, 124–126	396.04	0.3
124-768C-6R-1, 84–86	402.24	0.5
124-768C-6R-2, 0–3	402.90	0.3
124-768C-6R-2, 31–33	403.21	0.3
124-768C-6R-3, 54–56	404.94	0.2
124-768C-7R-1, 86–88	411.96	0.4
124-768C-7R-4, 0–3	415.60	2.8
124-768C-7R-4, 67–69	416.27	0.5
124-768C-7R-5, 28–30	417.38	0.3
124-768C-8R-1, 109–111	421.79	0.3
124-768C-8R-2, 0–3	422.20	1.0
124-768C-8R-2, 101–103	423.21	0.5
124-768C-8R-3, 73–75	424.43	0.5
124-768C-9R-1, 64–66	430.84	0.2
124-768C-9R-1, 147–150	431.67	0.3
124-768C-9R-2, 94–96	432.64	0.2
124-768C-10R-1, 52–54	440.42	1.0
124-768C-10R-2, 0–3	441.40	1.4
124-768C-10R-2, 82–84	442.22	3.9
124-768C-10R-3, 105–107	443.95	1.2
124-768C-11R-2, 56–58	451.66	1.5
124-768C-11R-4, 44–46	454.54	0.3
124-768C-11R-5, 0–3	455.60	1.0
124-768C-11R-5, 90–92	456.50	0.2
124-768C-12R-1, 74–76	459.94	0.4
124-768C-12R-2, 0–3	460.70	0.4
124-768C-13R-1, 76–78	469.66	1.2
124-768C-13R-2, 28–30	470.68	2.5
124-768C-13R-3, 79–81	472.69	0.4
124-768C-13R-4, 0–3	473.40	0.4
124-768C-14R-2, 53–55	480.53	0.8
124-768C-14R-3, 50–52	482.00	3.4
124-768C-14R-4, 0–3	483.00	1.9
124-768C-14R-4, 86–88	483.86	1.0
124-768C-15R-1, 81–83	489.01	1.4
124-768C-15R-3, 0–3	491.20	0.5
124-768C-15R-3, 73–75	491.93	0.7
124-768C-15R-4, 36–38	493.06	2.1
124-768C-16R-1, 37–39	498.27	2.0
124-768C-16R-2, 0–3	499.40	0.5
124-768C-17R-1, 135–137	508.85	0.7
124-768C-17R-2, 115–117	510.15	0.8
124-768C-17R-3, 0–3	510.50	0.7
124-768C-17R-3, 66–68	511.16	0.5
124-768C-17R-3, 111–113	511.61	0.6
124-768C-18R-1, 6–8	517.26	35.7
124-768C-18R-2, 112–114	519.82	2.0
124-768C-18R-4, 0–3	521.70	3.7
124-768C-18R-4, 44–47	522.14	0.5

Table 7 (continued).

Core, section interval (cm)	Depth (mbsf)	$CaCO_3$ (%)
124-768C-19R-1, 109–111	527.99	0.4
124-768C-19R-2, 0–3	528.40	1.0
124-768C-19R-2, 4–6	528.44	0.6
124-768C-20R-1, 116–118	537.76	0.8
124-768C-20R-2, 96–98	539.06	0.4
124-768C-20R-3, 0–3	539.60	1.1
124-768C-20R-3, 38–40	539.98	0.8
124-768C-21R-1, 0–3	546.30	1.2
124-768C-21R-1, 95–97	547.25	0.4
124-768C-21R CC, 21–23	548.03	34.3
124-768C-22R-1, 31–33	556.11	36.0
124-768C-22R-1, 58–60	556.38	0.3
124-768C-22R-3, 0–3	558.80	0.7
124-768C-23R-1, 5–7	565.55	68.6
124-768C-23R-2, 39–41	567.39	1.0
124-768C-23R-5, 0–3	571.50	0.4
124-768C-24R-1, 69–70	575.89	1.5
124-768C-24R-2, 0–3	576.70	1.9
124-768C-24R-3, 77–78	578.97	0.9
124-768C-24R-4, 34–36	580.04	0.5
124-768C-26R-1, 56–58	595.16	0.2
124-768C-26R-3, 45–47	598.05	1.2
124-768C-26R-5, 0–3	600.60	3.1
124-768C-26R-5, 41–43	601.01	2.7
124-768C-27R-1, 36–38	604.66	0.5
124-768C-27R-2, 83–85	606.63	1.5
124-768C-27R-3, 113–115	608.43	1.4
124-768C-27R-4, 0–3	608.80	0.4
124-768C-28R-1, 37–39	614.27	0.2
124-768C-28R-3, 45–47	617.35	2.7
124-768C-28R-4, 137–140	619.77	0.4
124-768C-28R-5, 59–61	620.49	0.7
124-768C-29R-2, 47–49	625.47	0.2
124-768C-29R-4, 25–27	628.25	0.7
124-768C-29R-6, 0–3	631.00	0.3
124-768C-29R-6, 120–122	632.20	1.9
124-768C-30R-1, 100–102	634.10	1.0
124-768C-30R-3, 117–119	637.27	0.2
124-768C-30R-6, 0–3	640.60	0.9
124-768C-30R-6, 91–93	641.51	0.3
124-768C-31R-1, 39–41	643.19	0.2
124-768C-31R-3, 44–46	646.24	0.7
124-768C-31R-4, 0–3	647.30	0.5
124-768C-31R-4, 91–93	648.21	0.7
124-768C-32R-1, 38–40	652.78	0.3
124-768C-32R-3, 10–12	655.50	0.5
124-768C-32R-3, 144–146	656.84	0.9
124-768C-32R-5, 66–68	659.06	1.2
124-768C-32R-6, 0–3	659.90	0.3
124-768C-33R-2, 73–75	664.33	0.3
124-768C-33R-4, 86–88	667.46	0.2
124-768C-33R-5, 53–55	668.63	1.0
124-768C-33R-6, 0–3	669.60	0.2
124-768C-34R-1, 85–87	672.65	0.2
124-768C-34R-3, 55–57	675.35	1.6
124-768C-34R-6, 0–3	679.30	1.2
124-768C-34R-6, 71–73	680.01	0.4
124-768C-35R-1, 135–137	682.75	0.6
124-768C-35R-3, 112–114	685.52	1.1
124-768C-35R-5, 0–3	687.40	0.7
124-768C-35R-5, 69–71	688.09	0.9
124-768C-36R-1, 134–136	692.44	2.2
124-768C-36R-3, 0–3	694.10	2.2
124-768C-36R-3, 73–75	694.83	1.2
124-768C-36R-6, 25–27	698.85	0.3
124-768C-37R-1, 131–133	702.11	0.6
124-768C-37R-3, 134–136	705.14	0.7
124-768C-37R-5, 0–3	706.80	0.8
124-768C-37R-5, 100–102	707.80	1.1
124-768C-38R-1, 61–63	711.11	1.1
124-768C-38R-2, 64–66	712.64	0.2
124-768C-38R-3, 0–3	713.50	1.6
124-768C-38R-3, 124–126	714.74	0.2
124-768C-39R-2, 52–54	722.22	0.2
124-768C-39R-2, 147–150	723.17	1.1
124-768C-39R-3, 0–3	723.20	0.6
124-768C-39R-3, 100–102	724.20	0.7
124-768C-39R-4, 67–69	725.37	0.7

Table 7 (continued).

Core, section interval (cm)	Depth (mbsf)	$CaCO_3$ (%)
124-768C-40R-1, 78-80	730.68	2.1
124-768C-40R-1, 129 131	731.19	11.3
124-768C-40R-2, 48-50	731.88	36.6
124-768C-40R-4, 0-3	734.40	0.3
124-768C-40R-4, 92-94	735.32	0.9
124-768C-41R-1, 87-89	740.47	0.7
124-768C-41R-3, 60-62	743.20	0.2
124-768C-41R-5, 0-3	745.60	0.4
124-768C-41R-6, 56-58	747.66	0.2
124-768C-42R-1, 33-35	749.63	0.2
124-768C-42R-3, 0-3	752.30	0.4
124-768C-42R-3, 43-45	752.73	0.2
124-768C-43R-1, 84-86	759.34	0.3
124-768C-43R-3, 0-3	761.50	0.2
124-768C-43R-3, 23-25	761.73	0.3
124-768C-44R-1, 103-105	769.13	0.3
124-768C-44R-2, 0-3	769.60	0.4
124-768C-44R-3, 89-91	771.99	0.5
124-768C-45R-1, 129-131	778.99	0.3
124-768C-45R-3, 0-3	780.70	0.3
124-768C-45R-3, 39-41	781.09	0.3
124-768C-46R-1, 0-3	787.40	0.3
124-768C-46R-1, 107-109	788.47	0.3
124-768C-46R-2, 27-29	789.17	0.2
124-768C-47R-1, 0-3	796.90	0.4
124-768C-47R-1, 111-112	798.01	0.2
124-768C-48R-1, 111-113	807.71	0.4
124-768C-48R-2, 27-29	808.37	0.3
124-768C-48R-4, 83-85	811.93	0.4
124-768C-48R-5, 0-3	812.60	0.4
124-768C-49R-3, 7-9	818.57	0.2
124-768C-49R-5, 0-3	821.50	0.2
124-768C-49R-6, 129-131	824.29	0.4
124-768C-50R-1, 48-50	825.68	0.2
124-768C-50R-2, 0-3	826.70	0.2
124-768C-50R-2, 17-19	826.87	0.2
124-768C-50R-3, 69-71	828.89	0.2
124-768C-51R-2, 24-26	836.64	0.3
124-768C-51R-2, 104-106	837.44	0.2
124-768C-51R-4, 92-94	840.32	0.3
124-768C-51R-CC, 0-3	841.57	0.4
124-768C-52R-1, 0-3	844.60	0.3
124-768C-52R-1, 110-111	845.70	0.2
124-768C-52R-5, 129-131	851.89	0.2
124-768C-53R-2, 0-3	855.80	0.4
124-768C-53R-2, 95-97	856.75	0.5
124-768C-53R-3, 112-114	858.42	0.3
124-768C-54R-1, 20-22	864.20	0.2
124-768C-54R-3, 0-3	867.00	0.4
124-768C-54R-3, 49-51	867.49	0.4
124-768C-55R-2, 53-55	875.73	1.9
124-768C-55R-3, 0-3	876.70	0.3
124-768C-55R-3, 118-120	877.88	0.6
124-768C-56R-1, 19-21	883.59	0.2
124-768C-56R-2, 11-13	885.01	0.4
124-768C-56R-4, 60-62	888.50	0.4
124-768C-56R-5, 0-3	889.40	0.2
124-768C-57R-1, 17-19	893.27	0.2
124-768C-58R-1, 22-24	902.62	0.4
124-768C-58R-2, 35-37	904.25	0.3
124-768C-58R-4, 57-59	907.47	0.6
124-768C-58R-4, 147-150	908.37	0.7
124-768C-59R-1, 73-75	912.73	0.5
124-768C-59R-4, 16-18	916.66	0.4
124-768C-59R-5, 16-18	918.16	0.4
124-768C-59R-6, 0-3	919.50	0.5
124-768C-60R-3, 0-3	924.70	0.3
124-768C-60R-3, 97-99	925.67	0.3
124-768C-60R-6, 69-71	929.89	0.3
124-768C-61R-2, 125-127	934.15	0.6
124-768C-61R-3, 147-150	935.87	0.3
124-768C-61R-4, 144-146	937.34	0.2
124-768C-62R-2, 22-24	942.72	0.2
124-768C-62R-3, 0-3	944.00	0.2
124-768C-62R-4, 54-56	946.04	0.7
124-768C-63R-1, 145-147	951.75	0.2
124-768C-63R-4, 22-24	955.02	0.3
124-768C-63R-6, 0-3	957.80	0.2
124-768C-64R-1, 54-56	960.54	0.6

Table 7 (continued).

Core, section interval (cm)	Depth (mbsf)	$CaCO_3$ (%)
124-768C-64R-2, 0-3	961.50	0.2
124-768C-64R-2, 124-126	962.74	0.2
124-768C-65R-2, 36-38	971.56	0.2
124-768C-65R-5, 0-3	975.70	0.2
124-768C-65R-5, 83-85	976.53	0.1
124-768C-66R-2, 11-13	981.01	1.7
124-768C-66R-3, 0-3	982.40	0.3
124-768C-66R-3, 108-110	983.48	1.0
124-768C-66R-4, 43-45	984.33	0.6
124-768C-67R-5, 32-34	995.32	0.4
124-768C-67R-6, 147-150	997.97	0.3
124-768C-68R-1, 32-34	999.02	0.6
124-768C-68R-5, 0-3	1004.70	0.2
124-768C-68R-5, 100-110	1005.70	0.7
124-768C-69R-2, 88-90	1010.68	0.3
124-768C-69R-4, 30-32	1013.10	0.3
124-768C-69R-5, 0-3	1014.30	0.3
124-768C-70R-1, 60-62	1018.20	3.7
124-768C-70R-1, 147-150	1019.07	0.4
124-768C-70R-2, 61-63	1019.71	0.7
124-768C-70R-3, 69-71	1021.29	0.4
124-768C-70R-4, 55-57	1022.65	1.0
124-768C-71R-1, 106-108	1028.26	0.2
124-768C-71R-2, 0-3	1028.70	0.4
124-768C-71R-3, 134-136	1031.54	1.1
124-768C-71R-4, 99-101	1032.69	0.7
124-768C-72R-2, 0-3	1038.40	0.3
124-768C-72R-2, 8-10	1038.48	0.6

Interstitial Water Chemistry

A total of 34 interstitial water (IW) samples were collected at Site 768: 19 from Hole 768B and 15 from Hole 768C. They were retrieved from every core (approximately 10 m apart) in the uppermost 100 mbsf, by means of standard ODP squeezing techniques (see "Explanatory Notes" section, this volume). Below this depth, IW samples were taken every third core (about 30 m apart). With the exception of a few samples in the deeper sections of Hole 768C, whole-round core samples, 5-10 cm in length, provided sufficient IW (> 10 ml) for shipboard chemical analysis. The results are summarized in Table 8, and the depth distributions are shown in Figure 47. Some analyses were not performed on the deeper samples because of insufficient amounts of IW recovered.

Salinity and Chloride

Salinity is somewhat variable in the uppermost 100 mbsf and then decreases rapidly to 31.5‰ at about 200 mbsf. The sharp drop in salinity coincides with the rapid decrease in sulfate and magnesium (Fig. 47). Between 200 and 550 mbsf, salinity is rather constant and concurs with the dissolved calcium, magnesium, chloride, sulfate, and silica, which also show constant low values within this depth interval. Below 550 mbsf salinity increases with depth.

From the uppermost sample to 550 mbsf, chloride remains essentially constant. Chloride then increases abruptly to an abnormally high value of 570 mM at 619.8 mbsf, followed by a gradual decrease to 506 mM in the deepest sample at 812 mbsf.

pH

The downcore pH distribution (Fig. 47) shows similar features to the one observed at Site 767. The pH values are generally less variable and lower in the uppermost 120 m, as compared with those in the deeper sections of the core. Below 120 mbsf, the pH increases to a maximum value of 8.35 at about 200 mbsf. The higher pH values in the mid-section of the hole (from 120 to 500 mbsf) are probably the result of the alteration

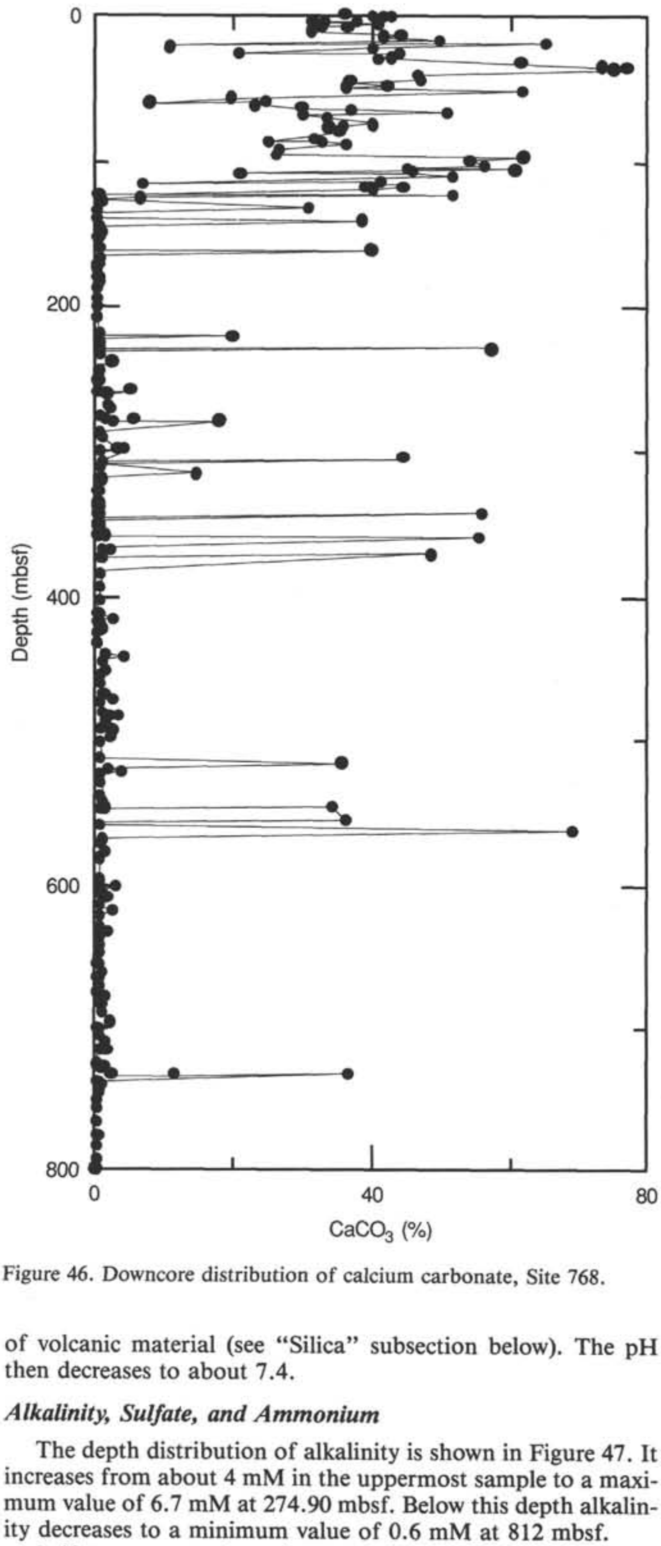

Figure 46. Downcore distribution of calcium carbonate, Site 768.

of volcanic material (see "Silica" subsection below). The pH then decreases to about 7.4.

Alkalinity, Sulfate, and Ammonium

The depth distribution of alkalinity is shown in Figure 47. It increases from about 4 mM in the uppermost sample to a maximum value of 6.7 mM at 274.90 mbsf. Below this depth alkalinity decreases to a minimum value of 0.6 mM at 812 mbsf.

Sulfate concentrations decrease almost linearly from 27.12 mM near the sediment-seawater interface to 0.77 mM at 172.90 mbsf and continue at low levels to the bottom of the hole (Fig. 47). The complete depletion of sulfate at ~200 mbsf results from a high sedimentation rate and organic matter degradation by sulfate reduction (see "Organic Geochemistry" and "Sedimentation Accumulation Rates" sections, this chapter).

At Site 768, the alkalinity distribution does not correspond to the observed decrease in dissolved sulfate (Fig. 48) in the uppermost 120 mbsf. The alkalinity deficit indicates that the pore water is saturated with respect to calcite and that bicarbonate has been removed from the pore water to form carbonates. Such a carbonate saturation state helps preserve the calcareous oozes found in the uppermost 120 m of the core (see "Lithostratigraphy" section, this chapter).

The downhole distribution of ammonium is also shown in Figure 47. Ammonium increases from 26 μM near the sediment surface to a maximum value of 1378 μM at about 500 mbsf as a result of organic matter degradation. Below this depth, ammonium drops to about 400 mM at the bottom of the profile.

Silica

The silica concentration increases from 411 μM at 2.95 mbsf to 836 μM at 68.45 mbsf. It then sharply drops to 230 μM at 115.95 mbsf, below which it remains essentially constant, at around 200 μM, throughout the remainder of the hole (Fig. 47). The variation in the dissolved silica profile mirrors the pH distribution. It is generally very similar to the one found at Site 767, and it can be attributed to a silicification reaction during the alteration of volcanic material (Kastner and Gieskes, 1976).

Calcium and Magnesium

Dissolved calcium and magnesium distributions at Site 768 are shown in Figure 47. The small, yet almost negligible, increase in calcium is accompanied by a larger decrease in Mg in the uppermost 150 mbsf. These distributions, together with the alkalinity deficit, suggest dolomitization of biogenic carbonate through a combination of the following reactions:

$$CaCO_3 + Mg^{2+} + 2HCO_3^- \rightarrow CaMg(CO_3)_2 + CO_2 + H_2O, \quad (1)$$

$$Ca^{2+} + Mg^{2+} + 4HCO_3^- \rightarrow CaMg(CO_3)_2 + 2CO_2 + 2H_2O, \text{ and} \quad (2)$$

$$2CaCO_3 + Mg^{2+} \rightarrow CaMg(CO_3)_2 + Ca^{2+}. \quad (3)$$

Further evidence is given by the presence of a dolomitic limestone recovered in the core catcher of Core 124-768C-25X and of the dolomite nodules present in various intervals of Unit II (see "Lithostratigraphy" section, this chapter). The first appearance of dolomitic phases corresponds with the zone of sulfate depletion in the pore water. Baker and Kastner (1981) have shown the necessity for sulfate depletion before dolomitization may begin.

The alteration of volcanogenic material also takes place in Units II and III, as evidenced by the pH and dissolved silica distributions, as well as by the presence of altered ashes in the sediments below 150 mbsf (see "Lithostratigraphy" section, this chapter). Its effect on the dissolved Ca and Mg distributions is overprinted on those from the dolomitization reactions, and therefore the observed distributions between 150 and 600 mbsf are the result of the combination of all these processes. As observed on Site 767, the basalt-seawater alteration reactions are evidenced by the calcium increase and the magnesium decrease below 600 mbsf.

All of these mechanisms (alteration of ashes, basalt-seawater reactions, carbonate recrystallization), and their relative importance at any given depth result in changes in the Ca^{2+}/Mg^{2+} ratio, as illustrated in Figure 49. This figure shows the deviation of dissolved calcium (ΔCa^{2+}) and magnesium (ΔMg^{2+}) from the seawater concentrations at both Sites 767 and 768. Although the reactions in the sediment column and in the sediment basement interface result in an overall calcium increase and a magnesium decrease, we can identify two distinct zones in Figure 49B.

Table 8. Interstitial water geochemical data, Site 768.

Core, section, interval (cm)	Depth (mbsf)	Vol. (cm^3)	pH	Alk. (mM)	Sal. (g/kg)	Mg^{2+} (mM)	Ca^{2+} (mM)	Cl^- (mM)	SO_4^{2-} (mM)	NH_4^+ (μM)	SiO_2 (μM)	Mg^{2+}/Ca^{2+}
124-768B-												
1H-2, 145-150	2.95	60	7.56	3.013	35.9	51.48	10.86	553.00	27.12	26	411	4.74
2H-5, 145-150	11.45	45	7.56	4.922	34.5	50.07	11.01	555.00	27.33	68	542	4.54
3H-5, 145-150	20.95	57	7.50	3.909	35.5	48.85	11.06	551.00	26.16	116	625	4.42
4H-5, 145-150	30.45	84	7.48	3.832	35.0	46.76	10.95	557.00	24.90	146	655	4.27
5H-4, 145-150	38.45	76	7.45	4.399	35.0	46.23	11.24	547.00	22.79	284	674	4.11
6H-5, 145-150	49.45	61	7.41	4.360	34.5	44.67	11.39	547.00	23.88	285	689	3.92
7H-5, 145-150	58.95	46	7.51	4.382	35.7	42.90	11.43	547.00	22.72	280	751	3.75
8H-5, 145-150	68.45	61	7.41	4.354	35.5	41.17	11.43	553.00	21.08	277	836	3.60
9H-5, 145-150	77.95	50	7.49	3.291	35.0	39.41	11.62	552.00	19.99	277	765	3.39
10H-5, 145-150	87.45	59	7.49	3.343	34.0	37.68	11.94	547.00	19.13	419	793	3.16
13H-5, 145-150	115.95	65	7.50	2.809	33.2	33.86	12.00	544.00	12.97	453	230	2.82
16H-5, 145-150	144.45	24	7.84	3.558	32.5	30.78	12.56	550.00	7.21	488	206	2.45
19H-5, 140-150	172.90	29	7.70	4.422	31.7	26.75	9.14	544.00	0.77	561	224	2.93
22H-4, 140-150	198.70	24	8.35	4.439	31.5			542.00	0.22	748	158	
26X-2, 140-150	222.20	39	7.87	3.936	32.5	23.05	10.24	543.00	0	814	179	2.25
28X-4, 140-150	244.50	19	8.12	5.424	31.7	24.85	11.57	536.00	1.44	738	171	2.15
31X-5, 140-150	274.90	16	7.87	6.687	32.0	25.19	11.95	542.00	0	751	198	2.11
34X-2, 140-150	299.30	18	7.80	4.837	32.0	25.09	11.10	551.00	0	847	166	2.26
37X-2, 140-150	328.40	17	7.85	5.724	32.1	27.45	11.97	542.00	5.44	506		2.29
124-768C-												
1R-3, 140-150	357.60	26	7.82	5.504	32.5	26.72	12.54	545.00	6.46	1134	172	2.13
4R-1, 140-150	383.50	27	7.82	5.914	32.0	23.35	13.56	547.00	4.05	825	211	1.72
7R-3, 140-150	415.50	18	7.89	5.444	32.0	21.80	14.94	545.00	1.14	977	201	1.46
10R-3, 140-150	444.30	10	8.01	5.660	32.0	20.15	16.52	544.00	1.20	951	156	1.22
13R-3, 140-150	473.30	25	8.04	4.699	32.2	18.09	17.40	547.00	2.43	1093	134	1.04
16R-1, 140-150	499.30	29	7.98	3.869	32.3	19.06	18.86	547.00	5.30	1378	146	1.01
19R-1, 140-150	528.30	12	7.75	3.145	32.0	17.37	20.79	543.00	3.01	911	187	0.84
22R-2, 140-150	558.70	29	7.77	2.943	31.5	14.83	22.23	562.00	4.12	1155	148	0.67
26R-4, 140-150	600.50	12	7.74	4.092	34.0	41.98	29.13	559.00	0.72	714	158	1.44
28R-4, 140-150	619.80	12	7.93	3.125	33.0	10.60	31.80	570.00	0.32	860	121	0.33
37R-4, 140-150	706.70	3	7.31	1.676	35.5				1.76	568		
40R-3, 140-150	734.30	6	7.41	0.588	34.5	9.09	54.04	536.00	6.88	405	127	0.17
43R-2, 140-150	761.40	4				3.30	63.28	533.00	5.23	412	130	0.05

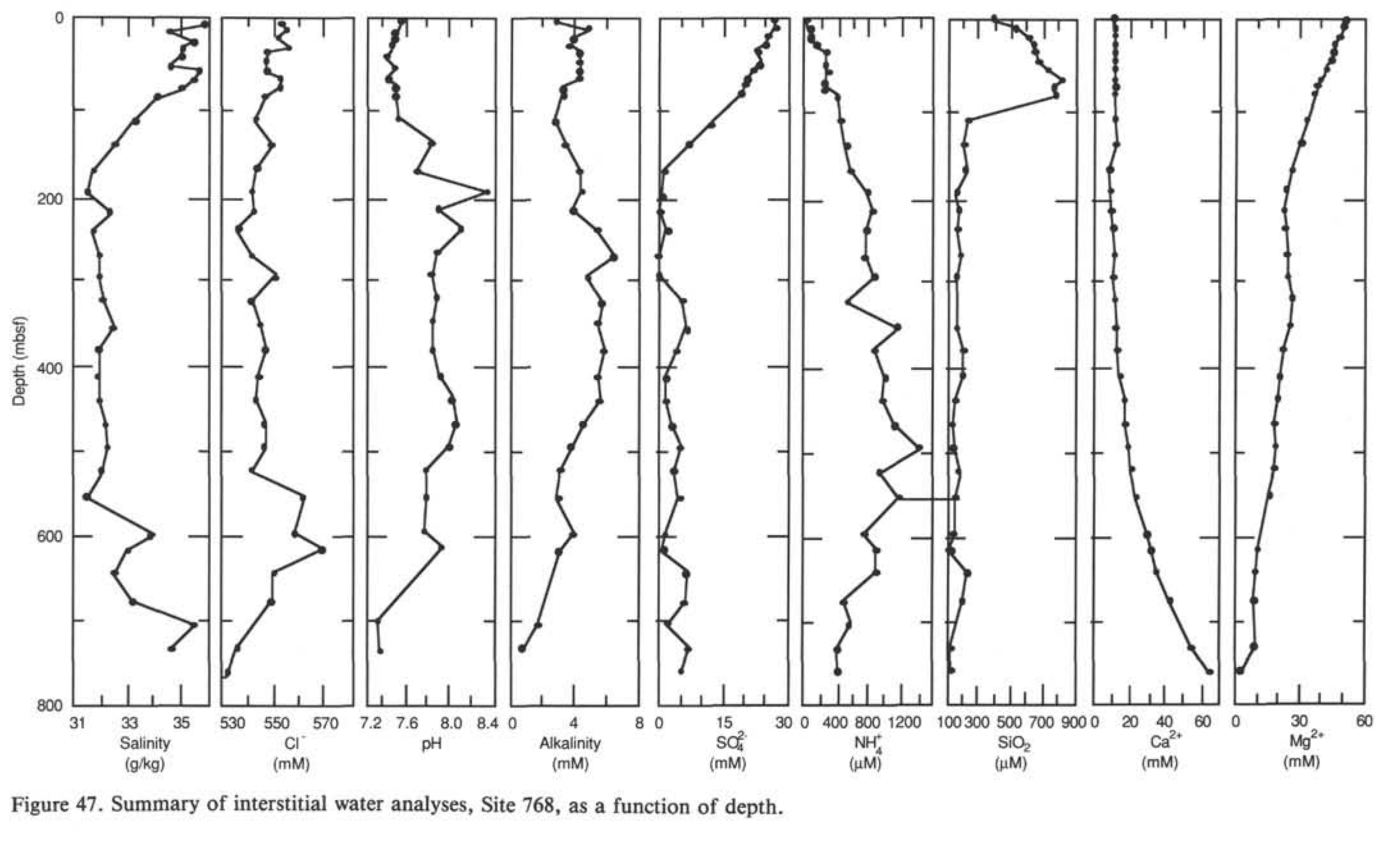

Figure 47. Summary of interstitial water analyses, Site 768, as a function of depth.

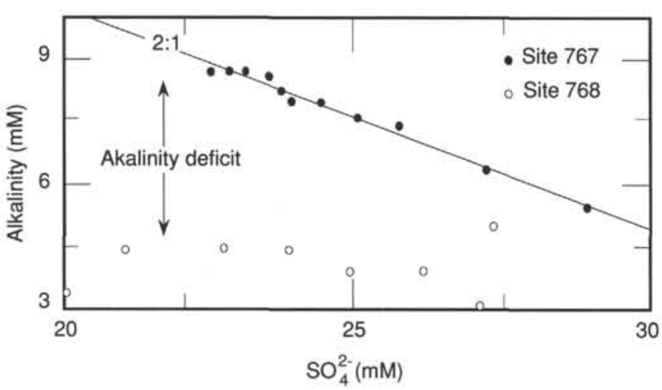

Figure 48. Relationship between alkalinity and dissolved sulfate in pore water from Sites 767 and 768. Note the deficit in dissolved alkalinity in Site 768 relative to the stoichiometric ratio for sulfate reduction shown by the pore-water samples from Site 767.

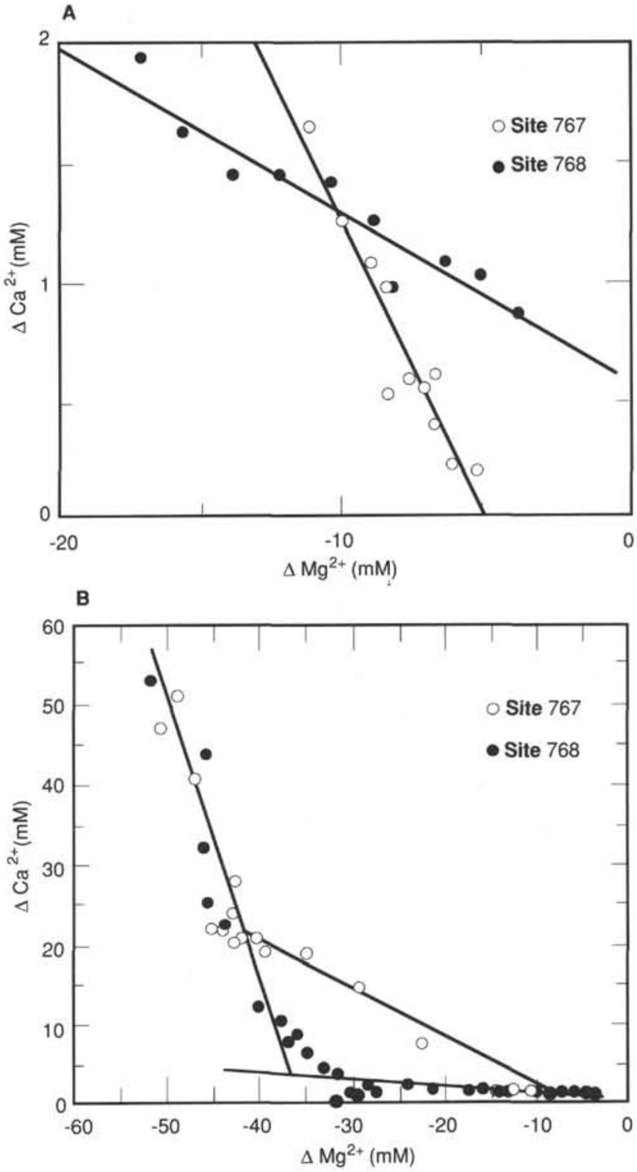

Figure 49. Dissolved calcium-magnesium relationships at Sites 767 and 768 expressed as the deviations from seawater concentrations ΔCa^{2+} and ΔMg^{2+}. **A.** Relationships of sediments above 100 mbsf. **B.** Relationships of all sediments for both sites.

In the upper section of the holes (< 100 mbsf), there is a rapid magnesium consumption relative to the calcium increase; the Ca^{2+}/Mg^{2+} ratio, however, varies between both sites. This is probably the result of the increased involvement of carbonate chemistry at Site 768. The presence of biogenic carbonates at this site, buffers the calcium uptake relative to magnesium, as evidenced by the slopes of the lines shown in Figure 49A.

In contrast, in the pore water from the bottom sediments overlying the basement (at Site 767) and pyroclastic flows (at Site 786), the Ca^{2+}/Mg^{2+} ratio shows a significant increase. The fact that the Ca^{2+}/Mg^{2+} concentrations at each site change at the same rate suggests that similar reactions lead to the observed Ca release and Mg uptake at both sites. The loci of these reactions must lie below 800 mbsf, as indicated by the linear gradients in the concentration of these cations below 600 mbsf (Fig. 47).

ORGANIC GEOCHEMISTRY

The scientific purposes of Leg 124 shipboard organic geochemistry studies were previously outlined (see "Organic Geochemistry" section, "Site 767" chapter, this volume). The following summarizes the preliminary shipboard results of Site 768 (Sulu Sea).

Samples

We collected 141 sediment samples from Site 768: 3 samples from Hole 768A, 49 from Hole 768B, and 89 from Hole 768C. Of these sediment samples, 109 were analyzed for their composition of light hydrocarbons by means of headspace gas analyses. Total organic carbon content (TOC), hydrogen and oxygen indexes (HI and OI), and the maturity of the organic matter (T_{max}) were determined by Rock-Eval pyrolysis. In addition to the headspace gas analyses, we also analyzed 47 gas samples (collected from gas pockets in Hole 768C using vacutainers) for their molecular composition.

The details of the analytical methods used are given in the "Explanatory Notes" (this volume).

Results and Discussion

Amount, Type, and Maturity of Organic Matter

Except for four samples, TOC values were below 1%, with most of them below 0.5%. Given the amount of organic matter, four zones can be distinguished in the sedimentary column of Site 768 (Tables 9 and 10 and Fig. 50).

In the first zone between 0 and 128 mbsf, TOC is low (< 0.1%, average = 0.06%), with the exception of Sample 124-768B-4H-6, 90–95 cm, where TOC reaches 0.4%. This zone corresponds to the deposition of hemipelagic to pelagic carbonate-rich sediments (see "Lithostratigraphy" section, this chapter). The poor preservation of organic matter suggests that sinking occurred through a well-oxygenated water column and that a significant portion of organic matter was probably consumed during diagenesis (Demaison and Moore, 1980).

A second zone was distinguished between 128 and 720 mbsf, showing TOC values mainly between 0.4% and 0.5%, and maximum and minimum values of 3.85% TOC (Sample 124-768B-33X-1, 56–59 cm) and 0% (Sample 124-768B-18H-6, 0–3 cm), respectively. The sediments of this zone consist of clayey to silty turbidites (see "Lithostratigraphy" section, this chapter), which indicates that the organic matter is transported through turbidite flows into the basin.

The third zone from 720 to 800 mbsf at the transition between pyroclastic and siliciclastic rocks (see "Lithostratigraphy"

Table 9. Rock-Eval data, Site 768.

Core, section, interval (cm)	Depth (mbsf)	S_1 (mg/g)	S_2 (mg/g)	S_3 (mg/g)	TOC (%)	C (%)	HI	OI	T_{max} (°C)	PI	S_2/S_3
124-768B-											
2H-6, 0-3	11.50	0.20	0.28	4.37	0.03	0.04	933	—	310	0.42	0.06
3H-6, 0-3	1.00	0.03	0.07	1.24	0	0	0	0	406	0.30	0.05
3H-7, 0-3	22.50	0.17	0.53	3.59	0.07	0.05	757	5128	329	0.24	0.14
4H-6, 0-3	30.50	0.09	0.49	3.69	0.04	0.04	1225	9225	278	0.16	0.13
4H-6, 90-95	31.40	0.29	1.50	6.05	0.40	0.14	375	1512	403	0.16	0.24
5H-5, 0-3	38.50	0.27	0.63	2.39	0.08	0.07	787	2987	310	0.30	0.26
6H-6, 0-3	49.50	0.04	0.15	3.24	0.01	0.01	1500	—	395	0.22	0.04
7H-6, 0-3	59.00	0.09	0.94	1.85	0.08	0.08	1175	2312	595	0.09	0.50
8H-6, 0-3	68.50	0.10	0.27	2.94	0.02	0.03	1350	—	375	0.28	0.09
9H-6, 0-3	78.00	0.04	0.05	2.64	0	0	0	0	351	0.50	0.01
10H-3, 94-99	83.94	0.11	0.57	3.11	0.05	0.05	1140	6220	347	0.16	0.18
10H-6, 0-3	87.50	0.07	0.28	2.28	0.02	0.02	1400	—	382	0.21	0.12
11H-6, 0-3	97.00	0.05	0.09	2.03	0.01	0.01	900	—	310	0.36	0.04
12H-6, 0-3	106.50	0.07	0.29	3.26	0.02	0.03	1450	—	473	0.19	0.08
13H-1, 65-67	109.15	0.16	0.62	3.38	0.06	0.06	1033	5633	307	0.21	0.18
13H-6, 0-3	116.00	0.06	0.58	1.27	0.06	0.05	966	2116	542	0.09	0.45
14H-6, 0-3	125.50	0.45	0.45	4.71	0.08	0.07	562	5887	312	0.50	0.09
15H-2, 18-21	129.18	0.15	3.48	0.23	0.39	0.30	915	60	501	0.04	15.13
15H-6, 0-3	135.00	0.12	2.81	0.97	0.35	0.24	802	277	468	0.04	2.89
16H-6, 0-3	144.50	0.10	2.07	0.92	0.36	0.18	575	255	473	0.05	2.25
17H-5, 0-3	152.50	0.15	1.66	1.12	0.36	0.15	461	311	508	0.08	1.48
18H-1, 100-105	157.00	0.17	1.88	0.22	0.28	0.17	671	78	457	0.08	8.54
18H-6, 0-3	163.50	0.02	0.11	4.28	0.00	0.01	0	0	356	0.17	0.02
19H-6, 0-3	173.00	0.08	1.30	0.21	0.18	0.11	722	116	518	0.06	6.19
20H-6, 28-30	180.08	0.07	0.01	2.32	0.28	0	3	828	270	0.87	0.00
20H-6, 0-3	181.30	0	1.12	0.44	0.21	0.09	533	209	485	0	2.54
21H-5, 0-3	189.30	0	0.96	0.84	0.15	0.08	640	560	493	0	1.14
22H-5, 0-3	198.80	0	0.90	0.81	0.18	0.07	500	450	490	0	1.11
23H-5, 0-3	207.00	0.22	0.94	0.86	0.33	0.09	284	260	428	0.19	1.09
26X-3, 0-3	222.30	0.05	0.39	0	0.03	0.03	1300	0	388	0.11	0
27X-3, 0-3	231.90	0.01	1.84	0	0.33	0.15	557	0	511	0.01	0
28X-1, 108-113	239.68	0.09	0.94	0.73	0.45	0.08	208	162	466	0.09	1.28
28X-5, 0-3	244.60	0.09	1.60	0.44	0.41	0.14	390	107	486	0.05	3.63
29X-3, 0-3	251.20	0.13	2.07	0.88	0.32	0.18	646	275	497	0.06	2.35
30X-2, 0-3	259.30	0.03	0.28	1.89	0.25	0.02	112	756	570	0.10	0.14
31X-6, 0-3	275.00	0.03	1.28	0.61	0.25	0.10	512	244	498	0.02	2.09
32X-2, 0-3	278.70	0.03	0.70	0.86	0.28	0.06	250	307	581	0.04	0.81
33X-1, 56-59	287.36	0.67	4.31	2.71	3.85	0.41	111	70	401	0.13	1.59
33X-2, 130-134	289.60	0.10	0.88	0.57	0.49	0.08	179	116	465	0.10	1.54
33X-3, 0-3	289.80	0.05	1.09	0.84	0.69	0.09	157	121	503	0.04	1.29
34X-3, 0-3	299.40	0.02	0.89	0.63	0.29	0.07	306	217	530	0.02	1.41
35X-2, 0-3	307.60	0.05	0.41	4.44	0.32	0.03	128	1387	408	0.11	0.09
36X-3, 0-3	318.80	0.01	1.02	0.36	0.23	0.08	443	156	496	0.01	2.83
37X-3, 0-3	328.50	0	1.43	0.32	0.21	0.11	600	152	537	0	4.46
38X-2, 88-90	337.48	0	0.77	0.28	0.24	0.06	320	116	526	0	2.75
38X-3, 0-3	338.10	0.01	1.20	0.28	0.33	0.10	363	84	498	0.01	4.28
38X-4, 87-90	340.47	0.02	0.39	0.75	0.25	0.03	156	300	470	0.05	0.52
39X-3, 0-3	347.80	0.06	1.37	0.22	0.26	0.11	526	84	517	0.04	6.22
124-768C-											
1R-3, 113-115	357.33	0.50	2.30	1.06	1.51	0.23	152	70	388	0.18	2.16
1R-4, 0-3	357.70	0.01	1.39	0	0.30	0.11	463	0	524	0.01	0
2R-4, 0-3	367.40	0.02	0.84	0.51	0.18	0.07	466	283	517	0.02	1.64
3R-1, 0-3	372.40	0.07	1.16	0.64	0.50	0.10	232	128	506	0.06	1.81
4R-2, 0-3	383.60	0.02	0.80	0.41	0.28	0.06	285	145	507	0.02	1.95
5R-3, 0-3	394.80	0.04	1.01	0.54	0.54	0.08	187	100	470	0.04	1.87
6R-2, 0-3	402.90	0	0.82	0.49	0.41	0.06	200	119	442	0	1.67
6R-2, 20-23	403.10	0.13	0.67	0.96	0.61	0.06	109	157	452	0.16	0.69
7R-4, 0-3	415.60	0.01	1.11	1.18	0.44	0.09	252	268	549	0.01	0.94
8R-2, 0-3	422.20	0.06	1.37	1.63	0.46	0.11	318	379	506	0.04	0.84
9R-1, 147-150	431.67	0.02	1.09	0.30	0.47	0.09	231	63	499	0.02	3.63
10R-2, 0-3	441.40	0	0.79	0.33	0.38	0.06	207	86	444	0	2.39
11R-5, 0-3	455.60	0.05	0.90	0.75	0.42	0.07	214	178	479	0.05	1.20
11R-5, 15-17	455.75	0.10	1.25	1.36	1.11	0.11	112	122	431	0.07	0.91
12R-2, 0-3	460.70	0.02	0.75	0.91	0.17	0.06	441	535	512	0.03	0.82
13R-4, 0-3	473.40	0.02	0.72	0.69	0.40	0.06	180	172	428	0.03	1.04
14R-4, 0-3	483.00	0.06	0.86	2.22	0.68	0.07	126	326	482	0.07	0.38
15R-3, 0-3	491.20	0.12	1.25	0.70	0.45	0.11	277	155	491	0.09	1.78
16R-2, 0-3	499.40	0	0.57	0.23	0.10	0.04	570	230	462	0	2.47
17R-3, 0-3	510.50	0.01	0.58	0.35	0.10	0.04	580	350	503	0.02	1.65
17R-3, 143-147	511.93	0.13	1.07	0.74	1.21	0.10	88	61	433	0.11	1.44
17R-4, 49-53	512.49	0.03	0.83	0.53	0.60	0.07	138	88	482	0.03	1.56
18R-4, 0-3	521.70	0.04	0.54	3.51	0.49	0.04	110	716	423	0.07	0.15
18R-4, 62-66	522.32	0.07	0.63	2.39	0.46	0.05	136	519	491	0.10	0.26
18R-4, 70-74	522.40	0.01	0.37	0.49	0.19	0.03	194	257	444	0.03	0.75
19R-2, 0-3	528.40	0.04	0.62	0.70	0.29	0.05	213	241	497	0.06	0.88

Table 9 (continued).

Core, section, interval (cm)	Depth (mbsf)	S_1 (mg/g)	S_2 (mg/g)	S_3 (mg/g)	TOC (%)	C (%)	HI	OI	T_{max} (°C)	PI	S_2/S_3
124-768C-											
20R-3, 0–3	539.60	0.02	0.50	0.76	0.37	0.04	135	205	393	0.04	0.65
21R-1, 0–3	546.30	0.11	1.55	1.79	0.57	0.13	271	314	507	0.07	0.86
22R-3, 0–3	558.80	0	0.69	0.89	0.95	0.05	72	93	436	0.00	0.77
23R-1, 92–94	566.42	0.27	0.84	0.89	0.30	0.09	280	296	470	0.25	0.94
23R-1, 104–106	566.54	0.09	0.90	0.69	0.44	0.08	204	156	465	0.09	1.30
23R-5, 0–3	571.50	0	1.09	0.25	0.29	0.29	375	86	544	0	4.36
24R-2, 0–3	576.70	0.06	0.98	2.03	0.55	0.08	178	369	530	0.06	0.48
26R-5, 0–3	600.60	0.01	0.69	1.01	0.25	0.05	276	404	532	0.01	0.68
27R-4, 0–3	608.80	0	0	0.40	0.20	0.00	0	200	361	0	0
28R-4, 137–140	619.77	0.04	1.13	0.01	0.34	0.09	332	2	534	0.03	
29R-4, 13–16	628.13	0.01	0.65	0.76	0.48	0.05	135	158	408	0.02	0.85
29R-6, 0–3	631.00	0.03	0.53	0.02	0.27	0.04	196	7	424	0.05	26.50
30R-6, 0–3	640.60	0.04	0.91	0.66	0.46	0.07	197	143	475	0.04	1.37
31R-4, 0–3	647.30	0.04	1.31	0.74	0.31	0.11	422	238	507	0.03	1.77
32R-3, 32–34	655.72	0.01	0.82	0.77	0.08	0.06	1025	962	525	0.01	1.06
32R-6, 0–3	659.90	0	0.43	0.44	0.30	0.03	143	146	457	0	0.97
33R-2, 94–98	664.54	0.01	0.44	0.72	0.37	0.03	118	194	427	0.02	0.61
33R-6, 0–3	669.60	0	0.37	0.46	0.23	0.03	160	200	397	0	0.80
34R-5, 17–21	677.97	0.08	1.17	0.60	0.38	0.10	307	157	492	0.06	1.95
34R-6, 0–3	679.30	0.14	0.86	0.98	0.52	0.08	165	188	415	0.14	0.87
35R-5, 0–3	687.40	0.01	0.22	0.44	0.47	0.01	46	93	341	0.05	0.50
36R-3, 0–3	694.10	0.05	0.33	0.77	0.19	0.03	173	405	339	0.13	0.42
37R-5, 0–3	706.80	0.04	0.92	0.49	0.54	0.08	170	90	507	0.04	1.87
38R-3, 0–3	713.50	0.01	0.27	1.73	0.52	0.02	51	332	484	0.04	0.15
39R-2, 147–150	723.17	0	0.37	0.91	0.08	0.03	462	1137	506	0	0.40
39R-4, 24–27	724.94	0.02	0.51	1.55	0.04	0.04	1275	3875	505	0.04	0.32
40R-4, 0–3	734.40	0	0.46	0.22	0.20	0.03	230	110	472	0	2.09
41R-5, 0–3	745.60	0	0.52	0.19	0.19	0.04	273	100	482	0	2.73
42R-3, 0–3	752.30	0	0.39	0.32	0.10	0.03	390	320	454	0	1.21
43R-3, 0–3	761.50	0	0.55	0.18	0.14	0.04	392	128	420	0	3.05
44R-2, 0–3	769.60	0	0.40	0.53	0.06	0.03	666	883	378	0	0.75
45R-3, 0–3	780.70	0	1.16	0.35	0.11	0.09	1054	318	536	0	3.31
46R-1, 0–3	787.40	0	1.13	0.26	0.09	0.09	1255	288	515	0	4.34
47R-1, 0–3	796.90	0	0.39	0.23	0.03	0.03	1300	766	514	0	1.69
48R-5, 0–3	812.60	0.02	0.47	0.45	0.03	0.04	1566	1500	517	0.04	1.04
49R-1, 52–54	816.02	0.04	0.03	0.50	0	0	0	0	331	0.67	0.06
49R-5, 0–3	821.50	0	0	0.13	0	0	0	0	298	0	0
50R-1, 2–4	825.22	0.01	0.59	0.39	0.04	0.05	1475	975	443	0.02	1.51
50R-2, 0–3	826.70	0.02	23.44	0	0	0	0	373	0.20	0.00	
50R-3, 55–57	828.75	0.01	0.09	0.61	0	0	0	0	357	0.10	0.14
51R-CC, 0–3	841.57	0.06	0.26	0.37	0.02	0.02	1300	1850	345	0.19	0.70
52R-1, 0–3	844.60	0.01	0.21	0.50	0	0	0	0	306	0.04	0
53R-2, 0–3	855.80	0.01	0.02	0.38	0.01	0.01	2000	3800	539	0.05	0.52
54R-3, 0–3	867.00	0.04	0.08	0.43	0	0.01	0	0	330	0.33	0.18
55R-3, 0–3	876.70	0.03	0.50	0.66	0.04	0.04	1250	1650	524	0.06	0.75
56R-5, 0–3	889.40	0.01	0.01	0.20	0	0	0	0	306	0.50	0.05
57R-1, 17–19	893.27	0.02	0.02	0.27	0	0	0	0	422	0.50	0.07
58R-4, 147–150	908.37	0.05	0.15	0.99	0.01	0.01	1500	9900	414	0.25	0.15
59R-6, 0–3	919.50	0	0.31	0.59	0.02	0.02	1550	2950	584	0	0.52
60R-3, 0–3	924.70	0.02	0.03	0.44	0	0	0	0	387	0.50	0.06
61R-3, 147–150	935.87	0	0.04	0.26	0	0	350	0	0.15		
62R-3, 0–3	944.00	0.01	0.03	0	0	0	0	0	454	0.25	0.00
63R-6, 0–3	957.80	0.01	0.39	0.28	0.03	0.03	1300	933	457	0.02	1.39
64R-2, 0–3	961.50	0.02	0.03	0.08	0	0	0	0	355	0.50	0.37
65R-5, 0–3	975.70	0.03	0.21	0	0.01	0.02	2100	0	477	0.12	0
66R-3, 0–3	982.40	0.01	0.36	0.45	0.02	0.03	1800	2250	484	0.03	0.80
67R-6, 147–150	997.97	0	0.16	0	0	0.01	0	0	465	0	0
68R-5, 0–3	1004.70	0.02	0.06	0	0	0	0	0	326	0.25	0
69R-4, 149–150	1014.29	0.06	0.98	0.26	0.08	0.08	1225	325	532	0.06	3.76
69R-5, 0–3	1014.30	0.04	0.90	0.26	0.07	0.07	1285	371	531	0.04	3.46
70R-1, 147–150	1019.07	0.01	0.17	0.27	0.01	0.01	1700	2700	304	0.06	0.62
71R-2, 0–3	1028.70	0	0.11	0.23	0	0	0	0	455	0	0.47
72R-2, 0–3	1038.40	0	0.36	0.29	0.02	0.03	1800	1450	416	0	1.24

Note: TOC = total organic carbon, HI = hydrogen index, OI = oxygen index, and PI = production index.

section, this chapter) shows low TOC values (<0.5%) that decrease with depth.

In the fourth zone, below 800 mbsf, the TOC values of the predominantly pyroclastic sediments are lower than 0.1%. This might be a result of the bad preservation of organic matter or, more likely, to the high sedimentation rates of the pyroclastic sediments (see "Sediment Accumulation Rates" section, this chapter).

Five organic-rich samples (TOC >0.9%; cf. Table 9) gave reliable pyrolysis results for the hydrogen and oxygen indexes, which indicate an abundance of terrestrial organic matter in these samples (Fig. 51).

Table 10. Total organic carbon content and molecular composition of headspace gas samples from sediments of Site 768 (Carle GC).

Core, section, interval (cm)	Depth (mbsf)	TOC (%)	HI	T_{max} (°C)	Methane (ppm)	Ethane (ppm)	Propane (ppm)	C_1/C_2
124-768A-								
1H-1, 40–45	0.42	0.06	1033	359				
1H-4, 0–3	4.52	0.04	1250	590	2.50	0	0	
1H-4, 40–45	4.95	0.05	980	310				
124-768B-								
1H-3, 0–3	3.02				2.30	0	0	
2H-6, 0–3	11.50	0.03	933	310	2.50	0	0	
3H-6, 0–3	21.02	0	0	406	2.70	0	0	
3H-7, 73–75	23.24	0.07	757	329				
4H-6, 0–3	30.52	0.04	1225	278	2.90	0	0	
4H-6, 90–95	31.42	0.40	375	403				
5H-5, 0–3	38.52	0.08	787	310	2.40	0	0	
6H-6, 0–3	49.52	0.01	1500	395	2.40	0	0	
7H-6, 0–3	59.02	0.08	1175	595	2.30	0	0	
8H-6, 0–3	68.52	0.02	1350	375	2.30	0	0	
9H-6, 0–3	78.02	0	0	351	2.30	0	0	
10H-3, 94–99	83.95	0.05	1140	347				
10H-6, 0–3	87.50	0.02		382	2.40	0	0	
11H-6, 0–3	97.00	0.01	900	310	2.40	0	0	
12H-6, 0–3	106.50	0.02	1450	473	2.40	0	0	
13H-1, 65–67	109.15	0.06	1033	307				
13H-6, 0–3	116.00	0.06	966	542	2.60	0	0	
14H-6, 0–3	125.50	0.08	562	312	2.70	0	0	
15H-2, 18–21	129.20	0.39	915	501				
15H-6, 0–3	135.00	0.35	802	468	2.70	0	0	
16H-6, 0–3	144.50	0.36	575	473	2.60	0	0	
17H-5, 0–3	152.50	0.36	461	508	2.70	0	0	
18H-1, 100–105	157.02	0.28	671	457				
18H-6, 0–3	163.50	0	0	356	3.09	0	0	
19H-6, 0–3	173.00	0.18	722	518	21.10	0	0	
20H-5, 28–30	180.09	0.28	3	270				
20H-6, 0–3	181.30	0.21	533	485	1319.20	0	0	
21H-5, 0–3	189.30	0.15	640	493	3399.00	0	0	
22H-5, 0–3	198.80	0.18	500	490	6259.30	0.90	0	6955
23H-5, 0–3	207.00	0.33	284	428	7659.00	1.30	0	5892
26X-3, 0–3	222.30	0.03	1300	388	1616.00	0	0	
27X-3, 0–3	231.90	0.33	557	511	9470.00	1.70	0	5571
28X-1, 108–113	239.70	0.45	208	466				
28X-5, 0–3	244.60	0.41	390	486	4186.00	1.00	0	4186
29X-3, 0–3	251.20	0.32	646	497	7980.00	1.50	0	5320
30X-2, 0–3	259.30	0.25	112	570	1461.00	0	0	
31X-6, 0–3	275.00	0.25	512	498	4509.00	1.30	0	3468
32X-2, 0–3	278.70	0.28	250	581	3776.00	0.90	0	4196
33X-1, 56–59	287.37	3.85	111	401				
33X-2, 130–134	289.62	0.49	179	465				
33X-3, 0–3	289.80	0.69	157	503	7040.00	2.90	0	2428
34X-3, 0–3	299.40	0.29	306	530	4002.00	1.80	0	2223
35X-2, 0–3	307.60	0.32	128	408	3087.90	1.40	0	2206
36X-3, 0–3	318.80	0.23	443	496	8228.50	3.50	0	2351
37X-3, 0–3	328.50	0.21	600	537	2859.40	1.50	0	1906
38X-2, 88–90	337.49	0.24	320	526				
38X-3, 0–3	338.10	0.33	363	498	8675.30	4.10	0	2116
38X-4, 87–90	340.47	0.25	156	470				
39X-3, 0–3	347.80	0.26	526	517	2847.90	2.30	0	1238
124-768C-								
1R-3, 113–115	357.34	1.51	152	388				
1R-4, 0–3	357.70	0.30	463	524	3289.90	3.50	0	941
2R-4, 0–3	367.40	0.18	466	517	7797.00	4.50	0	1733
3R-1, 0–3	372.40	0.50	232	506	8234.00	5.40	0	1525
4R-2, 0–3	383.60	0.28	285	507	22479.00	6.60	0	3406
5R-3, 0–3	394.80	0.54	187	470	522.00	2.68	0	195
6R-2, 0–3	402.90	0.41	200	442	5676.00	6.40	0	887
6R-2, 20–23	403.12	0.61	109	452				
7R-4, 0–3	415.60	0.44	252	549	3042.00	5.50	0	553
8R-2, 0–3	422.20	0.46	318	506	3857.00	3.20	0	1205
9R-1, 147–150	431.68	0.47	231	499	3361.00	5.30	0	634
10R-2, 0–3	441.40	0.38	207	444	9469.00	11.04	0	858
11R-5, 0–3	455.60	0.42	214	479	8049.00	8.20	0	982
11R-5, 15–17	455.76	1.11	112	431				
12R-2, 0–3	460.70	0.17	441	512	1936.00	2.50	0	774
13R-4, 0–3	471.40	0.40	180	428	9686.00	10.70	0	905
14R-4, 0–3	481.00	0.68	126	482	1371.00	7.90	0	174

Table 10 (continued).

Core, section, interval (cm)	Depth (mbsf)	TOC (%)	HI	T_{max} (°C)	Methane (ppm)	Ethane (ppm)	Propane (ppm)	C_1/C_2
124-768C- (Cont.)								
15R-3, 0–3	491.20	0.45	277	491	5246.50	9.00	0	583
16R-2, 0–3	499.40	0.10	570	462	1872.50	1.80	0	1040
17R-3, 0–3	510.50	0.10	580	503	8768.20	5.70	0	1538
17R-3, 143–147	511.95	1.21	88	433				
17R-4, 49–53	512.51	0.60	138	482				
18R-4, 0–3	521.70	0.49	110	423	1309.50	13.90	1.90	94
18R-4, 62–66	522.34	0.46	136	491				
18R-4, 70–74	522.42	0.19	194	444				
19R-2, 0–3	528.40	0.29	213	497	5431.00	8.30	0	654
20R-3, 0–3	539.60	0.37	135	393	1951.00	8.60	0	227
21R-1, 0–3	546.30	0.57	271	507	5057.80	18.60	2.80	272
22R-3, 0–3	558.80	0.95	72	436	3367.00	10.50	3.04	321
23R-1, 92–94	566.43	0.30	280	470				
23R-1, 104–106	566.55	0.44	204	465				
23R-5, 0–3	571.50	0.29	375	544	17558.00	18.50	3.03	949
24R-2, 0–3	576.70	0.55	178	530	8606.00	22.30	5.20	386
26R-5, 0–3	600.60	0.25	276	532	3266.50	9.50	3.40	344
27R-4, 0–3	608.80	0.20	0	361	1415.00	4.60	0	308
28R-4, 0–3	619.78	0.34	332	534	4507.00	14.50	4.60	311
29R-4, 13–16	628.15	0.48	135	408				
29R-6, 0–3	631.00	0.27	196	424	8403.00	17.10	4.80	491
30R-6, 0–3	640.60	0.46	197	475	1992.00	19.50	8.40	102
31R-4, 0–3	647.30	0.31	422	507	9900.00	20.60	3.20	481
32R-3, 32–34	655.73	0.08	1025	525				
32R-6, 0–3	659.90	0.30	143	457	4082.70	16.50	4.60	247
33R-2, 94–98	664.56	0.37	118	427				
33R-6, 0–3	669.60	0.23	160	397	1303.00	13.40	6.00	97
34R-6, 0–3	679.30	0.52	165	415	955.50	16.60	6.30	58
35R-5, 0–3	687.40	0.47	46	341	1277.60	16.10	6.70	79
36R-3, 0–3	694.10	0.19	173	339	52815.00	30.20	4.80	1749
37R-5, O-3	706.80	0.54	170	507	1435.90	23.30	9.20	62
38R-3, 0–3	713.50	0.52	51	484	9689.00	40.50	12.30	239
39R-2, 147–150	723.20	0.08	462	506	63340.00	33.30	4.80	1902
39R-4, 24–27	724.95	0.04	1275	505				
40R-4, 0–3	734.40	0.20	230	472	8693.00	21.30	4.90	408
41R-5, 0–3	745.60	0.19	273	482	1798.00	9.10	2.90	198
42R-3, 0–3	752.30	0.10	390	454	21091.00	22.00	3.20	959
43R-3, 0–3	761.50	0.14	392	420	3476.00	7.18	0	484
44R-2, 0–3	769.60	0.06	666	378	31077.00	19.50	2.10	1594
45R-3, 0–3	780.70	0.11	1054	536	42829.00	23.20	2.10	1846
46R-1, 0–3	787.40	0.09	1255	515	6886.40	9.80	Trace	703
47R-1, 0–3	796.90	0.03	1300	514	60444.30	27.80	2.20	2174
48R-5, 0–3	812.60	0.03	1566	517	32196.30	22.50	Trace	1431
49R-1, 52–54	816.03	0	0	331				
49R-5, 0–3	821.50	0	0	298	8975.90	21.10	0	425
50R-1, 2–4	825.23	0.04	1475	443				
50R-2, 0–3	826.70	0	0	373	53242.70	36.50	Trace	1459
50R-3, 55–57	828.76	0.04	1475	357				
51R-CC, 0–3	844.50	0.02	1300	345	5047.00	11.30	0	447
52R-1, 0–3	844.60	0	0	306	1807.00	6.30	0	287
53R-2, 0–3	855.80	0.01	2000	539	5840.00	13.50	0	433
54R-3, 0–3	857.00	0	0	330	7134.00	15.60	0	457
55R-3, 0–3	876.70	0.04	1250	524	7064.00	13.40	0	527
56R-5, 0–3	889.40	0	0	306	76578.00	18.50	0	4139
57R-1, 17–19	893.28	0	0	422	61575.00	22.40	0	2749
58R-4, 147–150	908.38	0.01	1500	414	9399.00	16.60	0	566
59R-6, 0–3	919.50	0.02	1550	584	6333.70	7.00	0	905
60R-3, 0–3	924.70	0	0	387	9543.50	22.40	0	426
61R-3, 147–150	935.87	0	0	350	35096.70	21.90	0	1603
62R-3, 0–3	944.00	0	0	454	56020.60	19.70	0	2844
63R-6, 0–3	957.80	0.03	1300	457	48684.80	17.40	0	2798
64R-2, 0–3	961.50	0	0	355	9660.20	16.30	0	593
65R-5, 0–3	975.70	0.01	2100	477	50384.40	14.30	0	3523
66R-3, 0–3	982.40	0.02	1800	484	9728.70	11.00	0	884
67R-6, 147–150	997.98	0	0	465	33546.00	13.90	0	2413
68R-5, 0–3	1004.70	0	0	326	6668.00	8.80	0	758
69R-4, 149–150	1014.28	0.08	1225	532				
69R-5, 0–3	1014.30	0.07	1285	531	4714.00	7.20	0	655
70R-1, 147–150	1019.10	0.01	1700	304	6471.00	6.20	0	1044
71R-2, 0–3	1030.20	0	0	455	2799.80	3.30	0	848
72R-2, 0–3	1038.40	0.02	1800	416	1627.40	2.60	0	626

Note: TOC = total organic carbon and HI = hydrogen index.

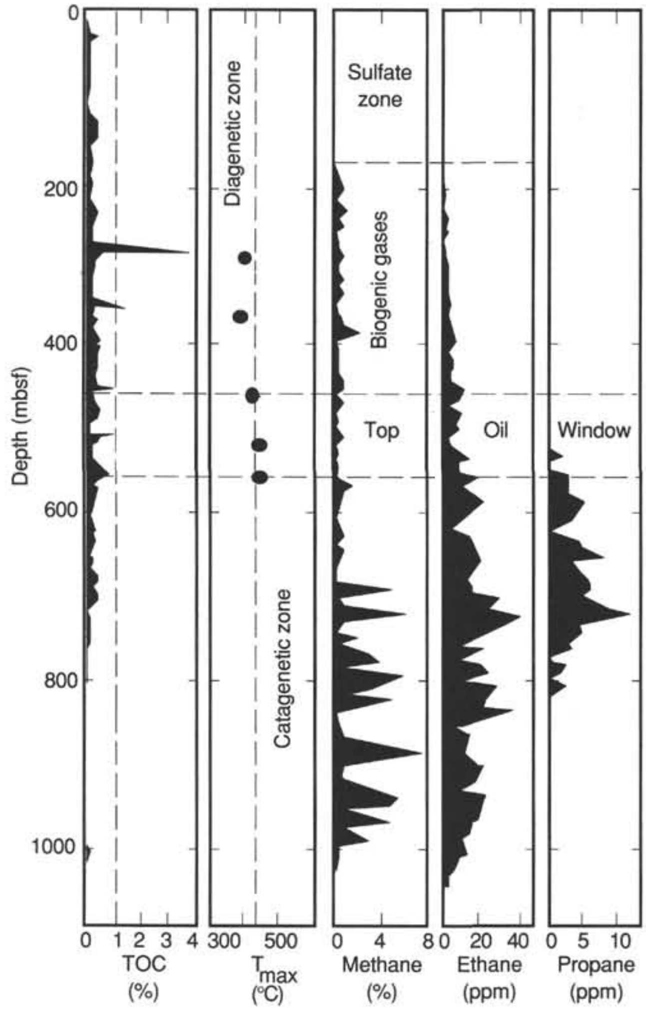

Figure 50. Total organic content, maturity of organic matter, and hydrocarbon composition of headspace gas samples, Site 768.

The thermal maturity of the organic matter was also evaluated in these five organic-rich sediments. The pyrolysis temperatures (T_{max}) for samples from 287.36 and 357.33 mbsf are below 430°C (Table 9), indicating that the organic matter in this depth range is thermally immature (zone of diagenesis, Fig. 50).

Deeper in the hole, the T_{max} values (430°C–436°C) of samples from 455.75, 511.93, and 558.8 mbsf show that the organic matter of these sediments has reached the catagenetic stage (top "Oil Window"). The maturity is high enough to generate thermogenic hydrocarbons (Tissot and Welte, 1984). This interpretation is supported by the observed onset of propane generation between 450 and 560 mbsf (Fig. 50).

Hydrocarbon Gases

Background concentrations were observed for headspace gases between 0 and 180 mbsf (Table 10 and Fig. 50), in which there is sulfate in interstitial waters (see "Sediment Inorganic Geochemistry" section, this chapter). Significant gas concentrations were recognized below 180 mbsf (Table 10 and Fig. 50). Methane and ethane are the only components up to a depth of 521 mbsf. This observation and the fact that methane is the dominant component, exceeding the ethane concentration by several orders of magnitude (Table 10), suggest a bacterial origin of the light hydrocarbons (Bernard, 1979; Claypool and Kvenvolden, 1983) between 180 and 521 mbsf. This interpretation is supported by the fact that the sulfate concentration (see "Sediment Inorganic Geochemistry" section, this chapter) reaches its minimum at 180 mbsf, which enables the bacteria to start significant hydrocarbon generation below this depth.

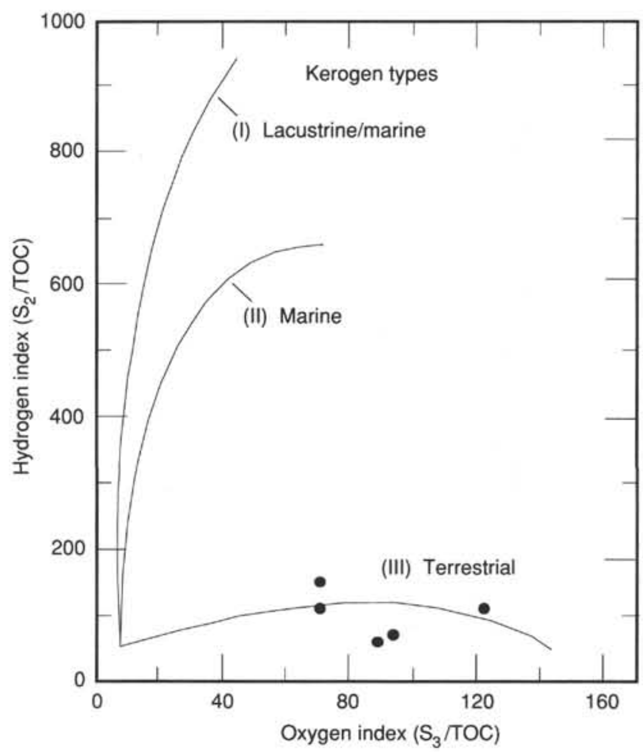

Figure 51. Kerogen classification of organic-rich samples, Site 768.

Although methane concentrations show no trend with depth between 180 and 694 mbsf, ethane concentrations increase with increasing depth (Fig. 50). This might be attributed to early thermal generation of hydrocarbons with increasing subsurface temperature and increasing maturity of the organic matter. This interpretation is supported by the observed onset of propane generation at 521 mbsf and a parallel increase of ethane and propane concentrations with depth and temperature.

The first appearance of propane in headspace gases marking the onset of significant thermogenic hydrocarbon generation is in accordance with the maturity of the organic matter determined by Rock-Eval pyrolysis. Given the molecular composition, gases below a depth of 521 mbsf can be classified as a mixture of hydrocarbons of biogenic and thermogenic origins (cf. Bernard, 1979; Claypool and Kvenvolden, 1983), with methane dominating over ethane and propane.

Below 690 mbsf methane concentrations are highly variable and reach peak concentrations of more than 70,000 ppm. These high amounts of gases cannot be explained by *in-situ* generation from the organic material of the sediments because TOC values are generally low in the siliciclastic sediments (<0.5%) and the pyroclastic sediments are lean in organic matter (Fig. 50 and Table 9). It is assumed that light hydrocarbons migrated into the turbidites and pyroclastic rocks by lateral and downward migration because no source rock was detected within the basin between the pyroclastic rocks and basement. The driving force for such a migration could have been water convection initialized by heat flow from the basement.

Given the molecular composition, gases between 690 and 830 mbsf are of a mixed biogenic and thermogenic origin because methane is the dominating component, but significant amounts of ethane and propane are still detectable (Fig. 50).

This preliminary explanation has to be verified by shore-based stable isotope analyses of methane, ethane, and propane. Below 830 mbsf only methane and ethane have been observed. Given the molecular composition, it is difficult to decide if these gases are biogenic and/or thermogenic.

Analyses of vacutainer gases in Hole 768C revealed higher gas concentrations than the analyses of headspace gases (Table 11 and Fig. 52). This is caused by the different sampling procedures. Also, the C_1/C_2 ratios show higher values for the vacutainer samples than for the headspace gas samples (Tables 10 and 11). This can be explained by a preferential degassing of methane from sediments before sealing the sediment in a glass flask, which will result in lower methane values for headspace gas samples than for hydrocarbons from gas pockets.

Generally, similar trends for headspace and vacutainer gases are observed between 430 and 700 mbsf (Figs. 50 and 52). Additional analyses on aliquots of vacutainer gases on the HP gas chromatograph revealed small amounts of isobutane between 517 and 730 mbsf. *N*-butane was observed between 677 and 703. Although butane analyses are only qualitative because of technical problems, these results verify the interpretation of thermogenic gas generation below 500 mbsf.

The drastic decrease of gas concentrations in vacutainers below 700 mbsf (Fig. 52) is a result of the poor sampling conditions. These concentrations do not reflect the actual gas amount in the sediments.

Table 11. Molecular composition of vacutainer gas samples from Site 768 (Carle GC).

Core, section, interval (cm)	Depth (mbsf)	Methane (ppm)	Ethane (ppm)	Propane (ppm)	C_1/C_2
124-768C-					
7R-2, 130	413.64	496.00	0	0	
7R-4, 5	413.90	176650.00	ND	ND	
9R-2, 43	432.13	361423.00	146.00	0	2475.50
11R-3, 69	453.29	832699.50	404.90	0	2056.56
12R-1, 125	460.44	549330.00	267.30	0	2055.11
13R-2, 103	471.40	779090.00	412.00	3.20	1891.00
13R-2, 103	471.40	887266.90	480.90	3.70	1845.01
14R-1, 60	479.10	169052.00	59.10	0	2860.44
15R-2, 40	490.10	193928.00	84.70	0	2289.59
15R-2, 130	491.00	903878.00	549.20	6.20	1645.81
16R-1, 83	498.73	240559.50	109.90	2.00	2188.89
17R-2, 98	509.98	495266.10	257.40	7.10	1924.11
18R-2, 38	519.08	681645.40	477.80	11.50	1426.63
19R-2, 20	528.60	212412.90	100.00	3.40	2124.13
20R-3, 23	539.83	901716.20	614.00	23.80	1468.59
22R-1, 120	557.00	633803.00	502.80	34.10	1260.55
23R-4, 113	571.13	540540.00			
24R-1, 38	575.58	12.70	0	0	
24R-1, 123	576.40	41.00	0	0	
26R-4, 32	599.42	500740.00	386.20	31.80	1296.58
27R-4, 2	608.82	526886.00	492.00	46.70	1070.91
28R-5, 56	620.46	532316.00	498.00	47.70	1068.91
29R-2, 21	625.21	540987.00	516.00	50.20	1048.42
30R-2, 122	635.82	706192.60	824.00	85.00	857.03
31R-2, 80	645.10	796367.00	849.20	82.90	937.78
32R-2, 104	654.94	598831.10	648.20	65.00	923.84
33R-5, 11	668.21	651716.20	806.00	0.80	808.58
34R-6, 6	679.36	718698.90	951.70	110.70	755.17
35R-5, 15	687.55	721752.60	890.00	94.00	811.00
36R-6, 73	699.33	647769.00	737.50	76.30	878.00
37R-2, 112	703.42	470139.00	605.50	60.90	776.00
38R-2, 90	712.90	148330.00	97.50	9.30	1521.00
39R-1, 80	721.00	42.60	0	0	
40R-2, 56	731.96	205678.00	208.50	20.20	986.50
41R-5, 6	745.66	444.60	0.00	0	
42R-2, 100	751.80	282069.00	352.00	33.50	801.00

Note: ND = no data.

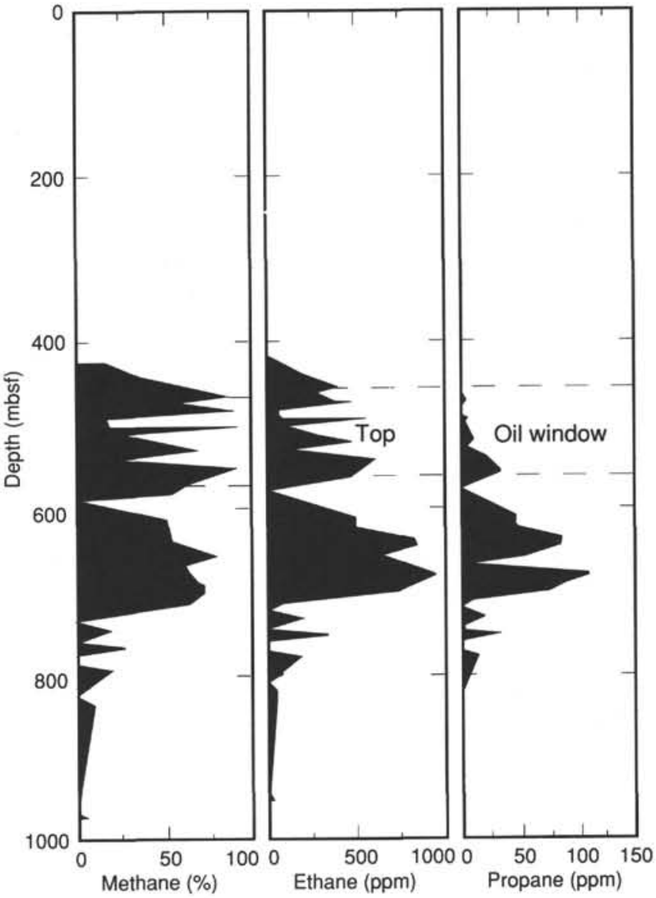

Figure 52. Molecular composition of vacutainer gas samples, Site 768 (Carle GC).

Conclusions

Organic carbon contents of sediments are low (<0.5%) between 0 and 128 mbsf, but they reach higher values between 128 and 720 mbsf with a maximum of 3.98% TOC. At the transition between siliciclastic and pyroclastic rocks between 720 and 800 mbsf, TOC values again decrease. We did not observe any detectable organic carbon within the pyroclastic series.

On the basis of the HI and OI values, the organic matter for the five samples with high TOC values was of terrestrial origin. The maturity of the organic matter is low for the two samples above 400 mbsf, whereas the three samples below 450 mbsf reveal T_{max} values that are related to the onset of thermogenic hydrocarbon generation.

Within the sulfate zone (0–180 mbsf), gas concentrations are low and are classified as background. After sulfate has been depleted at 180 mbsf, significant concentrations of bacterial gases (methane and ethane) were observed. Significant amounts of propane were recognized below 450 mbsf, indicating the onset of thermogenic hydrocarbon generation from kerogens. This corresponds to the measured maturity of the organic matter. Given the molecular composition, gases below 450 mbsf are classified as mixed gases of bio- and thermogenic origin.

High amounts of gaseous hydrocarbons were detected below 720 mbsf within carbon-lean sediments mainly consisting of pyroclastic rocks. This suggests a downward migration of hydrocarbons as no organic-rich layers were detected between basalt basement and pyroclastic rocks. The driving force for a downward migration of hydrocarbons in the basin might have been water convection initialized by heat flow from the basement.

PHYSICAL PROPERTIES

Introduction

The physical properties determined from sediments of Site 768 include bulk density, grain density, porosity, water content, and void ratio (determined by a pycnometer and balance), GRAPE bulk density, compressional wave velocity (measured on discrete samples with a Hamilton Frame apparatus), thermal conductivity, and vane shear strength, as described in the "Explanatory Notes" chapter (this volume).

The lithostratigraphic units referenced in this section are those described in the "Lithostratigraphy" section (this chapter). Velocity and index property values were measured on nearly all of the cores. The GRAPE bulk density measurements were performed to a depth of 209 mbsf in Hole 768B only. Thermal conductivity measurements were made on competent material in Holes 768B and 768C. Vane shear measurements from Hole 768B were obtained to a depth of 77 mbsf. The values of the various physical properties are listed in Tables 12–15, and the variations of these properties with depth are illustrated in Figures 53–58.

Results

Index Properties

The bulk density, grain (or matrix) density, porosity, and water content (dry basis) measurements of the samples from Site 768 are listed in Table 12 and plotted relative to depth in Figure 53. The bulk density data determined on APC cores from Hole 768B by the GRAPE technique are presented in Figure 54. The bulk density values determined from the index tests are compared with the bulk density values from the GRAPE in Figure 55.

The plot of bulk density obtained from the index properties (Fig. 53) shows a pattern of increasing density with depth through Units I and II (0–652 mbsf). Bulk density in Unit I ranges from about 1.3 to 1.4 g/cm^3 at the seafloor to about 1.5–1.6 g/cm^3 at the base of the unit (123 mbsf). Bulk density in Unit II shows more variability with depth and increases to about 2.15–2.3 g/cm^3 at the base of the unit. Bulk density increases at a faster rate in the upper part of the thick-bedded nannofossil marl (Unit 1) than in the claystone/siltstone sequences (Unit II). An inflection point in the bulk density trend is well defined in Figure 54 at a depth of 123 mbsf; it corresponds to the location of the transition from Unit I to Unit II. The rate of bulk density change slows near the bottom of Unit II.

Four samples plotted in Figure 53 have significantly higher bulk densities than the overall pattern of bulk density change with depth (between 2.67 and 2.80 g/cm^3). These points correspond to measurements from thin indurated, carbonate-rich layers.

In the unit below 652 mbsf (Unit III, 652–806 mbsf), the bulk density pattern exhibits increased scatter but shows a negligible increase with depth. Unit III contains variable lithologies of sandstone, siltstone, and claystone with very thick tuff beds and sporadic marlstone. The variability of the sediments manifests itself in the scatter of bulk density values. The bulk density in Unit III varies between 1.95 and 2.30 g/cm^3 with a few points lying outside this range.

Bulk densities show a prominent relative low in Unit IV (806–1004 mbsf). Unit IV is composed exclusively of pyroclastic material. Tuff and pumice have fairly low grain densities (as noted in Fig. 53), and therefore bulk densities reflect the low grain densities. Bulk density reaches a local minimum of 1.95

Table 12. Index property data, Site 768.

Core, section, interval (cm)	Depth (mbsf)	Wet-bulk density (g/cm^3)	Grain density (g/cm^3)	Porosity (%)	Water content (%)	Void ratio
124-768A-						
1H-1, 66–68	0.66	1.33	2.66	85.8	194.2	6.03
1H-2, 75–77	2.25	1.34	2.66	86.1	191.5	6.20
1H-3, 72–74	3.72	1.39	2.76	82.7	156.5	4.78
1H-4, 95–97	5.45	1.36	2.60	81.7	161.6	4.47
1H-5, 40–42	6.40	1.31	2.64	87.8	221.6	7.22
124-768B-						
1H-1, 137–140	1.37	1.32	2.55	85.1	193.3	5.73
1H-2, 75–78	2.25	1.36	2.66	85.6	182.7	5.95
1H-3, 23–26	3.23	1.29	2.62	87.7	227.9	7.13
2H-1, 68–71	4.68	1.34	2.64	86.6	198.0	6.46
2H-2, 111–114	6.61	1.37	2.64	84.6	171.6	5.47
2H-4, 28–31	8.78	1.31	2.44	87.5	216.5	7.02
3H-1, 65–68	14.15	1.31	2.54	85.2	198.0	5.76
3H-4, 69–72	18.69	1.37	2.51	81.6	156.2	4.45
3H-6, 51–54	21.51	1.40	2.46	78.5	135.3	3.65
4H-1, 40–43	23.40	1.39	2.65	81.8	151.7	4.50
4H-4, 66–69	28.16	1.37	2.71	85.7	178.5	6.01
4H-6, 39–42	30.89	1.34	2.47	83.1	173.9	4.90
5H-2, 98–100	34.98	1.42	2.59	78.7	132.2	3.70
5H-4, 61–63	37.61	1.36	2.80	86.0	182.6	6.13
5H-5, 75–77	39.25	1.39	2.74	83.2	159.3	4.94
6H-1, 103–105	43.03	1.41	2.56	77.6	128.6	3.46
6H-3, 69–71	45.69	1.43	2.71	79.9	133.0	3.97
6H-4, 37–39	46.87	1.42	2.73	81.2	141.6	4.32
6H-6, 105–107	50.55	1.39	2.60	81.1	147.7	4.29
7H-2, 45–47	53.45	1.36	2.60	81.0	157.6	4.25
7H-4, 63–65	56.63	1.47	2.68	76.3	113.1	3.22
7H-6, 60–62	59.60	1.51	2.67	74.0	100.3	2.85
8H-1, 82–84	61.82	1.54	2.59	69.7	86.3	2.30
8H-3, 99–101	64.99	1.42	2.63	79.5	135.2	3.87
8H-4, 25–27	65.75	1.43	2.60	78.4	127.4	3.64
8H-6, 66–68	69.16	1.49	2.69	75.7	107.8	3.11
9H-1, 63–65	71.13	1.43	2.69	78.3	127.1	3.61
9H-4, 75–77	75.75	1.45	2.68	77.7	121.9	3.48
9H-6, 67–69	78.67	1.46	2.75	78.1	120.5	3.57
10H-1, 80–82	80.80	1.48	2.57	73.4	104.1	2.77
10H-4, 75–77	85.25	1.55	2.65	70.9	87.8	2.44
10H-6, 84–86	88.34	1.47	2.71	76.8	115.4	3.31
11H-1, 77–79	90.27	1.44	2.63	77.0	122.1	3.35
11H-3, 83–85	93.33	1.57	2.58	69.1	82.5	2.24
11H-5, 73–75	96.23	1.53	2.56	70.9	90.2	2.43
12H-1, 71–73	99.71	1.43	2.46	81.0	139.4	4.26
12H-3, 71–73	102.71	1.56	2.67	67.7	80.0	2.09
12H-5, 60–63	105.60	1.54	2.77	74.1	97.5	2.85
12H-7, 52–54	108.52	1.54	2.70	80.4	114.5	4.11
13H-1, 47–49	108.97	1.48	2.71	77.0	113.6	3.34
13H-4, 103–106	114.03	1.58	2.63	72.0	88.1	2.57
13H-6, 42–44	116.42	1.58	2.73	72.3	88.4	2.61
13H-7, 48–51	117.98	1.58	2.77	74.5	93.7	2.93
14H-1, 82–84	118.82	1.52	2.58	73.1	96.8	2.71
14H-3, 9–12	121.09	1.51	2.61	76.0	106.6	3.17
14H-5, 74–77	124.74	1.53	2.64	77.1	107.6	3.38
14H-6, 29–31	125.79	1.60	2.79	75.8	94.6	3.13
15H-1, 41–43	127.91	1.51	2.63	77.3	110.7	3.40
15H-3, 68–70	131.18	1.55	2.59	74.5	97.2	2.92
15H-5, 63–65	134.13	1.55	2.59	75.5	99.6	3.08
16H-2, 66–69	139.16	1.63	2.60	66.2	71.3	1.96
16H-5, 55–58	143.55	1.67	2.72	65.7	67.6	1.92
16H-6, 71–74	145.21	1.60	2.55	67.3	75.8	2.06
17H-2, 59–51	148.59	1.62	2.74	68.8	76.8	2.21
17H-4, 97–100	151.97	1.63	2.66	68.4	75.7	2.16
17H-6, 71–74	154.71	1.62	2.77	70.8	81.0	2.42
18H-2, 85–87	158.35	1.66	2.79	67.2	71.0	2.05
18H-4, 82–84	161.32	1.61	2.71	69.2	79.0	2.25
18H-6, 75–77	164.25	1.63	2.78	68.7	76.2	2.19
19H-2, 60–62	167.60	1.67	2.77	65.9	67.6	1.94
19H-5, 78–80	172.28	1.70	2.66	62.3	60.2	1.65
20H-1, 68–70	174.48	1.70	2.69	63.0	61.0	1.70
20H-4, 76–78	179.06	1.69	2.71	64.5	64.0	1.82
20H-6, 89–91	182.19	1.84	2.77	73.6	69.8	2.79
21H-1, 95–97	184.25	1.68	2.67	64.2	64.6	1.79
21H-3, 64–66	186.94	1.68	2.70	64.5	64.9	1.82
12H-6, 85–87	191.65	1.78	2.77	61.2	54.5	1.58
22H-1, 87–89	193.67	1.81	2.76	58.2	48.9	1.39
22H-3, 91–93	196.71	1.79	2.78	60.2	52.4	1.51

Table 12 (continued).

Core, section, interval (cm)	Depth (mbsf)	Wet-bulk density (g/cm^3)	Grain density (g/cm^3)	Porosity (%)	Water content (%)	Void ratio
124-768B-						
22H-5, 84-86	199.64	1.75	2.67	59.9	54.2	1.49
23H-1, 66-68	201.66	1.74	2.74	61.8	57.3	1.62
23H-3, 70-72	204.70	1.93	2.76	71.2	60.8	2.47
23H-5, 82-84	207.82	1.88	2.75	53.8	41.4	1.17
26X-1, 68-70	219.98	1.79	2.69	59.0	51.1	1.44
26X-3, 44-46	222.74	1.79	2.75	60.5	52.8	1.53
27X-1, 95-97	229.85	1.82	2.74	57.4	47.8	1.35
27X-2, 137-139	231.77	1.86	2.90	58.6	47.6	1.41
27X-3, 80-82	232.70	2.05	2.71	44.2	28.4	0.79
28X-1, 60-62	239.20	1.84	2.69	56.7	46.1	1.31
28X-3, 69-71	242.29	1.88	2.76	56.5	44.6	1.30
28X-5, 43-45	245.03	1.77	2.74	62.2	56.4	1.65
29X-1, 85-87	249.05	1.81	2.76	58.3	49.2	1.40
29X-3, 77-79	251.97	1.89	2.94	42.3	29.7	0.73
29X-4, 67-69	253.37	2.04	2.62	41.3	26.2	0.70
30X-1, 104-106	258.84	1.90	2.68	51.3	38.2	1.05
30X-2, 65-67	259.95	1.86	2.94	43.1	31.1	0.76
30X-3, 29-31	261.09	1.86	2.64	53.3	41.6	1.14
31X-1, 33-35	267.83	1.78	2.84	59.8	52.6	1.49
31X-2, 43-46	269.43	1.81	2.65	57.8	48.6	1.37
31X-3, 33-35	270.83	1.86	2.63	56.4	45.2	1.29
32X-1, 126-129	278.46	1.89	2.77	54.1	41.6	1.18
32X-2, 10-12	278.80	1.90	2.75	54.6	41.8	1.20
32X-3, 10-12	280.30	1.92	2.74	52.8	39.2	1.12
33X-1, 62-64	287.42	1.93	2.68	51.2	37.3	1.05
33X-2, 69-72	288.99	1.92	2.70	52.1	38.5	1.09
33X-3, 60-62	290.40	1.91	2.68	52.7	39.6	1.12
34X-1, 57-60	296.97	1.96	2.75	50.2	35.7	1.01
34X-2, 59-61	298.49	1.98	2.78	50.4	35.2	1.02
34X-3, 16-18	299.56	1.97	2.69	48.1	33.4	0.93
35X-1, 97-100	307.07	1.94	2.70	49.7	35.5	0.99
35X-2, 74-76	308.34	1.99	2.71	50.0	34.6	1.00
35X-3, 27-29	309.37	2.03	2.72	47.6	31.7	0.91
36X-1, 33-36	316.13	1.88	2.79	57.5	45.6	1.35
36X-2, 95-97	318.25	1.92	2.67	51.7	38.1	1.07
36X-3, 29-31	319.09	1.96	2.75	52.1	37.4	1.09
37X-1, 42-45	325.92	1.91	2.77	53.0	39.7	1.13
37X-2, 77-79	327.77	1.95	2.77	52.7	38.4	1.12
37X-CC, 42-44	329.98	1.98	2.58	53.2	37.9	1.14
38X-1, 41-44	335.51	1.95	2.72	50.1	35.8	1.01
38X-3, 67-69	338.77	2.03	2.66	44.3	28.8	0.80
38X-4, 84-86	340.44	2.01	2.73	47.0	31.4	0.89
39X-1, 53-55	345.33	2.02	2.72	45.1	29.7	0.82
39X-2, 15-17	346.45	1.92	2.81	53.5	40.0	1.15
39X-2, 84-86	347.14	1.97	2.76	50.6	35.8	1.03
39X-3, 95-97	348.75	1.99	2.75	48.2	33.0	0.93
39X-4, 15-17	349.45	2.00	2.74	48.4	33.0	0.94
124-768C-						
1R-1, 13-15	353.33	2.04	2.76	47.2	31.1	0.90
1R-3, 108-110	357.28	2.10	2.82	46.5	29.3	0.87
1R-4, 91-93	358.61	2.04	2.74	45.2	29.4	0.82
2R-1, 30-32	363.20	2.16	2.77	44.4	26.6	0.80
2R-3, 80-82	366.70	2.02	2.78	48.0	32.1	0.92
3R-1, 67-70	373.07	2.07	2.69	47.4	30.6	0.90
3R-CC, 13-16	373.35	2.73	2.85	16.0	6.4	0.19
4R-1, 119-121	383.29	2.07	2.75	44.3	28.1	0.80
5R-1, 113-116	392.93	1.99	2.76	48.1	32.8	0.93
5R-2, 107-109	394.37	2.05	2.78	45.9	29.7	0.85
5R-3, 124-126	396.04	2.06	2.73	45.6	29.3	0.84
6R-1, 84-86	402.24	2.05	2.70	49.3	32.7	0.97
6R-2, 31-33	403.21	1.83	2.66	60.5	51.1	1.53
6R-3, 54-56	404.94	2.00	2.80	52.7	37.0	1.12
7R-1, 86-88	411.96	2.05	2.66	38.4	23.8	0.62
7R-4, 67-69	416.27	2.22	2.82	48.6	29.0	0.95
7R-5, 28-30	417.38	2.08	2.68	45.4	28.7	0.83
8R-1, 109-111	421.79	2.00	2.75	47.3	31.9	0.90
8R-2, 101-103	423.21	1.91	2.68	48.8	35.5	0.95
8R-3, 73-75	424.43	1.96	2.69	45.4	31.1	0.83
9R-1, 64-66	430.84	2.07	2.70	42.7	26.9	0.75
9R-2, 94-96	432.64	2.08	2.69	43.4	27.2	0.77
10R-1, 52-54	440.42	2.11	2.74	42.2	25.7	0.73
10R-2, 82-84	442.22	2.17	2.77	40.5	23.6	0.68
10R-3, 105-107	443.95	2.14	2.71	40.3	23.9	0.67
11R-2, 56-58	451.66	2.10	2.74	42.5	26.1	0.74
11R-4, 44-46	454.54	1.77	2.67	59.5	52.4	1.47

Table 12 (continued).

Core, section, interval (cm)	Depth (mbsf)	Wet-bulk density (g/cm^3)	Grain density (g/cm^3)	Porosity (%)	Water content (%)	Void ratio
124-768C-						
11R-5, 90-92	456.50	1.88	2.75	56.0	43.9	1.27
12R-1, 74-76	459.94	2.11	2.72	41.0	24.8	0.70
13R-1, 76-78	469.66	2.10	2.75	43.0	26.5	0.75
13R-2, 28-30	470.68	2.16	2.70	38.6	22.4	0.63
13R-3, 79-81	472.69	2.16	2.76	42.4	25.2	0.74
14R-2, 53-55	480.53	2.12	2.75	39.2	23.3	0.65
14R-3, 50-52	482.00	2.19	2.75	39.5	22.6	0.65
14R-4, 86-88	483.86	2.11	2.66	40.0	24.0	0.67
15R-1, 81-83	489.01	2.10	2.70	41.6	25.5	0.71
15R-3, 73-75	491.93	1.98	2.63	43.7	29.2	0.78
15R-4, 36-38	493.06	2.09	2.68	41.7	25.7	0.72
17R-1, 135-137	508.85	2.01	2.69	44.5	29.3	0.80
17R-2, 115-117	510.15	1.90	2.69	52.3	39.4	1.10
17R-3, 66-68	511.16	1.97	2.69	46.1	31.5	0.85
17R-4, 111-113	513.11	1.95	2.68	46.4	32.2	0.87
18R-2, 112-114	519.82	2.03	2.71	48.4	32.3	0.94
18R-4, 44-47	522.14	2.13	2.72	42.9	26.0	0.75
19R-1, 109-111	527.99	2.09	2.70	40.4	24.7	0.68
19R-2, 4-6	528.44	2.16	2.72	44.7	26.9	0.81
20R-1, 116-118	537.76	2.20	2.68	44.3	26.0	0.79
20R-2, 96-98	539.06	2.19	2.78	40.8	23.6	0.69
20R-3, 38-40	539.98	2.15	2.58	40.3	23.8	0.67
21R-1, 95-97	547.25	2.15	2.73	49.0	30.5	0.96
21R-CC, 21-23	548.03	2.80	2.71	6.8	2.6	0.07
22R-1, 31-33	556.11	2.75	2.72	6.3	2.4	0.07
22R-1, 58-60	556.38	2.19	2.82	43.7	25.7	0.78
23R-1, 5-7	565.55	2.67	2.74	15.2	6.2	0.18
23R-2, 39-41	567.39	2.14	2.82	44.2	26.8	0.79
24R-1, 69-70	575.89	2.16	2.81	42.1	25.0	0.73
24R-3, 77-78	578.97	2.06	2.71	46.6	30.1	0.87
24R-4, 34-36	580.04	2.17	2.68	45.5	27.4	0.84
26R-1, 56-58	595.16	2.22	2.80	42.7	24.5	0.74
26R-3, 45-47	598.05	2.21	2.65	35.9	20.0	0.56
26R-5, 41-43	601.01	2.31	2.72	35.9	19.0	0.56
27R-1, 36-38	604.66	2.19	2.75	39.7	22.9	0.66
27R-2, 83-85	606.63	2.25	2.72	34.1	18.3	0.52
27R-3, 113-115	608.43	2.25	2.65	32.3	17.3	0.48
28R-1, 37-39	614.27	2.13	2.70	39.8	23.6	0.66
28R-3, 45-47	617.35	2.20	2.73	38.2	21.7	0.62
28R-5, 59-61	620.49	2.16	2.74	40.5	23.8	0.68
29R-2, 47-49	625.47	2.19	2.70	36.5	20.6	0.57
29R-4, 25-27	628.25	2.15	2.80	42.5	25.5	0.74
29R-6, 120-122	632.20	2.20	2.65	37.3	21.1	0.60
30R-1, 100-102	634.10	2.25	2.83	37.9	20.8	0.61
30R-3, 117-119	637.27	2.32	2.71	59.4	35.6	1.46
30R-6, 91-93	641.51	2.14	2.77	43.3	26.1	0.76
31R-1, 39-41	643.19	2.16	2.70	40.5	23.7	0.68
31R-3, 44-46	646.24	2.05	2.69	46.8	30.5	0.88
31R-4, 91-93	648.21	2.06	2.64	45.4	29.1	0.83
32R-1, 38-40	652.78	1.68	2.31	50.6	44.4	1.02
32R-3, 10-12	655.05	1.77	2.54	54.5	45.9	1.20
32R-3, 144-146	656.84	1.96	2.59	49.4	34.9	0.98
32R-5, 66-68	659.06	2.32	2.78	35.5	18.6	0.55
33R-2, 73-75	664.33	2.12	2.73	40.0	23.9	0.67
33R-4, 86-88	667.46	2.20	2.75	38.7	22.1	0.63
33R-5, 53-55	668.63	2.27	2.80	38.5	21.0	0.63
34R-1, 85-87	672.65	2.13	2.69	40.6	24.2	0.68
34R-3, 55-57	675.35	2.23	2.71	36.4	20.1	0.57
34R-6, 71-73	680.01	2.21	2.64	37.2	20.8	0.59
35R-1, 135-137	682.75	2.20	2.72	36.3	20.4	0.57
35R-3, 112-114	685.52	2.23	2.78	38.2	21.3	0.62
35R-5, 69-71	688.09	2.29	2.70	31.9	16.6	0.47
36R-1, 134-136	692.44	2.12	2.68	42.8	26.1	0.75
36R-3, 73-75	694.83	1.93	2.47	48.8	34.9	0.95
36R-6, 25-27	698.85	2.48	2.83	30.7	14.5	0.44
37R-1, 131-133	702.11	2.19	2.71	35.8	20.1	0.56
37R-3, 134-136	705.14	2.06	2.78	45.9	29.6	0.85
37R-5, 100-102	707.80	2.28	2.71	32.9	17.4	0.49
38R-1, 61-63	711.11	2.18	2.66	36.9	21.1	0.59
38R-2, 64-66	712.64	2.16	2.69	40.2	23.6	0.67
38R-3, 124-126	714.74	2.23	2.81	42.7	24.4	0.74
39R-2, 52-54	722.22	2.18	2.68	39.2	22.7	0.65
39R-3, 100-102	724.20	1.96	2.58	50.7	36.1	1.03
39R-4, 67-69	725.37	1.99	2.62	50.6	35.3	1.02
40R-1, 78-80	730.68	2.10	2.69	37.8	22.6	0.61
40R-1, 129-131	731.19	2.23	2.71	31.8	17.1	0.47
40R-2, 48-50	731.88	2.56	2.70	27.6	12.4	0.38

Table 12 (continued).

Core, section, interval (cm)	Depth (mbsf)	Wet-bulk density (g/cm³)	Grain density (g/cm³)	Porosity (%)	Water content (%)	Void ratio
124-768C-						
40R-4, 92–94	735.32	2.08	2.69	46.3	29.6	0.86
41R-3, 60–62	743.20	2.18	2.76	39.4	22.7	0.65
41R-4, 87–89	744.97	1.97	2.67	47.9	33.2	0.92
41R-6, 56–58	747.66	2.11	2.79	40.7	24.6	0.69
42R-1, 33–35	749.63	2.20	2.75	37.0	20.8	0.59
42R-3, 43–45	752.73	2.20	2.76	38.0	21.6	0.61
43R-1, 84–86	759.34	2.18	2.74	38.1	21.9	0.62
43R-3, 23–25	761.73	2.35	2.72	58.0	33.8	1.38
44R-1, 103–105	769.13	2.24	2.75	35.1	19.1	0.54
44R-3, 89–91	771.99	2.17	2.69	37.7	21.7	0.61
45R-1, 129–131	778.99	2.21	2.75	36.9	20.6	0.59
45R-3, 39–41	781.09	2.25	2.72	36.8	20.1	0.58
46R-1, 107–109	788.47	2.25	2.75	35.3	19.2	0.55
46R-2, 27–29	789.17	2.23	2.59	31.6	17.0	0.46
47R-1, 111–112	798.01	2.19	2.63	35.3	19.7	0.54
48R-1, 111–113	807.71	2.09	2.52	33.6	19.7	0.51
48R-2, 27–29	808.37	2.11	2.51	31.7	18.2	0.46
48R-4, 83–85	811.93	2.11	2.52	33.0	19.0	0.49
49R-3, 7–9	818.57	1.84	2.30	38.5	27.2	0.63
49R-6, 129–131	824.29	2.14	2.52	39.8	23.5	0.66
50R-1, 48–50	825.68	1.94	2.44	49.3	35.3	0.97
50R-2, 17–19	286.87	2.06	2.44	37.3	22.8	0.59
50R-3, 69–71	828.89	2.28	2.65	32.4	17.0	0.48
51R-2, 24–26	836.64	1.92	2.38	42.4	29.3	0.74
51R-2, 104–106	837.44	2.16	2.51	34.5	19.6	0.53
51R-4, 92–94	840.32	2.21	2.58	33.3	18.2	0.50
52R-1, 110–112	845.70	2.22	2.65	33.1	18.1	0.50
52R-5, 129–131	851.89	2.08	2.45	37.3	22.5	0.59
53R-2, 95–97	856.75	2.16	2.61	33.5	18.9	0.50
53R-3, 112–114	858.42	2.21	2.59	34.1	18.8	0.52
54R-1, 20–22	864.20	2.01	2.35	37.2	23.4	0.59
54R-3, 49–51	867.49	2.22	2.62	38.5	21.7	0.63
55R-2, 53–55	875.73	2.11	2.59	35.7	21.0	0.56
55R-3, 118–120	877.88	2.05	2.53	39.6	24.7	0.66
56R-1, 19–21	883.59	1.97	2.31	30.2	18.6	0.43
56R-2, 11–13	885.01	1.98	2.41	36.3	23.1	0.57
56R-4, 60–62	888.50	2.02	2.38	33.4	20.4	0.50
58R-1, 22–24	902.62	1.94	2.28	31.6	20.0	0.46
58R-2, 35–37	904.25	2.02	2.34	28.6	16.9	0.40
58R-4, 57–59	907.47	2.00	2.28	27.1	16.1	0.37
59R-1, 73–75	912.73	1.96	2.34	32.5	20.5	0.48
59R-4, 16–18	916.66	1.99	2.37	31.1	19.1	0.45
59R-5, 16–18	918.16	1.97	2.34	32.5	20.4	0.48
60R-3, 97–99	925.67	1.99	2.33	30.7	18.8	0.44
60R-6, 69–71	929.89	2.01	2.48	37.5	23.7	0.60
61R-2, 125–127	934.15	2.01	2.37	29.6	17.8	0.42
61R-4, 144–146	937.34	2.04	2.41	31.9	19.1	0.47
62R-2, 22–24	924.72	2.09	2.48	33.3	19.5	0.50
62R-4, 54–56	946.04	2.04	2.44	33.0	19.8	0.49
63R-1, 145–147	951.75	2.15	2.44	41.3	24.4	0.70
63R-4, 22–24	955.02	2.07	2.37	35.9	21.6	0.56
64R-1, 54–56	960.54	2.16	2.50	35.0	19.9	0.54
64R-2, 124–126	962.74	2.14	2.44	34.3	19.6	0.52
65R-2, 36–38	971.56	2.11	2.58	37.4	22.2	0.60
65R-5, 83–85	976.53	2.05	2.41	36.9	22.6	0.58
66R-2, 11–13	981.01	2.05	2.38	33.4	20.1	0.50
66R-3, 108–110	983.48	2.05	2.33	32.8	19.6	0.49
66R-4, 43–45	984.33	2.07	2.34	32.3	19.0	0.48
67R-5, 32–34	995.32	2.06	2.42	34.6	20.8	0.53
68R-1, 32–34	999.02	2.19	2.48	32.8	18.1	0.49
68R-5, 108–110	1106.78	2.12	2.39	30.0	17.0	0.43
69R-2, 88–90	1010.68	2.03	2.33	27.6	16.1	0.38
69R-4, 30–32	1013.10	2.09	2.38	26.8	15.1	0.37
70R-1, 60–62	1018.20	2.23	2.65	29.3	15.6	0.42
70R-2, 61–63	1019.71	2.11	2.37	23.9	13.1	0.31
70R-3, 69–71	1021.29	2.08	2.46	17.7	9.5	0.22
70R-4, 55–57	1022.65	2.12	2.60	24.1	13.2	0.32
71R-1, 106–108	1028.26	2.28	2.60	25.1	12.8	0.34
71R-3, 134–136	1031.54	2.08	2.37	29.7	17.2	0.42
71R-4, 99–101	1032.69	2.05	2.41	30.6	18.0	0.44
72R-2, 8–10	1038.48	2.35	2.80	32.5	16.5	0.48
74R-2, 37–39	1058.12	2.40	2.66	19.9	9.3	0.25
75R-2, 45–47	1067.85	2.44	2.74	26.1	12.3	0.35
76R-1, 134–137	1076.94	2.45	2.76	25.8	12.1	0.35
77R-2, 52–54	1082.56	2.81	2.94	30.2	12.4	0.43
78R-1, 27–29	1085.87	2.33	2.61	20.7	10.0	0.26
79R-1, 38–40	1090.98	2.35	2.62	21.7	10.4	0.28

Table 12 (continued).

Core, section, interval (cm)	Depth (mbsf)	Wet-bulk density (g/cm³)	Grain density (g/cm³)	Porosity (%)	Water content (%)	Void ratio
124-768C-						
80R-1, 77–79	1096.37	2.32	2.60	22.4	11.0	0.29
81R-1, 19–21	1100.79	2.32	2.60	23.6	11.6	0.31
82R-2, 17–19	1107.22	2.32	2.61	23.5	11.6	0.31
83R-1, 137–139	1111.97	2.35	2.84	10.3	4.7	0.12
84R-2, 93–95	1118.03	2.37	2.57	18.4	8.6	0.23
85R-1, 37–39	1120.97	2.50	2.67	9.6	4.1	0.11
86R-1, 46–48	1127.06	2.55	2.79	25.7	11.5	0.35
87R-1, 37–39	1136.67	2.48	2.67	21.8	9.9	0.28
88R-1, 28–30	1146.28	2.47	2.62	14.6	6.4	0.17
88R-2, 114–116	1148.46	2.58	2.79	3.9	1.6	0.04
89R-1, 77–79	1156.47	2.77	2.81	17.2	6.8	0.21
89R-2, 5–7	1157.25	2.60	2.65	0.7	0.3	0.01
89R-4, 50–52	1160.12	2.75	2.74	5.4	2.1	0.06
90R-2, 59–61	1167.20	2.66	2.76	8.7	3.5	0.10
90R-3, 50–52	1168.41	2.81	2.76	13.5	5.2	0.16
90R-5, 72–74	1171.49	2.83	2.77	11.6	4.4	0.13
90R-7, 104–106	1174.12	2.82	2.74	12.2	4.6	0.14
91R-1, 32–34	1175.22	2.74	2.74	4.5	1.7	0.05
92R-2, 22–24	1186.17	2.78	2.80	3.4	1.3	0.04
92R-3, 135–137	1188.55	2.75	2.76	3.8	1.4	0.04
93R-3, 60–62	1195.05	2.59	2.71	14.1	5.9	0.16
94R-1, 90–92	1201.60	2.62	2.72	10.3	4.2	0.12
95R-1, 24–28	1210.64	2.50	2.75	20.9	9.4	0.26
96R-3, 126–128	1244.13	2.67	2.76	11.5	4.6	0.13
97R-3, 46–48	1232.92	2.68	2.65	8.0	3.1	0.09
98R-1, 48–50	1239.88	2.31	2.62	17.8	8.6	0.22
98R-2, 54–56	1241.44	2.43	2.60	10.1	4.5	0.11
99R-3, 98–100	1252.92	2.40	2.68	20.3	9.5	0.26
100R-1, 26–38	1259.06	2.36	2.44	12.6	5.8	0.14

g/cm³ near the center of Unit IV. Bulk densities of up to 2.20 g/cm³ are measured at the top and bottom of the unit.

Unit V (1004–1047 mbsf) consists of alternating claystone and tuff. The bulk densities in this unit depend on whether the samples were taken from the tuff or the claystone, with values ranging from 2.05 to 2.35 g/cm³.

The abrupt increase in bulk density below 1047 mbsf coincides with the basement basalts encountered at 1047 mbsf. The bulk density of the altered pillow basalts ranged from 2.32 to about 2.60 g/cm³. The dolerite sills were significantly denser, with bulk densities ranging from about 2.70 to 2.80 g/cm³.

Figure 53 presents the grain density as a function of depth. The grain densities of the nannofossil marls in Unit I are slightly lower than the grain densities in the claystones and siltstones of Units II and III. Furthermore, the grain density in the marls shows more scatter than for the other units, with values ranging between 2.44 and 2.80 g/cm³. The claystones and siltstones of Units II and III have similar grain densities, with most values falling between 2.65 and 2.80 g/cm³.

The most pronounced feature in Figure 53 is the zone of low grain density lying between 806 and 1033 mbsf. This zone corresponds to all of Unit IV and the upper part of Unit V. The sediments in this interval are dominated by pyroclastic material that consists of vitric tuff and pumice. These materials result in grain densities of 2.30 to 2.50 g/cm³.

The pillow basalts and dolerite sills of the basement have grain densities similar to those of the claystone and siltstone, with most values falling between 2.60 and 2.80 g/cm³.

Variations in porosity, water content, and void ratio with depth are plotted in Figure 53. These figures show an expected decrease of these properties with increasing depth.

Porosity (Fig. 53) starts from about 82% to 88% at the seafloor and decreases at approximately 11%/100 m until about 310 mbsf. Between about 340 and 940 mbsf, porosity decreases

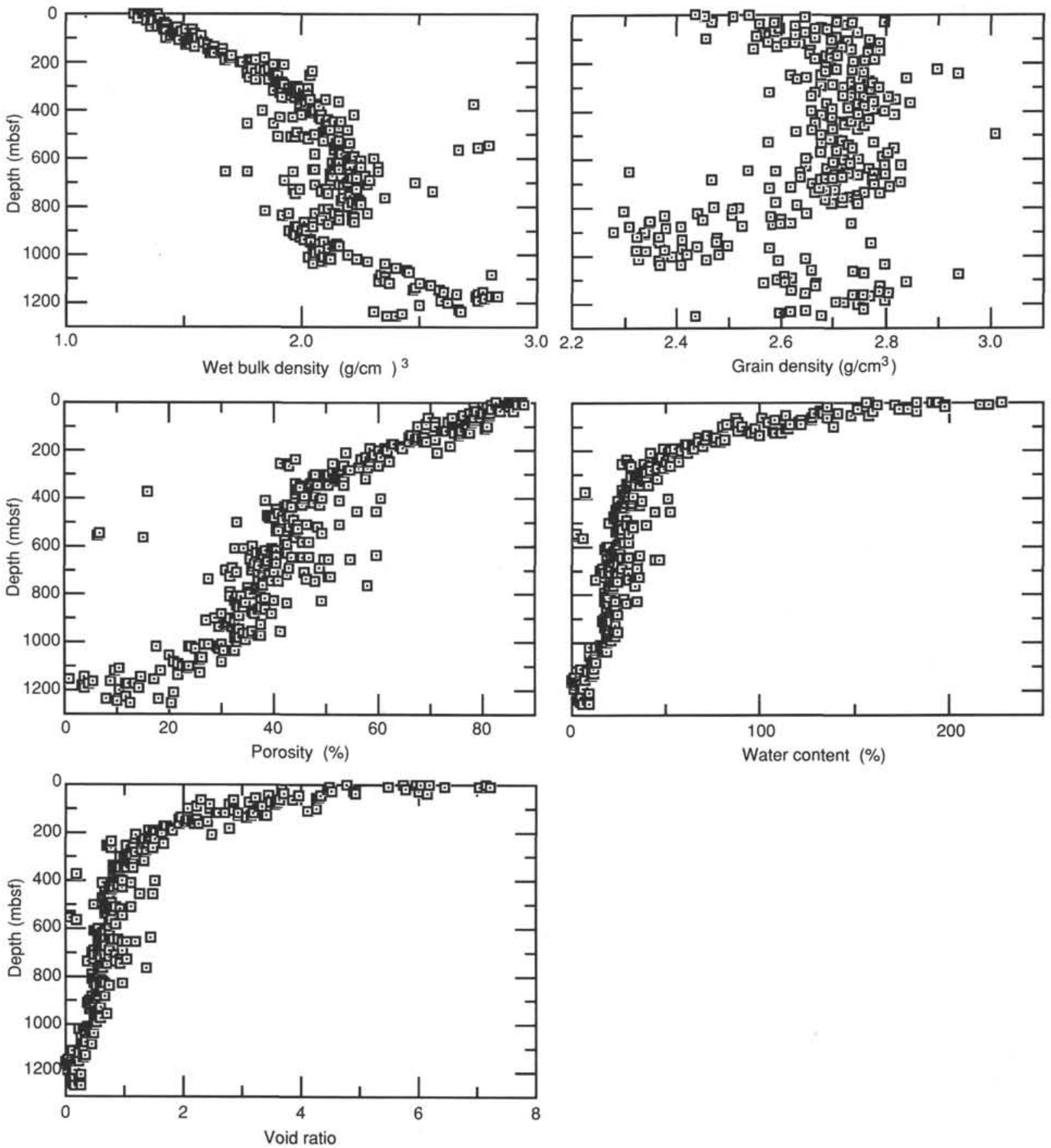

Figure 53. Downhole changes in index properties (wet-bulk density, grain density, porosity, water content, and void ratios) depth, Site 768A.

at a slower rate of roughly 3%–4%/100 m depth. Localized variations in porosity are present and may reflect lithostratigraphic changes. The four points with low porosities relate to the thin indurated, carbonate-rich layers noted above.

The porosity of the pyroclastic sediments varies between about 30% and 40%. The basalt and the dolerite sills gave porosities between 1% and 30%, with significantly lower porosity in the dolerite than in the altered pillow basalts.

The plot of water content vs. depth (Fig. 53) shows that the decrease in water content is strongly nonlinear, with the greatest rate of change taking place near the seafloor. Water contents near the seafloor range from 160% to 230%, whereas in Unit III (652–807 mbsf) water contents range from 15% to 35%. The decrease in porosity and water content is related to the compaction (or consolidation) of the deeper sediments from the gravitational loading caused by sediments deposited above.

The pillow basalt has water contents ranging from around 8% to 12% that are marginally lower than the overlying sediment. In contrast, the dolerite has low water contents of 1%–5%.

Figure 53 shows that the void ratio (the ratio of voids to solids) follows a nearly coincidental pattern as the water content. This is to be expected for sediment that is completely saturated with fluid.

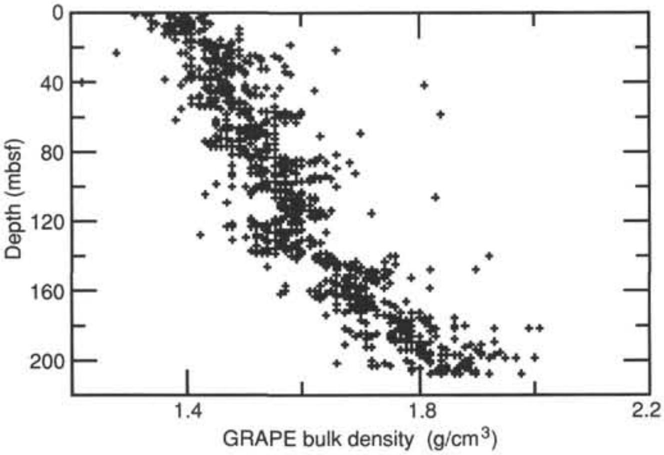

Figure 54. GRAPE bulk density vs. depth, Hole 768B.

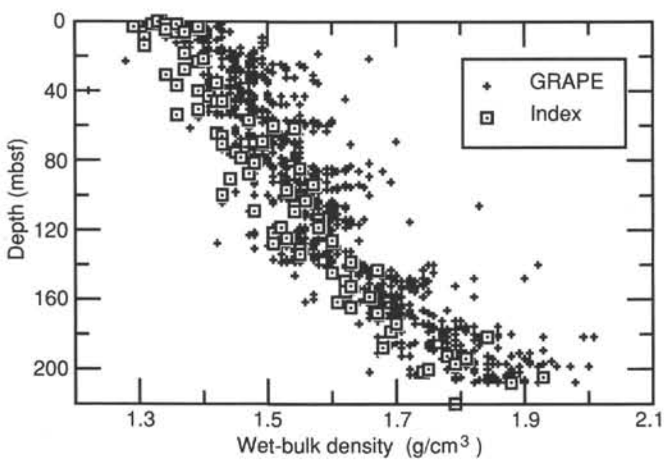

Figure 55. Wet-bulk-density comparison of index property discrete samples and continuous GRAPE testing vs. depth, Site 768.

GRAPE

The bulk density values determined with the gamma-ray attenuation porosity evaluation technique (GRAPE) are presented in Figure 54 and are compared with the bulk density values from the index property testing in Figure 55. Grape bulk densities were obtained only for APC cores from Hole 768B. No GRAPE measurements were taken on RCB cores from Holes 768B and 768C.

GRAPE measurements were conducted to a depth of 209 mbsf in Hole 768B. Only RCB cores were obtained below this depth, and the core diameters became significantly smaller than the inside diameter of the liner tube, which precluded the use of the GRAPE technique to obtain accurate bulk densities. GRAPE measurements were taken at 10-cm intervals but were averaged over 0.2 m for presentation in Figures 54 and 55.

Figure 54 shows that bulk density increased linearly from about 1.38 g/cm^3 at the seafloor to 1.50 g/cm^3 at 123 mbsf. Bulk density shifts lower at 123 mbsf but continues to increase at a faster rate from about 1.50 g/cm^3 at 123 mbsf to roughly 1.90 g/cm^3 at 209 mbsf. The shift in bulk density and the change in rate of density increase corresponds to the boundary between Units I and II at 123 mbsf. The bulk densities also display localized oscillations of a sawtooth shape, which may be related to fining-upward sequences in the sediments.

Figure 55 shows that discrete bulk density and GRAPE bulk densities are in very close agreement over the whole interval for which GRAPE measurements were obtained. Index bulk density values tend to be slightly lower than GRAPE bulk density values, although the GRAPE yielded several high density points, which are probably associated with the thin, more indurated layers of sediment that did not get sampled for index property determination.

Velocity

The compressional wave velocities of discrete samples from Holes 768B and 768C are presented in Table 13 and plotted in Figure 56. The plot of velocity shows a general increase in velocity with depth. Because compressional wave velocity is, in part, a function of the bulk density, the increase in velocity with depth is generally compatible with the same trend in bulk density.

One exception to this correspondence of bulk density and velocity increases with depth exists in the pyroclastic rocks of Unit IV. The samples measured from Unit IV have fairly low bulk density, but the velocity appears to be higher than in the overlying sediments. The bulk density is an indicator of the degree of grain-to-grain contact. The greater the grain-to-grain contact, the higher the macroscopic velocity through a sample. However, for the samples of pyroclastic sediments, the markedly low grain density results in a low bulk density; in this case, however, the low bulk density does not correspond to reduced grain-to-grain contact. Therefore, the velocity can be fairly high even with low bulk density.

The sporadic points with significantly higher velocities correspond to samples of sediment with anomalously high bulk density such as the sporadic, thin, highly indurated carbonate-rich layers in Unit II. Aside from these points, the velocity values tend to fall within a narrow range at any particular depth. The sediments near the seafloor have velocities of about 1.5–1.6 km/s. The velocity increases gradually with depth and reaches about 2.3 km/s at 800 mbsf.

The contact between the sediments and the basalt is reflected in an abrupt increase in velocity from approximately 2.5–3.0 km/s in the sedimentary section to 3.1–3.4 km/s in the basalt. A further abrupt increase in velocity is associated with the dolerite sills. Velocity values in the dolerite range from roughly 4 to over 5 km/s.

Thermal Conductivity

The thermal conductivity measurements of cores from Holes 768B and 768C are given in Table 14 and are graphically presented in Figure 57. All values in the sediments were obtained by means of needle probes inserted through core liners into full core sections. An attempt was made to insert the probes at locations along each core section that appeared to be the least disturbed. However, an annulus of disturbed sediment and drill fluid was often present along the inside of the liner, which prevented visual identification of the more intact segments in the core. The core sections were allowed to reach thermal equilibrium with the laboratory temperature (about 24 °C), which usually took from 2 to 3 hr. The readings were then obtained over a 9–12-min period.

The thermal conductivity of the pillow basalt and dolerite sills was determined with the half-space technique with polished 8–15-cm segments of the split core. The pieces of rock were placed in a salt-water bath at room temperature and allowed to reach thermal equilibrium prior to taking readings over a 9-min period.

Thermal conductivity at Site 768 ranges from about 0.9 to 1.0 W/m · K at the seafloor and tends to increase with depth to

Table 13. Compressional wave velocity data, Site 768.

Core, section, interval (cm)	Depth (mbsf)	Velocity (km/s)
124-768B-		
1H-1, 137–140	1.37	1.51
1H-2, 75–78	2.25	1.52
1H-3, 23–26	3.23	1.51
2H-2, 111–114	6.61	1.50
2H-4, 28–31	8.78	1.51
3H-1, 65–68	14.15	1.53
3H-4, 69–72	18.69	1.51
3H-6, 51–54	21.51	1.56
4H-1, 40–43	23.40	1.52
4H-6, 39–42	30.89	1.57
6H-1, 93–96	42.93	1.53
6H-4, 80–83	47.30	1.51
6H-7, 54–57	51.54	1.52
12H-5, 60–63	105.60	1.52
13H-4, 103–106	114.03	1.55
13H-7, 48–51	117.98	1.52
16H-2, 66–69	139.16	1.53
16H-5, 55–58	143.55	1.51
16H-6, 71–74	145.21	1.56
17H-2, 59–61	148.59	1.52
17H-4, 97–100	151.97	1.62
19H-1, 59–62	166.09	1.54
19H-5, 134–137	172.84	1.56
20H-1, 61–64	174.41	1.54
20H-6, 97–100	182.27	1.56
21H-1, 91–94	184.21	1.55
21H-3, 56–59	186.86	1.56
21H-6, 77–80	191.57	1.57
22H-1, 90–93	193.70	1.57
22H-3, 88–91	196.68	1.58
23H-3, 73–76	204.73	1.60
23H-5, 77–80	207.77	1.59
25X-CC, 3–5	209.63	4.21
25X-CC, 49–51	210.09	2.41
28X-1, 110–112	239.70	1.57
124-768C-		
2R-1, 30–32	363.20	2.76
3R-CC, 13–16	373.35	4.70
7R-2, 19–21	412.79	2.32
11R-3, 126–128	453.86	1.80
11R-4, 44–46	454.54	1.85
11R-4, 105–107	455.15	1.79
12R-C, 12–14	461.14	1.67
14R-4, 63–65	483.63	1.73
17R-1, 148–150	508.98	1.79
17R-2, 99–100	509.99	1.95
17R-2, 110–112	510.10	2.04
17R-4, 24–26	512.24	1.95
17R-4, 105–107	513.05	2.03
18R-1, 6–8	517.26	5.36
21R-1, 95–97	547.25	2.04
21R-CC, 21–23	548.03	4.70
22R-1, 31–33	556.11	4.72
23R-1, 5–7	565.55	3.48
24R-4, 35–37	580.05	2.11
30R-3, 110–112	637.20	1.80
30R-3, 117–119	637.27	1.77
31R-3, 43–46	646.23	1.97
32R-1, 37–39	652.77	1.72
32R-2, 14–16	654.04	1.91
32R-3, 10–12	655.50	1.81
32R-3, 146–148	656.86	2.02
33R-5, 116–118	669.26	1.62
36R-3, 73–75	694.83	2.18
40R-1, 77–79	730.67	2.32
40R-1, 139–141	731.29	2.68
40R-2, 48–50	731.88	3.54
41R-1, 87–89	740.47	2.05
48R-1, 111–113	807.71	2.26
48R-2, 27–29	808.37	2.26
48R-4, 83–85	811.93	2.32
49R-3, 7–9	818.57	2.58
49R-3, 47–49	818.97	2.36
49R-6, 129–131	824.29	2.30
50R-3, 68–70	828.88	3.98
51R-2, 23–25	836.63	2.72
51R-4, 92–94	840.32	2.31

Table 13 (continued).

Core, section, interval (cm)	Depth (mbsf)	Velocity (km/s)
124-768C-		
52R-3, 121–123	848.81	2.66
52R-5, 129–131	851.89	2.86
53R-2, 95–97	856.75	2.48
53R-3, 112–114	858.42	2.39
54R-3, 49–51	867.49	2.42
55R-2, 53–55	875.73	2.40
55R-3, 118–120	877.88	2.30
56R-1, 19–21	883.59	2.73
56R-2, 11–13	885.01	2.53
56R-4, 60–62	888.50	2.34
58R-1, 22–24	902.62	2.83
58R-2, 35–37	904.25	2.51
58R-4, 57–59	907.47	2.68
59R-1, 73–75	912.73	2.70
59R-4, 16–18	916.66	2.44
59R-5, 16–18	918.16	2.53
60R-3, 97–99	925.67	2.56
60R-6, 69–71	929.89	2.37
61R-2, 125–127	934.15	2.56
61R-4, 144–146	937.34	2.69
62R-2, 22–24	942.72	2.78
62R-4, 54–56	946.04	2.48
63R-1, 145–147	951.75	2.68
63R-4, 22–24	955.02	2.71
64R-1, 54–56	960.54	2.72
64R-2, 124–126	962.74	2.53
65R-2, 36–38	971.56	2.42
66R-2, 11–13	981.01	2.80
66R-3, 108–110	983.48	2.94
66R-4, 43–45	984.33	3.07
67R-3, 134–136	993.34	2.58
67R-4, 52–54	994.02	2.48
67R-5, 32–34	995.32	2.70
68R-1, 32–34	999.02	2.59
68R-2, 91–93	1001.11	2.59
68R-3, 78–80	1002.48	2.91
68R-4, 82–84	1004.02	2.47
68R-5, 108–110	1105.78	2.90
69R-2, 88–90	1010.68	3.02
69R-4, 30–32	1013.10	2.66
70R-1, 60–62	1018.20	2.38
70R-2, 61–63	1019.71	3.02
70R-3, 69–71	1021.29	2.96
70R-4, 55–57	1022.65	2.55
71R-1, 106–108	1028.26	2.72
71R-3, 134–136	1031.54	2.49
71R-4, 99–101	1032.69	2.63
74R-1, 115–117	1057.45	3.46
74R-2, 37–39	1058.12	3.27
75R-2, 45–47	1067.85	3.18
77R-1, 48–50	1081.08	3.11
78R-1, 27–29	1085.87	3.18
79R-1, 38–40	1090.98	3.25
80R-1, 77–79	1096.37	3.19
81R-1, 19–21	1100.79	3.11
82R-2, 17–19	1107.22	3.31
83R-1, 137–139	1111.97	3.20
84R-2, 93–95	1118.03	3.37
85R-1, 37–39	1120.97	3.04
86R-1, 46–48	1127.06	3.35
88R-1, 28–30	1146.28	3.75
88R-2, 114–116	1148.46	4.11
89R-1, 77–79	1156.47	4.28
89R-2, 5–7	1157.25	4.56
89R-4, 50–52	1160.12	5.00
90R-2, 59–61	1167.20	4.11
90R-3, 50–52	1168.41	4.69
90R-5, 72–74	1171.49	4.92
90R-7, 104–106	1174.12	4.99
91R-1, 32–34	1175.22	5.15
92R-2, 22–24	1186.17	4.88
92R-3, 135–137	1188.55	4.90
93R-2, 12–14	1193.12	4.62
94R-1, 76–78	1201.46	4.26
95R-1, 4–6	1210.44	3.54
96R-1, 106–108	1221.06	3.52
97R-3, 65–67	1233.11	4.90
98R-2, 54–56	1241.44	4.32
100R-1, 36–38	1259.16	3.41

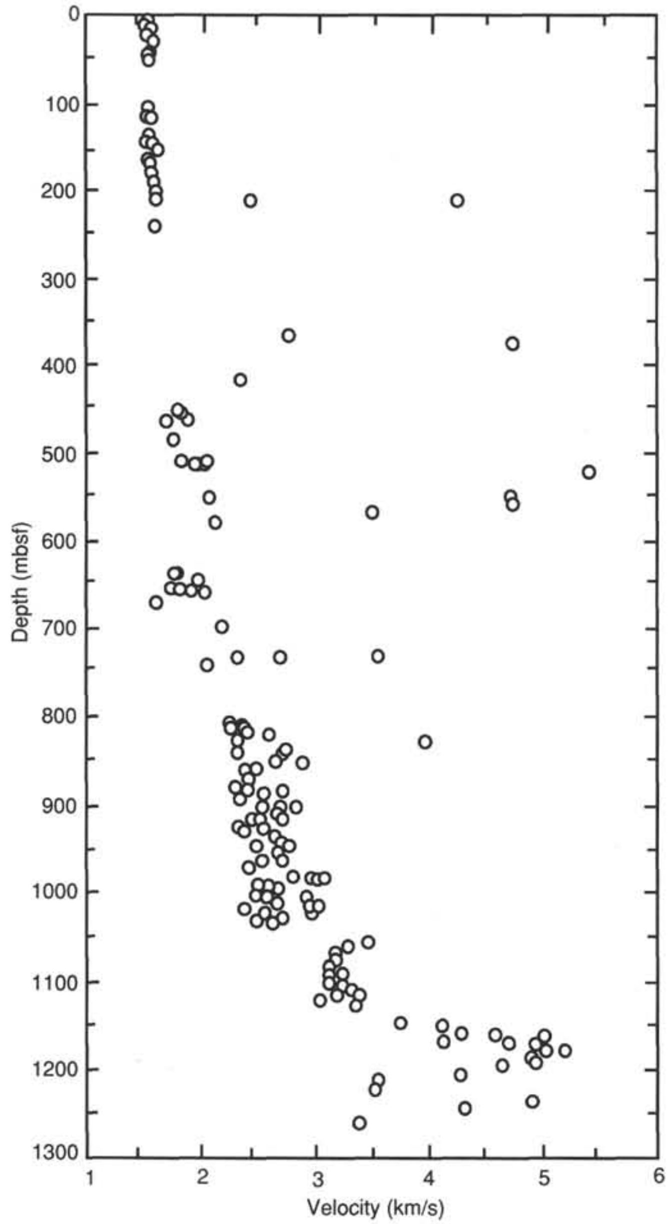

Figure 56. Hamilton Frame compressional velocity vs. depth, Site 768.

about 200 mbsf. Below 200 mbsf the values of thermal conductivity begin to exhibit considerable scatter. The increased scatter in thermal conductivity is probably related to core disturbance and core biscuiting, both of which tend to increase with depth. A heavily biscuited core contains individual segments of intact sediments separated and often surrounded by a slurry of sediment and drilling fluid. The placement of the thermal conductivity probes in these types of cores will often result in the probe being inserted into slurry rather than into intact segments of sediment. This causes the thermal conductivity measurement to fluctuate between the slurry and the intact sediment values. Scatter was largest for sediments obtained between 360 and 750 mbsf.

Thermal conductivity values from the pyroclastic sediments are lower than the claystones and siltstone located above and the basement rocks located below. The pyroclastic rocks had thermal conductivity values that ranged from 1.1 to 1.4 W/m · K, whereas the claystone and siltstone had more variable thermal conductivities that ranged from 1.0 to 2.0 W/m · K, with the smaller values generally found at shallower depths. The few

Table 14. Thermal conductivity data, Site 768.

Core, section, interval (cm)	Depth (mbsf)	Thermal conductivity (W/m · K)
124-768B-		
1H-2, 75-76	2.25	1.02
1H-3, 40-41	3.40	1.04
2H-2, 60-61	6.10	0.94
2H-3, 75-76	7.75	0.93
2H-5, 60-61	10.60	0.90
2H-7, 40-41	13.40	0.96
3H-1, 90-91	14.40	0.93
3H-3, 75-76	17.25	0.94
3H-5, 75-76	20.25	1.00
3H-7, 40-41	22.90	0.99
4H-1, 50-51	23.50	0.88
4H-3, 50-51	26.50	0.95
4H-5, 75-76	29.75	0.97
4H-7, 45-46	32.45	0.99
5H-1, 50-51	33.00	0.91
5H-3, 65-66	36.15	0.91
5H-5, 90-91	39.40	0.93
5H-7, 30-31	41.80	0.98
6H-1, 75-76	42.75	1.07
6H-3, 75-76	45.75	1.11
6H-5, 75-76	48.75	0.95
6H-7, 40-41	51.40	1.06
7H-1, 75-76	52.25	0.92
7H-3, 75-76	55.25	0.91
7H-5, 75-76	58.25	1.01
7H-7, 35-36	60.85	0.92
8H-1, 75-76	61.75	0.99
8H-3, 75-76	64.75	0.99
8H-5, 60-61	67.60	1.01
8H-7, 30-31	70.30	1.01
9H-1, 57-58	71.07	0.98
9H-3, 56-57	74.06	0.95
9H-5, 55-56	77.05	0.94
9H-7, 39-40	79.89	1.00
10H-1, 60-61	80.60	0.99
10H-3, 55-56	83.55	1.02
10H-5, 105-106	87.05	1.07
10H-7, 40-41	89.40	1.03
11H-1, 56-57	90.06	1.00
11H-3, 55-56	93.05	0.98
11H-5, 55-56	96.05	1.01
11H-7, 39-40	98.89	0.95
12H-2, 86-87	101.36	1.05
12H-3, 47-48	102.47	1.04
12H-5, 48-49	105.48	1.14
12H-6, 90-91	107.40	1.05
13H-1, 70-71	109.20	1.11
13H-3, 70-71	112.20	1.02
13H-4, 65-66	113.65	1.16
13H-6, 70-71	116.70	1.12
14H-1, 65-66	118.65	1.11
14H-3, 64-65	121.64	0.97
14H-4, 64-65	123.14	1.08
14H-6, 63-64	126.13	1.10
15H-1, 55-56	128.05	1.02
15H-3, 55-56	131.05	1.06
15H-4, 55-56	132.55	1.09
15H-6, 55-56	135.55	1.03
16H-1, 60-61	137.60	1.00
16H-3, 60-61	140.60	1.07
16H-4, 60-61	142.10	1.07
16H-4, 60-61	145.10	1.19
17H-1, 75-76	147.25	1.19
17H-3, 75-76	150.25	1.16
17H-5, 75-76	153.25	1.14
17H-7, 30-31	155.80	1.17
18H-1, 75-76	156.75	1.18
18H-3, 75-76	159.75	1.09
18H-5, 75-76	162.75	1.05
18H-7, 35-36	165.35	1.17
19H-1, 75-76	166.25	1.20
19H-3, 75-76	169.25	1.15
19H-5, 75-76	172.25	1.36
19H-6, 20-21	173.20	1.34
20H-1, 75-76	174.55	1.18

Table 14 (continued).

Core, section, interval (cm)	Depth (mbsf)	Thermal conductivity (W/m · K)
124-768B-		
20H-3, 75–76	177.55	1.20
20H-5, 75–76	180.55	1.24
20H-7, 35–36	183.15	1.21
21H-1, 90-91	184.20	1.22
21H-3, 85–86	187.15	1.32
21H-5, 75–76	190.05	1.44
21H-7, 11–12	192.41	1.36
22H-1, 75–76	193.55	1.18
22H-3, 75–76	196.55	1.24
22H-5, 75–76	199.55	1.31
22H-6, 18–19	200.48	1.23
23H-1, 75–76	201.75	1.09
23H-3, 75–76	204.75	1.32
23H-5, 75–76	207.75	1.56
23H-6, 22–23	208.72	1.31
26X-1, 50–51	219.80	1.49
26X-2, 55–56	221.35	1.31
26X-3, 45–46	222.75	1.49
28X-1, 80–81	239.40	1.49
28X-3, 50–51	242.10	1.31
28X-5, 65–66	245.25	1.49
29X-1, 65–66	248.85	1.23
29X-3, 65–66	251.85	1.44
29X-4, 50–51	253.20	1.01
30X-1, 92–93	258.72	1.35
30X-2, 70–71	260.00	1.27
30X-3, 20–21	261.00	1.51
31X-1, 75–76	268.25	1.50
31X-3, 75–76	271.25	1.36
31X-7, 20–21	276.70	1.28
32X-1, 44–45	277.64	1.40
32X-2, 102–103	279.72	1.30
32X-3, 13–14	280.33	1.51
33X-2, 69–70	288.99	1.30
33X-3, 86–87	290.66	1.19
33X-3, 43–44	290.23	1.22
33X-4, 31–32	291.61	1.22
34X-1, 40–41	296.80	1.28
34X-1, 96–98	297.36	1.24
34X-2, 52–53	298.42	1.37
34X-3, 22–23	299.62	1.51
35X-1, 81–82	306.91	1.48
35X-2, 101–102	308.61	1.32
35X-3, 21–22	309.31	1.49
36X-1, 70–71	316.50	1.43
36X-2, 70–71	318.00	1.32
36X-3, 70–71	319.50	1.69
37X-1, 60–61	326.10	1.54
37X-2, 60–61	327.60	1.55
37X-3, 60–61	329.10	1.51
124-768C-		
2R-1, 70–71	363.60	1.52
2R-3, 70–71	366.60	1.86
2R-4, 75–76	368.15	1.62
2R-5, 20–21	369.10	1.46
4R-1, 60–61	382.70	1.71
4R-2, 10–11	383.70	1.32
3R-1, 45–46	372.85	1.55
5R-1, 60–61	392.40	1.95
5R-2, 60–61	393.90	1.37
5R-3, 60–61	395.40	1.56
6R-1, 70–71	402.10	1.52
6R-2, 60–61	403.50	1.52
6R-3, 60–61	405.00	1.58
7R-1, 60–61	411.70	1.62
7R-3, 60–61	414.70	1.58
7R-5, 48–49	417.58	1.51
7R-6, 20–21	418.80	1.65
8R-1, 75–76	421.45	1.49
8R-2, 85–86	423.05	1.65
9R-1, 73–74	430.93	1.40
9R-2, 70–71	432.40	1.49
9R-3, 25–26	433.45	1.74
10R-1, 48–49	440.38	1.42

Table 14 (continued).

Core, section, interval (cm)	Depth (mbsf)	Thermal conductivity (W/m · K)
124-768C-		
10R-1, 105–106	440.95	1.65
10R-3, 34–35	443.24	1.60
11R-1, 71–72	450.31	1.48
11R-3, 61–62	453.21	1.39
11R-4, 49–50	454.59	1.26
11R-5, 92–93	456.52	1.36
13R-1, 83–84	469.73	1.45
13R-2, 67–68	471.07	1.37
13R-3, 41–42	472.31	1.37
13R-4, 51–52	473.91	1.46
14R-1, 80–81	479.30	1.40
14R-2, 39–40	480.39	1.37
14R-3, 110–111	482.60	1.26
15R-1, 95–96	489.15	1.38
15R-2, 78–79	490.48	1.31
15R-3, 95–96	492.15	1.82
15R-4, 38–39	493.08	1.83
17R-1, 78–79	508.28	1.49
17R-2, 75–76	509.75	1.28
17R-3, 63–64	511.13	1.95
17R-4, 62–63	512.62	1.58
18R-1, 80–81	518.00	1.89
18R-2, 64–65	519.34	1.98
18R-3, 53–54	520.73	1.46
18R-4, 79–80	522.49	1.79
19R-1, 75–76	527.65	1.65
19R-2, 75–76	529.15	1.90
20R-1, 75–76	537.35	1.72
20R-2, 65–66	538.75	1.65
20R-3, 65–66	540.25	1.70
20R-4, 30–31	541.40	1.67
21R-1, 52–53	546.82	2.03
22R-1, 70–71	556.50	1.82
22R-3, 20–21	559.00	2.00
23R-1, 73–74	566.23	1.44
23R-2, 67–68	567.67	1.51
23R-4, 80–81	570.80	1.55
23R-5, 60–61	572.10	1.27
24R-1, 76–77	575.96	2.19
24R-2, 85–86	577.55	1.66
24R-5, 47–48	581.67	1.63
26R-1, 69–70	595.29	1.39
26R-3, 80–81	598.40	1.74
26R-5, 72–73	601.32	1.82
26R-6, 49–50	602.59	1.62
27R-1, 68–69	604.98	1.59
27R-3, 69–70	607.99	1.53
27R-5, 63–64	610.93	1.54
27R-6, 60–61	612.40	1.73
28R-1, 71–72	614.61	1.43
28R-5, 71–72	620.61	1.51
28R-3, 68–69	617.58	1.58
28R-7, 8–9	622.98	1.36
29R-1, 67–68	624.17	1.39
29R-3, 83–84	627.33	1.54
29R-4, 76–77	628.76	1.61
29R-6, 85–86	631.85	1.45
30R-1, 33–34	633.43	1.42
30R-3, 47–48	636.57	1.78
30R-4, 90–91	638.50	1.90
30R-6, 77–78	641.37	1.53
32R-3, 71–72	656.11	1.16
32R-4, 109–110	657.99	1.58
32R-6, 63–64	660.53	1.59
34R-1, 77–78	672.57	1.55
34R-3, 90–91	675.70	1.96
34R-4, 60–61	676.90	1.54
34R-6, 74–75	680.04	1.82
35R-1, 80–81	682.20	1.75
35R-2, 70–71	683.60	1.60
35R-4, 75–76	686.65	1.49
35R-6, 15–16	689.05	2.19
36R-3, 65–66	694.75	1.23
36R-5, 65–66	697.75	1.26
36R-5, 65–66	699.25	1.62
37R-1, 70–71	701.50	1.30

Table 14 (continued).

Core, section, interval (cm)	Depth (mbsf)	Thermal conductivity (W/m · K)
124-768C-		
37R-3, 70–71	704.50	1.62
37R-4, 54–55	705.84	1.61
37R-6, 27–28	708.57	1.51
38R-1, 72–73	711.22	1.35
38R-2, 72–73	712.72	1.53
38R-3, 72–73	714.22	1.60
38R-4, 23–24	715.23	1.37
39R-1, 72–73	720.92	1.39
39R-3, 74–75	723.94	1.37
40R-3, 47–48	733.37	1.45
40R-4, 63–64	735.03	1.49
41R-1, 91–92	740.51	1.28
41R-3, 88–89	743.48	1.34
41R-5, 53–54	746.13	2.12
41R-6, 71–72	747.81	1.70
44R-2, 49–50	770.09	1.36
44R-2, 97–98	770.57	1.39
44R-3, 95–96	772.05	1.23
48R-2, 48–49	808.58	1.40
49R-2, 50–51	817.50	1.16
51R-4, 85–86	840.25	1.32
52R-3, 122–123	848.82	1.28
54R-3, 119–120	868.19	1.18
62R-2, 15–16	942.65	1.25
64R-1, 116–117	961.16	2.06
66R-2, 3–4	980.93	1.30
68R-2, 5–6	1000.25	1.15
74R-2, 15–16	1057.90	1.39
76R-2, 10–11	1077.20	1.44
81R-1, 50–55	1101.10	1.40
83R-1, 127–133	1111.87	1.42
89R-1, 10–20	1155.80	1.49
89R-2, 42–49	1157.62	1.91
90R-2, 61–69	1167.22	1.66
98R-2, 56–63	1241.46	1.50

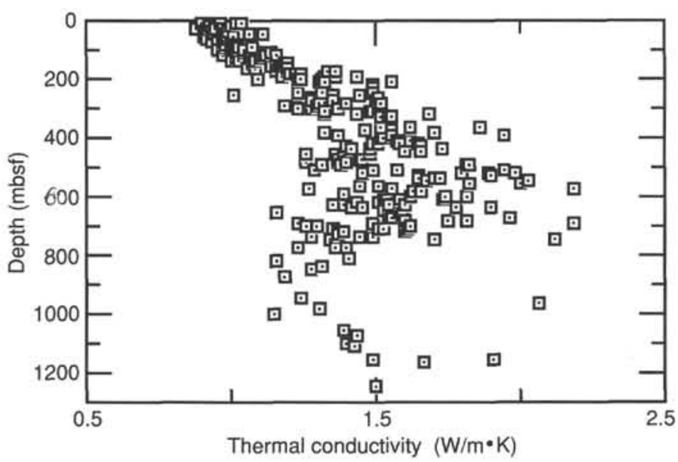

Figure 57. Thermal conductivity vs. depth, Site 768.

measurements obtained in the basalt and dolerite yielded thermal conductivities of 1.4–1.9 W/m · K, with the larger values associated with the less-altered basalt and the dolerite.

Vane Shear Strength

Values of undrained shear strength were obtained with a four-bladed, motorized vane shear apparatus on samples taken from APC cores from Holes 768A and 768B. The APC cores displayed evidence of sample disturbance, and thus the measured shear strengths may vary significantly from those *in situ*. More importantly, post-site testing of the torque transducer on the motorized shear vane device indicated that torque measurements may be low. The error in the calibration of the transducer may have been up to 100%. Therefore, the shear strength values discussed in this chapter may be roughly half of the actual values. However, even though the absolute magnitudes of the shear strength data may be in error, the relative changes in shear strength should be valid because the drift or change in the transducer calibration over the duration of testing at Site 768 is negligible.

Peak and remolded shear strength values are given in Table 15 and are plotted as a function of depth in Figure 58. The vane was set to rotate at about 90°/min, which generally resulted in 8°–14° of rotation before peak shear strength was achieved. The vane was permitted to continue rotation for at least 120°, which allowed shear strength to drop to a fairly constant value that could be measured for remolded shear strength.

Table 15. Shear strength data, Site 768.

Core, section, interval (cm)	Depth (mbsf)	Shear strength (kPa)		
		Peak	Remolded	Sensitivity
124-768A-				
1H-1, 72–73	0.72	1.3	0.4	3.3
1H-1, 124–125	1.24	1.1	0.4	2.8
1H-2, 53–54	2.03	1.0	0.4	2.5
1H-3, 84–85	3.84	3.1	0.1	31.0
1H-4, 112–113	5.62	5.0	2.6	1.9
1H-5, 76–77	6.76	5.9	2.4	2.5
124-768B-				
1H-6, 30–31	7.80	7.4	3.9	1.9
1H-1, 145–146	1.45	2.0	0.9	2.2
1H-3, 15–16	3.15	3.3	1.8	1.8
2H-1, 121–122	5.21	4.7	1.1	4.3
2H-2, 103–104	6.53	6.8	4.4	1.6
2H-3, 55–56	7.55	4.3	2.2	2.0
3H-1, 90–91	14.40	8.5	2.6	3.3
3H-3, 92–93	17.42	6.5	3.3	2.0
3H-5, 127–128	20.77	12.3	5.3	2.3
3H-7, 50–51	23.00	16.7	7.4	2.3
4H-5, 77–78	29.77	16.2	5.9	2.8
6H-1, 73–74	42.73	19.1	7.7	2.5
6H-6, 65–66	50.15	20.4	8.3	2.5
7H-4, 50–51	56.50	23.4	8.1	2.9
7H-4, 85–86	56.85	29.4	11.2	2.6
8H-4, 58–59	66.08	26.3	13.1	2.0
8H-4, 88–89	66.38	34.0	14.2	2.4
9H-5, 44–45	76.94	28.5	9.9	2.9
9H-5, 98–99	77.48	25.2	—	—

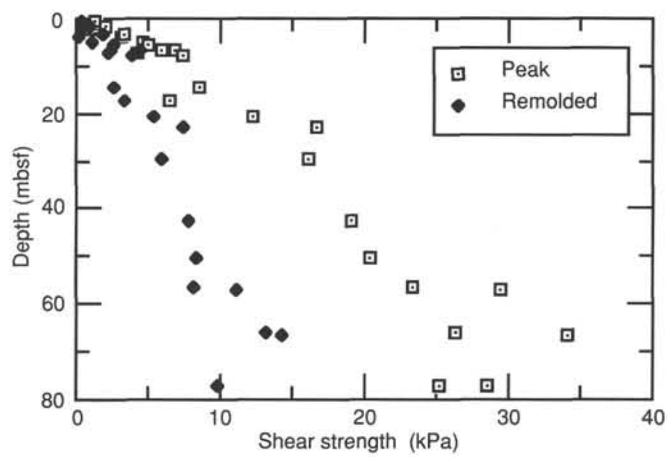

Figure 58. Peak and remolded shear strength vs. depth, Site 768.

Undrained peak shear strength increased rapidly with increasing depth below seafloor until a depth of approximately 8 mbsf was reached. Below this depth the rate of strength increase gradually dropped. Shear strength extrapolated to 0 kPa at the seafloor and increased to about 8 kPa at 8 mbsf. By 70–80 mbsf shear strength increased to approximately 30 kPa. Below about 75 mbsf shear vane testing ended because the failure mechanism around the vane became dominated by cracks that propagated away from the ends of the vane. Thus, the equations for shear strength determination based on a cylindrical failure surface around the vane were no longer valid. The remolded shear strength displayed a similar increase with depth over the interval from 0 to 77 mbsf, with typical sensitivities ranging from 2 to 4.

Conclusions

Sediment index properties, compressional wave velocity, thermal conductivity, and vane shear strength measurements were used to characterize the physical properties of sediments and basement rocks at Site 768. In general, all physical properties displayed the expected depth-dependent variations.

Bulk density increased with depth, almost certainly a result of compaction caused by gravitational loading. This observation is corroborated by the porosity, water content, and void ratio values, all of which decreased with depth.

Grain densities showed a slight increase with depth in Unit I; were essentially constant in Units II, III, and V; and exhibited a prominent low in response to the low grain density of the pyroclastic sediments in Unit IV. This zone of low grain density was imitated to a lesser extent in the bulk density values. The contrast in physical properties at the boundary between the sediments and the basalt was not distinct, although the dolerite located below the sediment/basalt contact had significantly different physical properties.

Compressional wave velocity values provide the most obvious indicator of the contacts between the basalt as well as between the sediments and the dolerite. The basalt had a noticeably higher velocity than the sediments, and conversely the dolerite sills had distinctly higher velocities than the basalt.

Thermal conductivity values were variable but showed an increase with depth near the seafloor. The pyroclastic rocks yielded fairly low values of thermal conductivity. Peak shear strength values displayed a strong increase with depth over the interval from 0 to 77 mbsf.

BASEMENT LITHOLOGY

Basaltic rocks were first recovered at 1046.6 mbsf (Core 124-768C-73R). A total of 221.9 m of igneous rocks was penetrated, including a dolerite sill and a microgabbro sill, which have an aggregate thickness of 62.4 m. These mafic rocks underlie red pelagic clays with some gray laminated units of silty ash, which are of late early Miocene age (see "Lithostratigraphy" section, this chapter). The bottom of the hole is at 1271 mbsf and lies within a sequence of pillowed and brecciated basalts. The depth at which the igneous rocks are present corresponds closely to that of the acoustic basement estimated on the basis of seismic velocities, and there are no sedimentary intercalations within the sequence. It is regarded as the basement of the Sulu Sea.

The lithostratigraphy, depth, and recovery data for the igneous rocks at Site 768 are summarized in Figure 59. Igneous rocks compose 99% of the core recovered from Core 124-768C-73R and 100% of the rock recovered from Cores 124-768C-74R through -100R. Total recovery averaged 39.4% and ranged in individual cores from a low of 10% in Core 124-768C-73R to a high of 86.9% in Core 124-768C-90R. The Schlumberger logs (see "Downhole Measurements" section, this chapter) generally confirm the thicknesses of the individual units calculated from the cores.

The lava units are generally very similar petrographically, and it has proven extremely difficult to identify their textures correctly as well as estimate the proportions of phenocrysts and vesicles present. Thus, we divided the sequence into eight separate units, mainly on the basis of appearance (Fig. 59). Units 1, 4, 6, and 8 comprise sequences of pillowed and brecciated olivine basalts, Units 5 and 7 are made up of thin sheet flows of olivine basalt, and Units 2 and 3 are dolerite and microgabbro sills, respectively, which can be distinguished from each other by their mineralogy, texture, and vein fillings. The drift of the hole from the vertical is 7°. The boundaries, lithologies and thickness of these units are described below.

All basement rock units of Site 768, except for Unit 8, are represented by thin section slides that were studied under the microscope. We analyzed a total of 57 thin sections: thirty from Unit 1, eleven from Unit 2, four from Unit 3, five from Unit 4, one from Unit 5, three from Unit 6, and three from Unit 7. The results are summarized in Table 16.

Unit 1

Moderately to highly olivine-phyric basalt, brecciated and pillowed

Unit 1 is present between 1046.6 and 1148.0 mbsf or between Sections 124-768C-73R-1 at 10 cm and 124-768C-88R-21 at 50 cm. It has a thickness of 101.3 m, of which 46 m was recovered. Laminated gray, fine-grained silty ash is present in the top 10 cm of Core 124-768C-73R-1, but it is not in contact with the lavas. No individual cooling units were defined in this unit. The upper part of the unit is made up mainly of small fractured and veined pillows, up to 50 cm in diameter. These pillows have well-developed margins composed of up to 5 cm of fractured green glass on the outside, followed by a zone of up to 5 cm of gray cryptocrystalline, variolitic material containing quenched skeletal crystals of olivine and grading into the main body of the pillow.

Interpillow filling comprising fragments of green glass, fine-grained gray material, and brown clay is common in this part of the section. The pillows are larger, up to 1 m in diameter, in a zone about 5 m thick, between Sections 124-768C-84R-1 and 124-768C-85R-1. They are characterized by thinner margins composed of up to 1 cm of green glass and 1 cm of gray cryptocrystalline material. All of the pillows are made up of highly vesicular, fine-grained olivine-phyric basalts that contain between 3% and 15% olivine.

Abundant, very small vesicles are present throughout the groundmass of the basalts, together with less numerous larger vesicles. They make up from 30% to 50% of the rock and are filled with carbonate and clay. The fractures are irregular, vertical to steeply dipping, up to 3 cm thick, and filled with green glassy fragments, carbonate, and red clay. The petrography of all of the pillows is very similar, and it is not possible to recognize separate cooling units.

The pillow basalts of Unit 1 vary from moderately to highly olivine phyric basalts (Ol = 5%–15%). Olivine is the only phenocryst phase observed, ranging in size from 0.03 to 1.5 mm. The grains occur as euhedral, equant, prismatic, and sometimes hexagonal sections. Rarely are they rounded, and sometimes they are fragmented. They can be distributed as isolated crystals and/or as glomerocrysts. Twinned crystals are present, although not common. Included within the olivine grains are sparsely disseminated, idiomorphic, square- and diamond-shaped, chromium-spinel granules.

Alteration of the olivine is complete, leaving only the crystal form and cleavage fractures as relic structures of the mineral. Clays, calcite, iron oxide, and iddingsite, all associated in various proportions, pseudomorph every olivine crystal. The iron oxides and iddingsite occur as brown and orange rims along the

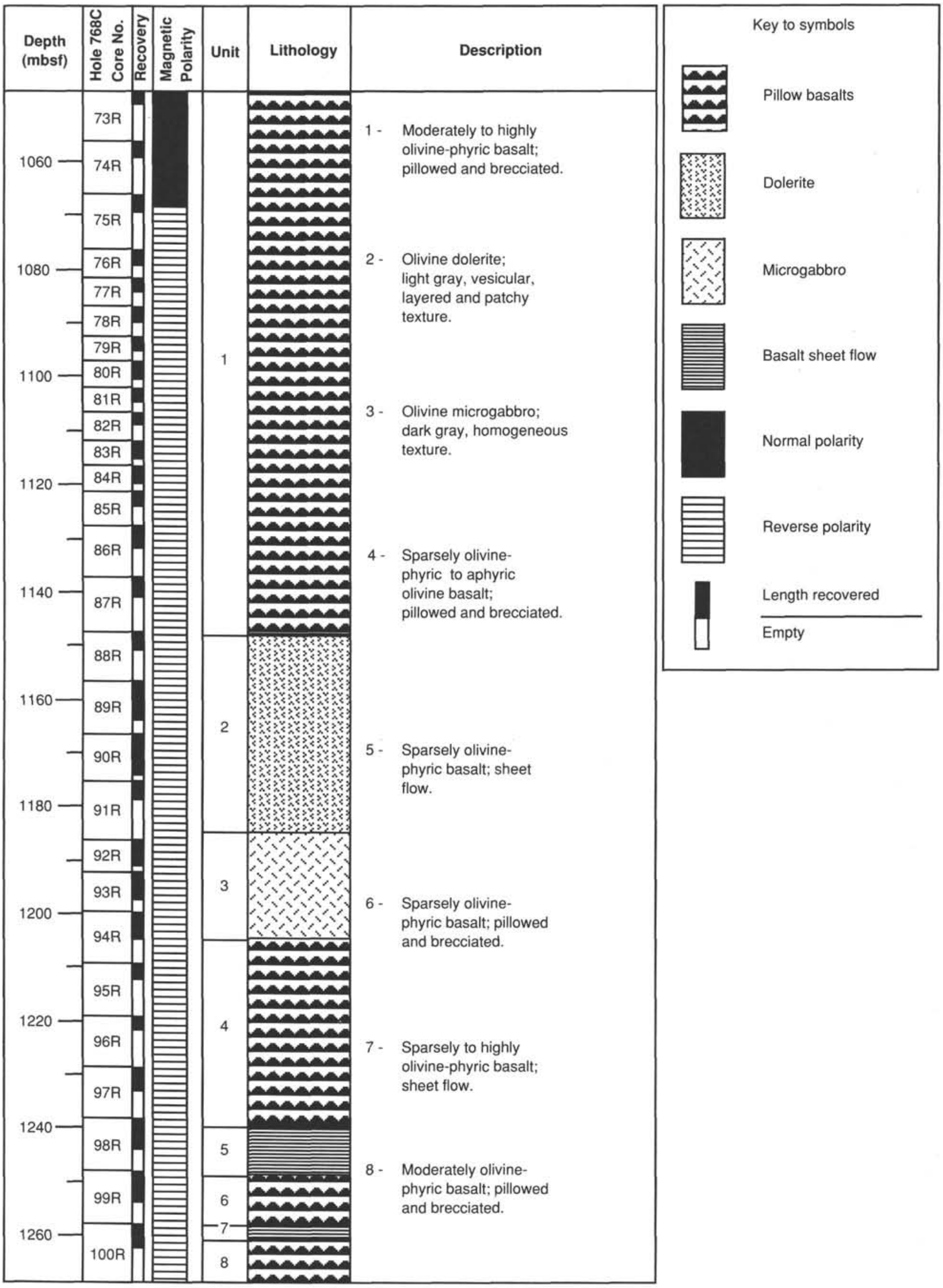

Figure 59. Lithology and recovery of basement rocks, Site 768.

Table 16. Modal proportions of major phases observed in thin section slides of basement rock samples from Site 768.

Core, section interval (cm)	Depth (mbsf)	Phenocryst	Groundmass					Secondary minerals[a]
		Ol	Pl	Ol	Px	Ms	Ves	
Unit 1 (moderately to highly olivine-phyric basalt):								
73R-1, 7-9	1046.66	10	10	—	20	40	20	31
73R-1, 19-22	1046.79	12	37	—	10	15	25	32
73R-1, 67-69	1047.27	15	5	—	7	53	20	50
73R-1, 115-117	1047.75	12	22	—	10	26	30	49
74R-1, 14-16	1056.44	12	20	—	15	23	30	42
74R-1, 127-129	1057.57	15	25	—	10	23	25	41
75R-2, 48-50	1067.88	10	29	—	7	29	25	46
76R-1, 137-139	1076.97	10	25	—	10	37	15	41
76R-3, 53-55	1078.98	7	37	—	3	33	20	34
77R-1, 49-51	1081.09	10	36	2	2	24	26	50
77R-1, 106-108	1081.66	5	40	1	2	20	32	49
77R-2, 81-83	1082.85	12	22	—	1	40	25	57
77R-2, 122-125	1083.26	8	35	1	1	30	25	35
78R-1, 15-18	1085.75	8	18	—	12	30	32	57
78R-2, 114-116	1087.99	10	5	3	22	36	24	37
79R-2, 86-87	1092.90	12	32	—	>1	31	25	40
79R-2, 124-125	1093.28	12	8	2	18	38	22	43
80R-2, 120-121	1098.29	10	32	—	3	35	20	30
80R-3, 35-36	1098.80	5	34	<1	<1	30	35	35
80R-3, 65-66	1099.10	5	30	4	<1	35	25	33
81R-2, 33-34	1102.14	15	30	—	<1	31	23	49
82R-2, 85-87	1107.90	8	37	—	2	30	20	44
83R-1, 139-140	1111.99	3	28	—	3	38	28	38
83R-2, 16-20	1112.26	—	—	—	—	19	1	56
82R-2, 109-111	1118.19	12	18	—	7	23	25	47
85R-2, 52-54	1122.54	12	20	7	4	30	27	53
86R-1, 51-53	1127.11	10	20	—	10	27	33	52
87R-1, 107-109	1137.37	8	35	—	12	25	20	49
87R-2, 125-126	1138.96	8	31	—	10	25	25	42
88R-2, 30-31	1147.62	10	18	—	2	40	30	48
Unit 2 (olivine dolerite):								
88R-2, 100-101	1148.32	—	50	2	25	18	3	27
89R-1, 69-70	1156.39	—	50	—	27	18	2	18
89R-2, 3-4	1157.23	15	52	—	<1	30	1	28
89R-2, 7-10	1157.27	10	54	—	<1	30	4	26
89R-3, 62-63	1159.12	—	52	—	12	25	6	16
89R-5, 36-37	1161.32	—	55	—	30	12	—	21
90R-3, 58-59	1168.49	—	55	8	8	15	10	28
90R-4, 123-126	1170.49	—	54	3	12	20	5	22
90R-7, 117-118	1174.25	—	42	10	25	20	—	15
91R-1, 135-136	1176.25	—	37	2	30	8	20	35
91R-2, 104-107	1177.44	15	25	—	30	28	2	30
Unit 3 (olivine microgabbro):								
92R-1, 60-61	1185.10	—	40	20	24	10	5	42
93R-1, 115-116	1192.65	—	50	15	30	—	—	29
93R-3, 77-78	1195.22	—	35	20	28	—	—	39
94R-1, 74-77	1201.44	—	47	13	27	—	—	30
Unit 4 (sparsely olivine-phyric to aphyric olivine basalt):								
95R-1, 30-33	1210.70	10	15	—	5	38	30	46
96R-1, 106-108	1221.06	—	35	—	15	22	25	62
96R-3, 126-128	1224.13	1	40	4	20	5	15	44
97R-3, 55-59	1233.01	—	25	2	33	20	20	41
98R-1, 67-69	1240.07	2	7	—	1	65	25	44
Unit 5 (sparsely olivine-phyric basalt):								
98R-3, 68-69	1242.85	<1	25	12	15	26	20	56
Unit 6 (sparsely olivine-phyric basalt):								
99R-2, 100-104	1251.54	2	<1	—	<1	20	35	52
99R-4, 49-50	1253.82	1	10	7	<1	62	20	59
100R-1, 34-35	1259.14	3	22	12	<1	38	25	57
Unit 7 (sparsely to highly olivine-phyric basalt);								
100R-1, 115-119	1259.95	3	25	—	2	51	15	66
100R-2, 17-19	1260.47	—	50	—	20	15	10	15
100R-2, 53-55	1260.83	15	32	2	18	18	13	46
Unit 8 (moderately olivine-phyric basalt):								
Not represented.								

Note: Ol = olivine, Pl = plagioclase, Px = pyroxene, Ms = mesostasis, and Ves = vesicles.
[a] Secondary minerals in vesicles and fractures are also considered here and therefore do not reflect the degree of the rock's alteration.

crystal boundary and as continuous and branching trails along the cleavage and fracture traces.

At least three types of clays were observed to alter the olivine. The dominant type is a colorless to very pale brown or very pale green fibrous mineral exhibiting a distinctively high relief and weak to very strong birefringence. There are lesser amounts of pale green, low relief, weakly birefringent crypto- to microcrystalline fibrous clay and a similar very light brown and fibrous, though slightly more birefringent, mineral.

The groundmass is, on the whole, fine grained and varies from entirely glass at or near the chilled margins to holocrystalline in the interior. Abundant vesicles (15%-32%) are present, which give the rock a frothy texture. One sample (124-768C-83R-2, 16-20 cm), however, is an almost nonvesicular (1% vesicles), aphyric glassy rock with abundant cryptocrystallites and varioles replaced wholly by calcite.

Beyond the massive glassy rim and going to the interior is an abrupt change in texture defined by a zone of highly vesicular holocrystalline rock with variolitic texture. The varioles are composed of bow-tie plagioclase microlites (5%-8%) and glass mesostasis (30%-50%) that form radiate dendritic branches. The dendricity is a function of the closely spaced, minute (0.008-0.1 mm), round to elongate vesicles (20%-24%).

Dark iron-oxide-stained rings, composed of plumose crystallites and mesostasis, define the spherule shape of the varioles and also compose the intervariole material. The variolitic zone grades to divergent and intersertal textures toward the interior. Subhedral (0.002-0.8 mm), colorless clinopyroxene crystals (<1%-22%), glass mesostasis (approximately 30% average), and very minute (0.002 mm) magnetite granules (<1%-2%) fill the interstices between the abundant (18%-40%) plagioclase (An_{50-70}) laths (0.006-1.0 mm).

The clinopyroxene crystals are always fresh and occur as granules and as quenched skeletal to plumose crystals. The plagioclase is present as well-defined laths with either clear or mesostasized cores, microlitic crystallites, and skeletal and hopper crystals. In some sections, the plagioclase laths or at least their cores, exhibit parallel extinctions, which indicate a possible replacement (by zeolites or potassic feldspar). Clay alteration of the plagioclase is slight to moderate.

Included in the groundmass of several samples are sparse (<1%-4%) skeletal and hopper olivines, which are entirely altered to iron oxides and clay. The glass mesostasis, which is interstitial to plagioclase laths, is generally suffused with a dark brown pigment as a result of devitrification or the late crystallization of magnetite within the feldspar interstices.

At least two sets of vesicles were identified. Those classified as "big" are 0.4-2.6 mm in diameter, round to lobate and arcuate, and are thought to represent the early vesiculation of the lava. The other set consists of more minute (0.02-0.3 mm), round- to lobate-shaped vesicles that were possibly produced during a second boiling after the lava's extrusion and subsequent expansion of its volatile content.

The mineralogical and textural features described here more or less also reflect the morphological character of the basalts from the other units. Subsequent unit descriptions, therefore, will be more synoptical. Significant differences and other characteristics of the other units that are unique from those of Unit 1, however, will be discussed.

Unit 2

Olivine dolerite

Unit 2 is a light gray, massive unit that is present between 1148.0 and 1184.5 mbsf or between Sections 124-768C-88R-2 at 50 cm and 124-768C-92R-1 at 0 cm. The total thickness drilled in this unit is 36.5 m, and <20 m was recovered. Unit 2 has been identified as a 33-m-thick unit from data collected during logging (see "Downhole Measurements" section, this chapter).

The upper contact with Unit 1 lies in Section 124-768C-88R-2 between 45 and 50 cm, where 5 cm of broken rock is present. Below this, the rocks of the sill are very fine grained and contain quenched plates of olivine and numerous extremely small vesicles. There is a gradual increase in grain size from this aphanitic top into the body of the unit, which is generally phaneritic (average grain size = 2 mm). This increase in grain size, when combined with the thickness, homogeneity, and phaneritic texture, indicates that Unit 2 is a sill with a chilled margin against the lavas of Unit 1 above.

The rock is made up of olivine, plagioclase, and pyroxene in intergranular intergrowths and is classified as an olivine dolerite. In detail, the unit is characterized by a patchy or veinlike and layered distribution of coarser and finer texture, and by abundant vesicles up to 2 mm in diameter. The vesicles are most abundant in the coarser-textured parts of the unit and are filled with green clay. The bottom contact with the lavas below was not recovered. There are a few thin (<2 mm), irregular, vertical to steeply dipping veins filled with carbonate or green and red clay present in the rock. In addition, one flat-lying thin fracture (<1 mm) contains hematite.

Unit 2 consists of olivine dolerite that is rarely porphyritic. Where phyric, the samples contain olivine (0.26–1.3 mm) as the sole phenocryst mineral, making up 10%–15% of the rocks. Although evidently euhedral, the crystals are subrounded and are severely altered to clay, actinolite, and calcite, such that grains in Samples 124-768C-89R-2, 3–4 cm, and 124-768C-89R-2, 7–10 cm, are almost completely dark and amorphous.

The groundmass of these two samples consists of 52%–54% labradoritic, sporadic bytownitic plagioclase (0.04%–1.85 mm) laths, <1% subhedral colorless clinopyroxene (0.01–1.6 mm), about 20% glass mesostasis, and 1%–3% magnetite grains in intersertal relation. Devitrification and moderate alteration has obscured and darkened the interstitial glass. Actinolite is also present in the interstices, probably altering fine-grained pyroxene or olivine crystals.

In Sample 124-768C-91R-2, 104–107 cm, the olivine is totally replaced by clays. Spinel inclusions are not encountered very often. The rock groundmass is made up of fine- to medium-grained (0.05–2.22 mm), simple to polysynthetically twinned, plagioclase (An_{50-70}), subhedral clinopyroxene, interstitial glass mesostasis, and crystallites and magnetites. The pyroxenes are fresh, but the plagioclase laths show slight to moderate clay (kaolinite/illite?) alteration along cracks. The same alteration replaces the interstitial materials.

The rest of the eleven samples taken from this unit are aphyric. The texture varies from intersertal to intergranular, and the mineralogical composition is similar to the phyric varieties. Olivine, however, is not present in some samples. Vesicles are sparse to abundant. Sample 124-768C-88R-2, 100–101 cm, represents the top portion of the unit. This rock, compared with the rest of the dolerites, is the most fine-grained sample.

Abundant plagioclase (50%) and clinopyroxene (25%) are more intersertal than intergrown and may exhibit divergent orientation. Interstitial to the laths and prisms are clay, actinolite, and carbonate, which probably replaced glass mesostasis. Crystallites are superimposed on the well-crystallized phases, forming divergently distributed granules with birefringence similar to that of pyroxene. These crystallites are more often masked by turbid, dark, optically indeterminable, muddy or clayey aggregates that could have developed from devitrification. Relic olivine pseudomorphed by clay and iron oxides are sparsely present (2%).

In one section (124-768C-89R-1, 69–70 cm), there are ponds and bays of glassy material, with abundant plagioclase that ranges from microlitic to fine- and medium-grained crystals. The grain boundaries of the coarser crystals that delimit these glassy portions are corroded and penetrated, similar to features described earlier for the phyric dolerites. Although grain size and textural changes are very subtle, there is a very slight coarsening of Unit 2 at depth.

The intergranularity between the plagioclase and the pyroxene crystals also becomes more pronounced with depth. In Sample 124-768C-91R-2, 104–107 cm, penetrations of plagioclase to plagioclase, plagioclase to pyroxene, and pyroxene to plagioclase were observed. Pyroxene to pyroxene penetration is absent or cannot be distinguished in the relationships between subhedral minerals. Although pyroxene invades the plagioclase crystals, it only does so along the immediate edges of the latter. More commonly, the minute pyroxene crystals are delimited along the plagioclase edges and end up as interstitial material.

The vesicularity of this unit ranges from 0% to 20%. The vesicles are not very obvious because of the coarse nature of the rocks and their similarity in appearance to interstitial mesostasis. Clays similar to those in Unit 1 and calcite fill the vesicles. Alteration is moderate and consists mainly of (1) turbid, dark to amorphous clay that obscures the general appearance of certain sections; (2) actinolite, which partly replaces mesostasis, olivine, and—rarely—pyroxene; (3) green and yellow-green clays that alter the mesostasis and the olivine; and (4) iron oxides that stain the groundmass and partly replace the olivine.

Unit 3

Olivine microgabbro and sill

Unit 3 is a dark gray, massive unit that is present between 1184.5 and 1210.4 mbsf or between Sections 124-768C-92R-1 at 0 cm and 124-768C-95R-1 at 0 cm. The total thickness of this unit is 25.9 m, and <12 m were recovered. Logging shows the unit as 22 m thick (see "Downhole Measurements" section, this chapter).

There is a gap of >6.6 m in the core above the top of this unit, and the nature of the contact with Unit 2 is unknown. At the base of this unit, 8.2 m of core is missing. The discrepancy between the thickness calculated from the core and the thickness shown on the logs indicates that the majority of this missing material is from the pillow basalt unit that is present below the sill.

The rock has a phaneritic, hypidiomorphic-granular texture with an average grain size from 1 to 2 mm; it contains very few vesicles. Unit 3 is composed mainly of an intergrowth of olivine, plagioclase, and pyroxene and is classified as an olivine microgabbro. Orthopyroxene, minor hornblende, and biotite are also present in Unit 3, which distinguishes it from the olivine dolerite of Unit 1. The petrography of this sill is very homogeneous and is interpreted as representing one cooling unit.

The microgabbro is cut by numerous steeply dipping to horizontal fractures that are filled with gypsum, carbonate, and hematite. The hematite generally is present on the outside of the veins, which indicates that it was emplaced earlier than the gypsum-carbonate mixtures. The nature of the contact between Units 3 and 4 cannot be determined because of the missing part of the core described above.

This basement unit, which is regarded as an olivine microgabbro, aside from having major components similar to those of Units 1 and 2 (plagioclase, clinopyroxene, olivine, and mesostasis), also contains orthopyroxene (65%–10%), hornblende (<1%–3%), biotite (<1%–10%), and accessory apatite. The general texture is hypidiomorphic granular.

Olivine, which composes 13%–20% of the rocks of this unit, is present as wholly altered idiomorphic but rounded crystals, not unlike those of the dolerites. These crystals are partly or entirely engulfed by plagioclase and pyroxene crystals. Pyroxenes (clinopyroxene = 24%–30% and orthopyroxene = 6%–10%) are anhedral to subhedral and are ophitically to subophitically intergrown with the plagioclase. The inclusion of complete plagioclase crystals within the pyroxene is not uncommon.

The abundant (35%–50%) plagioclase appears to be marginally more calcic (An_{75-85}) than those of the previous units. Some crystals show polysynthetic twinning and colloform zoning but lack the corroded cores common to the plagioclases of the dolerites. Hornblende, which exhibits light brown cores and greenish rims, is present as isolated subhedral crystals, as epitaxial intergrowths with clinopyroxene, and as rare, minute, whole inclusions in the pyroxene.

In Sample 124-768-93R-3, 77–78 cm, biotite is abundant (20%) and exhibits bright pleochroism from light brown to green. In contrast to the epitaxially grown hornblende, the biotite encloses pyroxenes, plagioclases, and olivine crystal grains. In some instances, the biotite appears to have grown at the expense of the pyroxene grains, such that it seems to replace peripheral areas of the latter incipiently. Biotite is also present as occasional networks that invade the fractured plagioclase crystals and as sheafs superimposed on some olivine grains.

Apatite needles are present only in accessory amounts.

Vesicles are hardly noticeable because of the coarse texture, granularity, and hypocrystallinity of Unit 3. Where they have been identified, they are completely filled with the high-relief, highly birefringent mineral described in Unit 1, which persists throughout the entire basement lithology.

Abundant (5%–20%) hydrous micas, mainly celadonite and illite, form patches and reticulating networks, respectively, that invade and replace the primary crystals. Bright green to blue-green celadonite forms from the mafic minerals, and illite partly replaces plagioclase along the borders and cracks and completely alters mesostasis between the plagioclase laths.

Chlorite and actinolite are in close association and also alter the mafic rocks. The rounded olivine grains are rendered dark and turbid by the "dusty" clay that masks all of the crystals entirely and obscures the highly birefringent secondary mineral common to the olivines and the vesicles.

Unit 4

Sparsely olivine-phyric to aphyric basalt, pillowed and brecciated

Unit 4 is present between 1210.4 and 1240.9 mbsf or between Sections 124-768C-95R-1 and 124-768C-98R-2. The thickness of the unit as defined by coring is 30.5 m, and <12.5 m was recovered. It is made up of fractured and brecciated pillows that vary in diameter from <50 cm to >1 m. No separate cooling units were recognized.

The larger pillows are most abundant in the lower part of Unit 4 in Sections 124-768C-96R-1 to 124-768C-98R-1. The smaller pillows have thicker selvages and variolitic zones than the larger ones. Generally, the rocks are aphyric basalts, and some of the larger pillows in Section 124-768C-96R-1 have a particularly well-developed intersertal texture. There is a very oxidized zone in the pillows that starts in Section 124-768C-96R-2 and becomes increasingly prominent throughout Sections 124-768C-97R-1 and 124-768C-97R-2.

All of the basalts contain large numbers of small vesicles throughout the groundmass that also include several larger, more scattered vesicles, which taken together compose up to 50% of the rock. They are filled or partially filled with dark green clay and carbonate/chalcedony mixtures. The fractures in Unit 4 are irregular and vertical to steeply dipping, and are filled with red clay and mixtures of carbonate and chalcedony. Three cooling units may be present in this lithologic unit: (1) the fairly small pillows at the top of the sequence down to Section 124-768C-96R-1; (2) the larger pillows with the well-developed intersertal texture that are present in Sections 124-768C-96R-1 to 124-768C-96R-3; and (3) the larger pillows, which lack this texture, at the base of the section.

Unit 4 is represented by pillow basalts that consist of sparse to moderate (1%–10%), olivine phyric and aphyric basalt and olivine dolerites. The basalts are similar to the rocks of the Unit 1 pillows. At chilled margins, the extremely glassy rocks exhibit a variolitic texture. The more crystalline varieties have intersertal and divergent textures. As in Unit 1, the only observable phyric phase in this unit is olivine as isolated crystals and glomerocrysts. Where present, the olivine crystals are euhedral and show the same type of alteration as those in Unit 1.

The vesicular groundmass consists of plagioclase, clinopyroxene, and mesostasis in the proportions shown in Table 16. Sample 124-768C-96R-1, 106–108 cm, however, is virtually olivine free. The rock is composed of acicular and microlitic plagioclase and clinopyroxene microlites, crystallites, and darkly pigmented (devitrified) glass mesostasis. Compared with the basalts of Unit 1 and others of this unit, the acicular plagioclase crystals in this sample are more elongated. Furthermore, the pyroxenes, though minute, are prismatic and not granular. Of the 25% vesicles present, <1% are filled with green smectite, and the rest are empty.

The olivine dolerites represent the interior of the larger pillows. One of the two samples (124-768C-96R-3, 126–128 cm) is an intersertal to intergranular rock with subhedral clinopyroxene prisms interlocking or subophitically intergrowing with the plagioclase laths. Olivine is a minor constituent and is altered to clay and calcite. Ponds and bays of finer and glassier material are analogous to those of Unit 2. Brown globular clays, probably smectite, either fill or line the rims of vesicles and partly replace some olivine crystals. The omnipresent high birefringence fibrous clay are a later filling and replacement to vesicles and olivine, respectively.

The other dolerite sample (124-768C-97R-3, 58–59 cm) is quite different from the previous one in that it contains concentrations of clinopyroxene crystals as prisms and prismlets arranged in a radiate fashion. The idiomorphic nature of the prismatic microcrysts, their arrangement, and their relation to the groundmass indicate that they are not of xenocrystic derivation (i.e., their formation is within the crystallization process of the groundmass). Zeolites filling vesicles and replacing plagioclases are another distinguishing characteristic of this sample. Beside the zeolites, green smectite and chlorite are also present as earlier fillings or as linings to the vesicles.

Unit 5

Sparsely olivine-phyric basalt, sheet flow

Unit 5 is present between 1240.9 and 1249.35 mbsf or between Sections 124-768C-98R-2 and 124-768C-99R-1 at 25 cm. It is 8.45 m thick according to the drilling logs, and <3 m was recovered. There is 10 cm of broken rock at the bottom of Section 124-768C-98R-1 immediately above the top of Unit 5; therefore, no core seems to be missing at the boundary between the two units. However, the nature of the contact is not seen, and there is no evidence of a quenched or scoriaceous upper surface on the lava.

All of the recovered section is uniform in lithology, and the unit is thought to comprise one lava flow. It is made up of vesicular olivine-phyric basalt with <5% olivine phenocrysts. Small vesicles are distributed throughout the groundmass, and larger vesicles are scattered through the rock. They are filled with green clay and carbonate. The lava is cut by a few thin (<2 mm) irregular fractures, which are vertical or steeply dipping and are filled with carbonate and red clay, with minor hematite.

The lava sheet composing Unit 5 is represented by one sample (124-768C-98R-3, 69–69 cm), which is a very sparsely (<1%) olivine phyric basalt composed of intersertally related acicular plagioclase laths, subhedral to prismatic, and microlitic pyroxene, skeletal olivine, and crystallites and glass mesostasis. Compared with the basalts of the previous units, the crystals of this sample are similar to those in Sample 124-768C-96R-1, 106–108 cm, which was described in Unit 4. Unlike that sample, the Unit

5 rock has well-crystallized idiomorphic prisms and subhedral granules of clinopyroxene.

Another marked distinction of this sample is the filling of some of the vesicles by tabular zeolites and the apparent absence of the high-relief clay filling, which is persistent in all the above units. As opposed to the gray birefringence and fibrous appearance in crossed polars of the zeolite discussed in Unit 4, the zeolite fillings of this sample are characterized by white to lower first-order yellow birefringence and a consistent tabular habit even in crossed polars. Only about 3%–5% of the vesicles present are filled with the zeolite amygdules. The rest are empty.

The mesostasis in between the laths is speckled by acicular opaque minerals, probably secondary iron oxides. The mesostasis and the plagioclases show moderate kaolinite alteration. The skeletal olivine crystals are all largely altered to iddingsite and iron oxides.

Unit 6

Sparsely olivine-phyric basalt, pillowed and brecciated

Unit 6 is present between 1249.35 and 1259.35 mbsf or between Sections 124-768C-99R-1 at 25 cm and 124-768C-100R-1 at 55 cm. It is 10 m thick according to the drilling records, and <5.5 m was recovered. No core is missing at the top of the unit, but the sheet lava above is fractured at the base. The fractures are filled with red clay, and the lava lies directly on pillow fragments below. Unit 6 consists entirely of rather small pillows (<50 cm in diameter) with very well-developed pillow margins and interpillow fill.

The rocks are olivine-phyric basalts, which contain numerous small vesicles that are present together with less abundant larger vesicles (<2 mm), composed of approximately 30% of the rock and filled with dark green clay. The fractures are fairly abundant and are irregular, vertical to steeply dipping, and filled with mixtures of carbonate, chalcedony, and red clay. The lithology and size of the pillows are very uniform, and the unit is thought to represent one cooling unit.

The three samples analyzed for Unit 6 are sparsely olivine-phyric basalts with analogous characteristics to the basalts of Unit 1. The texture varies from variolitic to divergent. The 1%–3% olivine phenocrysts are, as in the other units, wholly altered to iron oxides and clay. Microlitic and skeletal plagioclase crystals are present as bow-tie structured aggregates with abundant glass mesostasis along their interstices. Pyroxene is a very minor constituent that is present mostly as microlites. Vesicles are of two size ranges (as in Unit 1) and are filled or lined with the high relief-highly birefringent fibrous clay mineral.

One sample from a chilled portion (124-768C-99R-2, 100–104 cm) consists dominantly of plumose crystallites without any definite mineral character. Within the feathery aggregates are very rare granules and sporadic dendritic-quenched crystals of pyroxene. The even sparser microlites of plagioclase are present only inside varioles, where they exhibit a bow-tie structure along with the turbid, radially distributed crystallites. The whole section, in general, is obscured by a murky dark brown devitrification pigment.

We recognized two filling stages in the vesicles. The first stage deposited a colorless, fibrous, high-relief clay mineral that lined the walls of the vesicles. The second stage filled the remaining space with light green scaly to fibrous microcrystalline clay aggregates that are possibly smectites. These same minerals, plus a yellow-green, highly birefringent clay mineral and calcite, also replace the relic olivine crystals and fill the 1–3-mm fractures that traverse the section.

Unit 7

Sparsely to highly olivine-phyric basalt, sheet flow

Unit 7 is present between 1259.35 and 1261.2 mbsf or between Sections 124-768C-100R-1 at 55 cm and 124-768C-100R-2 at 90 cm. It is 1.85 m thick according to the drilling logs. There is no core missing between this unit and Unit 6 above, but 10 cm of broken rock fragments is present at the actual contact. No pillow margins or fragments are present in Unit 7, and its general characteristics indicate that it is a single lava flow.

Below the contact, the rock is fine grained and full of pipes and vesicles. The grain size and olivine content of the rock increase, and the number of vesicles decrease, toward the base of the unit. The vesicles are filled principally with chalcedony and minor carbonate, and the green clay and irregular fractures with mixtures of carbonate and chalcedony.

Unit 7 is another sheet flow, which ranges from sparsely to highly olivine phyric basalt. One of the three samples (124-768C-100R-2, 17–19 cm), however, is aphyric. Except for this contrast, it is very similar to Sample 124-768C-100R-2, 53–55 cm, which is a phyric rock with 15% totally altered olivine phenocrysts (0.3–1.0 mm) set in an intersertal to subophitic groundmass composed of 32% plagioclase (0.03–1.0 mm), 18% subhedral clinopyroxene (0.05–1.0 mm), and 18% glass mesostasis. Two sets of vesicles are present, which are filled with the same clay material as in Unit 6, and calcite.

Sample 124-768C-100R-1, 115–119 cm, of this unit differs from the other two described above in terms of pyroxene content, vesicle size, and vesicle fillings. This sample contains less microlitic pyroxene (2%) and has a maximum vesicle size of 6 mm. Zeolites (mainly thomsonite) and carbonates (aragonite partly inverted to calcite) are present in the vesicles with the clay.

As a whole, alteration of the rocks is moderate. The clinopyroxenes are fresh whereas the plagioclase laths may show some clay alteration along with the mesostasis and the crystallites. All olivine crystals are completely altered and pseudomorphed by iron oxides and clay. The zeolite-bearing sample seems to be the most altered, with stains of reddish iron oxides obscuring the section. Devitrification of the mesostasis and the crystallites impart a dark turbid appearance to the rocks.

Unit 8

Moderately olivine-phyric basalt, pillowed and brecciated

This unit is present between 1261.2 mbsf and the bottom of the cored material at 1268.5 mbsf. Only 50 cm of this unit was recovered in Section 124-768C-100R-2 from 90 to 140 cm.

The contact with the sheet lava above was not seen, but 10 cm of broken rock is present in the core between the two units. The unit comprises moderately olivine-phyric basalt pillow lavas very similar to the pillow lava units above. The rocks contain 8%–10% olivine phenocrysts set in a fine-grained, intersertal groundmass of plagioclase, clinopyroxene, and mesostasis.

BASEMENT GEOCHEMISTRY

We analyzed a total of 33 rock samples from Hole 768C on board by X-ray fluorescence (XRF). Major elements and some trace elements (Nb, Zr, Y, Sr, Rb, Zn, Cu, Ni, Cr, V, Ce, and Ba) were determined for all samples. The sample preparation technique and the analytical procedures are outlined in the "Explanatory Notes" chapter (this volume).

Sampling was addressed mainly to a chemical characterization of the lithologic units distinguished by petrography and structure. Two main aspects were considered for sampling strategy: the overall high degree of alteration of the rocks through all the basement section and the highly variable petrography, in particular the variation in the olivine content of the pillow lavas. Each aspect implies problems of representing the chemical data as a whole, as well as that of each analyzed sample.

To minimize these problems, samples were taken from homogeneous, mostly fine-grained rocks that were expected to keep their original composition the best, at least for those elements that are less mobile during secondary processes. In the pillow lava sequences, samples were taken mostly from inner parts of pillows and with fairly high frequency to provide average compositions. Suitable samples for chemical analysis were taken from the two upper pillow lava units (Units 1 and 4); however, no analyzable samples were found in the lower two units (Units 6 and 8), given the high degree of alteration.

The location of the analyzed samples and their essential petrography are reported in Table 17. Major element analyses are listed in Table 18, trace element analyses in Table 19, and CIPW norms in Table 20. Normative values were calculated on a dry basis with $Fe_2O_3/(Fe_2O_3 + FeO) = 0.15$.

Magmatic and Secondary Features

As reported in the "Basement Lithology" section (this chapter), basement rocks from Site 768 have been pervasively altered to a variable, but generally large extent, so that, for instance, no olivine or glass has been preserved. Furthermore, all basalts and dolerites are characterized by finely amygdaloidal textures related to the filling of disseminated vesicles by secondary minerals. To evaluate the chemical data, the effects of magmatic phase replacement and the addition of secondary minerals to the rock volume must be considered as partially responsible for major chemical changes. These aspects are briefly summarized below for the rock units distinguished by petrography.

Olivine Basalts from Pillow Lava Units (Units 1 and 4)

The most deeply altered basement rocks were encountered among pillow basalts. Alteration generally increases downward in the section. The rocks are glass rich or glassy and highly vesicular in origin. The magmatic minerals present are plagioclase, clinopyroxene (even in skeletal crystals), and chrome spinel. Olivine is pseudomorphed by clay minerals, calcite, or both, and accompanied by iron hydroxides.

Plagioclase is typically replaced in cores by K-feldspar, but it also appears partially to completely replaced by clay minerals. The glassy mesostasis is devitrified and replaced by variable amounts of clay minerals and sometimes by zeolites. With the only exception being the glassy margins of pillows, the filling of ubiquitous vesicles with clays, minor iron hydroxides, and carbonates constitutes a significant component, which adds about 10% average volume to the original rock.

Olivine Basalt from Massive Lava (Units 5 and 7)

The thin lava sheets are similar in primary features and alteration to the pillow lavas. The two thick lava sheets from the lower section contain more abundant and coarser magmatic minerals, particularly pyroxene. Pyroxene and chromium-spinel are unaltered, and plagioclase is largely replaced by clay minerals and K-feldspar in Unit 5 and by clay minerals and zeolites in Unit 7. Olivine is mostly calcitized, and the mesostasis is replaced by clays and zeolites. Vesicles are filled with clays and zeolites.

Olivine Dolerite from Upper Sill (Unit 2)

Primary minerals include olivine, labradorite, clinopyroxene, and minor iron-titanium oxides and chromium-spinel. With the exception of olivine, they are fresh. Hypocrystalline-altered mesostasis and amygdules filled with clays and zeolites are abundant.

Olivine Microgabbro from the Lower Sill (Unit 3)

The texture is holocrystalline and vesicles are absent. Olivine is completely altered; chromium-spinel and clinopyroxene are fresh; and plagioclase, iron-titanium oxides, orthopyroxene, hornblende, and biotite are moderately to largely altered. The secondary minerals consist mostly of actinolite, chlorite, and celadonite.

Table 17. Summary of hard rock units, XRF-analyzed samples, sample depth, and petrography of basement rocks from Site 768.

Hard rock unit	Core, section, interval (cm)	Depth (mbsf)	Rock type (modal composition)
Olivine basalt (pillows lava):			
1	124-768C-73R-1, 124–127	1047.84	Ol phyric basalt (12% Ol, 22% Pl, 10% Cpx, 26% Ms, 30% Amg)
1	124-768C-74R-1, 23–28	1056.53	Ol phyric basalt (12% Ol, 20% Pl, 15% Cpx, 23% Ms, 30% Amg)
1	124-768C-75R-1, 137–142	1067.27	Ol phyric basalt (10% Ol, 29% Pl, 7% Cpx, 29% Ms, 25% Amg)
1	124-768C-76R-1, 134–137	1076.94	Ol phyric basalt (10% Ol, 25% Pl, 10% Cpx, 37% Ms, 15% Amg)
1	124-768C-76R-3, 72–75	1079.17	Ol phyric basalt (7% Ol, 37% Pl, 3% Cpx, 33% Ms, 20% Amg)
1	124-768C-77R-1, 65–68	1081.25	Ol phyric basalt (6% Ol, 40% Pl, 2% Cpx, 20% Ms, 32% Amg)
1	124-768C-77R-2, 51–55	1082.55	Ol phyric basalt (10% Ol, 20% Pl, 12% Cpx, 30% Ms, 32% Amg)
1	124-768C-77R-2, 108–111	1083.12	Ol phyric basalt (10% Ol, 5% Pl, 22% Cpx, 39% Ms, 24% Amg)
1	124-768C-78R-1, 7–10	1085.67	Ol phyric basalt (8% Ol, 18% Pl, 12% pcx, 30% Ms, 32% Amg)
1	124-768C-79R-2, 122–124	1093.26	Ol phyric basalt (14% Ol, 8% Pl, 18% Cpx, 38% Ms, 22% Amg)
1	124-768C-80R-3, 5–7	1098.50	Ol phyric basalt (8% Ol, 32% Pl, 35% Ms, 25% Amg)
1	124-768C-82R-2, 89–92	1107.94	Ol phyric basalt (10% Ol, 37% Pl, 30% Ms, 20% Amg)
1	124-768C-83R-1, 134–137	1111.94	Ol phyric basalt (6% Ol, 28% Pl, 38% Ms, 28% Amg)
1	124-768C-84R-2, 102–105	1118.12	Ol phyric basalt (12% Ol, 18% Pl, 7% Cpx, 23% Ms, 25% Amg)
1	124-768C-85R-2, 59–61	1122.61	Ol phyric basalt (16% Ol, 20% Pl, 4% Cpx, 30% Ms, 27% Amg)
1	124-768C-86R-1, 48–50	1127.08	Ol phyric basalt (10% Ol, 20% Pl, 10% Cpx, 27% Ms, 33% Amg)
1	124-768C-87R-1, 50–53	1136.80	Ol phyric basalt
1	124-768C-87R-2, 132–136	1139.03	Ol phyric basalt (8% Ol, 31% Pl, 10% Cpx, 25% Ms, 25% Amg)
1	124-768C-88R-2, 30–34	1147.62	Ol phyric basalt (10% Ol, 18% Pl, 2% Cpx, 40% Ms, 30% Amg)
Olivine dolerite (sill):			
2	124-768C-88R-2, 58–62	1147.90	Ol dolerite
2	124-768C-88R-2, 96–100	1148.28	Ol dolerite (2% Ol, 50% Pl, 25% Cpx, 18% Ms, 3% Amg)
2	124-768C-90R-3, 59–63	1168.50	Ol dolerite (8% Ol, 55% Pl, 8% Cpx, 15% Ms, 10% Amg)
2	124-768C-91R-1, 136–140	1176.26	Ol dolerite (2% Oi, 37% Pl, 30% Cpx, 8% Ms, 20% Amg)
Olivine microgabbro (sill):			
3	124-768C-92R-1, 61–65	1185.11	Ol-Cpx microgabbro (20% Ol, 40% Pl, 25% Cpx, 15% Other)
3	124-768C-93R-1, 116–119	1192.66	Ol-Cpx-Opx microgabbro (15% Ol, 50% Pl, 20% Cpx, 10% Opx, 5% Other)
3	124-768C-93R-3, 78–81	1195.23	Ol-Cpx-Opx microgabbro (20% Ol, 35% Pl, 20% Cpx, 6% Opx, 19% Other)
3	124-768C-94R-1, 72–77	1201.42	Ol-Cpx microgabbro (13% Ol, 47% Pl, 27% Cpx, 23% Other)
Olivine basalt (pillow lavas)			
4	124-768C-95R-1, 30–38	1210.70	Ol phyric basalt (10% Ol, 15% Pl, 5% Cpx, 38% Ms, 30% Amg)
4	124-768C-96R-1, 108–111	1221.08	Aphyric basalt (35% Pl, 15% Cpx, 22% Ms, 25% Amg)
4	124-768C-97R-3, 55–59	1233.01	Ol basalt (2% Ol, 25% Pl, 33% Cpx, 20% Ms, 20% Amg)
Olivine basalt (massive lava)			
5	124-768C-98R-3, 69–72	1242.86	Ol basalt (2% Ol, 7% Pl, 1% Cpx, 65% Ms, 25% Amg)
Aphyric basalt (massive lava)			
7	124-768C-100R-2, 13–19	1260.43	Aphyric basalt (50% Pl, 20% Cpx, 15% Ms, 10% Amg)
7	124-768C-100R-2, 53–59	1260.83	Ol phyric basalt (15% Ol, 32% Pl, 18% Cpx, 20% Ms, 13% Amg)

Note: Ol = olivine, Pl = plagioclase, Cpx = clinopyroxene, Opx = orthopyroxene, Ms = glassy or cryptocrystalline mesostasis, Amg = amygdules, Other = accessory and secondary minerals.

Major Element Chemistry

Major element chemistry (Table 18) shows that the basement rocks are basaltic, are high in MgO, and contain large compositional variations. The alteration is clearly evidenced by the high

Table 18. Major element composition of the igneous rocks from Site 768.

Core, section, interval (cm)	SiO_2	TiO_2	Al_2O_3	Fe_2O_3	MnO	MgO	CaO	Na_2O	K_2O	P_2O_5	Total[a]	LOI	Mg#
124-768C-													
73R-1, 124–127	47.82	0.80	15.48	9.75	0.29	14.06	8.2	1.73	0.58	0.16	98.87	8.08	77
74R-1, 23–28	47.68	0.82	15.65	9.16	0.21	13.29	9.81	1.65	0.45	0.17	98.89	6.68	77
75R-1, 137–142	48.55	0.80	15.26	8.77	0.19	12.35	10.02	2.03	0.69	0.15	98.81	6.76	76
76R-1, 134–137	49.26	1.07	17.18	9.73	0.2	8.13	8.92	2.19	1.89	0.17	98.74	5.94	66
76R-3, 72–75	49.79	1.02	16.45	9.15	0.25	10.97	7.81	2.02	1.79	0.18	99.43	6.95	73
77R-1, 65–68	49.22	1.04	17.04	10.29	0.17	9.85	8.04	2.23	0.98	0.18	99.04	6.03	69
77R-2, 51–55	49.94	1.02	16.61	9.76	0.17	10.07	7.12	2.35	1.07	0.2	98.31	5.82	70
77R-2, 108–111	50.27	1.06	16.53	8.95	0.19	9.61	8.88	2.39	1.08	0.17	99.13	9.88	71
78R-1, 7–10	49.31	0.99	16.42	9.43	0.18	10.68	8.47	2.21	1.16	0.18	99.05	8.37	72
79R-2, 122–124	49.51	0.94	16.28	10.28	0.16	10.97	7.82	2.37	0.93	0.2	99.45	8.58	71
80R-3, 5–7	48.86	1.11	17.17	9.68	0.19	10.83	8.43	2.61	0.7	0.18	99.75	7.41	72
82R-2, 89–92	48.95	0.98	16.48	10.73	0.18	11.25	8.12	2.08	0.56	0.17	99.5	5.58	71
83R-1, 134–137	48.97	0.98	16.18	10.01	0.18	10.1	7.93	2.83	1.47	0.19	98.84	6.49	70
84R-2, 102–105	48.46	0.99	16.19	10.2	0.21	12.59	7.12	1.87	1.68	0.17	99.5	9.2	74
85R-2, 43–61	49.52	0.98	16.13	9.37	0.2	11.84	7.29	2.23	1.02	0.17	98.75	5.67	74
86R-1, 48–50	50.22	0.98	15.66	10.44	0.19	10.42	7.76	1.94	1.38	0.25	99.25	8.4	70
87R-1, 50–53	48.95	0.96	15.92	9.61	0.18	13.55	7.01	2.13	0.79	0.17	99.27	7.25	76
87R-1, 109–112	48.5	1.01	16.14	9.45	0.2	12.14	7.82	2.05	1.05	0.19	98.56	0.49	75
87R-2, 132–136	48.77	1.03	16.58	9.15	0.22	11.84	8.51	2.1	1.27	0.19	99.65	6.47	75
88R-2, 30–34	49.24	1.08	16.09	10.31	0.18	11.7	6.5	2.35	1.03	0.19	98.67	7.31	72
88R-2, 58–62	51.69	1.04	16.27	9.23	0.18	7.97	8.18	4.01	0.43	0.18	99.18	3.76	66
88R-2, 96–100	50.03	1.05	16.63	8.78	0.2	7.88	9.87	3.19	0.54	0.16	98.33	3.48	67
90R-3, 59–63	52.86	1.05	16.01	9.03	0.16	6.89	9.52	3.29	0.37	0.15	99.33	4.09	64
91R-1, 136–140	49.69	0.89	17.51	8.05	0.19	8.14	11.2	2.24	0.95	0.11	98.97	3.53	70
92R-1, 61–65	48.85	0.83	15.14	9.15	0.14	15.11	9.13	1.46	0.07	0.1	99.97	4.02	79
93R-1, 116–119	48.12	0.65	11.65	11.79	0.17	17.17	7.16	0.96	0.07	0.1	97.86	4.86	77
93R-3, 78–81	47.19	0.75	12.54	10.42	0.14	18.89	7.98	0.76	0.05	0.1	98.83	6.89	81
94R-1, 72–77	48.12	0.82	12.9	10	0.18	15.3	8.83	1.7	0.08	0.17	98.11	6.41	78
95R-1, 30–38	48.66	1.02	15.99	9.52	0.34	11.94	8.58	1.86	0.84	0.18	98.93	5.94	74
96R-1, 108–111	52.95	1.10	14.56	9.24	0.23	8.17	6.25	3.96	1.97	0.17	98.6	4.22	67
97R-3, 55–59	49.34	0.94	16.98	8.41	0.15	6.83	9.85	4.75	0.34	0.16	97.75	5.77	65
98R-3, 69–72	49.82	1.13	17.91	9.99	0.21	8.52	7.27	3.52	1.33	0.18	99.88	6.48	66
100R-2, 13–19	50.17	1.09	16.2	9.26	0.22	7.45	9.91	3.05	0.79	0.15	98.29	4.15	65
100R-2, 53–59	49.44	1.04	14.19	10.9	0.2	8.47	10.68	3.35	1.12	0.16	99.56	5.79	64

Note: Major element values are given in wt% oxide.

[a] Totals systematically below 100% have been obtained from on-board analyses and are interpreted as resulting from hydration of the sample between ignition and weighing.

values during loss on ignition (LOI), particularly in lavas, and by the high and variable contents of K_2O. These results mostly reflect the water content of secondary phases and the replacement of plagioclase by K-feldspar at various stages, also evident in the petrographic observations.

Variations of other elements, particularly Na, Ca, and Mg, are difficult to evaluate in terms of alteration vs. primary abundances. However, the nature of the secondary minerals, in addition to K-feldspar (e.g., smectites and sodic zeolite), and their appearance in large amounts as vesicle fillings also indicates that the abundance of other elements, particularly Ne, Ce, and Mg, was significantly changed during alteration. The MgO shows, however, systematic variations relative to Zn within the different lithologic groups, a feature which indicates that its variations are controlled mostly by magnetic processes.

Major elements were used to classify and compare the distinct petrologic groups. The CIPW norms (Table 20) indicate that most basement rocks are olivine tholeiites. Two samples are quartz and nepheline normative. Major element distributions (particularly TiO_2, MgO, and Fe_2O_3) and Mg# (molar ratio = 100 MgO/[MgO + FeO], with FeO normalized to Fe_2O_3/[Fe_2O_3 + FeO] = 0.15) are significantly distinct for each lithologic unit.

The geochemical data allow a further distinction within the upper pillow lavas of Unit 1 into two separate units. Subunit 1A is represented by Samples 124-768C-73R-1, 124–127 cm, 124-768C-74R-1, 23–28 cm, and 124-768C-75R-1, 137–142 cm (1047.84–1067.27 mbsf). Subunit 1B was observed between Samples 124-768C-76R-1, 134–137 cm, and 124-768C-88R-2, 30–34 cm. Logging results show the interval between 1047 and 1057 mbsf to differ in its potassium content, resistivity, and density from the underlying unit (see "Downhole Measurements" section, this chapter). Major element variation patterns of the lithologic units downhole are shown in Figure 60, and their average compositions, normalized to 100% on a dry basis, are reported in Table 21.

The chemical differences in terms of primary magmatic features are unexpectedly significant for rocks that were severely affected by alteration. Consistent variations of major elements, except alkalis, and of Mg# clearly indicate variably fractionated magmas.

Units 1 and 4 (basaltic pillow lavas) are characterized by high MgO abundances and high Mg# ratio. If the absolute concentrations have not been drastically changed by alteration, they represent primitive magmas, with a picritic character. Olivine is present mostly as quench crystals and not as phenocrysts, which are present in chilled pillow margins. This implies that these magmas were erupted largely as liquids containing few olivine crystals, and that crystallization of olivine took place after eruption. It is therefore inferred that the MgO abundances reflect primary magnetic composition rather than olivine accumulation.

Unit 3 (microgabbroic sill) is characterized by high MgO and TiO_2 content. The K_2O is low and is probably close to the primary content, given the low degree of alteration. The high anorthite content of the normative plagioclase (83%–66%) is also distinctive. A possible enrichment in MgO, with an accumulation of olivine prior to the intrusion, may have taken place.

Table 19. Trace element chemistry of the igneous rocks from Site 768.

Core, section, interval (cm)	Nb	Zr	Y	Sr	Rb	Zn	Cu	Ni	Cr	V	Ce	Ba	Ti	Ti/Zr	Y/Zr	Ce/Zr	Ti/V
124-768C-																	
73R-1, 124–127	2	44	16	138	7	67	16	288	579	280	7	29	4796	109	0.36	0.16	17
74R-1, 23–28	0	48	16	158	5	74	42	280	470	268	10	5	4916	102	0.33	0.21	18
75R-1, 137–142	2	46	14	152	8	67	49	304	623	253	6	40	4796	104	0.30	0.13	19
76R-1, 134–137	2	65	25	129	16	81	17	181	586	374	11	30	6415	99	0.38	0.17	17
76R-3, 72–75	2	60	20	118	13	78	32	216	463	258	2	31	6115	102	0.33	0.03	24
77R-1, 65–68	3	63	29	134	15	92	40	234	478	315	16	13	6235	99	0.46	0.25	20
77R-2, 51–55	2	61	24	121	13	75	45	162	368	307	20	11	6115	100	0.39	0.33	20
77R-2, 108–111	2	64	20	129	12	84	56	189	384	303	12	1	6355	99	0.31	0.19	21
78R-1, 7–10	3	60	26	128	14	77	66	194	433	322	9	31	5935	99	0.43	0.15	18
79R-2, 122–124	3	57	30	130	14	84	59	229	432	331	14	10	5635	99	0.53	0.25	17
80R-3, 5–7	3	66	22	130	10	77	88	239	529	326	14	33	6654	101	0.33	0.21	20
82R-2, 89–92	3	61	23	126	9	85	55	230	490	294	13	0	5875	96	0.38	0.21	20
83R-1, 134–137	3	59	24	116	16	72	47	173	410	312	10	0	5875	100	0.41	0.17	19
84R-2, 102–105	2	56	21	112	15	71	52	200	457	312	8	31	5935	106	0.38	0.14	19
85R-2, 43–61	2	60	20	120	12	72	93	247	594	286	16	0	5875	98	0.33	0.27	21
86R-1, 48–50	3	58	33	120	18	63	31	175	415	311	18	12	5875	101	0.57	0.31	19
87R-1, 50–53	3	57	21	120	8	76	39	222	486	286	5	19	5755	101	0.37	0.09	20
87R-1, 109–112	3	61	23	129	11	71	40	215	461	316	6	12	6055	99	0.38	0.10	19
87R-2, 132–136	3	61	19	128	12	67	25	125	269	275	15	25	6175	101	0.31	0.25	22
88R-2, 30–34	2	66	22	124	15	70	49	212	410	302	12	8	6475	98	0.33	0.18	21
88R-2, 58–62	3	63	24	115	6	68	27	120	345	272	2	43	6235	99	0.38	0.03	23
88R-2, 96–100	3	66	24	135	8	60	24	88	250	282	8	23	6295	95	0.36	0.12	22
90R-3, 59–63	4	72	25	144	8	41	42	46	47	236	9	38	6295	87	0.35	0.13	27
91R-1, 36–140	2	48	20	138	11	38	32	78	106	279	10	30	5336	111	0.42	0.21	19
92R-1, 61–65	2	45	17	104	1	67	96	459	707	185	14	30	4976	111	0.38	0.31	27
93R-1, 116–119	2	40	16	71	2	67	119	758	1370	201	5	1	3897	97	0.40	0.13	19
93R-3, 78–81	2	42	16	79	2	83	32	691	1249	187	10	10	4496	107	0.38	0.24	24
94R-1, 72–77	3	63	23	102	0	64	33	541	1029	208	17	25	4916	78	0.37	0.27	24
95R-1, 30–38	3	66	21	126	12	75	55	218	408	294	10	0	6115	93	0.32	0.15	21
96R-1, 108–111	3	74	25	170	16	79	71	110	210	318	12	92	6594	89	0.34	0.16	21
97R-3, 55–59	3	58	24	111	6	60	65	98	251	278	13	15	5635	97	0.41	0.22	20
98R-3, 69–72	3	72	26	231	16	72	39	92	214	280	5	48	6774	94	0.36	0.07	24
100R-2, 13–19	2	73	26	180	9	78	21	132	214	289	19	18	6535	90	0.36	0.26	23
100R-2, 53–59	2	68	25	164	7	87	18	176	440	290	23	45	6235	92	0.37	0.34	21

Note: Trace element values are given in ppm.

The crystallization sequence (chromium-spinel/olivine-plagioclase/clinopyroxene-orthopyroxene, followed by the segregation of hydrous phases [i.e., amphibole and biotite], probably under intermediate conditions between magmatic and sub-solidus) and texture imply that the magma was injected already in a largely crystallized form. An accumulation of early crystallized phases (i.e., chrome spinel and olivine) could have taken place.

The dolerite sill (Unit 2) has a more fractionated basaltic composition relative to the previous ones. This is shown particularly by lower MgO, higher CaO and silica, and lower Mg# contents.

The two massive lavas from the lower basement section (Units 5 and 7) seem to be geochemically distinct from the other units, and from each other, on some major elements (MgO, CaO, Al_2O_3, and CaO/Al_2O_3 ratios). They are further characterized by trace element abundances.

Trace Element Chemistry

Given the high degree of alteration of the basement rocks, only trace elements that are known to be less mobile or immobile during secondary processes can provide reliable reference for a magmatic characterization. Particularly significant for the rocks studied are Zr, Y, Nb, V, and Cr. Concentrations of Nb and, in most samples, Ce show small values that are affected by relative large errors. Their variations, therefore, must be considered with care. Nickel is considered to be among the less-stable elements because its values appear to be significantly correlated with whole-rock chemistry.

Ranges of variations of trace elements within the lithologic units show significant differences that provide further evidence for their identification and characterization. Downhole variations for selected trace elements are shown in Figure 60, and average values are reported in Table 21 together with Ti abundances and some significant interelement ratios.

The basaltic pillow lavas are clearly distinguished by their Cr and Ni contents and by their incompatible elements, particularly Zr, Y, and Ce, which indicate a more primitive and depleted magma for Subunit 1A relative to Subunits 1B and 4. Units 5 and 6 (massive sheet lavas) are clearly distinct from pillow lavas by their higher Zr and Y contents and lower Cr and Ni values. The Ni and Cr variations between the two units reflect the differences in olivine and chromium-spinel contents.

The olivine dolerite (Unit 2) shows the lowest values of the compatible elements Ni and Cr among the basement rocks, implying an origin from evolved magma mainly by olivine fractionation. No significant increase in incompatible elements is concurrently displayed. Trace element concentrations in the olivine microgabbro (Unit 3) relative to the other units corroborate the marked differences observed in the major elements composition. In particular, Ni and Cr values are more than twice as large as those measured in the less-fractionated pillow lava unit. Zr, V, and Ti have lesser values.

Ratios of stable elements Zr, Ti, Y, and V, reported in Table 19, show fairly uniform values, which reflect systematic covariances of Ti, Y, and V relative to Zr, considered as fractionation indexes. Such covariations, displayed for Ti and Zr in Figure 61, can be related to fractionation from a common parent magma. Given the available data, therefore, it is inferred that the basement rocks could be cogenetic.

A preliminary investigation of the magmatic affinities of the basement rocks can be carried out with the available geochemical data in comparison with oceanic-ridge tholeiites and island-

Table 20. CIPW norms of the igneous rocks of Site 768.

Core, section, interval (cm)	Qz	Ne	Or	Ab	An	Di	Hy	Ol	Ap	Il	Mt
124-768C-											
73R-1, 124–127	0	0	3.5	14.91	33.37	5.76	21.29	17.28	0.36	1.55	1.98
74R-1, 23–28	0	0	2.71	14.21	34.58	11.24	17.34	16.1	0.38	1.59	1.86
75R-1, 137–142	0	0	4.16	17.5	31.05	15.03	12.17	16.42	0.33	1.55	1.78
76R-1, 134–137	0	0	11.42	18.9	32.09	9.83	12.02	11.31	0.38	2.08	1.98
76R-3, 72–75	0	0	10.73	17.31	30.9	5.89	18.24	12.72	0.4	1.96	1.84
77R-1, 65–68	0	0	5.91	19.2	34.17	4.37	22.82	9.03	0.4	2.01	2.09
77R-2, 51–55	0	0	6.49	20.38	32.39	2.15	28.03	6.13	0.45	1.99	1.99
77R-2, 108–111	0	0	6.49	20.54	31.66	9.78	19.7	7.6	0.38	2.05	1.81
78R-1, 7–10	0	0	6.99	19.02	31.98	7.84	17.72	12.23	0.4	1.92	1.91
79R-2, 122–124	0	0	5.58	20.32	31.44	5.44	20.64	12.25	0.44	1.81	2.07
80R-3, 5–7	0	0	4.19	22.3	33.38	6.32	13.0	16.35	0.4	2.13	1.95
82R-2, 89–92	0	0	3.36	17.83	34.42	4.4	25.59	9.97	0.38	1.89	2.16
83R-1, 134–137	0	0	8.87	24.41	27.62	9.22	4.93	20.59	0.42	1.9	2.03
84R-2, 120–105	0	0	10.08	16.03	31.21	2.91	16.41	19.02	0.38	1.91	2.06
85R-2, 43–61	0	0	6.16	19.24	31.59	3.48	23.84	11.51	0.38	1.9	1.9
86R-1, 48–50	0	0	8.3	16.67	30.4	5.87	28.71	5.48	0.55	1.89	2.11
87R-1, 50–53	0	0	4.75	18.29	32	1.87	23.33	15.6	0.38	1.85	1.94
87R-1, 109–112	0	0	6.35	17.73	32.42	4.93	19.41	14.84	0.42	1.96	1.92
87R-2, 132–136	0	0	7.6	17.95	32.38	7.39	13.07	17.37	0.42	1.98	1.84
88R-2, 30–34	0	0	6.23	20.31	30.95	0.73	24.87	12.29	0.42	2.1	2.1
88R-2, 58–62	0	0	2.59	34.45	25.5	11.91	10.49	10.8	0.4	2.01	1.87
88R-2, 96–100	0	0	3.27	27.63	30.15	15.45	9.26	10.03	0.36	2.04	1.79
90R-3, 59–63	1.29	0	2.22	28.21	28.2	15.34	20.57	0	0.33	2.02	1.82
91R-1, 136–140	0	0	5.72	19.26	35.48	16.49	11.91	7.55	0.24	1.72	1.63
92R-1, 61–65	0	0	0.42	12.44	34.79	8.22	28.74	11.74	0.22	1.59	1.83
93R-1, 116–119	0	0	0.43	8.38	28.13	6.38	43.3	9.46	0.23	1.28	2.42
93R-3, 78–81	0	0	0.3	6.56	31.27	6.84	34.43	16.81	0.22	1.46	2.12
94R-1, 72–77	0	0	0.49	14.77	28.07	12.77	25.13	14.74	0.38	1.6	2.05
95R-1, 30–38	0	0	5.06	16.02	33.39	7.18	22.25	11.79	0.4	1.98	1.93
96R-1, 108–111	0	0	11.91	34.22	16.46	11.53	8.88	12.61	0.38	2.14	1.88
97R-3, 55–59	0	6.09	2.07	30.13	24.71	20.06	0	13.01	0.36	1.84	1.72
98R-3, 69–72	0	0	7.94	30.04	29.38	4.86	2.85	20.35	0.4	2.17	2.01
100R-2, 13–19	0	0	4.79	26.44	28.86	16.8	10.22	8.53	0.34	2.12	1.89
100R-2, 53–59	0	0	6.72	22.84	20.63	26.18	0	15.9	0.35	2	2.2

Note: Values were calculated on the basis of an $Fe_2O_3/(Fe_2O_3 + FeO)$ ratio of 0.15 and normalized to 100%. Qz = quartz, Ne = nephaline, Or = orthoclase, Ab = albite, An = anorthite, Di = diopside, Hy = hypersthene, Ol = olivine, Ap = apatite, Il = ilmenite, and Mt = magnetite.

arc tholeiites. Basaltic magmas that range from normal MORB of variably transitional types to island-arc tholeiites are dominant in back-arc and marginal basins, together with basalts of calc-alkaline characteristics (Tarney et al., 1981; Pierce, 1982; Saunders and Tarney, 1984).

A comparison of selected basement samples with normal MORB (Fig. 62) shows that Site 768 basalts have lower contents of high-field-strength elements (Nb, Zr, Ti, and Y). These values are higher than in island-arc tholeiites. The Nb, Y, and Ti abundances are similar to average values of back-arc tholeiites (Holmes, 1985). The typical enrichment of hygromagmatophile (HYG) elements that characterize the transitional magmas flooring back-arc basins is also shown. However, with the possible exception of Sr, the contents of the analyzed HYG elements (Rb, Ba, K, and Sr) cannot be considered primary, but are mainly related to secondary changes by seawater alteration.

We can conclude, therefore, that the basement rocks from Site 768 have the main geochemical characteristics of MORB-related magmas mostly of primitive composition. Transitional features to island-arc tholeiite composition are possible, but they cannot be proven from the available data. However, the highly vesicular nature of the lavas and the appearance of hydrous minerals in the microgabbro point to an abnormal high water content, as is typical of arc-related magmas, and they testify to one of the magmatogenetic processes for island-arc tholeiites, that is, the contamination of mantle melts by fluids of crustal provenance.

Conclusions

The prominent petrochemical features of Site 768 basement rocks can be summarized as follows:

1. Site 768 basement rocks are dominantly olivine tholeiites of primitive composition and picritic tendency erupted at early crystallization stages, with olivine and chromium-spinel as liquidus phases.
2. Lavas are characterized by high vesicularity, an uncommon feature for magmas rich in MgO erupted at early crystallization stages, indicating a high water content of the magmas. Similar features have been observed in marginal and back-arc basalts, and are considered distinctive from MORB-type basalts with similar chemistry (Saunders and Tarney, 1984).
3. Chemical variations in lavas and the dolerite sill indicate a restricted range of fractionation products that are probably cogenetic.
4. The youngest erupted magmas represented by the upper pillow lavas and probably by the microgabbro sill have the most primitive compositions. This may indicate that a magma chamber was not present, as a consequence of a short-lived magmatism. A low spreading rate in the genesis of the basaltic seafloor may also be inferred.
5. Site 768 basement rocks are similar in crystallization order and contents of most stable elements to N-MORB type basalts. Observed depletions of high-field-strength elements could

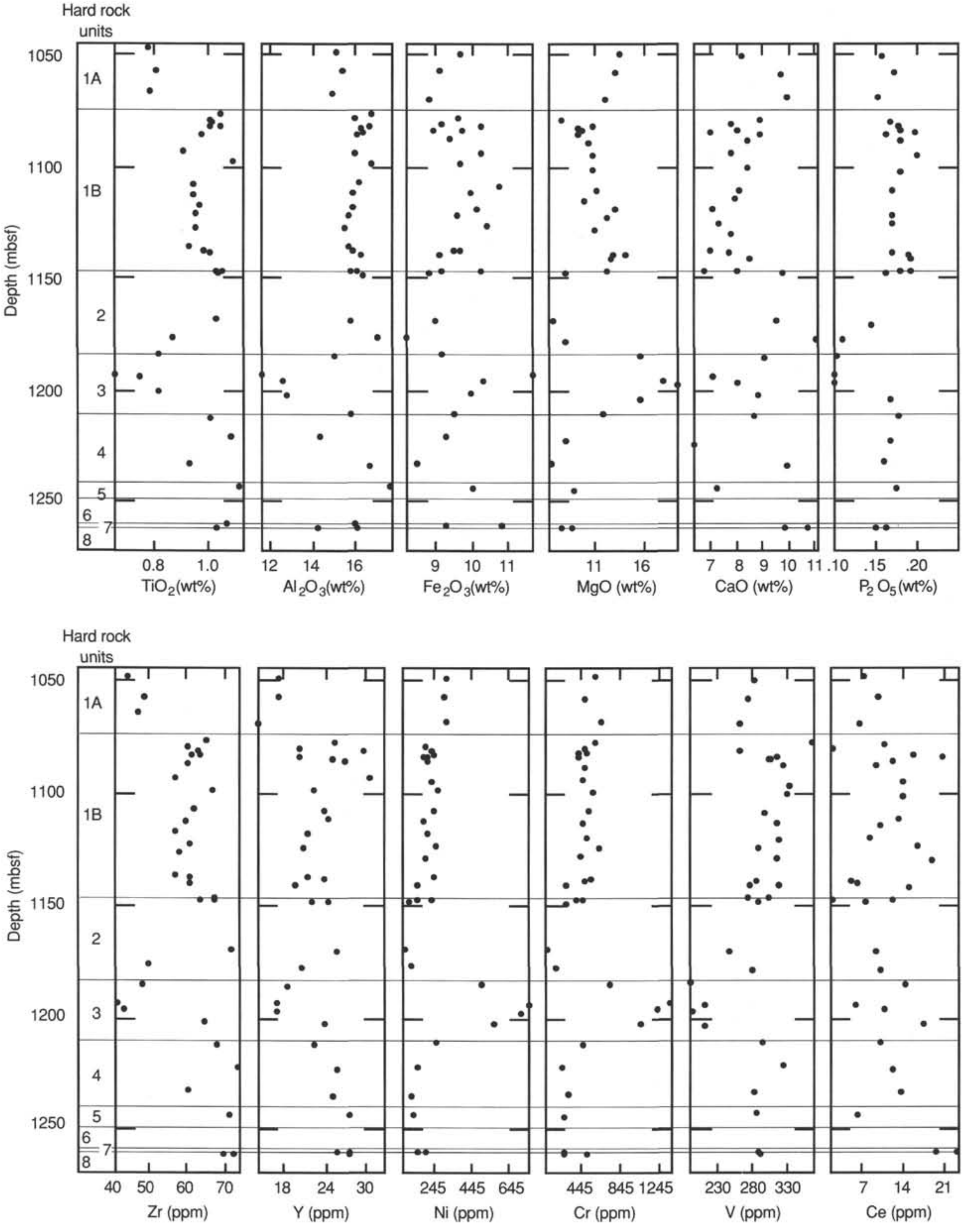

Figure 60. Downhole variations of selected major and trace elements in the basement rocks, Site 768. The boundaries of the petrologically recognized hard rock units and between Subunits 1A and 1B distinguished by chemistry are indicated.

Table 21. Average concentrations of major and trace elements of the hard rock units of Site 768 basement rocks.

Hard rock unit	Major elements											
	SiO_2	TiO_2	Al_2O_3	Fe_2O_3	MnO	MgO	CaO	Na_2O	K_2O	P_2O_5	LOI	Mg#
1A	48.02	0.81	15.46	9.23	0.23	13.23	9.34	1.80	0.57	0.16	7.17	77
1B,4	49.43	1.02	16.33	9.69	0.20	10.67	7.91	2.43	1.15	0.18	6.59	72
2	51.07	1.01	16.61	8.77	0.18	7.72	9.69	3.18	0.57	0.15	3.72	67
3	48.07	0.76	13.06	10.34	0.16	16.62	8.28	1.22	0.07	0.12	5.55	79
5	49.82	1.13	17.91	9.99	0.21	8.52	7.27	3.52	1.33	0.18	6.48	66
7	49.81	1.07	15.20	10.08	0.21	7.96	10.30	3.20	0.96	0.16	4.97	64

	Trace elements												
	Nb	Zr	Y	Sr	Rb	Ni	Cr	V	Ce	Ba	Ti	Ti/Z	Y/Zr	Ti/V
1A	1	46	15	149	7	291	557	267	8	25	4836	105	0.33	18
1B, 4	3	62	24	126	13	193	427	306	12	19	6085	99	0.38	20
2	3	62	23	133	8	83	187	267	7	34	6040	98	0.38	23
3	2	48	18	89	1	612	1089	195	12	17	4571	98	0.38	23
5	3	72	26	231	16	92	214	280	5	48	6774	94	0.36	24
7	2	71	26	172	8	154	327	290	21	32	6385	91	0.36	22

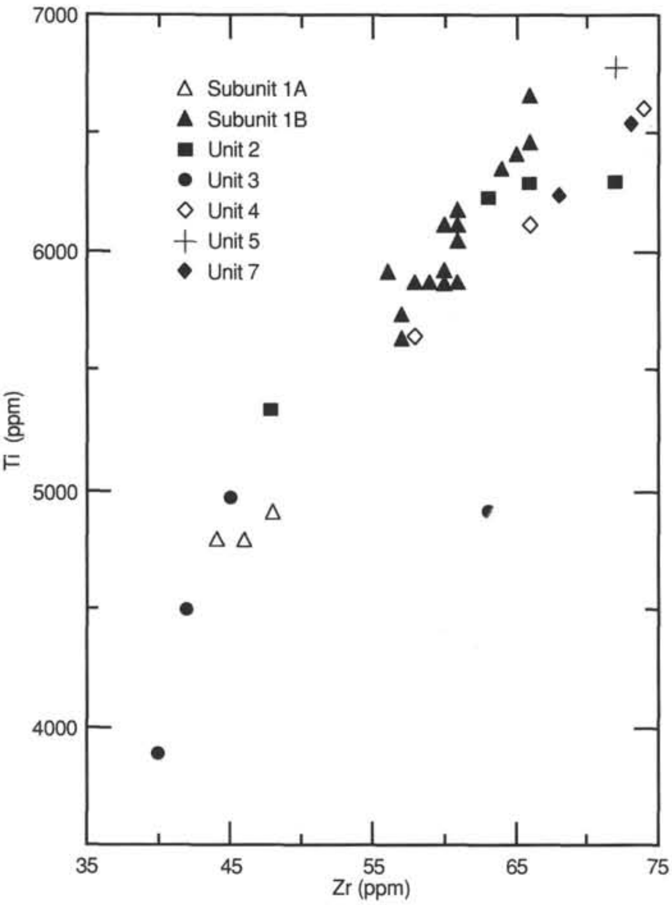

Figure 61. Ti-Zr variations of the igneous rocks, Site 768.

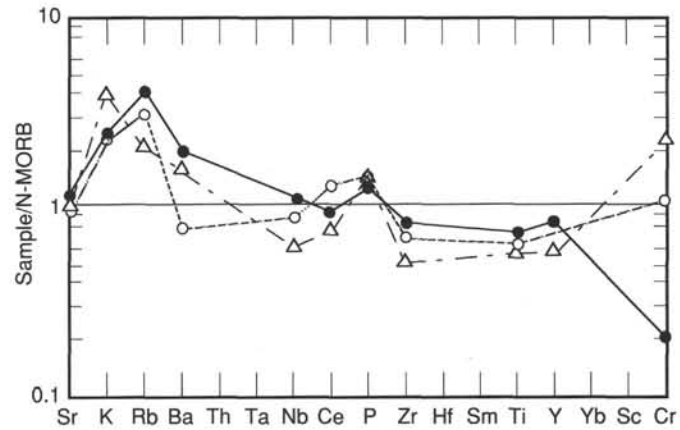

Figure 62. N-MORB normalized minor and trace element patterns of selected samples of basement rocks, Site 768. Normalizing values of normal MORB are from Pierce (1982). Triangle = Sample 124-768C-73R-1, 124-127 cm; closed circle = Sample 124-768C-90R-3, 59-63 cm; and open circle = Sample 124-768C-97R-3, 55-59 cm.

be compatible, however, with a transitional character to island-arc tholeiites.

DOWNHOLE MEASUREMENTS

Log Quality and Processing

Log quality at Hole 768C was generally very good, and little editing or reprocessing was required. Only two raw logs were poor quality: sonic and density. The raw sonic log had very serious cycle skipping throughout the bottom half of the hole (see the raw log plots that follow the barrel sheets at the back of this volume). This cycle skipping may be attributed to increased noise and tool vibration associated with running the seismic stratigraphic tool string uncentralized. The cycle skipping was successfully removed by reprocessing (see "Explanatory Notes" chapter, this volume) the sediments (Fig. 63) as well as the basalts (Fig. 64).

The quality of the reprocessed velocity log is very good. The density log above 630 mbsf exhibits a large number of spikes to very low density (often <1.5 g/cm^3); rarer spikes occur deeper in the section. These spikes are artifacts attributable to poor contact of the tool with the borehole wall, and they are not readily correctable.

Tool sticking was less pervasive at Hole 768C than at 767C, although sticking did prevent openhole logging of the interval from 634.5 to 689.5 mbsf for the seismic stratigraphic combination and of the interval from 645.8 to 764.5 mbsf for the litho-porosity combination. Consequently, the continuous correlation between logging runs used to remove depth shifts at Hole 767C was not employed at Hole 768C. Minor depth mismatches of up

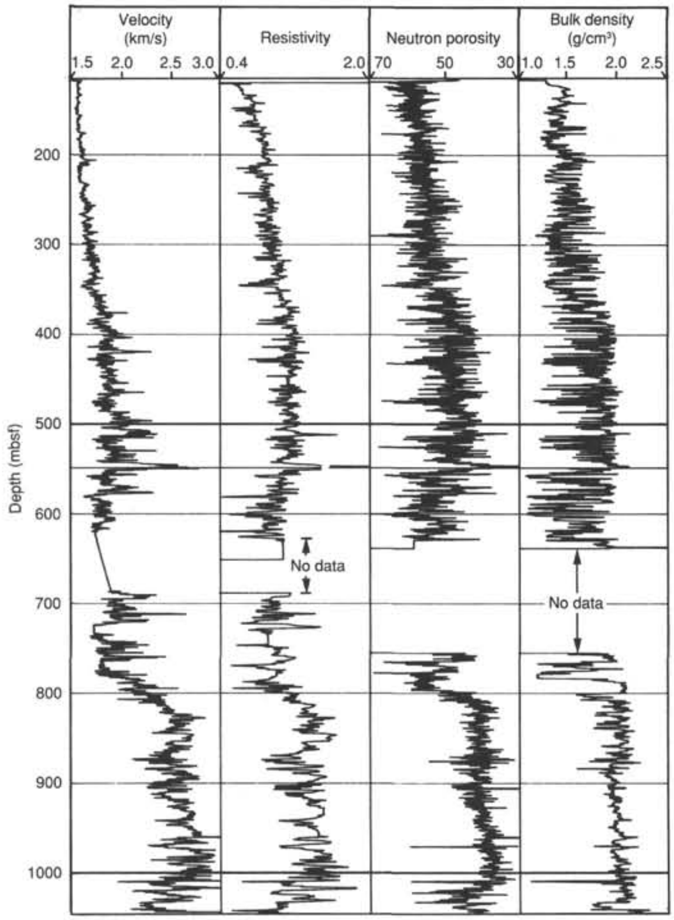

Figure 63. Logs of velocity, resistivity, neutron porosity, and bulk density in the portion of the Hole 768C sedimentary sequence for which openhole logs were obtained.

to 3 m are common between the two runs. A depth mismatch of over 5 m at the very top of the basalts is indicated by replicate gamma-ray logs; tool sticking was unusually high at this depth.

Through-pipe correction of logs from the natural gamma tool was not undertaken at Hole 768C. Although such a correction was warranted, carbonate dilution caused a low gamma-ray signal in the through-pipe interval from 0 to 124.8 mbsf. Consequently, signal-to-noise ratios for corrected logs would be low. In subsequent discussions, we considered only the openhole logs obtained below 124.8 mbsf.

Sedimentary Units

Unit I (0–122.5 mbsf), which consists of nannofossil marl with rare thin ash layers, was not logged openhole. The transition from Unit I to Unit II is an interval (119.0–133.2 mbsf) of decreasing carbonate content downhole (see "Lithostratigraphy" section, this chapter). A rapid increase in clay content for this transition zone is indicated by the potassium, thorium, resistivity, and photoelectric effect logs for 125–138 mbsf (Fig. 65).

Unit II (122.5–652.4 mbsf) is primarily clay, silty clay, clayey silt, and silt with some sand and rare thin ash interbeds. Hemipelagic clay dominates the interval from 123 to 200 mbsf, but turbidites increase in percentage below this depth and are dominant in the interval from 480 to 652 mbsf (see "Lithostratigraphy" section, this chapter). The change downhole from hemipelagic to turbidite dominance is associated with a change in clay mineralogy, from smectite dominance above 150 mbsf to increasingly strong illite dominance below that depth (see "Lithostratigraphy" section, this chapter).

Because illite is much higher in potassium than smectite is, a gradual downhole increase in the potassium log throughout Unit II was expected. Some increase was observed (Fig. 65), but the correspondence with illite changes was only fair. Probably, the decreasing total clay associated with the increasingly silty turbidites downhole diminished the potassium rise that took place as a result of the clay mineralogy change alone.

The small-scale character of the log responses in Unit II differs from the one commonly found in turbidites. One might expect velocity and resistivity to be inversely correlated with potassium, thorium, and perhaps photoelectric effect. Such a pattern indicates that all of the logs responded primarily to variations in the relative proportions of clay minerals and coarser grains. This pattern is present sometimes: silt or sand beds are identified by this pattern and by unusually high velocities at 494.5–496.5, 510–512, 546–547, 570–571.5, and 575–577 mbsf (Fig. 66).

The beds at 510–512 and 546–547 mbsf grade upward into clay, as indicated by the logs (Fig. 66) and, for the upper bed, by the cores. However, more often velocity and resistivity fluctuations are positively correlated with changes in potassium, thorium, and photoelectric effect (Fig. 66). This change indicates that the siltier sediments are often higher in potassium, thorium, and photoelectric effect than the clays. Such a pattern probably results from the difference between the illite-rich clays/silty clays of the turbidites and the montmorillonite-rich hemipelagic clays. Log inversion is needed for development of a continuous record of both clay mineralogy and grain-size variations in Unit II.

Unit III (652.4–806.6 mbsf), like Unit II, consists predominantly of turbidites and hemipelagic clay. The bottom half is dominantly hemipelagic claystone, and the turbidite component increases uphole (see "Lithostratigraphy" section, this chapter). Only through-pipe logs were obtained in the upper third of the unit, and openhole logs for the central third were obtained only with the seismic stratigraphic combination, because the clays of Unit III caused tool sticking.

Unlike Unit II, rare thick tuffs are found in the top half of Unit III. Tuff beds 2.5–4.7 m thick are found at about 657, 696, and 725 mbsf (see "Lithostratigraphy" section, this chapter). The lower two of these are within the logged interval and are recognizable as velocity and resistivity spikes to high values (Fig. 63). An additional, thinner tuff is present at 711 mbsf, given the log responses, which are the same.

Major changes in clay mineralogy within Unit III are indicated by the limited X-ray diffraction (XRD) data (see "Lithostratigraphy" section, this chapter) and confirmed by the log responses. In addition to the fine-scale turbidite/hemipelagic alternations, similar to those observed in Unit II, lower-frequency variations in clay mineralogy are present in Unit III. For example, the interval from 685 to 746 mbsf is fairly constant in K (except for two thin beds at 703 and 733 mbsf), but it exhibits broad swings in Th; the Th-poor portions are probably higher in illite than the Th-rich portions.

On the other hand, the interval from 746 to 788 mbsf is particularly high in Th, K, and porosity and low in resistivity (Figs. 65 and 67). It is probably a fairly pure clay with high illite content. In contrast, the underlying interval from 788 to 800 mbsf is high in bound water and very low in K and Th, indicative of montmorillonite dominance; its high photoelectric effect is unexplained. This lower interval is a sedimentologically distinctive brown claystone of pelagic origin, in contrast to the overlying hemipelagic greenish grey claystone (see "Lithostratigraphy" section, this chapter).

From the log response data, the base of Unit III is placed at 800 mbsf, at the base of the brown claystone (Fig. 67). At this

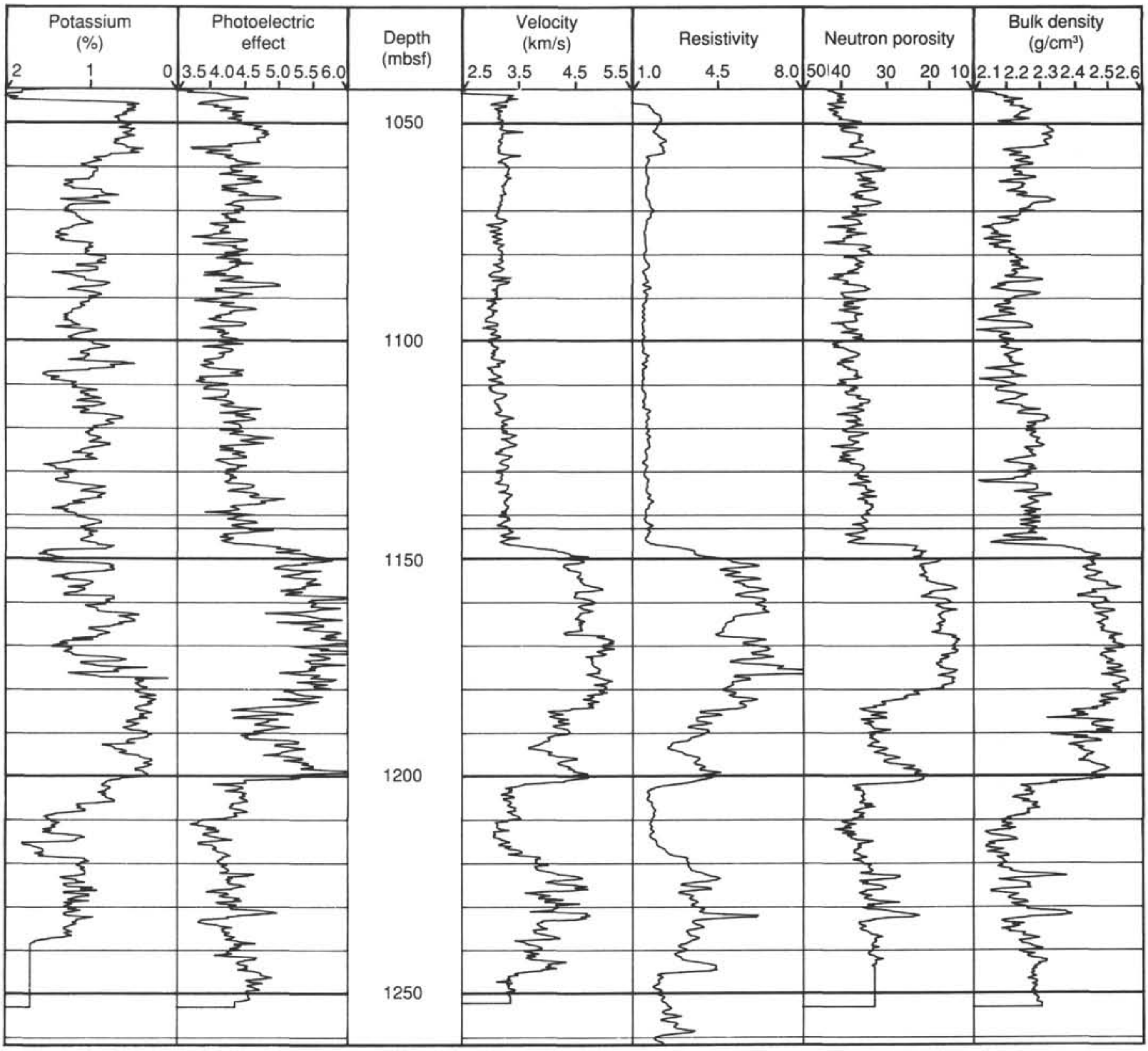

Figure 64. Logs of potassium, photoelectric effect, velocity, resistivity, neutron porosity, and bulk density for the basement section of Hole 768C.

depth, neutron porosity drops substantially, and resistivity and density porosity increase, consistent with a decrease in bound water. In contrast, the base is placed at 806.6 mbsf as a result of the incomplete core recovery (see "Lithostratigraphy" section, this chapter). Core 124-768C-47R (796.9–806.6 mbsf) recovered only 1.8 m and is entirely brown claystone of Unit III, whereas Core 124-768C-48R (806.6–815.5 mbsf) is tuff of Unit IV.

Unit IV (806.6–1003.6 mbsf) is composed almost entirely of vitric tuff and lapillistone, with a few clay beds at the top and base of the unit (see "Lithostratigraphy" section, this chapter). The unit is much higher in velocity and resistivity and lower in neutron porosity than the overlying units (Fig. 63) because of its very low clay content. The distinctive mineralogy of the unit is reflected by its low photoelectric effect, Th, and U in comparison with the overlying units (Fig. 65).

The chemical heterogeneity of Unit IV is most noticeable in the potassium log (Fig. 65). Although potassium is commonly only about 1% in the unit, many spikes to >3% are present near the top and bottom of the unit. Figure 67 shows the K variations near the top of the unit in greater detail. The K-rich horizons below 800 mbsf are high in photoelectric effect without noticeable Th enrichment. This pattern is caused by potassium feldspar and indicates that these horizons are more rhyolitic in composition than the dominant andesitic tuff composition.

In this upper part of Unit IV, K-rich horizons are often high in density (low-density porosity), yet resistivity and neutron porosity responses to these layers are variable. Thus, the alternation between rhyolitic and andesitic compositions is not consistently accompanied by a distinctive porosity difference, such as would happen if pumice were confined to one compositional endpoint.

On the basis of chemical log responses, the tuffs of Unit IV may be compositionally divided into four major eruptive subunits. The uppermost subunit (800–878 mbsf), just described, is

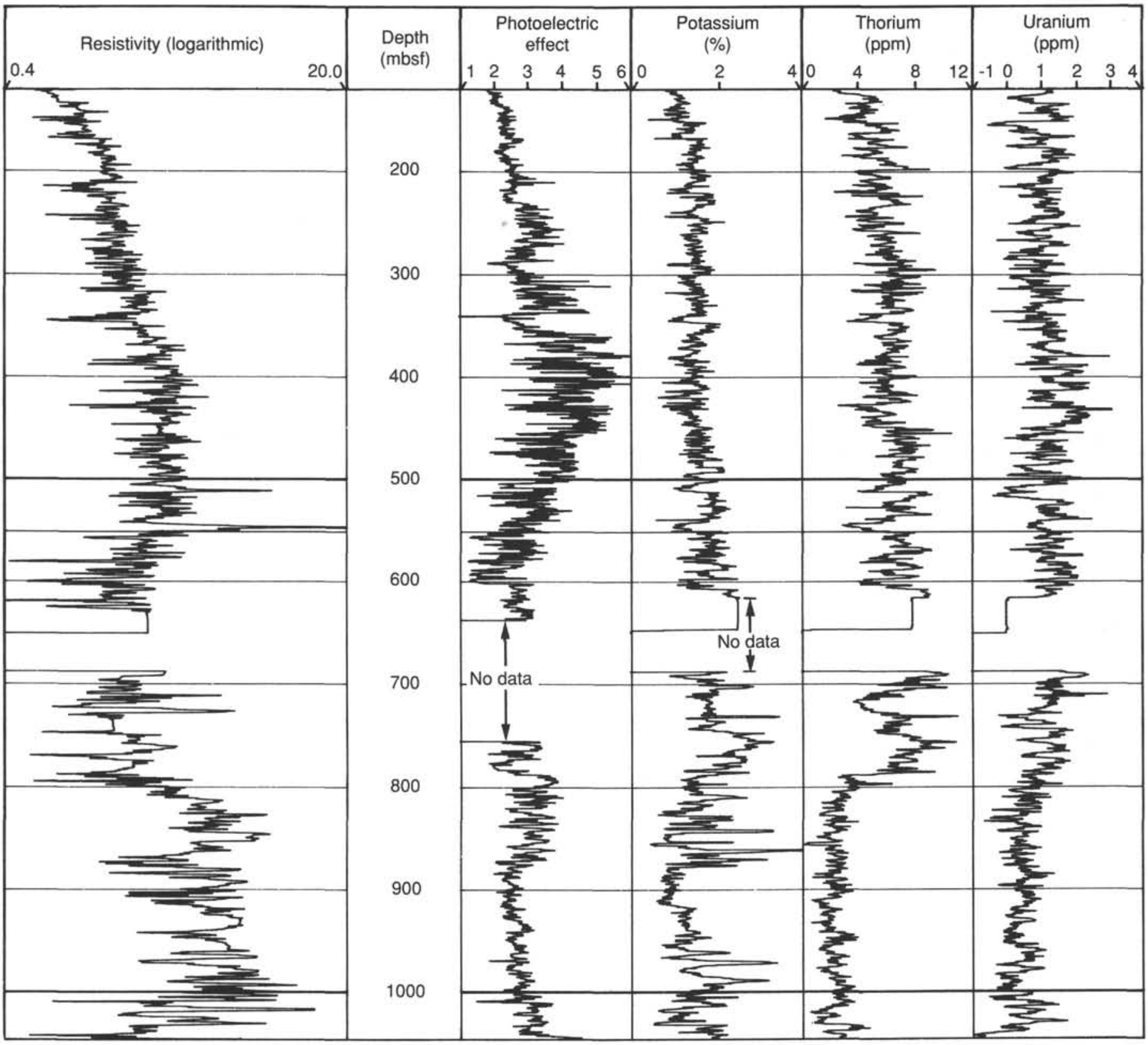

Figure 65. Logs of resistivity, photoelectric effect, potassium, thorium, and uranium in the portion of the Hole 768C sedimentary sequence for which openhole logs were obtained.

characterized by frequent fluctuations between andesitic and rhyolitic compositions. The next subunit (878–910 mbsf) is fairly uniform and andesitic and is characterized by very low potassium and photoelectric effect and moderate thorium (Fig. 65). The next subunit (910–941 mbsf) is also rather uniform and is distinguished from the overlying subunit by its higher K and lower Th and U.

Thick-graded beds with upwardly decreasing photoelectric effect and increasing resistivity are evident within the two central subunits at 879.7–883.3, 891.6–898.9, and 924.4–941.2 mbsf. The lowest subunit (941–1004 mbsf), like the top subunit, exhibits fluctuations between rhyolitic and andesitic composition. Unlike the top subunit, the beds are thicker and the K-rich intervals are consistently lower in resistivity (higher in porosity) than the more andesitic intervals, possibly indicating a greater proportion of pumice. In the bottom 10 m of this subunit, K and Th are correlated, probably indicating clay beds within these lower tuffs.

Unit V (1003.6–1046.6 mbsf) consists of claystone with graded interbeds of tuff (see "Lithostratigraphy" section, this chapter). The claystone beds are evident in the log responses as intervals with low velocity and resistivity and generally high neutron porosity, K, and Th. The tuffs are generally similar to the andesitic end member of Unit IV tuffs.

Elastic Properties of Sediments

Velocity values in the upper 500 m of Hole 768C increase gradually as a result of compaction, with a few spikes to high velocity caused by silt or sand beds (Fig. 63). For this interval, the velocity measurements are in close agreement with the empirical velocity/depth trend of Hamilton (1979a) for terrigenous sediments. However, velocity values actually decrease downhole

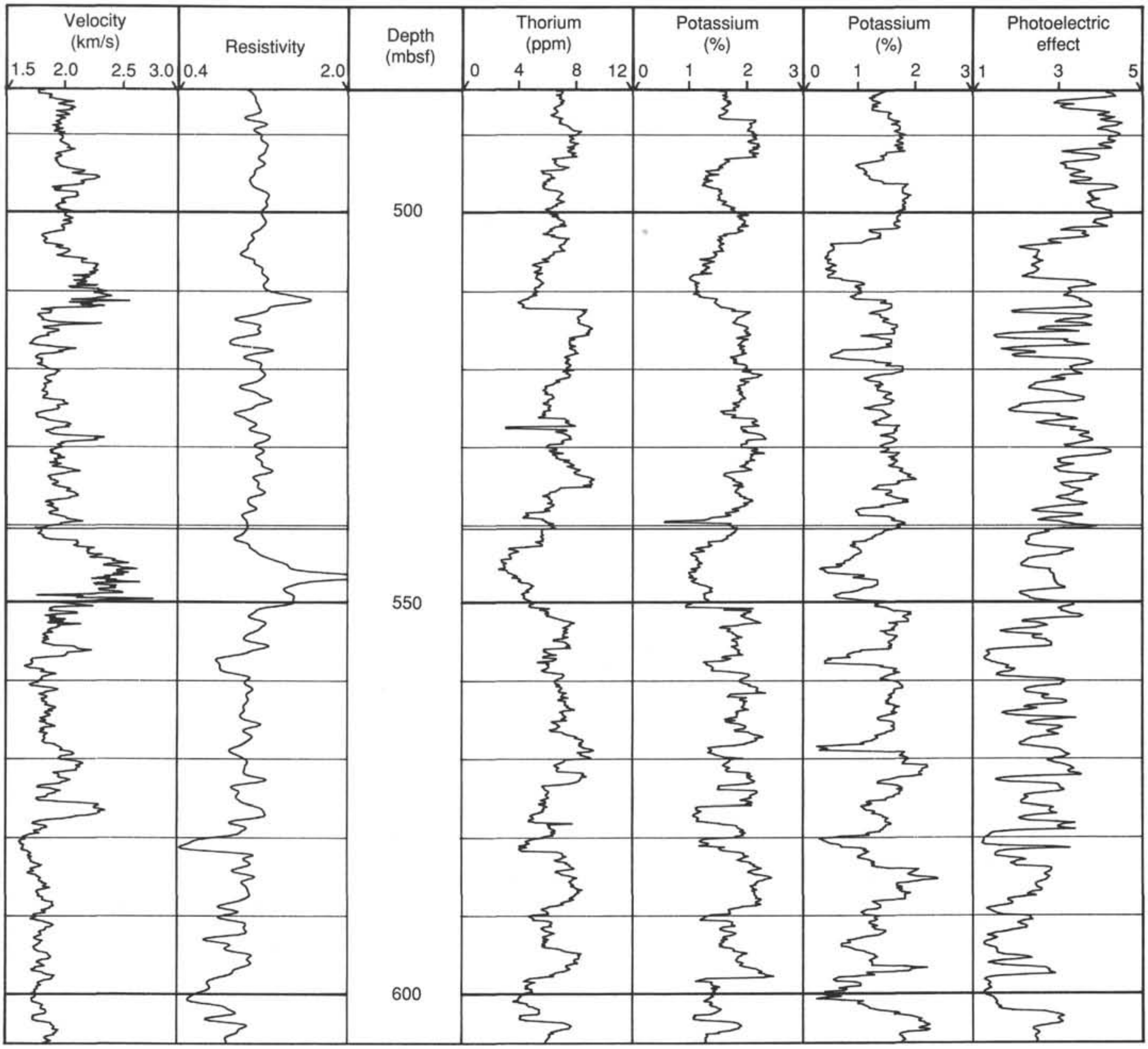

Figure 66. Logs of velocity, resistivity, thorium, potassium, and photoelectric effect for a portion of lower Unit 2. The four logs on the left are from the seismic stratigraphic run, and the two logs on the right are from the lithoporosity run. Potassium logs from both runs are shown to indicate potassium replicability and possible slight depth shifts between the two runs. Note that the high-velocity silts at depth of 506–513 mbsf and 543–551 mbsf are low in Th and K, in contrast to the more common pattern of a positive correlation among all of the logs shown.

below about 510 mbsf in Units II and III, again with the exception of several silt interbeds. This decrease is probably caused by a greater proportion of clay minerals compared to larger grain sizes. Such a change is consistent with the similar inversion in neutron porosity (Fig. 63), because clays are higher in porosity and bound water than the coarser sediments. The general velocity/depth trend of Figure 63 agrees well with the discrete measurements on cores (see "Physical Properties" section, this chapter).

As previously discussed, the density log for Units II and III has pervasive spikes to unreliably low densities, caused by poor tool contact with the borehole. For these units, only the trend of highest densities as a function of depth is in agreement with discrete measurements on cores (see "Physical Properties" section, this chapter). For the tuffs of Unit IV the density log is reliable and is consistent with core data. However, grain densities determined from neutron and density logs are 2.65–2.70 g/cm^3 for the tuffs, lower than adjacent units but much higher than the 2.2 g/cm^3 determined from cores (see "Physical Properties" section, this chapter). This discrepancy indicates that the logs are detecting much more water in the tuffs than the amount liberated by freeze drying of the cores. The unliberated water probably resides as bound water in clays and glass and as pore water in such nonpermeable grains as pumice.

Basement

The uppermost basement interval (1047–1147 mbsf) consists of weathered pillow basalts (see "Basement Lithology" section,

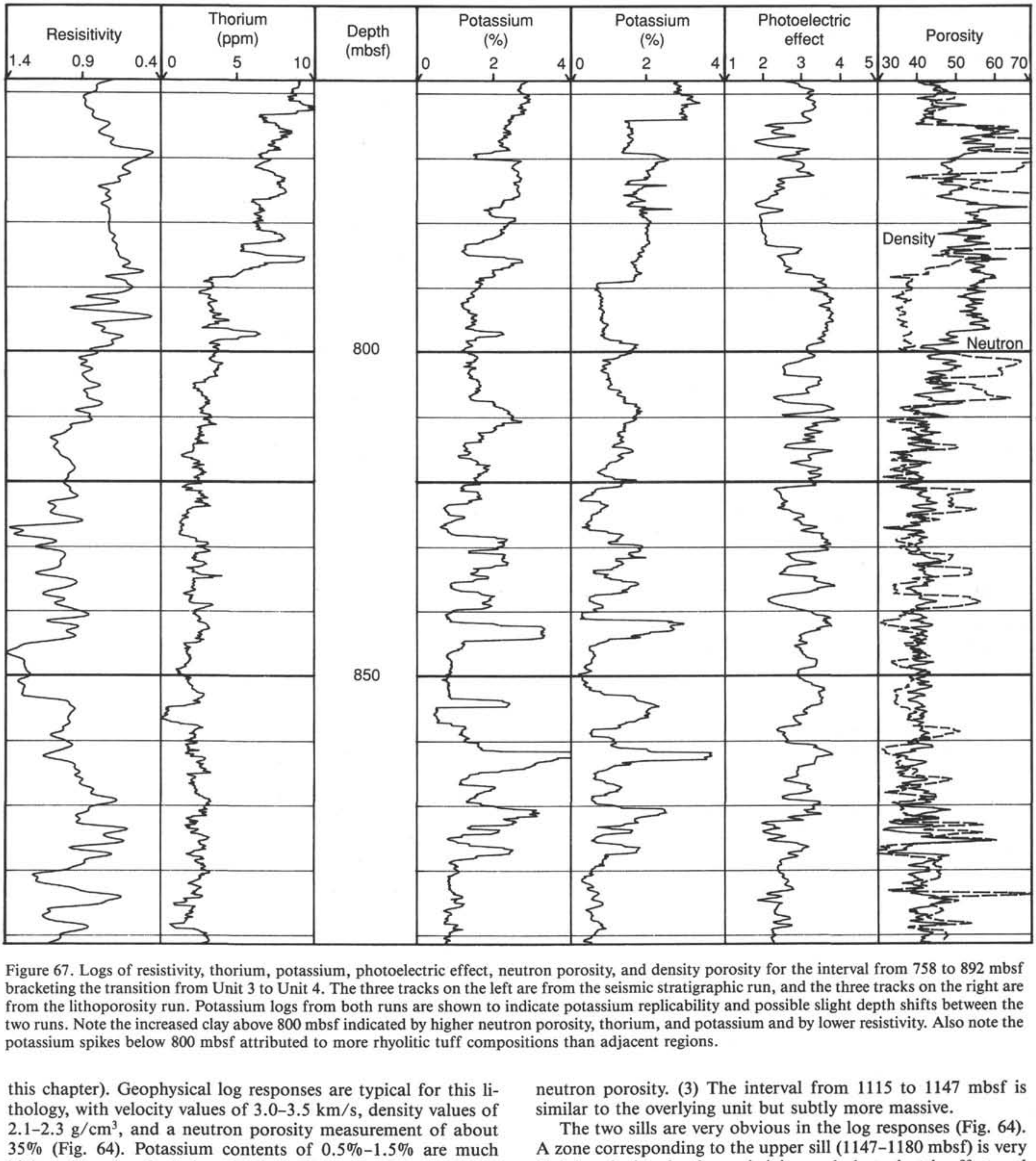

Figure 67. Logs of resistivity, thorium, potassium, photoelectric effect, neutron porosity, and density porosity for the interval from 758 to 892 mbsf bracketing the transition from Unit 3 to Unit 4. The three tracks on the left are from the seismic stratigraphic run, and the three tracks on the right are from the lithoporosity run. Potassium logs from both runs are shown to indicate potassium replicability and possible slight depth shifts between the two runs. Note the increased clay above 800 mbsf indicated by higher neutron porosity, thorium, and potassium and by lower resistivity. Also note the potassium spikes below 800 mbsf attributed to more rhyolitic tuff compositions than adjacent regions.

this chapter). Geophysical log responses are typical for this lithology, with velocity values of 3.0–3.5 km/s, density values of 2.1–2.3 g/cm^3, and a neutron porosity measurement of about 35% (Fig. 64). Potassium contents of 0.5%–1.5% are much higher than for fresh basalts, reflecting potassium addition from seawater during alteration.

These upper pillow basalts are fairly uniform but can be divided into three subunits on the basis of the log responses. (1) The interval from 1047 to 1057 mbsf is low in K and high in resistivity and density. It appears to be more massive and therefore less altered than the underlying unit. (2) The interval from 1057 to 1115 mbsf exhibits fine-scale variability but is generally the most porous, on the basis of velocity, resistivity, density, and neutron porosity. (3) The interval from 1115 to 1147 mbsf is similar to the overlying unit but subtly more massive.

The two sills are very obvious in the log responses (Fig. 64). A zone corresponding to the upper sill (1147–1180 mbsf) is very high in velocity, density, resistivity, and photoelectric effect and low in neutron porosity. Actual porosity is even lower than neutron porosity, because most of the water is probably bound water in clay alteration minerals. Potassium in this sill is comparable with that in the overlying pillows. Like the bound water, the potassium is probably primarily in the clays that fill vesicles.

The contact between the upper and lower sills is somewhat uncertain, since the lower sill is quite heterogeneous, with a wide transition zone of most properties to values similar to the upper sill. In general, the middle of the lower sill appears to have the highest density of fractures, on the basis of lower velocity, resistivity, and density, with gradual decreases in fracture intensity toward both edges.

Gypsum filling of many fractures (see "Basement Lithology" section, this chapter) may account for the unusually high neutron porosities in the center of the lower sill. The rapid vertical variations in inferred fracture intensity are consistent with a dominance of near-horizontal over near-vertical fractures. The very low potassium content of the lower sill, in spite of the pervasive evidence of fracturing, implies that the sill was intruded after the main phase of crustal alteration and associated potassium addition.

Below the lower sill lies Unit 4, between 1210.4 and 1240.9 mbsf, a zone of altered pillow basalts (see "Basement Lithology" section, this chapter). Log properties in the zone between 1202 and 1218 mbsf are virtually identical to those of the upper pillows, consistent with their inferred continuity prior to sill intrusion. This zone is underlain by a more massive zone of larger pillows and sheet flows (see "Basement Lithology" section, this chapter), 28 m thick on the basis of log responses. The short potassium log is fairly uniform, but other logs indicate substantial variations in porosity, with 2-m-thick, particularly dense intervals centered at 1223, 1226, 1232, and 1244 mbsf. Below 1245 mbsf, pillows again dominate.

Primarily on the basis of the log responses, we constructed a tentative relative chronology for the basement interval at Hole 768C. The pillow basalts and rare sheet flows of 1068–1147 and 1202–1258 mbsf were erupted in original stratigraphic continuity, followed by intrusion of the upper sill. The uppermost pillows (1047–1068 mbsf) were extruded after intrusion of the upper sill, given their opposite magnetic polarity to all other penetrated basement (see Fig. 68 and "Paleomagnetism" section, this chapter). Pervasive hydrothermal alteration with associated potassium addition may have partly preceded extrusion of the uppermost pillows and certainly continued after their extrusion. Finally, the lower sill was intruded after the period of substantial potassium addition had ended.

Borehole Televiewer

The two runs of the borehole televiewer (BHTV) were quite successful, but the quality of shipboard photographs was too low to permit determination of structural dips or fracture patterns. Identification of these will require post-cruise digital processing. The shipboard photos were dominated by borehole ellipticity and slight tool eccentricity. The implications of the ellipticity measurements for regional stress directions are discussed in another section (see "Stress Measurements" section, this chapter).

Hole Deviation and Magnetization

A hole deviation survey was run as part of the lithoporosity combination. Measured deviations are consistent with sporadic discrete measurements made during drilling; the discrete measurements did not determine azimuth of the deviation. Hole deviation increases gradually to a maximum of 6° at the top of the tuffs, decreases within the tuffs, and then increases slowly within basement (Fig. 68). Hole azimuth drifts somewhat within the upper units and is rather constant at about 70° within the tuffs and at about 55° within basement.

A three-component fluxgate magnetometer was run as part of the same general purpose inclinometer tool that measured hole deviation (Fig. 68). Interpretation of the magnetometer data is nontrivial, because the measured magnetic field includes a dominant component from the earth's magnetic field, small components from tool magnetization and diurnal variation, and induced (IRM), viscous (VRM), and thermal (TRM) remanent magnetizations of the formation.

In the sedimentary section, the gradual drift in inclination was caused by a gradual change in hole deviation, since inclination is measured relative to the borehole rather than in geographic coordinates. Small-scale fluctuations in the tuff of Unit IV probably reflect susceptibility variations, because the induced component is larger than the remanent component in this unit (see "Paleomagnetism" section, this chapter).

The VRM and TRM measurements are much stronger than the IRM values in the basement rocks. Core demagnetization indicates that VRM is larger than TRM in these rocks (see "Paleomagnetism" section, this chapter). The uppermost portion of the basalts (1047–1068 mbsf) has a strong normal component approximately parallel to the present earth's field, whereas the rest of the penetrated basement is slightly lower in total moment than the earth's field (Figs. 68 and 69).

This difference is most readily explained as constructive interference of normally polarized VRMs and TRMs in the top 21 m and destructive interference of normal VRM and reversed TRM in the interval below 1068 mbsf. This polarity difference is confirmed by a few discrete measurements on cores (see "Paleomagnetism" section, this chapter). However, the more positive inclinations in the reversed pillows than in the normally polarized pillows is not accounted for. The sills have a distinctly more negative inclination than the pillows. The smooth variation in magnetization of the lower sill probably indicates a magnetization intensity close to the noise level of the magnetometer.

Temperature

Temperature measurements were obtained on three logging runs. All temperature measuring systems used at Hole 768C had significant thermal lags, and we assume that the maximum temperature recorded on each run is associated with the greatest depth achieved by that run. On the first BHTV run, a maximum-recording thermometer measured 38.9°C and the L-DGO temperature tool peaked at 38°C, at 870.5 mbsf for each tool.

On the seismic stratigraphic run to 1260.5 mbsf, two maximum-recording thermometers measured 71.1°C and 70.6°C, the internal temperature of the phasor resistivity tool was 72°C, and the L-DGO temperature tool peaked at 75°C. The L-DGO temperature tool has not been calibrated above 50°C. On the lithoporosity run to 1257.5 mbsf, both maximum-recording thermometers measured 87.8°C.

None of these temperatures represents equilibrium formation temperature, because of the cooling effect of circulation during and immediately after drilling. The lithoporosity temperature of 87.8°C is the closest to equilibrium, but no extrapolation of these limited data to equilibrium temperatures has been attempted.

STRESS MEASUREMENTS

Stress orientation was measured at Site 768 with the BHTV (see "Downhole Measurements" section, this chapter, and "Explanatory Notes" chapter, this volume). Two runs were made with the BHTV. The first run was between a bridge at 870 mbsf and the base of pipe at 805 mbsf. The second run was from 1250 to 995 mbsf. The first run was entirely within the tuffs, and the second run encompassed basalts and lower tuffs. Stress orientation was interpreted from the BHTV data by observing the orientation of ellipticity of the hole and sporadic breakouts.

The acoustic intensity pattern recorded by the BHTV allows determination of the shape of the borehole. If the tool were centered in a circular hole of constant reflectivity at all azimuths, the record would be uniformly bright. The BHTV records in the basement showed a consistent pattern of a weakly reflective sector, 90° in width, within a stronger reflectivity record. Down the center of the weakly reflective zone is a narrow line of high reflectivity. This pattern can be interpreted as the result of poor reflectivity along the semimajor axis of the ellipse, on the far

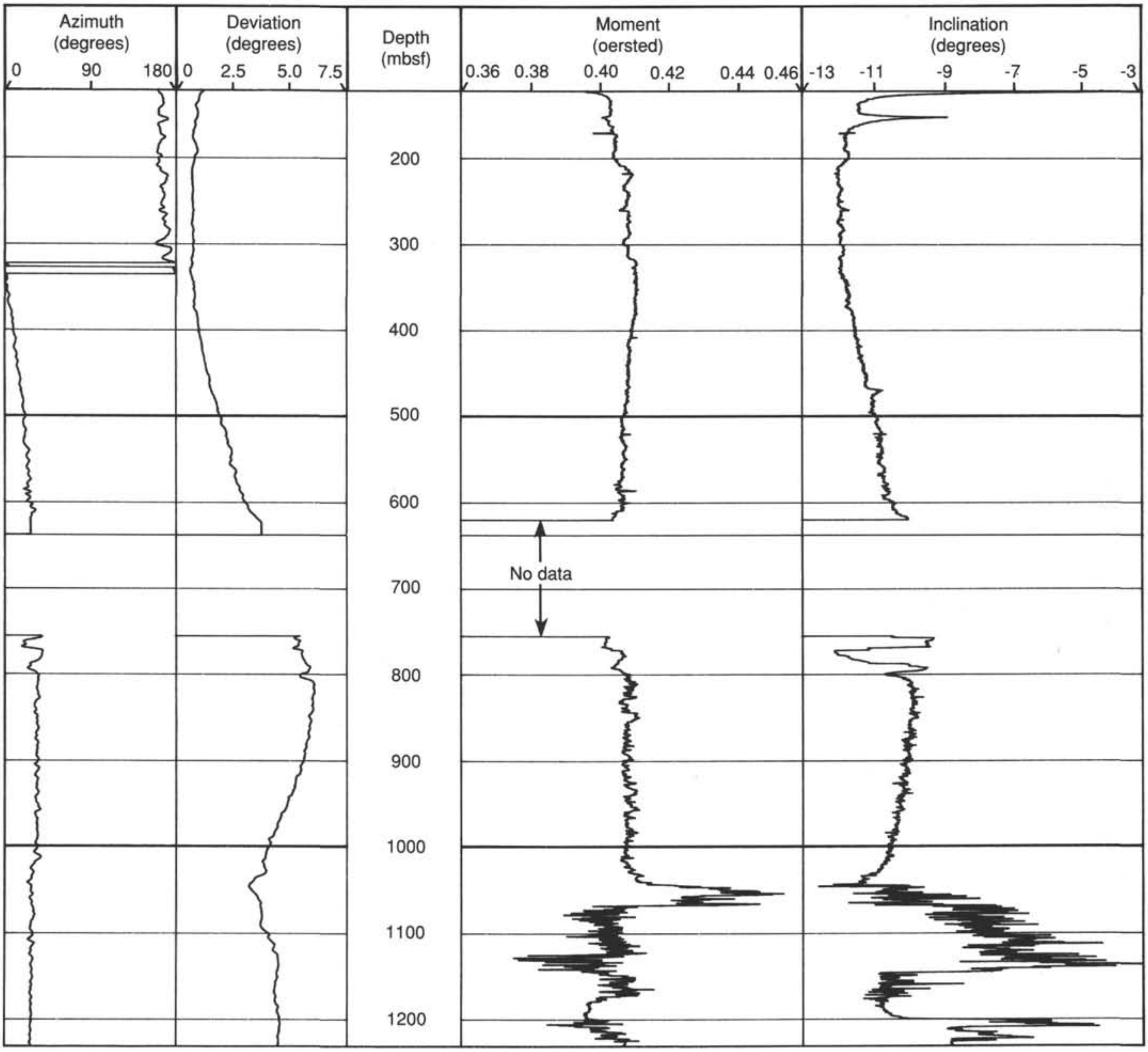

Figure 68. Deviation of the borehole from vertical and the azimuth of that deviation (left). Total moment and inclination of magnetization measured by a downhole magnetometer (right). Note the strong magnetization of the basement (below 1047 mbsf).

side of the asymmetrically hanging tool. The narrow line of high reflectivity would be caused by reflection along the exact axis of the ellipse, giving us a very precise indication of the shape of the hole. This interpretation is supported by the observation that in some instances the two broad, dark areas of low reflectivity coalesce into one, more narrow band, indicating the start of a breakout.

An alternate explanation for the reflectivity pattern is also possible. The pattern may indicate an off-center placement of the tool because of the departure of the hole from vertical. A deviation of 4°–5° was measured in the basement section at 1090 mbsf, and the direction of deviation was 055°. As the long axis of the ellipse (see below) lies mainly between 110° and 120°, it seems unlikely that hole deviation is responsible for the asymmetrical reflectivity pattern seen in the BHTV record at Site 768.

The orientation of the long axis of the ellipse and the direction of breakouts, where present, are graphed in Figure 70. Some scatter is seen in the data, but the general trends are very clear. Major deviations occur in the sediment above basement, about 1000 mbsf, and these should be disregarded as estimates of crustal stress directions. Another zone of deviation occurs in the pillow basalts just below 1100 mbsf; strong crustal magnetization (see "Downhole Measurements" section, this chapter) may cause significant errors in northern orientations in this zone. From 1120 to 1260 mbsf almost all the observations fall within the azimuths between 290° and 302° (110°–122° on the other axis).

This orientation, if stress related, indicates the least horizontal stress. Its complement, the inferred maximum horizontal stress direction, lies between 20° and 32°, giving a general northeast trend. Observations between 806 and 865 mbsf are very

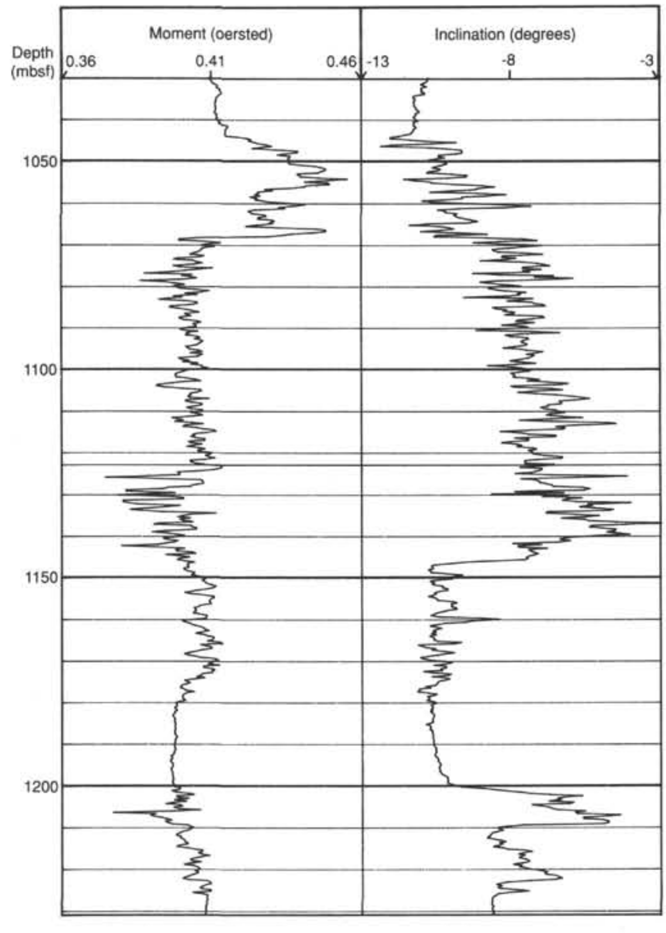

Figure 69. Total moment and inclination of magnetization for the basement (below 1047 mbsf) of Hole 768C.

consistent with those measured within the deepest part of the basement in the sill zone. The correspondence between these two widely separated zones lends additional support to the viability of this direction representing that of the dominant crustal stress axis.

A trend of northeast or north-northeast for the maximum horizontal stress axis is consistent with the trend of the Cagayan and Sulu ridges, which are colliding with the Philippine Mobile Belt. It is likely that this collision is most responsible for imparting deviational stress, not only to the ridges, but also to the intervening basins.

It should be emphasized that these data are only preliminary and will be extensively reprocessed after the cruise. At that time it is possible that some of the conclusions here will be altered.

SEISMIC STRATIGRAPHY

Multichannel seismic reflection profiles on Lines SO49-04, SO49-05, and SO49-07 were acquired aboard the *Sonne* in April 1987 and processed by the Bundesanstalt für Geowissenschaften und Rohstoffe (BGR) in 1988 (see Hinz and Block, this volume). Site 768 is located in the central part of the Sulu Sea, on Line SO49-04 (Figs. 71 and 72). In addition, a nonmigrated multichannel seismic reflection line (Line 16 of the Comite d'Etudes Petrolieres Marines [CEPM]) crosses Line SO49-04 near Site 768. Single-channel seismic data were also recorded by the *JOIDES Resolution,* prior to drilling, on 26 November 1988. *Sonne* navigation was obtained with transit satellites, Loran C, and doppler sonar. The *JOIDES Resolution* used the global positioning system (GPS) and transit satellites.

We made preliminary interpretations of these data before we drilled Site 768. The seafloor deepens toward the southeast because of the flexure of the Sulu Basin approaching the Sulu Trench. The trend of the deformation front of this thrust zone is well controlled by seismic data and SeaBeam, collected with *J. Charcot* in 1984 (Fig. 72). The trench trends north-south to northeast, bearing 20°E, and is located 55 km from Site 768. The site is located on a flat abyssal plain that is bordered 50 km

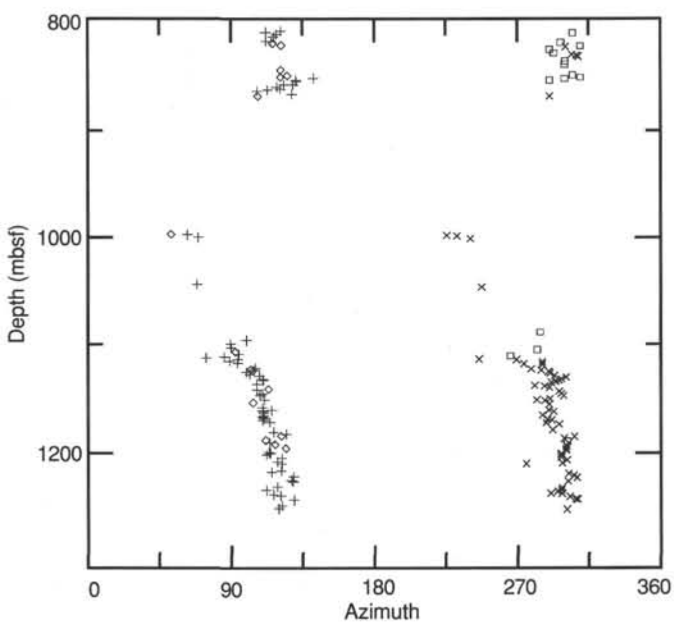

Figure 70. Graph of azimuth of the major axis of the elliptical hole in Hole 768C, including some breakouts. Depths measured were between 805 and 870 mbsf and between 995 and 1260 mbsf. Solid symbols are more reliable determinations than open symbols.

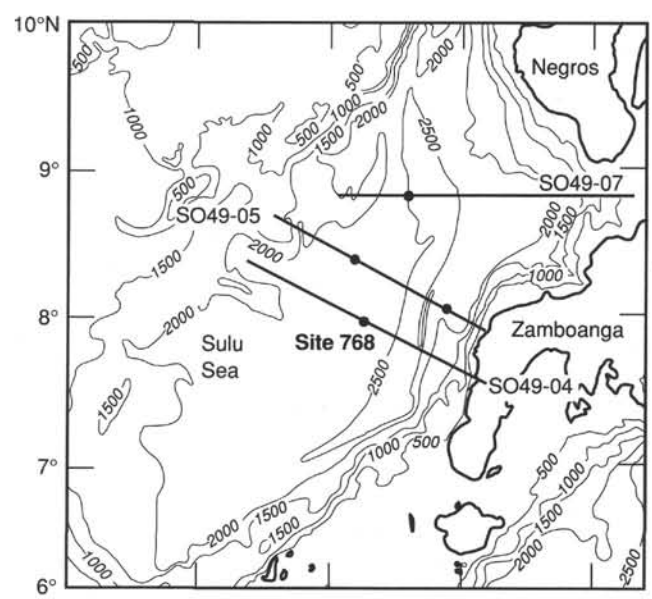

Figure 71. Simplified bathymetric map of the Sulu Sea, showing the location of Site 768 and seismic Lines SO49-07, SO49-05, and SO49-04 (Hinz and Block, this volume). Contour interval in meters.

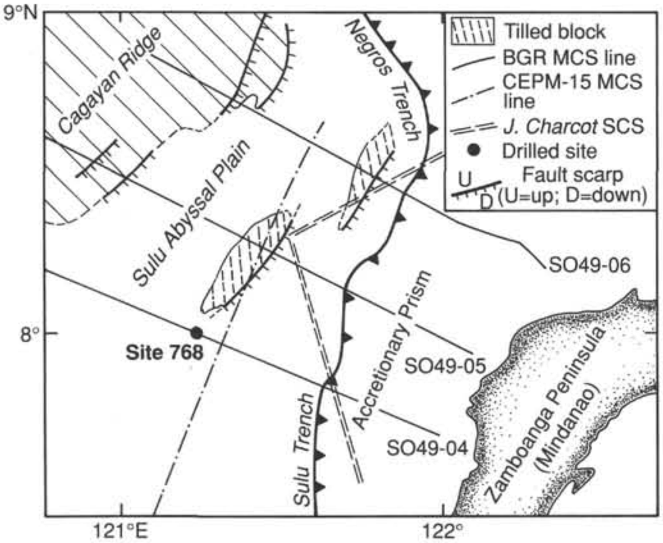

Figure 72. Location of geophysical profiles in the area of Site 768. The deformation front of the Sulu-Negros trenches is shown, as is the Cagayan Ridge bounded by normal faults. Small, tilted blocks are present within the Sulu Abyssal Plain.

to the northwest by the steep southeast-facing escarpments of the Cagayan Ridge.

Preliminary analyses of the seismic data show that this plain pinches out toward the northeast, where it is defined by rare northeast-trending (bearing 30° east) and southeast-facing tilted blocks. Site 768 is located 10 km from the southeastern axial termination of one of these blocks. Site 768 is located near shot point (SP 1738) on seismic Line SO49-04 (Fig. 73). Seismic Line SO49-04 at Site 768 (Fig. 72) was divided into six major seismic sequences (Fig. 74).

The upper Seismic Sequence 1 is 110 m thick and is continuous throughout a large part of the region. Cored material consists of nannofossils and foraminifer oozes with minor volcanic ashes. The age of the unit is Pleistocene. Underlying Seismic Sequence 2 is 350 m thick and is characterized by numerous parallel, flat-lying reflectors that can be followed for large distances. The contact between the two sequences is a high-amplitude reflector, which implies a major change in lithology. Cored material consists of claystones with minor nannofossil marl interbeds. Sporadic sandy turbidites occur in this sequence.

Subsequences could be distinguished on the basis of subtle pinchouts. Seismic Sequences 1 and 2 are unfaulted, although minor internal slumping occurs a few kilometers to the west of the site. Thus, these sequences are post rifting, and the age of the base of Seismic Sequence 2 has been dated in core material as lowermost late Miocene (see "Biostratigraphy section, this chapter).

Seismic Sequence 3 is 250 m thick and ends in the late middle Miocene. The entire sequence is in nannofossil Zone NN9 and represents an accumulation rate of 250 m/m.y. Small faults with minor offsets cut a small segment of the sequence, which indicates that the sequence represents the end of the rifting phase. Reflectors within this sequence are parallel, with only very minor evidence of onlap relations. The sequence thickens over the deep part of the small sub-basin in which the site is located and thins over its margins. To the west the lower part of Seismic Sequence 3 laps onto the lower sequence.

Seismic Sequence 4 is 55 m thick and shows evidence of truncation by the base of Seismic Sequence 3. It corresponds to sediments ranging in age from Zones NN5 to NN4, covering most of the middle Miocene. The increased accumulation of fish teeth in the section argues for slow rates of sedimentation, but the truncation of beds at the top imply an unconformity. The base of Seismic Sequence 3 corresponds to the depth at which samples containing nannofossils of Biozone NN8 were recovered. This makes the contact a good candidate for an unconformity. Red-brown claystone marks the base of Seismic Sequence 4.

Seismic Sequence 5 is broken into two subsequences. Seismic Subsequence 5A is 60 m thick at the site and contains no internal reflectors. The subsequence thickens to the west, toward the center of the basin. The cored material from Seismic Subsequence 5A is an ash-flow deposit, with both vitric and crystal ash. Seismic Subsequence 5B is 120 m thick at the site, and it also increases in thickness toward the center of the basin (westward). It contains several discontinuous internal reflectors that are cut by small normal faults. Subsequence 5A is also cut by a few small faults. The cored rocks are also ash-flow tuff. The base of Seismic Subsequence 5B corresponds to interbedded ash-flow tuff and red-brown claystone, the latter giving radiolarian ages of probable early Miocene.

Underlying Seismic Subsequence 5B is a high-amplitude reflector, which yielded pillowed olivine basalt flows (Seismic Sequence 6) 110 m thick. The basement beneath Seismic Sequence 6 is a diabase sill. We feel confident that basement is represented by the sill, rather than by the pillow basalts, because the seismic velocity contrast between the pillows (3.2 km/s) and the sill (4.9 km/s) is much greater than that between the pillows and the tuffs (2.6 km/s). If we use these velocities, the thicknesses of the units match those drilled at Site 768.

A critical problem is the source of the 250-m section of ash-flow tuff. An examination of seismic Lines SO49-04, SO49-05, SO49-06, and SO49-07 indicates that the tuff may have traveled from west to east in the Sulu Sea. Each of these lines shows the lower sequences (4 and 5) decreasing in thickness and pinching out to the east. These results are only hypothetical at present, but they tentatively imply the Cagayan Ridge may be a more reasonable source than the Sulu Ridge for these ashes.

The age of faulting of the lower sequences is critically important for the tectonic history of the basin. Seismic Sequence 3 can be traced across the faulted zone and is only weakly affected by faulting. In contrast, the underlying sequences are cut by the faults. Seismic Sequence 4 is offset by southeast-facing normal faults, and this sequence can be traced across the section over the top of the faulted blocks. Seismic Sequence 5 cannot be traced across the upthrown fault block on the northwest part of the section, and the sequence thickens toward the fault zone. This geometry could be interpreted as either syndepositional or postdepositional, the latter in light of the pyroclastic nature of Seismic Sequence 5. Faulting probably began in the early Miocene (controlled by the dating in Seismic Sequence 5) and stopped at the end of the middle Miocene (Zone NN8, which is the preliminary age for the base of Seismic Sequence 3).

SUMMARY AND CONCLUSIONS

Site 768 (proposed Site SS-2), is located in the southeastern part of the Sulu Sea, in a water depth of 4384 mbsl. The purpose of drilling the site was to determine the age and stratigraphic history of the Sulu Sea as well as the nature of the basement. This basin had been interpreted in various ways, including as a trapped marginal basin of Eocene age (Lee and McCabe, 1986) and as a backarc basin of Oligocene to Miocene age (Hamilton, 1979b; Holloway, 1981; Karig, 1983). Its origin has profound implications for the development of the broad collision zone from Borneo to the Philippines, and the stratigraphy of the basin was expected to record the collision history, as well as the paleoceanographic evolution of the region.

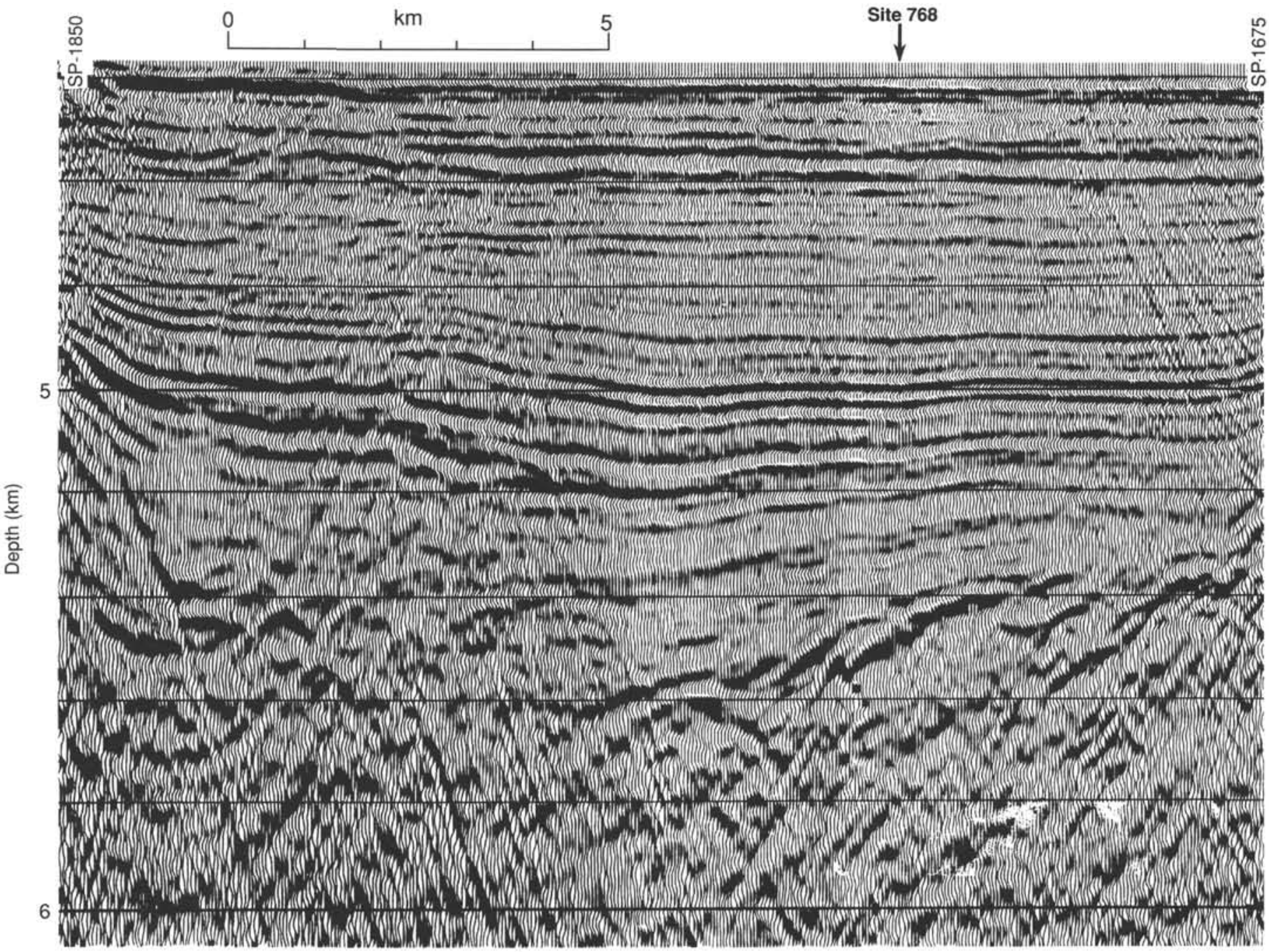

Figure 73. Migrated and depth-corrected multichannel seismic reflection profile of Line SO49-04, expanded between shotpoints 1675 and 1850. Vertical exaggeration is 4×.

Site 768 was located in a position to core the maximum record of sedimentation in the basin (see "Seismic Stratigraphy" section, this chapter). Sediment penetration in Site 768 was 1046 m and basement penetration 225 m. Five major lithologic units were defined at this site, each representing a significant phase in the evolution of the basin.

Unit I (0–123 mbsf) is late Pliocene to Holocene in age and consists of pelagic foraminifer-nannofossil marls with calcareous turbidites and vitric ash beds. The unit is rich in foraminifers, glass, and hornblende; is high in smectite; and contains no quartz. It has a low continentality index (see "Lithostratigraphy" section, this chapter). Diatoms are present at the very top of the unit and disappear below 20 mbsf, never to appear again at the site. The unit was deposited just above the CCD and records volcanic activity and biological productivity.

Unit II (123–652 mbsf) is late Pliocene to middle Miocene in age and consists of greenish gray claystone and siltstone, with silt, sand, and carbonate turbidites. It is rich in quartz and metamorphic grains, low in hornblende, high in illite and chlorite, and low in smectite. Turbidites in the unit are dominated by terrigenous components, and the unit has a high continentality index. The logs show it to be high in K and U. High sedimentation rates characterize this unit, very likely a result of its high component of terrigenous turbidites. Unit II represents a period of high continental influence in the basin, in a setting below the CCD.

Unit III (652–807 mbsf) is early to middle Miocene in age and consists of normally graded beds of sandstone, siltstone, and claystone, with thick tuff beds and rare marlstones. The basal part of the unit is red-brown radiolarian claystone of late(?) early Miocene age. Quartz and glass are present, as well as hornblende in minor amounts. Terrigenous and volcaniclastic turbidites are also present. The unit is high in smectite, low in illite, and very low in chlorite. It has a low continentality index at its base, but a high continentality index in the upper half of the unit. Potassium and uranium are high in the upper part of the unit, but uranium is low in the lower part (red-brown claystone).

Sediment accumulation rates are low in Unit III, compared with the units above and below. An unconformity appears to be present within the upper part of the unit, separating NN8 above from NN5. However, NN5 nannofossils found in the NN8 horizon could indicate reworking. This reworking would indicate a possible hiatus between NN8 and the underlying radiolarian-bearing red clays. Unfortunately, several of the cores are barren of fossils, so some uncertainty remains.

An unconformity was noted within this unit in the seismic record (top of Seismic Sequence 4, at approximately 700 mbsf (see "Seismic Stratigraphy" section, this chapter), and could be tentatively correlated with this hiatus. Consequently, Unit III records a time period that includes the youngest Tertiary volcanic products, low accumulation rates, and a change from oceanic to terrigenous-domination of source material to the basin.

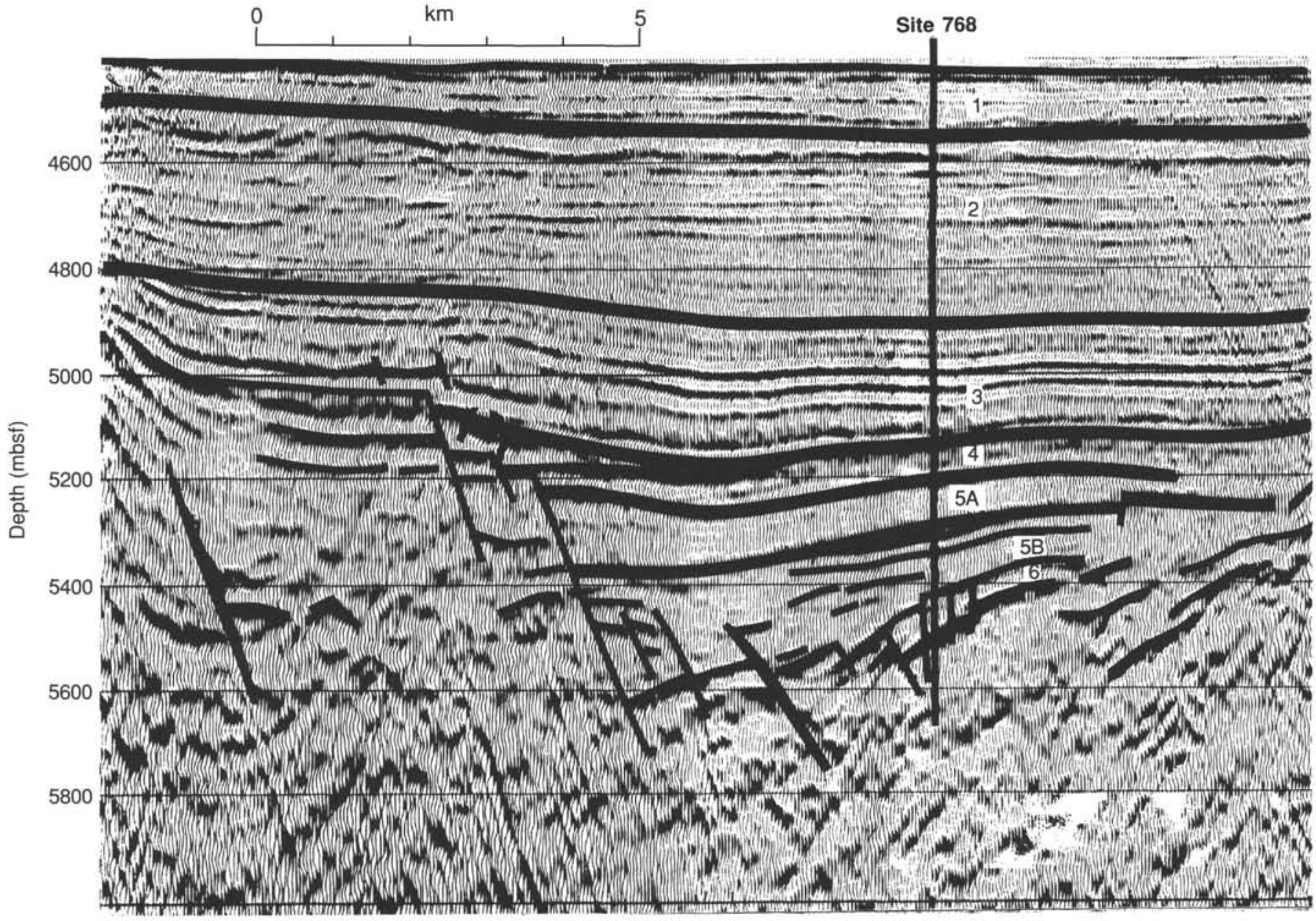

Figure 74. Interpretation of the seismic profile in Figure 73, illustrating the seismic stratigraphy interpreted in the region of Site 768.

Unit IV (807–1004 mbsf) is early Miocene in age and consists of pyroclastic material: coarse lapilli tuff at basal contacts with a matrix of vitric tuff. The unit has very abundant glass and very low quartz and hornblende. The only turbidites present are volcanic. The pyroclastic rocks have low bulk and grain density values, and contain low amounts of potassium and uranium. The sedimentation rate of the tuffs appears to be rapid because no intermixed clay accumulation was noted in the tuffs. Dating of the tuffs and the units below must await onshore studies. Dating of Unit IV was attempted from the paleomagnetism of the tuffs. Accepting the interpretation of several magnetic reversals within the tuffs limits the potential age of the tuffs to Anomaly 5D or 5E.

Unit V (1004–1047 mbsf) is early Miocene in age and consists of an alternation of dark brown claystone and greenish gray tuff. The contact between both rock types is gradational. Tuff beds may be the product of pyroclastic flows or turbidites, whereas claystone represents the background hemipelagic sedimentation. Rare, broken radiolarians found at the base of this unit are consistent with the *Stichocorys wolffii* Zone. The cores contain moderate glass, little quartz, and no hornblende. Potassium is present in moderate quantities and uranium is low. Unit V rests directly on basement and indicates a time of low sedimentation rates prior to the voluminous pyroclastic flows.

Basement rocks (1047–1268 mbsf) included olivine phyric basalt that is pillowed and brecciated and interbedded with basalt sheet flows. Within the drilled basement are two massive sills (1148–1210 mbsf) that are composed of olivine dolerite with a chilled top margin. The basement is cut by southeast-facing normal faults that strike northeast and are parallel to the long axis of the basin.

The basement sequence was divided into eight units, six of which occur as lavas and two as sills. The lavas are rather uniform petrographically and mostly comprise very vesicular olivine-phyric basalts and picritic basalts. None of the actual contacts between the units were seen, and subdivision of the lava sequence was made according to their appearance as either pillowed and brecciated basalts or lava flows. The sills were identified by their thickness, massive nature, and phaneritic grain size, and are composed of olivine dolerites and microgabbro. The two separate sills have different mineralogy, vesicularity, and vein filling.

The paleomagnetic results obtained at Site 768 were outstanding. We recorded an excellent reversal stratigraphy throughout the Gilbert (5 Ma), and possibly Reversals 5D and 5E in the tuffs of Unit IV. We recorded the reversed Cobb Mountain Event at 1.1 Ma. No paleolatitude change is indicated in the sedimentary section. Magnetic susceptibility is high in the upper 180 mbsf of the site, coinciding generally with the abundance of ash in the section. It is very low from 180 to 735 mbsf in the section of terrigenous control. Increasing susceptibility occurs from 735 to 805 mbsf, again coincident with appearances of ash, and it is very high from 805 mbsf to basement in the zone of pyroclastic deposits.

Dissolved sulfate and ammonium distributions up to 200 mbsf are characteristic of organic decomposition during bacterial sulfate reduction. The dissolved calcium and magnesium, silica, and pH profiles indicate the alteration of volcanic material, the formation of smectite, and the dolomitization of biogenic carbonates. The low dissolved silica levels probably explain the absence of diatoms below Unit I.

A good correspondence between the maturity of the organic material and the generation of thermogenic hydrocarbons was observed. The organic-lean pyroclastic sequence yielded high headspace gas concentrations, which indicated a migration of light hydrocarbons.

Logging was successful and included seismic stratigraphy and lithodensity logs, plus a very good BHTV log in the basement and the tuffs. The logs matched the results of physical properties analysis in the cores quite well, including a major velocity increase between the pillow basalts and the sill, which we can recognize as acoustic basement on the seismic line. Borehole breakouts were prominent in the basement, in the sill and the pillows, and in the upper 60 m of the tuffs. Basement breakouts trend approximately 300°, indicating a maximum horizontal stress direction of 030°.

Preliminary interpretations of these data could indicate that the Sulu Sea originated as a backarc basin in the late(?) early Miocene, although its exact time must await basement dating because of uncertainties in the age of the base of Unit 4. However, the initial depositional environment of this basin at Site 768, marked by radiolarian-bearing red clay, does not testify to abundant volcanic arc activity near the basin. The major part of the volcanism deposited on that basement is represented by the 250-m-thick pyroclastic flows that probably accumulated during a short period of time after the oceanic crust of Site 768 was formed.

The depositional depth of the tuffs is not known with certainty, but the presence of radiolarian-bearing red clay just above and below the tuffs could indicate abyssal depths below the CCD. The source of the pyroclastic rocks is not known for certain. The sedimentary section increases in thickness toward the west, and the lower units show bottom lapout to the east on the seismic records, tentatively implying a Cagayan source. We hope to test this idea at Site 769 on the Cagayan Ridge.

Red clay deposition continued above the tuffs, for about 30 m, after which the dominant lithology was greenish claystone. Sands and silts are abundant in the claystone, indicating much turbidity-current deposition. Quartz is abundant in Units II and III, and metamorphic grains are present, indicating a continental source. The clay mineralogy shows high illite and low smectite in these units, reversing in Unit I, again representing a dominant continental source in Units II and III. If the basin was really bounded northwestward by an important volcanic ridge, as the backarc basin model suggests, we should expect more volcanic material reworked in these turbidites.

The sudden development of continent-derived turbidites in the middle Miocene (NN8) and the stratigraphic hiatus in Unit III could be a response to the collision of the Cagayan Ridge with the north Palawan Ridge. Increasing terrigenous influx from the middle Miocene through the late Miocene may coincide with the development of this collision, magnified by the effects of the more recent collision of the Philippine Mobile Belt with the Cagayan, Palawan, and Sulu ridges.

Renewal of volcanism began during NN11 at 255 mbsf but with a noticeable increase in the Pleistocene. This period is also associated with higher oceanic productivity. Onset of volcanism and a decrease in terrigenous turbidites may coincide with the development of the Sulu Trench.

Drilling results at Site 768 could indicate a backarc-spreading origin behind the Cagayan Ridge for the Sulu Sea in early Neogene time. However, the paucity of volcanic-arc material erupted or reworked into this basin raises some doubt about this origin. A different interpretation is to consider this basin as having opened in a manner similar to that of the South China Sea (Taylor and Hayes, 1980, 1983), independent of a volcanic-arc environment. Consequently, the Cagayan Ridge volcanism would have been generated after formation of the oceanic crust in the Sulu Basin. This hypothesis has to be tested by drilling the Cagayan Ridge at Site 769. The complex depositional history of the continent-derived turbidites and brown clays, as well as the stratigraphic hiatus recorded in the sequence, provide a complete record of the Neogene subduction and collisions surrounding the Sulu Sea.

REFERENCES

Baker, P. A., and Kastner, M., 1981. Constraints on the formation of sedimentary dolomites. *Science,* 213:214–216.

Barron, J. A., Nigrini, C. A., Pujos, A., Saito, T., Theyer, F., Thomas, E., and Weinreich, N., 1985. Synthesis of biostratigraphy, central equatorial Pacific, Deep Sea Drilling Project Leg 85: refinement of Oligocene to Quaternary biochronology. *In* Mayer, L., Theyer, F., Thomas, E., et al., *Init. Repts. DSDP,* 85: Washington (U.S. Govt. Printing Office), 905–934.

Berger, W. H., Adelseck, C., and Mayer, L., 1976. Distribution of carbonate in surface sediments of the Pacific Ocean. *J. Geophys. Res.,* 81:2617–2627.

Berggren, W. A., Kent, D. V., Flynn, J. J., and Van Couvering, J. A., 1985a. Cenozoic geochronology. *Geol. Soc. Am. Bull.,* 96:1407–1418.

Berggren, W. A., Kent, D. V., and Van Couvering, J. A., 1985b. The Neogene: Part 2, Neogene geochronology and chronostratigraphy. *In* Snelling, N. J. (Ed.), *The Chronology of the Geological Record.* Geol. Soc. Mem. (London), 10:211–260.

Bernard, B. B., 1979. Light hydrocarbons in marine sediments [Ph.D. dissert.]. Texas A&M Univ., College Station.

Claypool, G. E., and Kvenvolden, K. A., 1983. Methane and other hydrocarbon gases in marine sediment. *Annu. Rev. Earth Planet. Sci.,* 11:299–327.

Demaison, G. J., and Moore, G. T., 1980. Anoxic environments and oil source bed genesis. *AAPG Bull.,* 64:1179–1209.

Ewart, A., 1979. A review of the mineralogy and chemistry of Tertiary-Recent dacitic, latitic, rhyolitic and related salic volcanic rocks. *In* Baker, F. (Ed.), *Trondhjemites, Dacites, and Related Rocks:* Amsterdam (Elsevier), 13–121.

Gartner, S., 1988. Paleoceanography of the mid-Pleistocene. *Mar. Micropaleontol.,* 13:23–46.

Hall, R., 1988a. Plate boundary evolution in the Halmahera region, Indonesia. *Tectonophysics,* 144:337–352.

Hall, R., Audley-Charles, M. G., Banner F. T., Hidayat, S., and Tobing, S. L., 1988b. Late Palaeogene–Quaternary geology of Halmahera, eastern Indonesia: initiation of a volcanic island arc. *J. Geol. Soc. (London),* 145:577–590.

Hamilton, E. L., 1979a. Sound velocity gradients in marine sediments. *J. Acoust. Soc. Am.,* 65:909–922.

Hamilton, W., 1979b. Tectonics of the Indonesian region. *Geol. Surv. Prof. Paper (U.S.),* No. 1078.

Haq, B. U., Hardenbol, J., and Vail, P. R., 1987a. The new chronostratigraphic basis of Cenozoic and Mesozoic sea level cycles. *In* Ross, C. A., and Haman, D., *Timing and Depositional History of Eustatic Sequences: Constraints on Seismic Stratigraphy.* Spec. Publ., Cushman Found. Foraminiferal Res., 24:7–15.

________, 1987b. Chronology of fluctuating sea levels since the Triassic. *Science,* 235:1156–1167.

________, 1988. Mesozoic and Cenozoic chronostratigraphy and eustatic cycles. *In* Wilgus, C. K., Hastings, B. S., Posamentier, H., Van Wagoner, J., Ross, C. A., and Kendall, C. G. St. C. (Eds.), *Sea Level Changes: An Integrated Approach.* Soc. Econ. Paleontol. Mineral., Spec. Publ., 42:71–108.

Harland, W. B., Cox, A. V., Llewellyn, P. G., Pickton, C.A.G., Smith, A. G., and Walters, R., 1982. *A Geologic Time Scale:* Cambridge (Cambridge Univ. Press).

Holloway, N. H., 1981. The North Palawan Block, Philippines: its relation to the Asian mainland and its role in the evolution of the South China Sea. *Bull. Geol. Soc. Malays.,* 14:19–58.

Holm, P. E., 1985. The geochemical fingerprints of different tectonomagmatic environments using hygromagmatophile element abundances of tholeiitic basalts and basaltic andesites. *Chem. Geol.,* 51: 303–323.

Jolivet, L., Huchon, P., and Rangin, C., 1989. Tectonic setting of western Pacific marginal basins. *Tectonophysics,* 160:23–47.
Karig, D. E., 1983. Accreted terrains in the northern part of the Philippine Archipelago. *Tectonics,* 2:211–236.
Kastner, M., and Gieskes, J. M., 1976. Interstitial water profiles and sites of diagenetic reactions, Leg 35, DSDP, Bellingshausen Abyssal Plain. *Earth Planet. Sci. Lett.,* 33:11–20.
Lee, C. S., and McCabe, R., 1986. The Banda-Celebes-Sulu basins: a trapped piece of Cretaceous-Eocene oceanic crust? *Nature,* 322:51–54.
Linsley, B. K., Thunell, R. C., Morgan, C., and Williams, D. F., 1985. Oxygen minimum expansion in the Sulu Sea, western equatorial Pacific, during the last glacial low stand of sea level. *Mar. Micropaleontol.,* 9:395–418.
McCabe, R., Almasco, J. N., and Yumul, G., 1988. Terranes of the Central Philippines. *Earth Sci.,* 1:142–436.
Mankinen, E. A., Donnelly, J. M., and Gromme, C. S., 1978. Geomagnetic polarity event recorded at 1.1 m.y. B.P. on Cobb Mountain, Clear Lake volcanic field, California. *Geology,* 6:653–656.
Martini, E., 1971. Standard Tertiary and Quaternary calcareous nannoplankton zonation. *In* Farinacci, A. (Ed.), *Proceedings of the Second International Conference on Planktonic Microfossils, Roma, 1970:* Rome (Tecnoscienza), 2:739–785.
Mascle, A., and Biscarrat, P. A., 1978. The Sulu Sea: a marginal basin in Southeast Asia. *In* Watkins, J. S., Montadert, L., and Dickerson, P. W. (Eds.), *Geological and Geophysical Investigations of the Continental Margins.* AAPG Mem., 29:373–381.
Mitchell, A.H.G., Hernandez, F., and Dela Cruz, A. P., 1986. Cenozoic evolution of the Philippine Archipelago. *J. Southeast Asian Earth Sci.,* 1:3–22.
Moore, T. C., 1969. Radiolaria: change in skeletal weight and resistance to solution. *Geol. Soc. Am. Bull.,* 80:2103–2108.
Müller, C., 1985. Late Miocene to Recent Mediterranean biostratigraphy and paleoenvironments based on calcareous nannoplankton. *In* Stanley, D. J., and Wezel, F. (Eds.), *Geological Evolution of the Mediterranean Basin:* Berlin-Heidelberg-New York (Springer-Verlag), 471–485.
Müller, C., and Daniel, C. J., 1981. Stratigraphical and paleo-environmental studies (Oligocene-Quaternary) in the Visayan Basin, Philippines. *Newsl. Stratigr.,* 10:52–54.
Murauchi, S., Ludwig, W. J., Den, N., Notta, H., Asanuma, T., Yoshii, T., Kubotera, A., and Hagiwara, K., 1973. Structure of the Sulu Sea and the Celebes Sea. *J. Geophys. Res.,* 78:3437–3447.
Pierce, J. A., 1982. Trace element characteristics of lavas from destructive plate boundaries. *In* Thorpe, R. S. (Ed.), *Andesites: Orogenic Andesites and Related Rocks:* New York (Wiley-Interscience), 525–548.
Rangin, C., 1989. The Sulu Sea: a back-arc basin setting within a Neogene collision zone. *Tectonophysics,* 161:119–161.
Rangin, C., Stephan, J. F., and Müller, C., 1985. Middle Oligocene oceanic crust of South China Sea jammed into Mindoro collision zone (Philippines). *Geology,* 13:425–428.
Riedel, W. R., and Sanfilippo, A., 1978. Stratigraphy and evolution of tropical Cenozoic radiolarians. *Micropaleontology,* 23:81–96.
Romine, K., and Lombari, G., 1985. Evolution of Pacific circulation in the Miocene: radiolarian evidence from DSDP Site 289. *In* Kennett, J. P. (Ed.), *The Miocene Ocean: Paleoceanography and Biogeography.* Mem. Geol. Soc. Am., 163:273–290.
Rottman, M. L., 1979. Dissolution of planktonic foraminifera and pteropods in the South China Sea sediments. *J. Foraminiferal Res.,* 9:41–49.
Saunders, A. D., and Tarney, J., 1984. Geochemical characteristics of basaltic volcanism within back-arc basins. *In* Kokelaar, B. P., and Howells, M. F. (Eds.), *Marginal Basin Geology.* Geol Soc. Spec. Publ. (London), 16:59–76.
Sclater, J. G., Karig, D. E., Lawver, L. A., and Louden, K., 1976. Heat flow, depth, and crustal thickness of the marginal basins of the south Philippine Sea. *J. Geophys. Res.,* 81:309–318.
Stainforth, R. M., Lamb, J. L, Luterbacher, H. P., Beard, J. H., and Jeffords, R. M., 1975. Cenozoic planktonic foraminiferal zonation and characteristics of index forms. *Univ. Kansas Paleontol. Contrib.,* No. 62.
Stephan, J. F., Blanchet, R., Rangin, C., Pelletier, B., Letouzey, J., and Müller, C., 1986. Geodynamic evolution of the Taiwan-Luzon-Mindoro Belt since the late Eocene. *Tectonophysics,* 125:245–268.
Tarney, J., Wood, D. A., Saunders, A. D., and Marsh, N.G.J., 1981. Geochemical aspects of back-arc spreading in the Scotia Sea and western Pacific. *Philos. Trans. R. Soc. London, Ser. A,* 300:263–285.
Taylor, B., and Hayes, D. E., 1980. The tectonic evolution of the South China Basin. *In* Hayes, D. E. (Ed.), *Tectonic and Geologic Evolution of Southeast Asian Seas and Islands.* Am. Geophys. Union Monogr., 23:89–104.
________, 1983. Origin and history of the South China Sea Basin. *In* Hayes, D. E. (Ed.), *Tectonic and Geologic Evolution of Southeast Asian Seas and Islands* (Pt. 2). Am. Geophys. Union Monogr., 27: 23–56.
Thompson, P. R., Bé, A.W.H., Duplessy, J. C., and Shackleton, N. J., 1979. Disappearance of pink-pigmented *Globigerinoides ruber* at 120,000 yr B.P. in the Indian and Pacific oceans. *Nature,* 280:554–558.
Tissot, B. P., and Welte, D. H., 1984. *Petroleum Formation and Occurrence* (2nd ed.): Berlin-Heidelberg-New York (Springer-Verlag).

Ms 124-111

NOTE: All core description forms ("barrel sheets") and core photographs have been printed on coated paper and bound as Section 3, near the back of the book, beginning on page 423.

Summary Log for Site 768

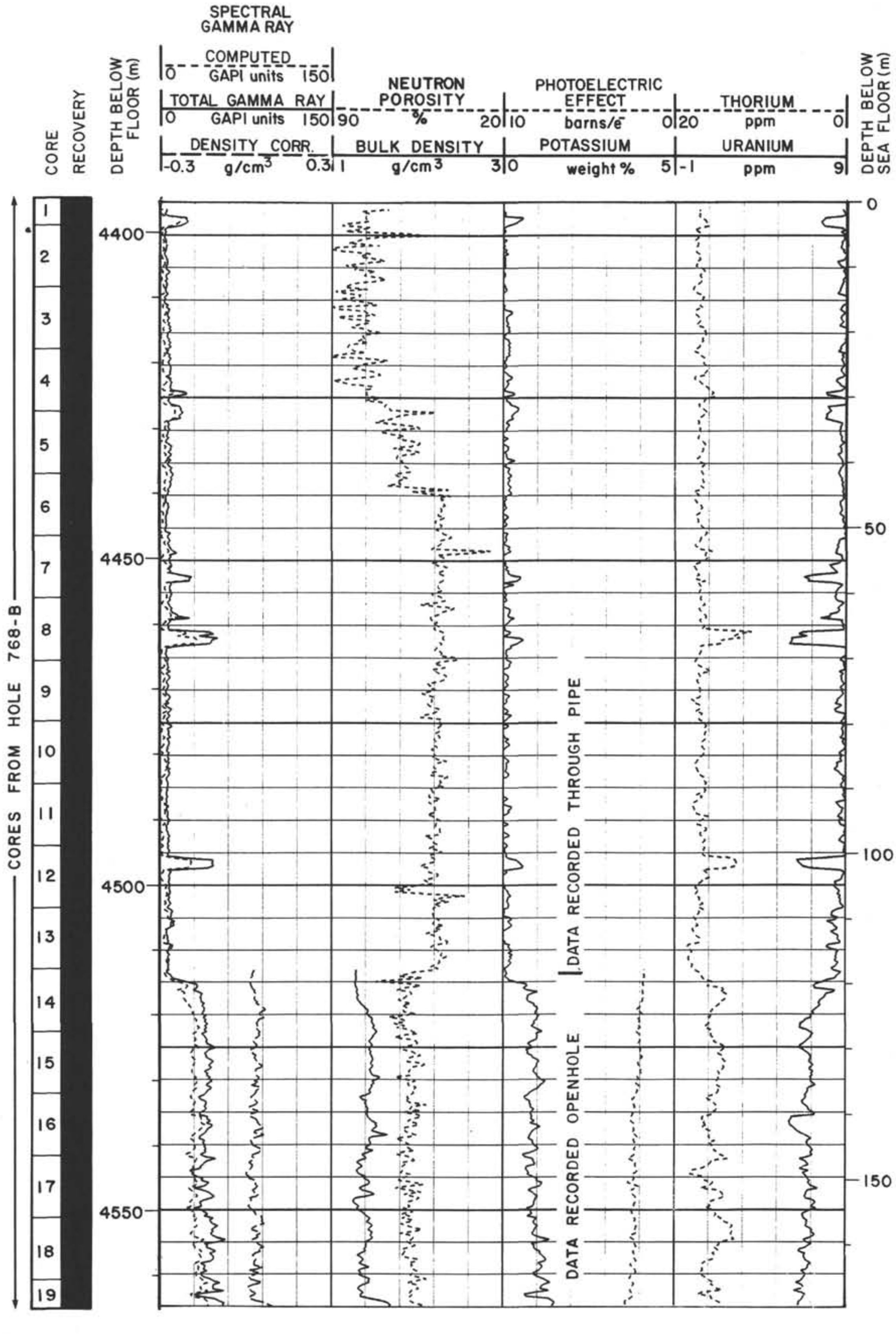

Summary Log for Site 768 (continued)

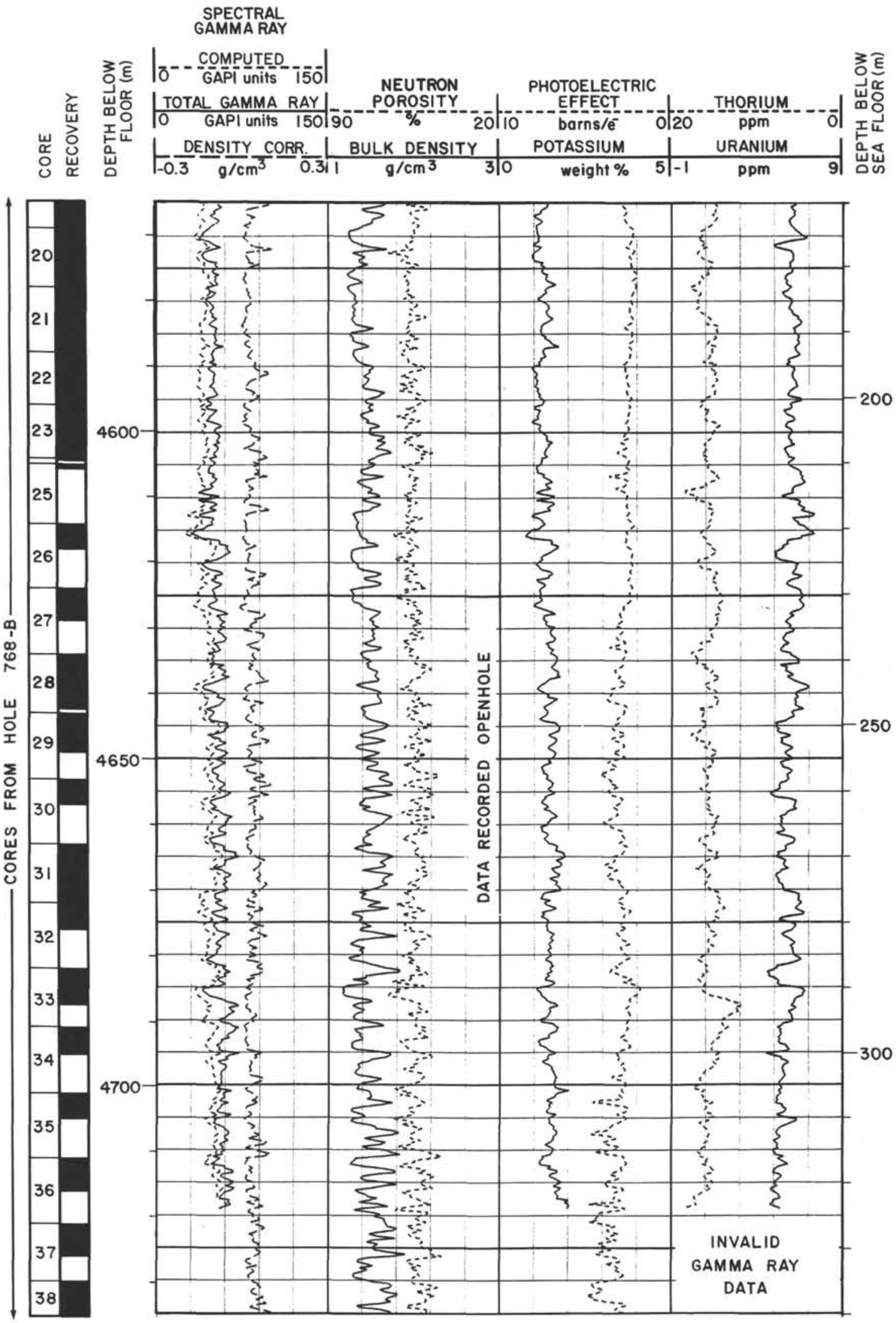

Summary Log for Site 768 (continued)

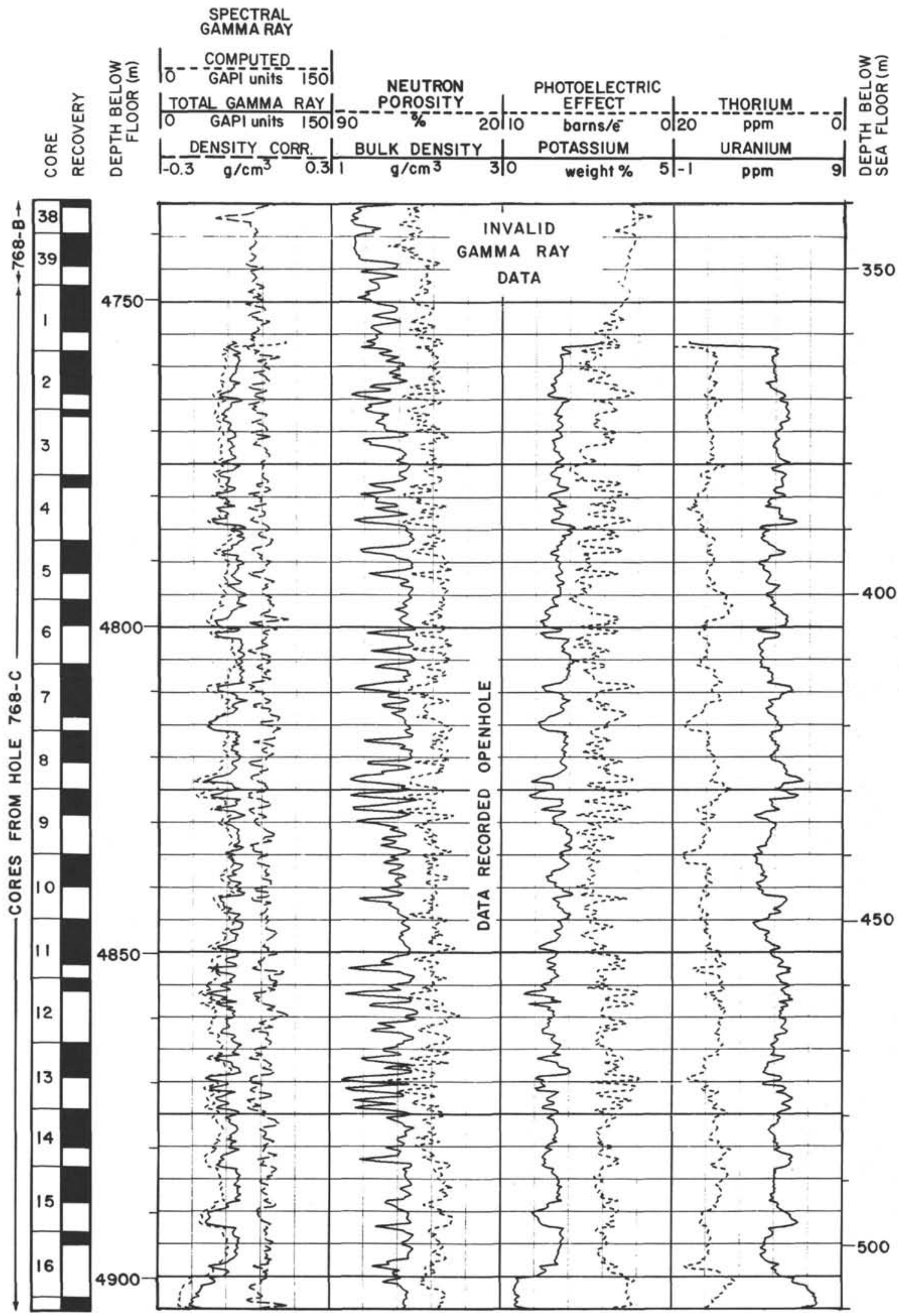

Summary Log for Site 768 (continued)

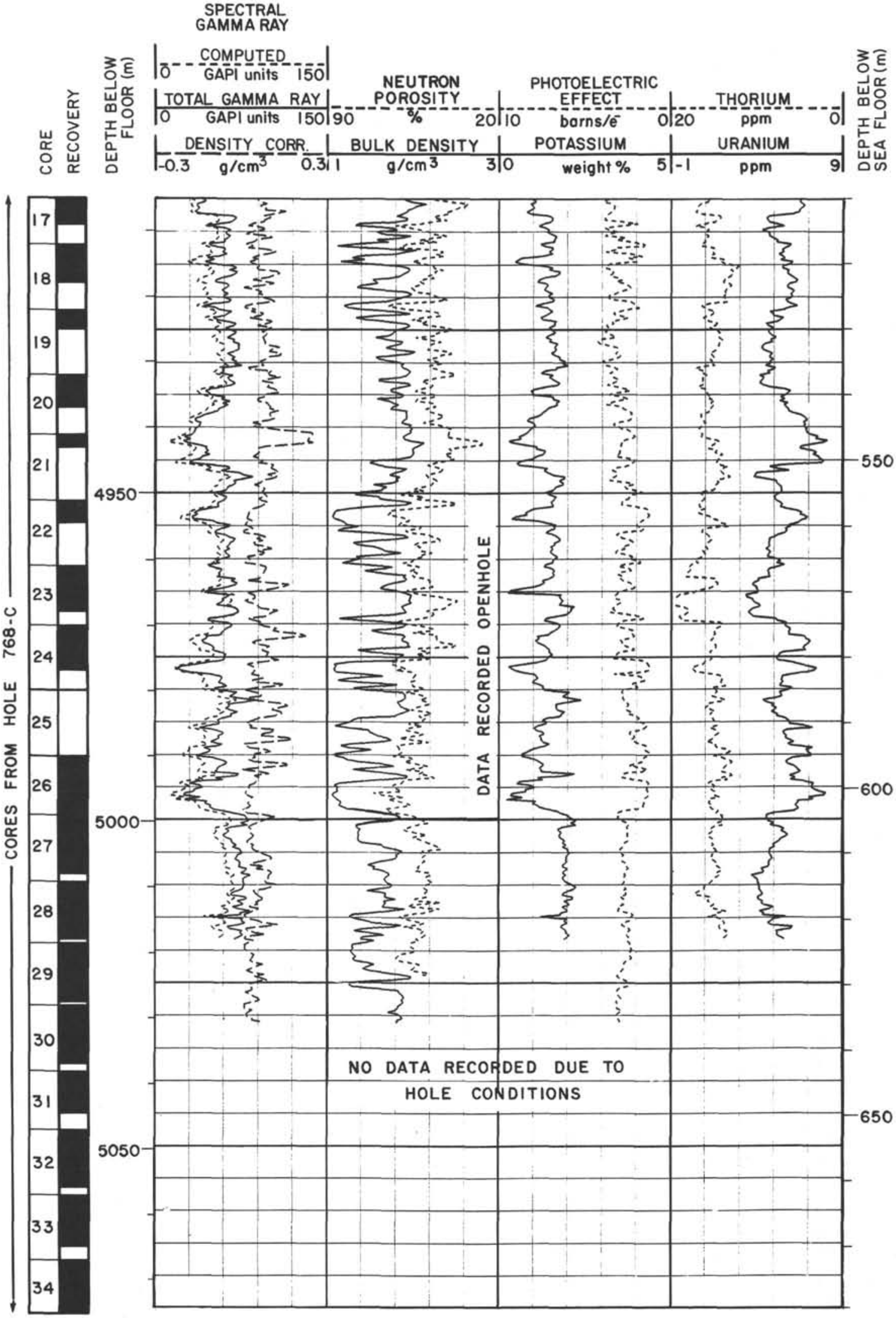

Summary Log for Site 768 (continued)

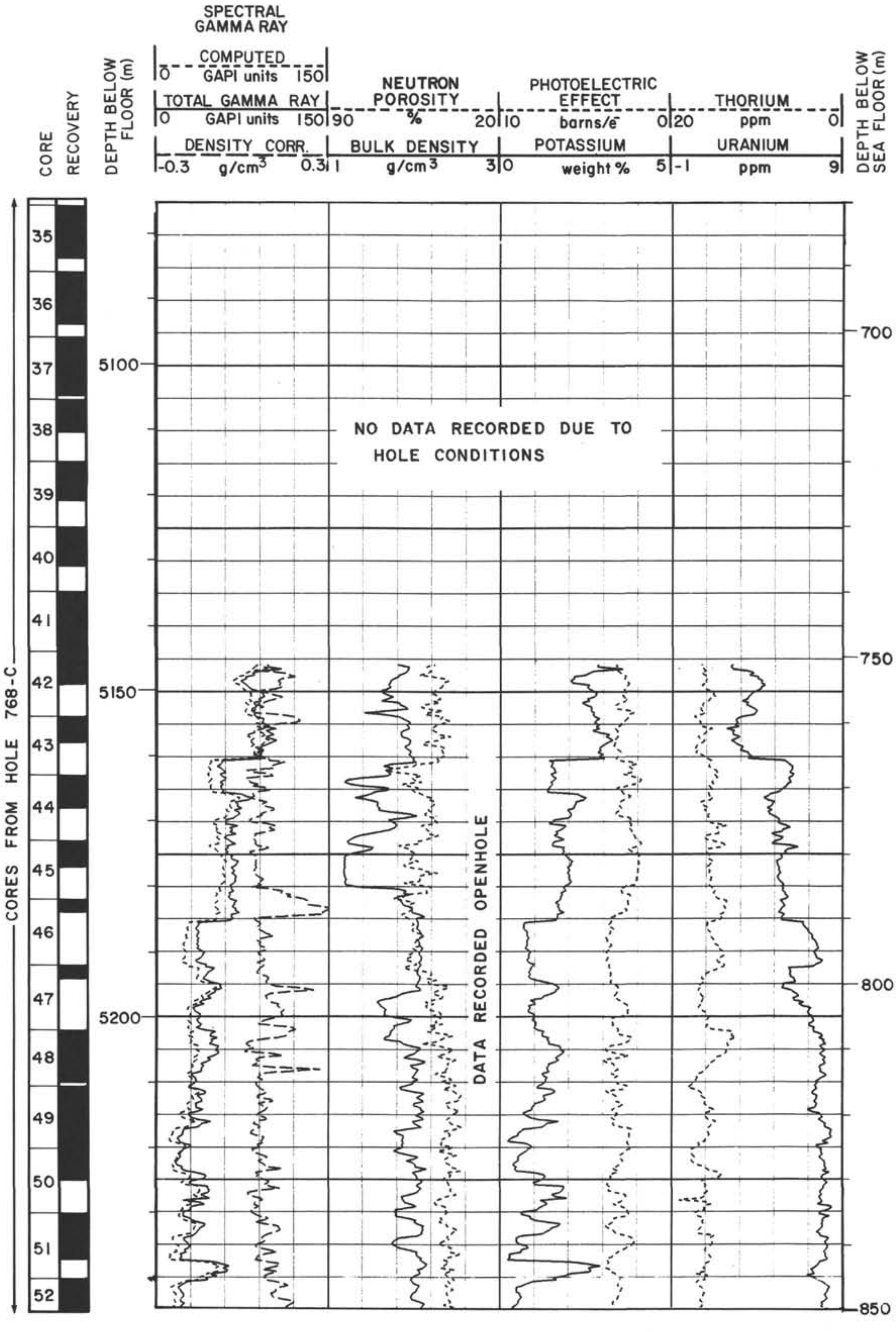

Summary Log for Site 768 (continued)

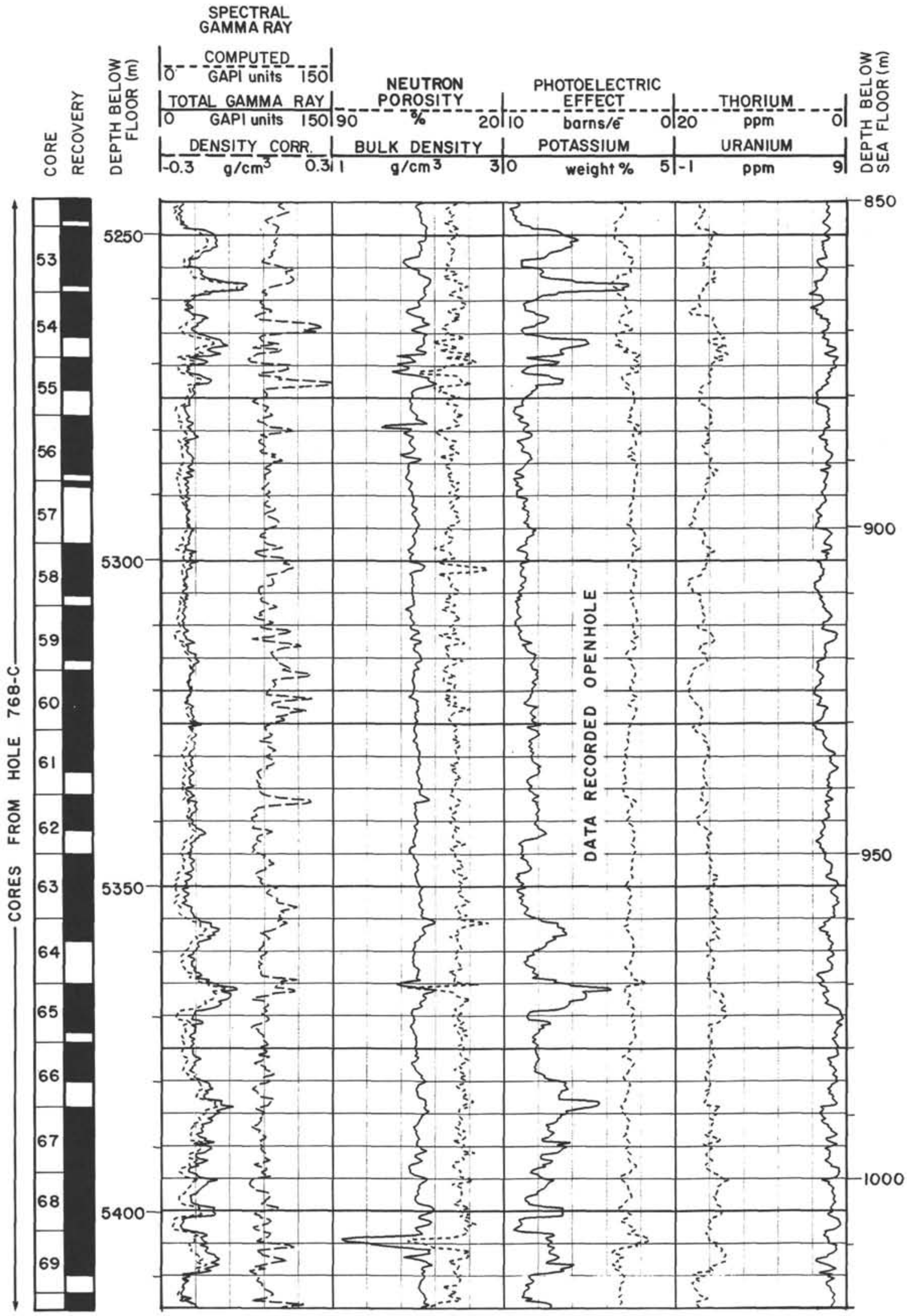

Summary Log for Site 768 (continued)

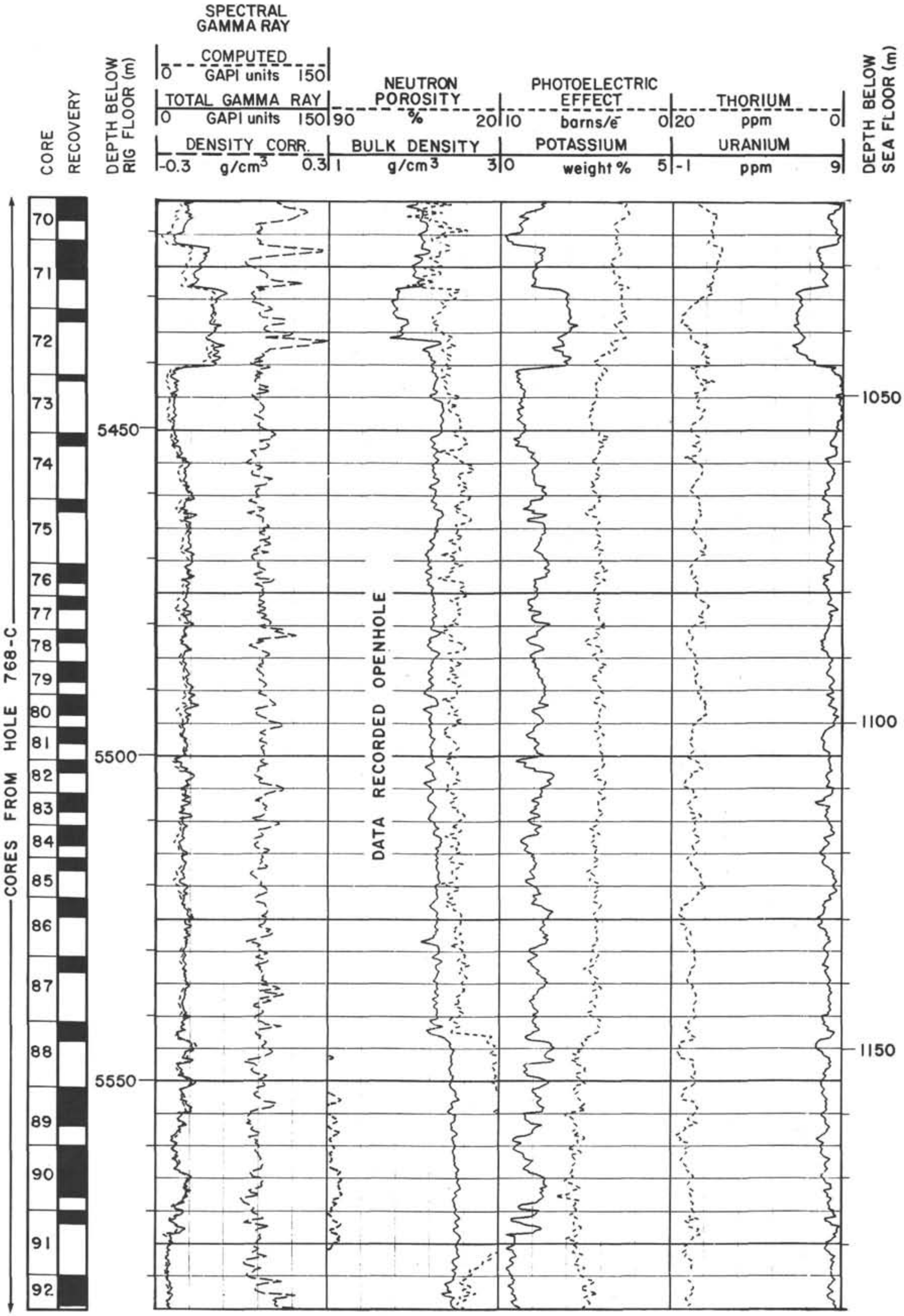

Summary Log for Site 768 (continued)

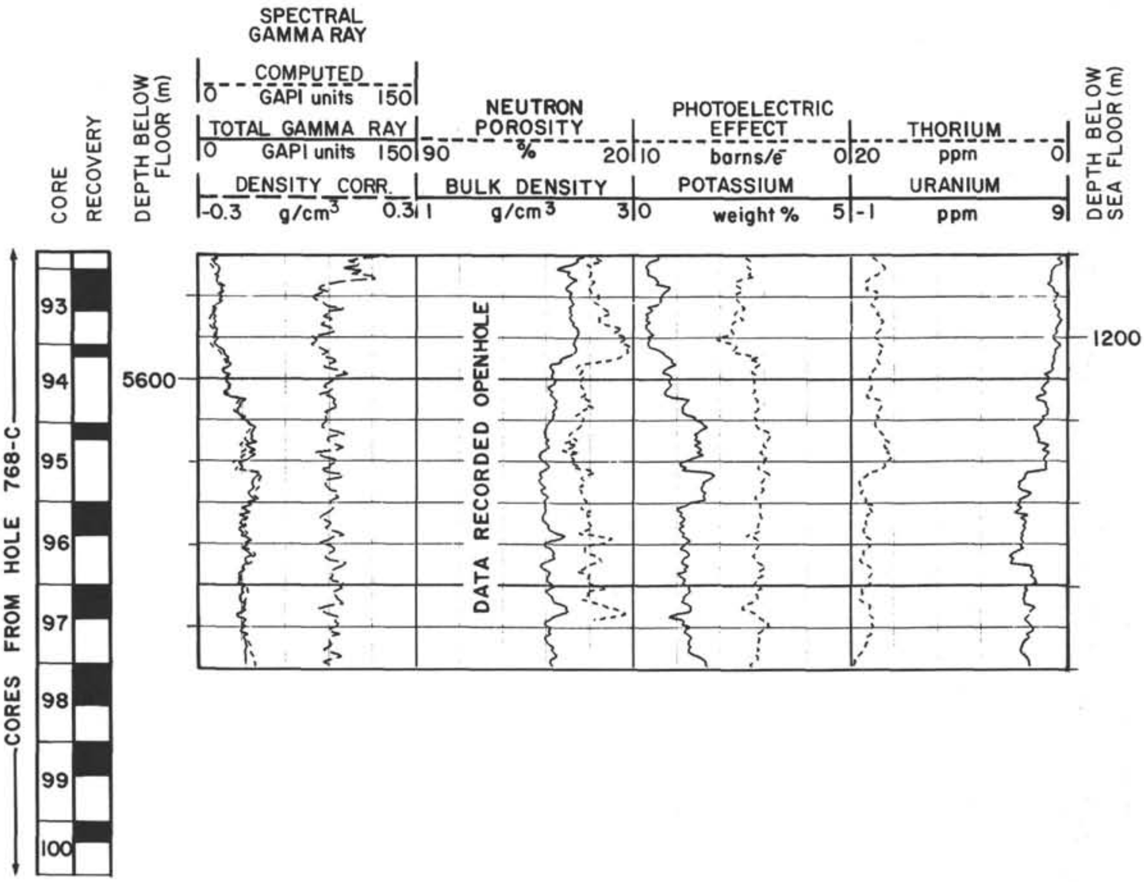

Summary Log for Site 768 (continued)

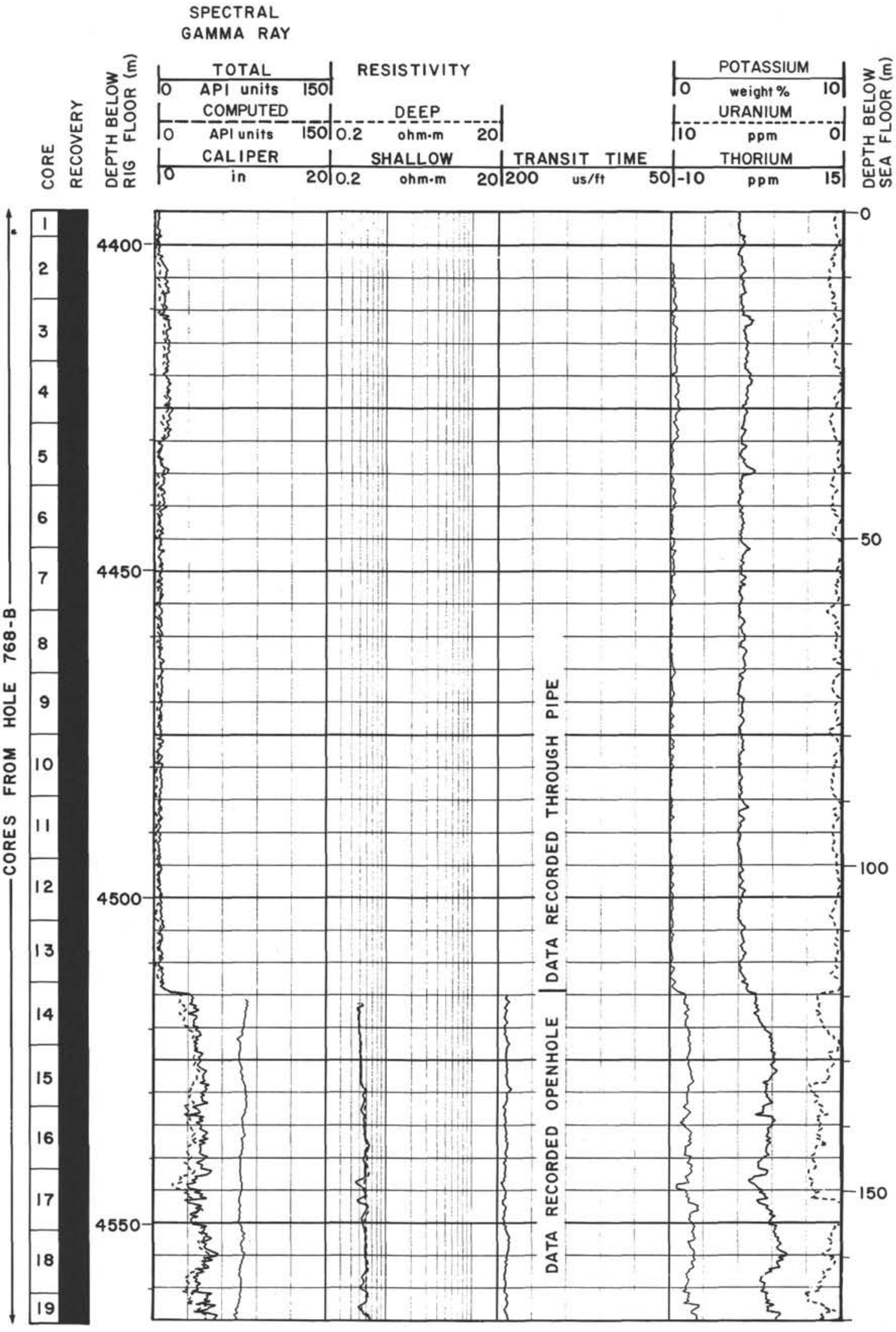

Summary Log for Site 768 (continued)

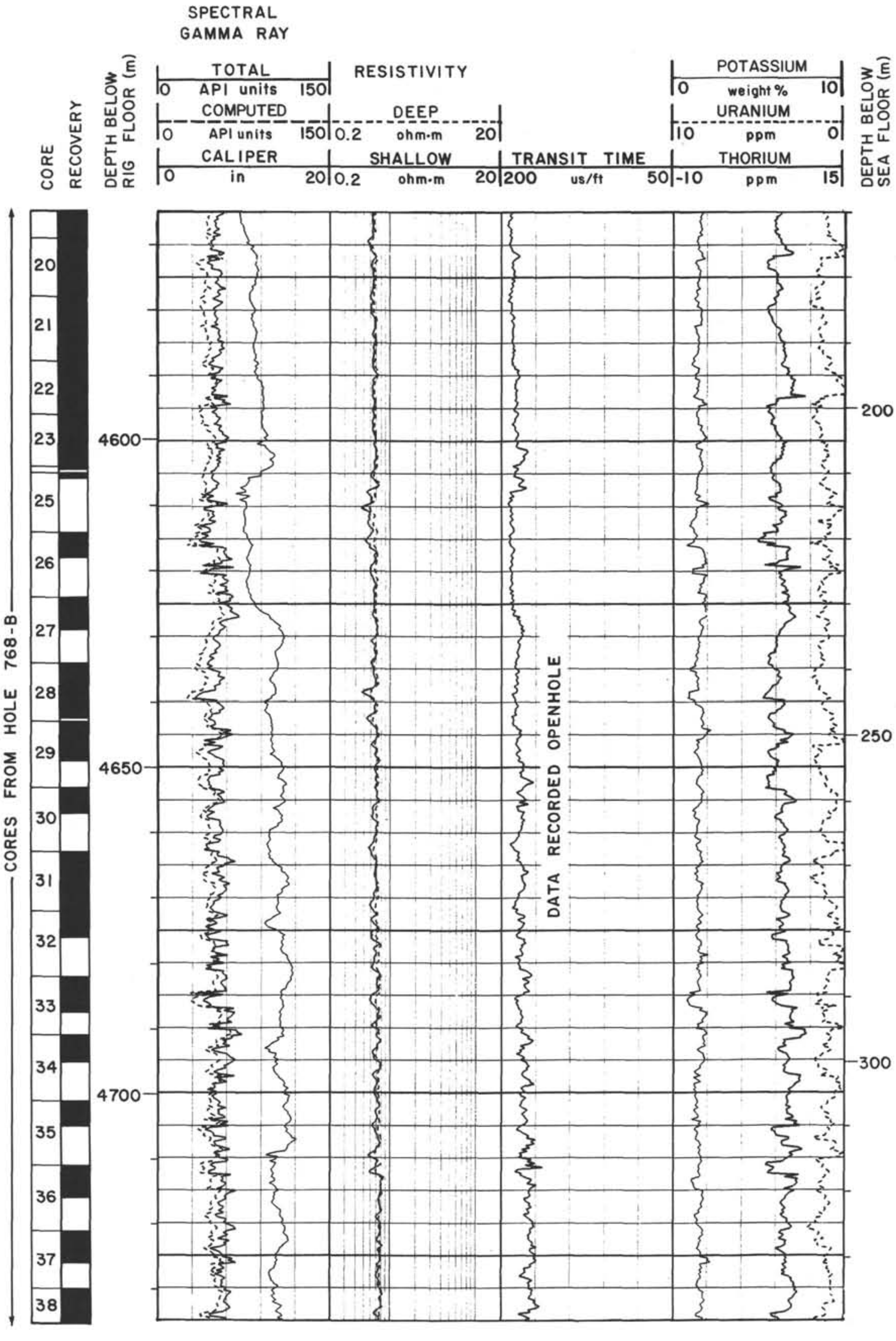

Summary Log for Site 768 (continued)

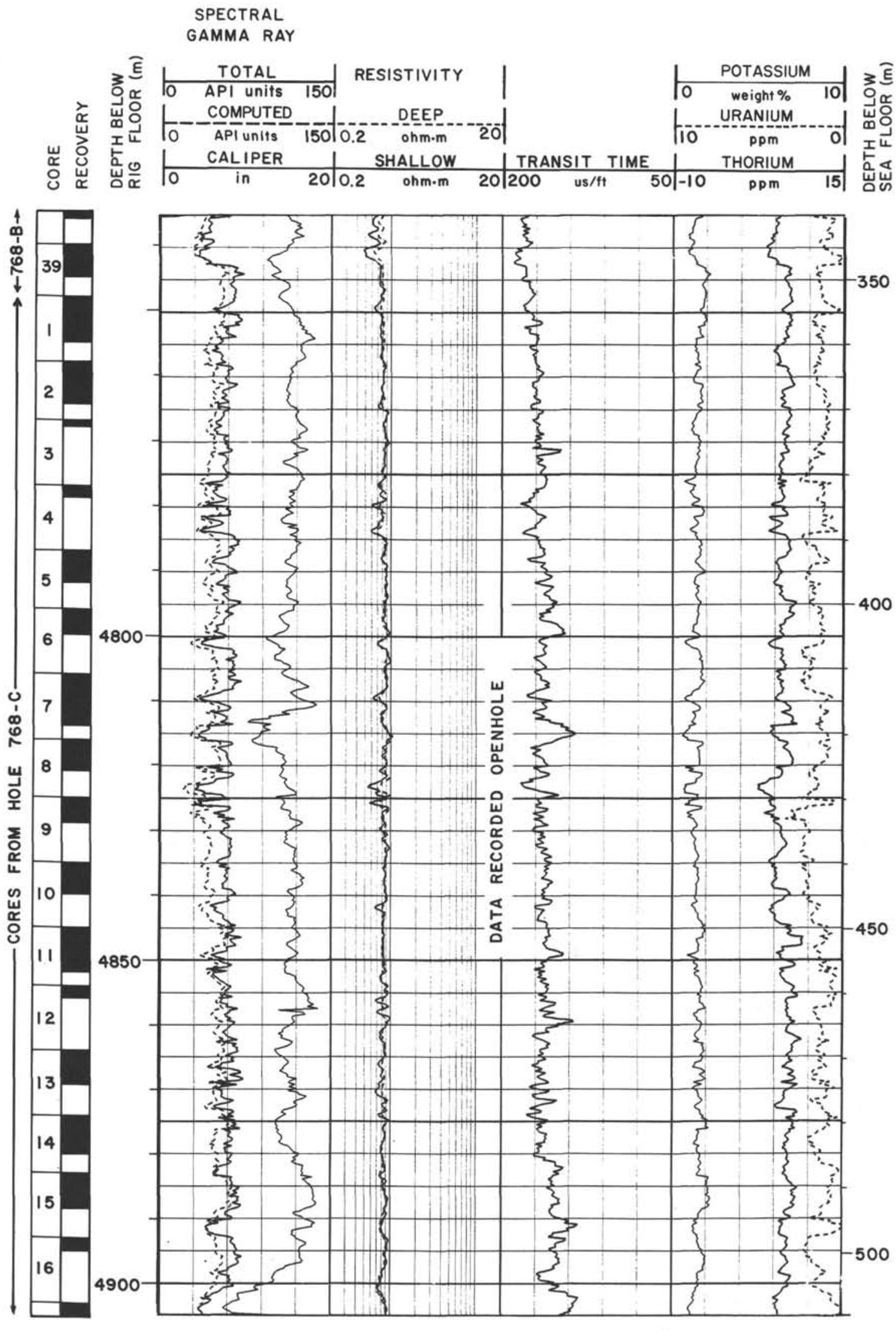

Summary Log for Site 768 (continued)

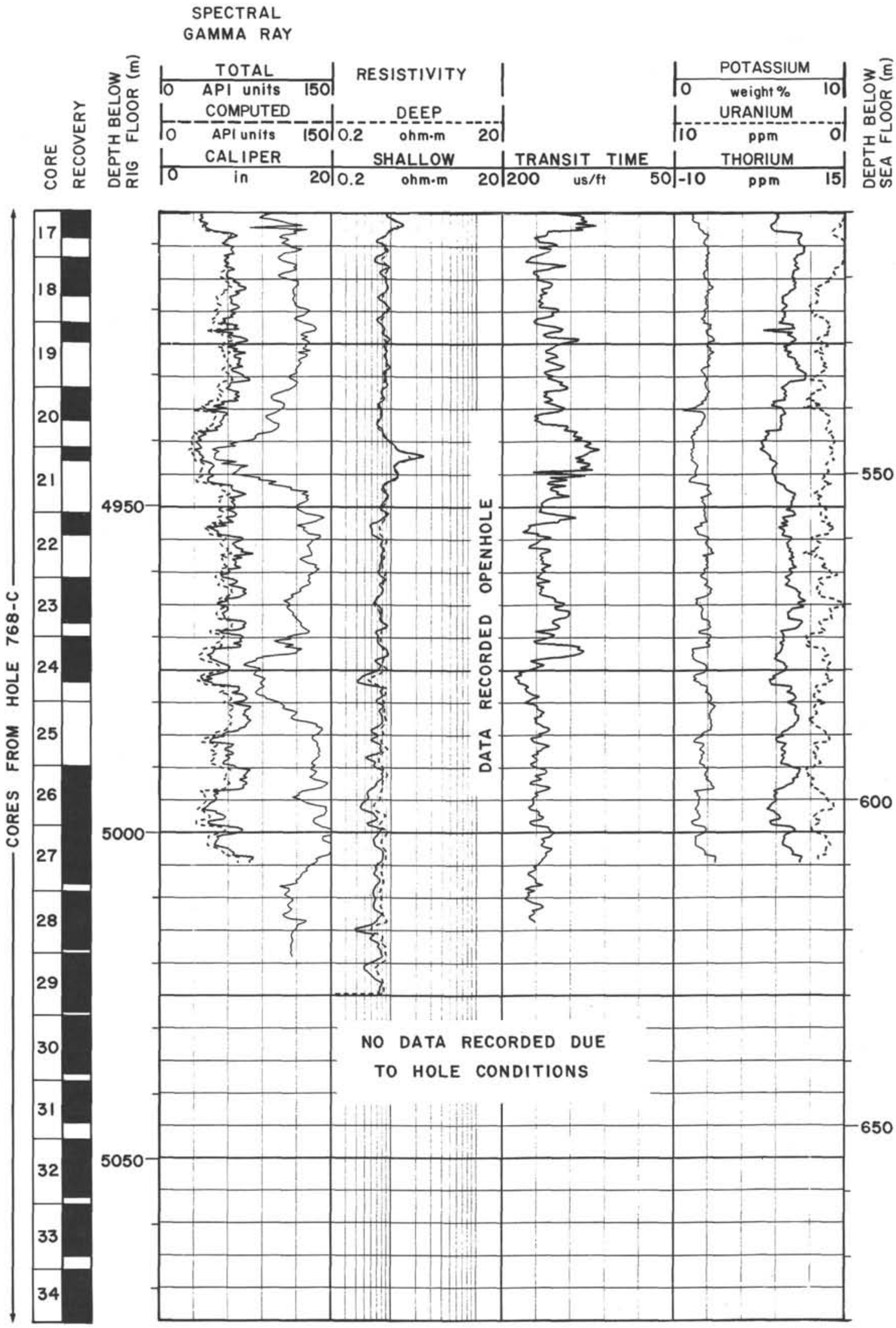

Summary Log for Site 768 (continued)

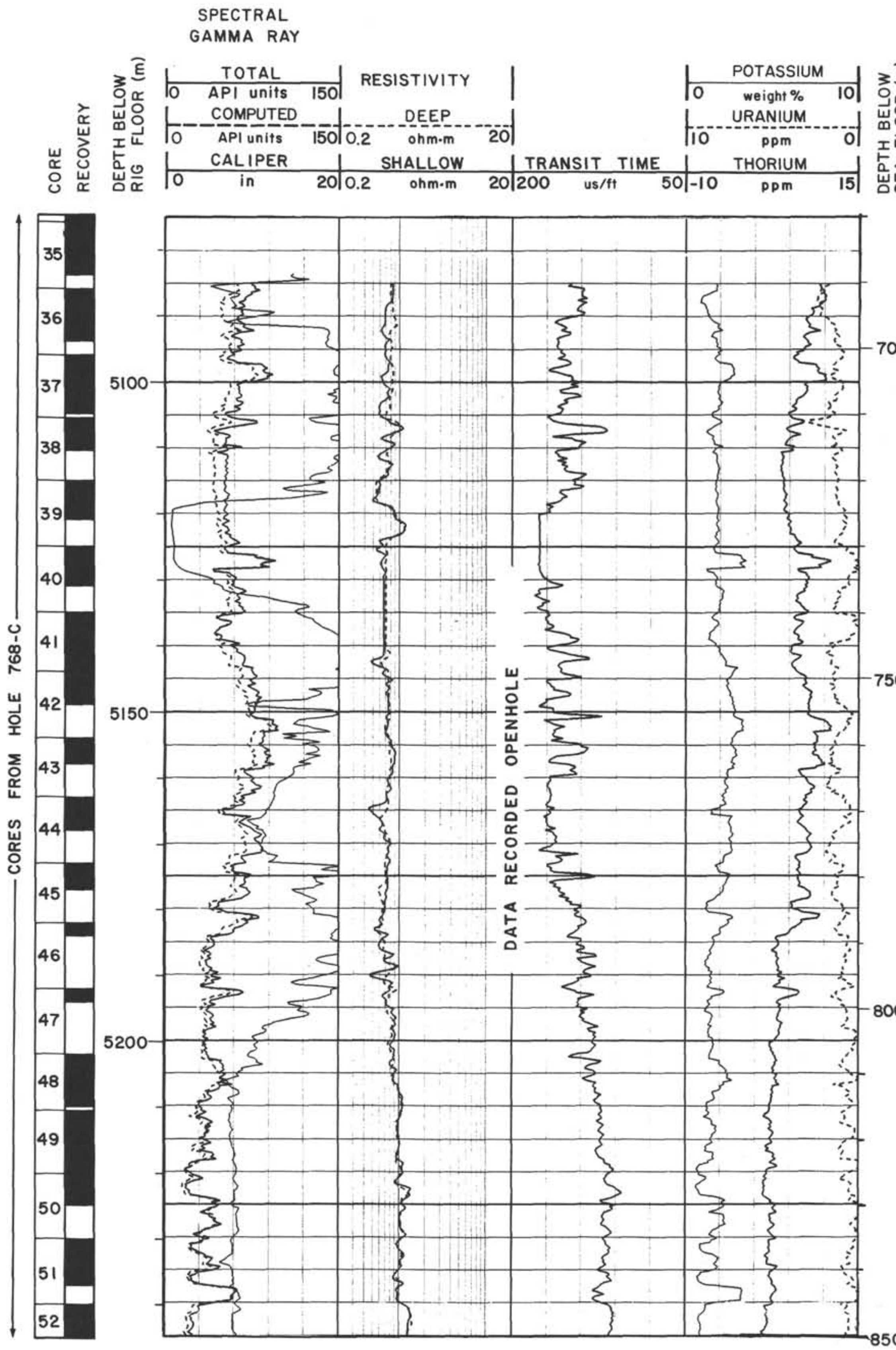

Summary Log for Site 768 (continued)

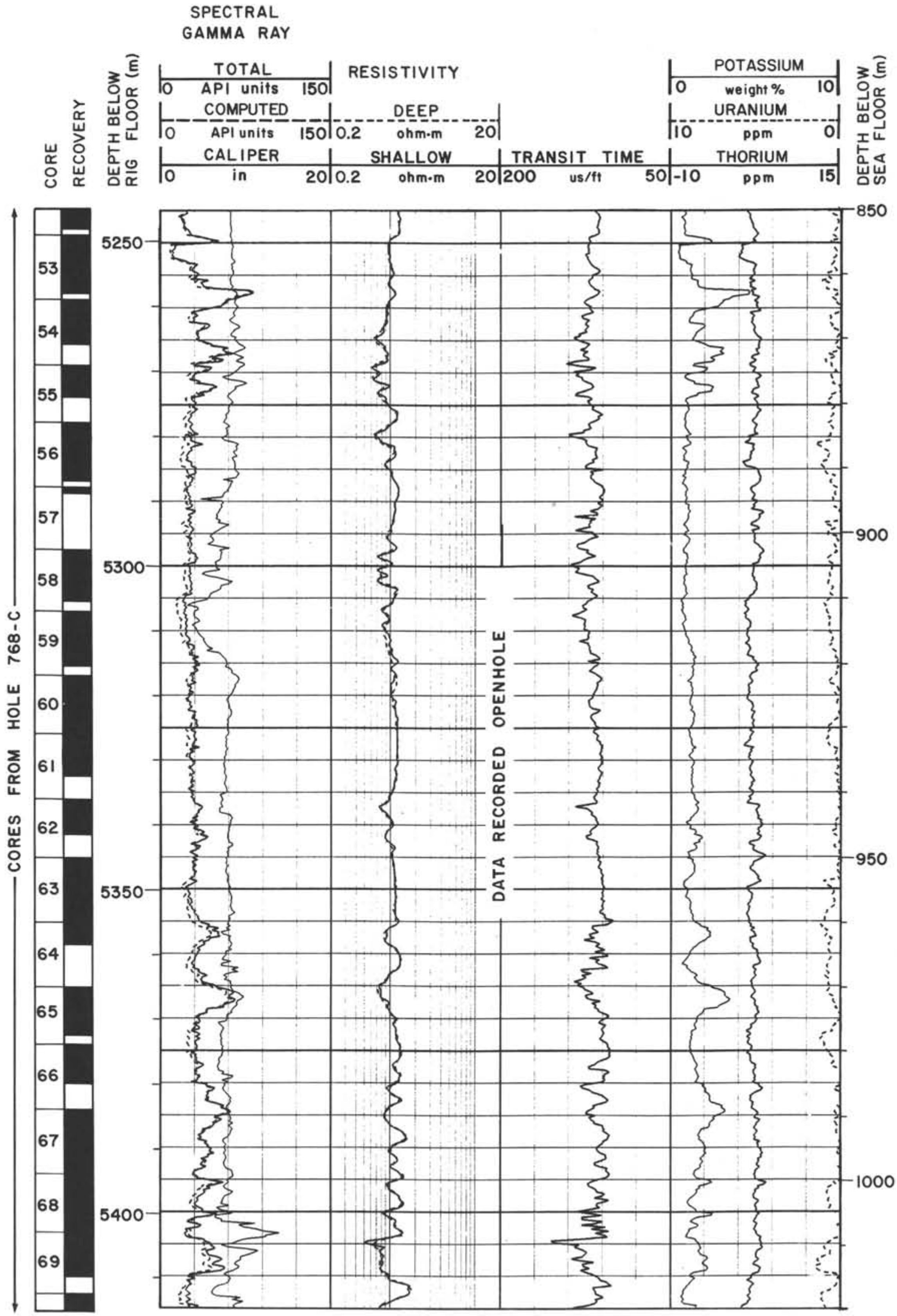

Summary Log for Site 768 (continued)

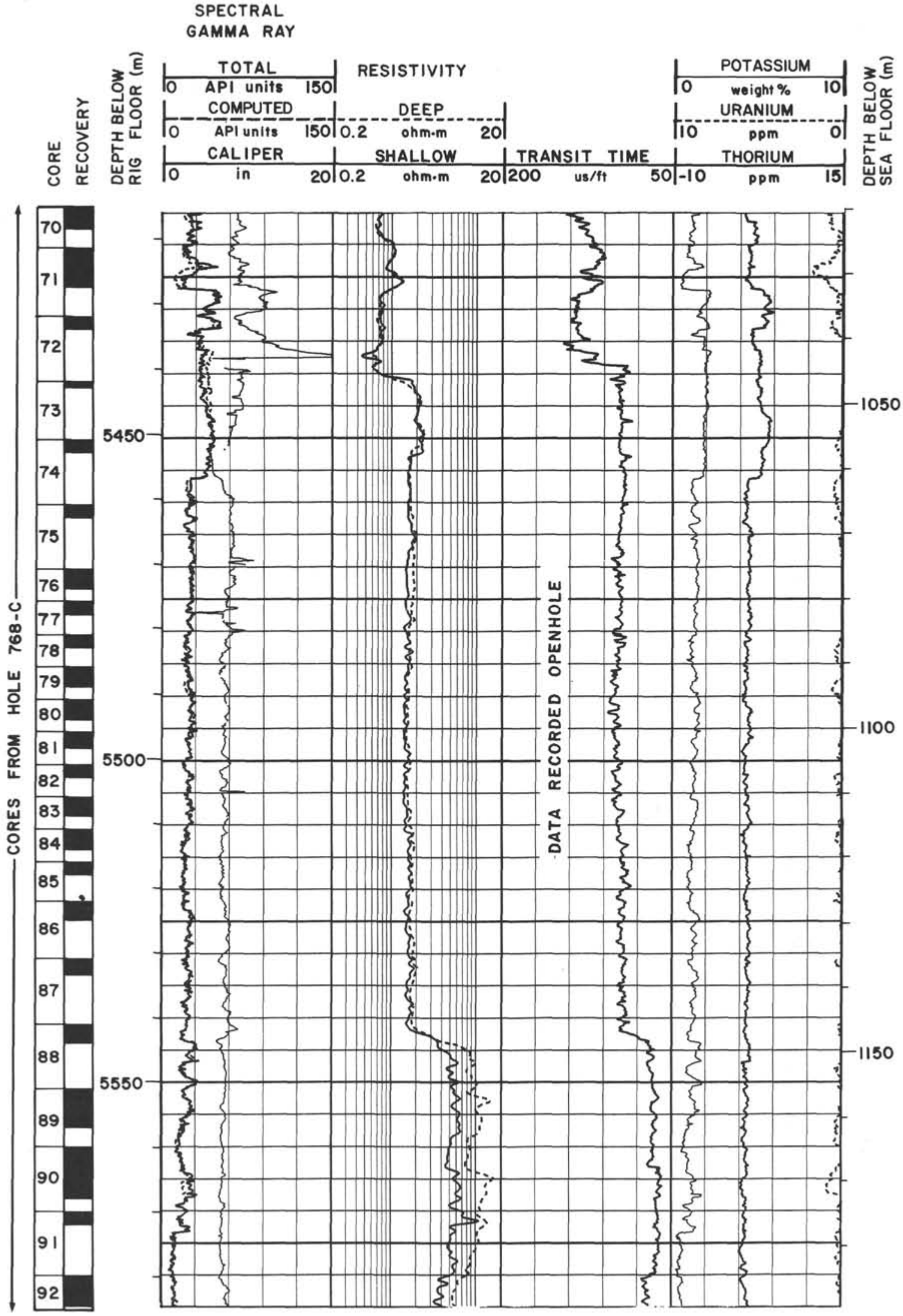

Summary Log for Site 768 (continued)